

Water Adsorption and
Ion Induced Defect Formation:
A Comparative Study of
Graphene and Noble Metal Surfaces

I n a u g u r a l - D i s s e r t a t i o n

zur

Erlangung des Doktorgrades

der Mathematisch-Naturwissenschaftlichen Fakultät

der Universität zu Köln

vorgelegt von

Diplom-Physiker Sebastian Standop

aus Köln

Köln 2013

Erster Berichterstatter: Prof. Dr. Thomas Michely
Zweiter Berichterstatter: Prof. Dr. Markus Morgenstern

Tag der mündlichen Prüfung: 28.06.2013

Abstract

The thesis at hand is subdivided into parts. In the first part we study the thermodynamics and structure of water adsorption on graphene and noble metal surfaces. The second part of this thesis is dedicated to surface damage caused by grazing incidence ion bombardment of graphene on Ir(111). Both parts are completed by a comparison of the various sample systems.

We study the structure and stability of the first water layer on Pt(111) by variable temperature scanning tunneling microscopy. Two structures observed previously by diffraction techniques are imaged for coverages at or close to completion of the wetting layer. At 140 K only a $\sqrt{37} \times \sqrt{37}$ R25.3° superstructure can be established, while at 130 K also a $\sqrt{39} \times \sqrt{39}$ R16.1° superstructure with slightly higher molecular density is formed. In the temperature range under concern the superstructures reversibly transform into each other by slight changes in coverage through adsorption or desorption. The superstructures exhibit a complex pattern of molecules in different geometries. We find that a high Pt step edge density considerably increases the long range order of the equilibrium superstructures, presumably due to the capability of step edges to trap residual adsorbates from the surface. Passivating the step edges with CO or preparing a flat metal surface leads to the formation of disordered structures, which still show the same structural elements as the ordered ones. Co-adsorption of Xe and CO proves that the water layer covers the metal surface completely. Moreover, we determine the two-dimensional crystal structure of Xe on top of the chemisorbed water layer which exhibits a Xe-Xe distance close to the one in bulk Xe and a rotation angle of 90° between the close-packed directions of Xe and the close-packed directions of the underlying water layer. CO is shown to replace H₂O on the Pt(111) surface as has been deduced previously. Finally, a so far not understood restructuring of the adlayer by an increased tunneling current has been observed.

We present experimental data regarding the wetting behaviour and structure formation of water on Ir(111). Studying the thermodynamics of water adsorption and pointing out the possibility to form a wetting layer, we perform a coverage dependent analysis of the sub-monolayer regime. We show that water molecules form planar, polar clusters upon adsorption. A continuous water layer forms out of the cluster phase for $\Theta > 0.5$ ML. The molecular arrangement is nearly identical to the wetting layer observed on Pt(111).

The water growth mode changes from wetting to non-wetting for $\Theta > 1$ ML as the closed water monolayer is hydrophobic. For both Pt(111) and Ir(111), we demonstrate that tunneling of electrons into the antibonding state or from the bonding state of H₂O leads to dissociation of the molecules and a corresponding reordering of the adlayer into a $\sqrt{3} \times \sqrt{3}$ R30°-structure.

An analogous study is carried out for water adsorption on a graphene covered Ir(111) surface. We show that water dewets graphene at 20 K and forms three-dimensional, electronically insulating clusters aligned in the Gr/Ir(111) moiré for $\Theta < 3.0$ ML. Higher coverage results in coalescence and the formation of an amorphous adlayer. The occurrence of this structure can be promoted by an increase of the adsorption temperature above 100 K.

By combining ion beam experiments and atomistic simulations we study the production of defects in graphene on Ir(111) under grazing incidence of low energy noble gas ions. Low fluences are chosen to make the damage patterns of individual ions visible. We demonstrate that the ions are channeled in between graphene and the substrate, giving rise to chains of vacancy clusters, and control the defect structure via tuning of the bombardment parameters. Combining our experiments on thermal stability of defects and density functional theory calculations, we discuss the atomic structure of defects in detail and show that their edges are bending down towards the substrate to saturate dangling bonds by the metal surface. With the onset of vacancy cluster mobility around 800 K, the vacancies sense formation energy differences within the graphene moiré supercell, which paves the way towards the formation of a graphene nanomesh.

In order to realize this structure a transition from isolated ion impacts towards a defect density in the magnitude of one per moiré cell has to be accomplished. We discuss the sample morphology and thermal evolution of the damage patterns following prolonged ion exposure. We show that the temperature during bombardment is of great importance to drive the carbon vacancies to these sites, where the formation energy is lowest, and thus allow for an immediate reconstruction of the graphene layer. Elaborating appropriate parameters for the formation of a high quality nanomesh regarding ion energy and fluence, we give an experimental realization of this structure.

Frequently used Symbols and Abbreviations

ARPES	-	Angle Resolved Photo-Emission Spectroscopy
CVD	-	Chemical Vapor Deposition
DFT	-	Density Functional Theory
(L)DOS	-	(Local) Density of States
DV	-	Divacancy, Double Vacancy
fcc	-	face centered cubic
GNM	-	Graphene Nano-Mesh
HAS	-	Helium-Atom Scattering
hoc	-	high-order commensurate
HOPG	-	Highly Ordered Pyrolytic Graphite
L	-	Langmuir, $1\text{ L} = 1 \times 10^{-6}\text{ Torr} \cdot \text{s} \approx 1.33 \times 10^{-6}\text{ mbar} \cdot \text{s}$
LEED	-	Low-Energy Electron Diffraction
MD	-	Molecular Dynamics
ML	-	Monolayer
MLE	-	Monolayer Equivalents
PKA	-	Primary Knock-On Atom
QMS	-	Quadropole Mass Spectrometer
STS/STS	-	Scanning Tunneling Microscopy/Spectroscopy
SV	-	Single Vacancy
SW	-	Stone-Wales
TDS	-	Thermal Desorption Spectroscopy
TEM	-	Transmission Electron Microscopy
TPG	-	Temperature Programmed Growth
UHV	-	Ultra High Vacuum
WPE	-	Wigner-Polanyi-Equation
XAS	-	X-Ray Adsorption Spectroscopy
XPS	-	X-Ray Photoemission Spectroscopy

Contents

I	Introduction	1
II	Water Adsorption	7
1	Fundamentals: Interaction of Water Molecules with Metal Surfaces and Graphene	9
1.1	Water Molecule Characteristics	10
1.2	General Aspects of Water Adsorption on Metals	11
1.3	Water Adsorption on Pt(111)	14
1.4	Water Adsorption on Ir(111)	21
1.5	Water Adsorption on Graphene	22
1.6	Manipulation of the Wetting Layer	26
2	Experimental	27
2.1	The Scanning Tunneling Apparatus TuMA II	28
2.2	Scanning Tunneling Microscopy	29
2.3	Thermal Desorption Spectroscopy	30
2.4	Sample Preparation	33
2.5	Preparation of H ₂ O Adsorbate Layers	34
3	Water Adsorption on Pt(111)	39
3.1	Influence of the Step Edge Density on the Structure of the Adlayer	40
3.2	The Ordered Structures and their Phase Diagram	45
3.3	Probing the Molecular Structure via Coadsorption	51
3.4	Manipulation of the Wetting Layer	54
3.5	Experimental Proof of the Structural Model	63
4	Water Adsorption on Ir(111)	69
4.1	Thermodynamics of Water Adsorption on Ir(111)	70
4.2	Structure and Stability of the Wetting Layer	75
5	Water Adsorption on Graphene	87
5.1	Thermodynamics of Water Adsorption on Graphene	88
5.2	Structure of the Water Adlayer	92
6	Comparison	99

III	Ion Induced Defect Formation	103
7	Fundamentals: Ion Surface Interaction and Defect Production	105
7.1	Ion Bombardment	106
7.2	Defect Production and Evolution	108
7.3	Grazing Incidence	112
7.4	Defects in Graphene	113
8	Experimental	123
8.1	Experimental Setup	124
8.2	Calibration of the Ion Flux	124
8.3	Sample Preparation	125
8.4	Molecular Dynamics Simulations	126
8.5	Density Functional Theory Calculations	128
9	Grazing Incidence Ion Impacts on Graphene	131
9.1	Defect Formation via Interface Channeling	132
9.2	Variation of Ion Energy and Species	145
9.3	Thermal Stability	148
9.4	Structure of Defects	151
10	Pattern Formation in Graphene: Towards a Graphene Nanomesh	159
10.1	Morphology and Thermal Evolution	160
10.2	Irradiation at Elevated Temperatures	166
10.3	Graphene Nanomesh	170
10.4	Looking for a Bandgap	174
11	Comparison	177
IV	Summary and Outlook	181
V	Appendix	191
A	Deutsche Kurzzusammenfassung (<i>German Abstract</i>)	193
B	Liste der Teilpublikationen (<i>List of Publications</i>)	197
C	Danksagung (<i>Acknowledgements</i>)	199
D	Bibliography	201
E	Offizielle Erklärung	221

PART I

Introduction

"Ice is central to climate, geology and life. Understanding its behaviour is essential for predicting the future of our planet and unravelling the emergence of life in the Universe." [1]

This quote illustrates the importance of water in its solid state. It is taken from a recent Nature article entitled "Ten things we need to know about ice and snow" in which the author states that the mechanism underlying environmental processes remain largely unknown which requires a better understanding of chemical reactions in ice and snow. In particular he asks: "What is the surface structure of ice?" [1] As the molecular order of ice breaks down several layers below the crystal surface already, the molecular arrangement is expected to be very sensitive towards impurities and temperature changes. In the first part of this work we will address this topic in a study of thin water films adsorbed on various crystal surfaces.

Water on metal surfaces is one of the most studied adsorbate systems in surface science [2, 3]. Here the dense-packed Pt(111) surface plays a decisive role as it catalytically promotes H₂O formation which finds prominent use in today's fuel cells. This technique may pave the way to a clean and renewable energy supply. In the course of his research Gerhard Ertl was able to image the catalytic conversion of hydrogen and oxygen species into water in contact with the Pt(111) surface [4]. He has been awarded the Nobel Prize in Chemistry in 2007 [5] for his work on visualizing chemical processes on crystal surfaces. In order to reveal the underlying principle of water adsorption many studies have been performed, addressing the wetting of the surface [6, 7], the structure of the adlayer [8–10] and its thermodynamics [11], respectively. As an important result they have shown that the molecule-metal bond is of comparable strength as the molecule-molecule interaction.

For several decades it was assumed that the structure of the first, chemisorbed layer on the dense-packed surfaces of transition metals can be rationalized by taking a symmetry-matched hexagonal (0001)-layer out of an ice I_h crystal and adjusting for the strain by slight distortions of the flexible hydrogen bonds. This leads to a $\sqrt{3} \times \sqrt{3}$ R30°-structure, a buckled honeycomb lattice of water molecules with their dense-packed rows perpendicular to the dense-packed rows of the metal substrate. However, progressing studies revealed that this simple picture is more the exception than the rule [3]. For the system of interest here, namely H₂O/Pt(111), diffraction studies [12] found rather complicated high-order commensurate (HOC) superstructures, referred to as $\sqrt{37} \times \sqrt{37}$ R25.3° and $\sqrt{39} \times \sqrt{39}$ R16.1°. The real-space structure of the respective unit cell remained obscure and the authors of Reference [12] had to rely on common assumptions to build a structural

model of the unit cell. Computational models failed to support these models due to the large size of the unit cell in combination with the weak bonding energies involved [13].

Water adsorption on graphene is of particular interest as this single atomic layer of graphite is envisioned as electrode material in future capacitors [14] and (dye sensitized) solar cells [15, 16] in which the interaction of the carbon atoms with the water based electrolyte is a key factor for electron transport. The sp^2 hybridization of the carbon atoms results in outstanding electronic and mechanical properties [17–19]. In combination with the pure two-dimensionality of the crystal and high perfection of the carbon lattice this makes graphene a promising candidate for post-CMOS technology [19–24]. The high charge carrier mobility evokes phenomena like room temperature ballistic transport [25] and a half-integer quantum hall effect [21]. Not only since its successful exfoliation (which has been awarded with the Nobel Prize in Physics 2010 [26]) graphene is in constant focus as a promising candidate for various applications including high-frequency transistors [27], gas sensors [28] and transparent electrode material as mentioned above. However, many envisioned applications require to tailor these properties like, e.g. a bandgap opening. Here a controlled introduction of defects into the two-dimensional lattice comes into play, as they are able to alter the macroscopic properties by modifications on an atomic scale.

Ion beam irradiation is nowadays not only considered in terms of perturbation effect but also a powerful tool for the creation of nanostructured surfaces [29]. Often even regular patterns appear spontaneously [30], thereby constituting a prominent example of self-organization. Ion bombardment can also be used to tailor the properties of nanoscale materials, including graphene [31, 32]. It is therefore tempting to explore the possibilities of using ion beams for the creation of nanostructures in supported graphene with the desired properties, such as arrays of graphene nanoislands [33], nanoribbons [34], and hole or antidot lattices (also called nanomesh) [35]. The latter structure has been predicted to cause bandgap opening at the Fermi level due to spatial confinement of electrons, offering a way to tune the electronic [36] and thermoelectric properties [37] of graphene-based devices. Furthermore, certain hole arrangements are predicted to induce magnetism in the patterned graphene sheet [38] which should have an impact on spin transport properties. The nanomesh structure may also be applied as a template for patterned adsorption. However, in spite of considerable success in nanostructuring graphene by plasma treatment through a nanoporous membrane [39], etching of graphene devices by a 30 keV He ion beam [40], or cutting of graphene by swift heavy ions [41], no experiment has yet exploited ion beams for pattern formation in graphene.

Besides being of technological interest, the production of defects in graphene compared to bulk materials gives rise to new phenomena which makes it a thrilling field of research. Although recent transmission electron microscopy (TEM) experiments have provided lots of insight into the structure and dynamics of point defects in graphene [42, 43], one can only study defect formation and evolution induced by the electron beam itself. Besides, applying this technique to graphene on metals - which allows for a growth of high perfection [44–47] - is much more challenging due to a weak contrast of carbon atoms as compared to the much heavier metal atoms. Meanwhile, scanning tunneling microscopy (STM) studies on supported graphene bombarded with low energy ions [48–50] made it possible to obtain direct information on the irradiation-induced defects. For graphene on Pt(111) localized states at the Fermi energy resulting from dangling carbon bonds were detected [49]. These electronic signatures of vacancies in graphene were significantly affected by the substrate, which indicates that the vacancy structure is different from the one in free-standing graphene and calls upon further studies. Also these studies leave the annealing behavior of vacancy defects in graphene unexplored.

In the following the content of this thesis is outlined. This work is divided into several topics: In Part II we study the physics of water adsorption on graphene and noble metal surfaces. The formation of ordered structures, the influence of impurities on their quality, the interaction of water with foreign molecular species, and the controlled manipulation of the wetting layer on Pt(111) is discussed in Chapter 3. Here we also give an experimental proof of the structural models derived from theoretical predictions. In Chapters 4 and 5 the findings obtained for Pt(111) are transferred to Ir(111) and a graphene surface, respectively. For each system the possibility to create an (ordered) wetting layer is examined. In both chapters the real space analysis using STM is complemented by thermal desorption spectroscopy measurements to gain insight on the binding conditions. The topic of water adsorption closes with a comparative study of the results we observed in the course of our experiments, giving an insight into the physical diversity of wetting and non-wetting surfaces, see Chapter 6.

Part III deals with the defect formation following keV ion bombardment in several crystal structures. In Chapter 9 we study the physics of single ion impacts in graphene on an Ir(111) support. In combination with molecular dynamics simulations and density functional theory calculations we will introduce a new mechanism to explain the diversity of defect patterns, study their thermal stability, and give an outlook on the ability to form a graphene nanomesh via self-assembly of carbon vacancies in the Gr/Ir(111) moiré. Chap-

ter 10 is devoted to the experimental realization of this structure. In that course we will discuss the dependence of pattern formation on the bombardment parameters, including temperature, ion energy and species. The results are contrasted to previous findings of ion bombardment on Pt(111), see Chapter 11.

In each part, the necessary background information is given (Chapters 1 and 7) and experimental methods are introduced (Chapters 2 and 8). Part IV summarizes our results and gives an outlook on future measurements to either apply or refine the findings obtained in this work.

PART II

Water Adsorption on Graphene and Noble Metal Surfaces

CHAPTER 1

Fundamentals: Interaction of Water Molecules with Metal Surfaces and Graphene

The discussion regarding the development of a structural model in the system $H_2O/Pt(111)$ is literally taken from Reference [51], as indicated in the respective section heading. I do not claim intellectual property on any of the results presented in this chapter.

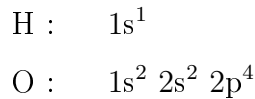
The following chapter offers an overview on water adsorption on various surfaces, illustrating the manifold findings obtained in both experimental and simulation works. It is subdivided into six parts, starting with a description of the isolated water molecule in Section 1.1. Right after that, general aspects of water adsorption on metal surfaces are discussed, see Section 1.2. Based on this discussion the physical properties of Pt(111) (Section 1.3), Ir(111) (Section 1.4) and Graphene (Section 1.5) are introduced. For every system a separate discussion is given regarding the interaction of water with the respective surface. Here the focus is on the nucleation of water layers and their structures formed on adsorption. Finally, in Section 1.6 we take a look at the stability of water adsorbates towards tunneling electrons.

1.1 Water Molecule Characteristics

To analyse the structure of a continuous layer on a metal surface one first has to deal with water on molecular level. Despite, an understanding of its geometric and electronic properties is meaningful beyond the scope of this work. From a physics point of view the interaction of water molecules can be seen exemplary for a variety of effects. Ferroelectricity, for example, can be induced by the ordering of hydrogen bonds in a solid, causing polarization within a larger unit cell.

This paragraph provides an overview on the electronic structure of the isolated molecule and its consequences on the crystalline structure. A more detailed explanation of the water molecule can be found in a fundamental work by P. A. Thiel and T. E. Madey [8].

A water molecule consists of two hydrogen atoms binding to a central oxygen atom. Their atomic electronic configuration is as follows:



With the O(1s) states lying energetically low, the orbital interaction occurs between the levels of O(2s/2p) and H(1s). A linear combination of the atomic orbitals results in an OH bond length of $d_{\text{OH}} = 0.95785 \text{ \AA}$ [52] for the isolated molecule in which two of the oxygen valence electrons contribute. With the remaining electrons populating unsaturated *lone pair* orbitals, a tetrahedral arrangement arises according to the rules of valence shell electron pair repulsion (VSEPR). Therefore, the hydrogen atoms enclose an angle of 104.5° .

The energy gain by the formation of these σ -bonds is accompanied by a transfer of electron density towards the oxygen atom. Due to the angled structure of the molecule this results in a dipole moment of $p = 1.84 \text{ D} = 0.37 \text{ e\AA}$ [53]. The net transfer amounts to 0.7 e [54].

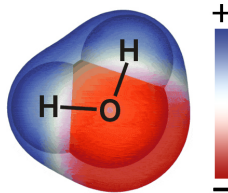


Figure 1.1: Illustration of the Polarity within the Water Molecule. Negative charge (red) accumulates at the oxygen terminated side, whereas the hydrogen terminated side shows electron deficiency (blue).

In liquid phase as well as in the solid the orbital energies are lowered [55] but their spatial arrangement remains unaffected. The exceptional molecular geometry with its polar character allows for a variety of structures in the solid state [56]. Though strongly dependent

on temperature and pressure all these structures are based on the same structural motif: A hydrogen bridge bond $\text{H}\cdots\text{O}$ connecting a hydrogen atom to adjacent molecules. Each hydrogen bridge bond lowers the energy of the system by approximately 0.2 eV [53] ($450\text{ meV}/\text{H}_2\text{O}$) (and with this much less compared to the intramolecular OH-bond) at an O-O spacing of $d_{\text{OO}} = 2.76\text{ \AA}$.

An important point here is to comply with the so-called *ice rules* first mentioned by D. J. Bernal and R. H. Fowler [57] and L. Pauling [58]. In short, these rules make for the formation of exactly four hydrogen bridge bonds per molecule in a tetragonal arrangement, each of them incorporating only one hydrogen atom. Note, that these bonds can be subdivided into hydrogen-donors (σ -type) and hydrogen-acceptors (hydrogen bridge bonds), when referred to a single oxygen atom. The particular arrangement of hydrogen atoms is arbitrary, provided that the number of donors and acceptors are in balance for each molecule.

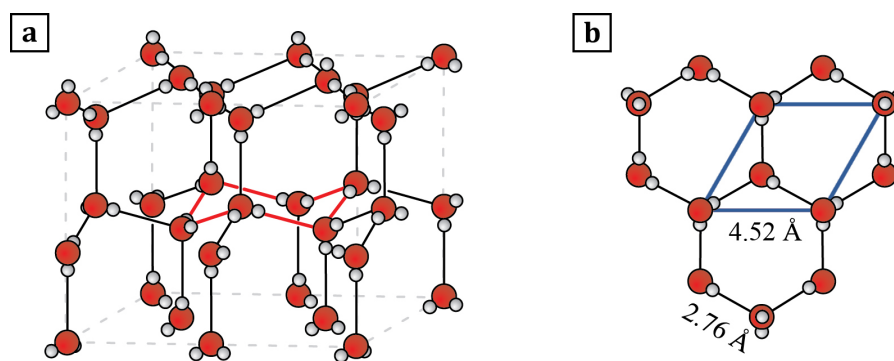


Figure 1.2: Schematic View of an Ice Crystal. (a) The I_h configuration of ice in isometric view. Each water molecule has four neighbors in a tetragonal surrounding while the arrangement of hydrogen atoms is arbitrary (in compliance with the ice rules). A hexagonal ring of molecules in the $I_h(0001)$ plane is highlighted in red, giving rise to a buckled layer. (b) Top view of the $I_h(0001)$ surface. The unit cell contains two molecules and is marked in blue.

1.2 General Aspects of Water Adsorption on Metals

The interaction of water and (transition) metal surfaces has been widely studied in surface science during the past decades [59–71]. These studies, including theory and experimental work, unveiled the binding mechanisms, adsorption energies and vibrational modes of individual molecules up to larger clusters. A very comprehensive report giving an impression on the complexity and diversity of this field is given by Hodgson and Haq [3].

In 1982 D.L. Doering and T.E. Madey proposed a model to describe the structure of a wetting layer formed on dense-packed transition metal surfaces [72]. Their model is based on the above mentioned ice rules, taking the hexagonal symmetry of the metal surface into account. According to this model, the resulting wetting layer is composed of hexagonal ice rings resembling the (0001) plane of ice I_h . This gives rise to a buckled *bilayer* structure as indicated in figure 1.2 with an in-plane bond length of $d_{OO} = 2.61 \text{ \AA}$. Due to the flexibility of the hydrogen bridge bonds a lattice mismatch in the range of $\alpha = +11 \% .. -5 \%$ can be accommodated when adjusting to the metal surface.

A graphical representation of this model is shown in figure 1.3. This simple commensurate structure forms a $\sqrt{3} \times \sqrt{3} R30^\circ$ superstructure with a saturation coverage of $\Theta_{\text{sat}} = 2/3 \text{ ML} = 0.67 \text{ ML}$.

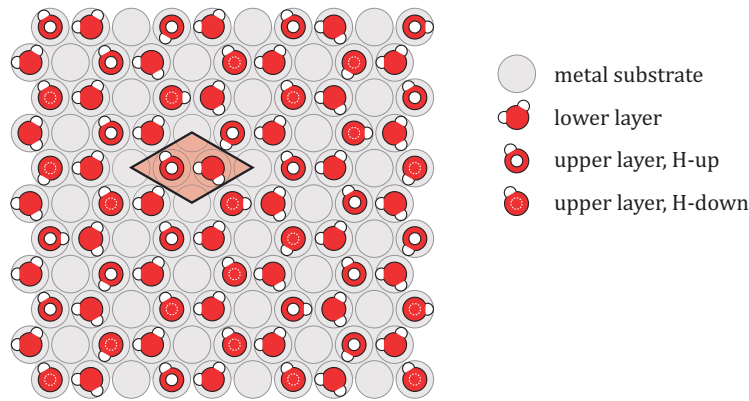


Figure 1.3: The Simple Commensurate Structure. A $\sqrt{3} \times \sqrt{3} R30^\circ$ superstructure is formed by periodically arranged ice rings. It can be described by a hexagonal lattice with a basis of two molecules: One in the upper half of the bilayer and one in the lower half, respectively. The arrangement of hydrogen atoms is arbitrary.

Photoelectron spectroscopy and theoretical studies have shown that water molecules preferably chemisorb on metal surfaces via the oxygen lone pair orbitals [73]. These orbitals interact with the outermost, unoccupied electronic states of the metal. In case of elements of the 6th period (like e.g. Pt and Ir) these are the 5d states, allowing for a bond strength of roughly 500 meV per molecule in the molecular compound [8]. This particular bond formation is equivalent to a charge transfer $\text{H}_2\text{O} \xrightarrow{\delta e^-} \text{M}$, with the metal surface acting as Lewis acid (electron acceptor). This simple picture is supported by density functional theory (DFT) calculations of individual molecules and clusters, shown in table 1.1 [73–75]. These calculations predict a preferential adsorption of water molecules on top of the underlying metal atoms, which can also be explained by the charge transfer model: According

Table 1.1: OH spacing d_{OH} , molecular angle α_{HOH} , adsorption height $d_{\text{O-Pt}}$ and adsorption energy E_{ads} of various cluster sizes and adsorption sites on a Pt(111) surface obtained by DFT [75]: E_{ads} shows variations by a factor of three for a water monomer with a clear maximum for on-top adsorption. The increase of d_{OH} and α_{HOH} with respect to the isolated molecule confirms the charge transfer model, weakening the intramolecular bonds. The results obtained by Meng *et al.* furthermore point out the preference for cluster formation.

	d_{OH} [Å]	α_{HOH} [°]	$d_{\text{O-Pt}}$ [Å]	E_{ads} $\left[\frac{\text{meV}}{\text{H}_2\text{O}} \right]$
isolated molecule (exp.)	0,957	104,52		
isolated molecule	0,973	104,85		
monomer (hollow site)	0,980	105,62	3,02	102
monomer (bridge site)	0,980	105,62	2,89	117
monomer (on-top)	0,980	105,62	2,40	304
dimer (on-top)	0,978 .. 1,012	103,52 .. 106,72	2,26 .. 3,05	433
trimer (on-top)	0,975 .. 0,985	107,71 .. 107,86	2,76	359
hexamer (on-top)	0,974 .. 1,001	104,49 .. 107,25	2,32 .. 3,39	520

to Smoluchowski [76] on-top sites feature an electron deficiency with respect to the surrounding hollow and bridge sites and therefore comply with the Lewis acid concept. This results in the above shown structural model, where two thirds of the metal atoms are covered by water molecules. The $\sqrt{3} \times \sqrt{3}$ R30° superstructure has been experimentally confirmed several times [10, 77, 78], although the particular arrangement of the hydrogen atoms could not be determined. Note that, according to this model, the adsorption mainly takes place via the molecules in the lower half of the bilayer, as the oxygen is in direct contact with the substrate. The molecules of the upper layer may be subdivided into "H-up" and "H-down", according to the particular orientation of their hydrogen atoms (cf. Figures 1.2 and 1.3).

While this structure is widely accepted for Pd(111), Rh(111), Ru(0001) and several other hexagonal transition metal surfaces [3], the set of data shown in table 1.1 clearly states that the interaction of water molecules with the substrate (chemisorption, $E_{\text{ads}} = 300 \dots 500 \text{ meV/H}_2\text{O}$) is comparable in strength to the lateral forces, i.e. the formation of hydrogen bridge bonds between adjacent molecules ($E_{\text{O}\dots\text{H}} = 450 \text{ meV/H}_2\text{O}$). A structural optimization in favor of the lateral binding may therefore overcompensate the loss in adsorption energy and lead to different structural motifs. A prominent example of this balance is Pt(111) which will be discussed in the following section.

1.3 Water Adsorption on Pt(111)

Monocrystalline platinum features a face-centered cubic crystal structure with a lattice constant of $a = b = c = 3.9242 \text{ \AA}$. The (111) surface is hexagonal and dense-packed along the $\langle 1\bar{1}0 \rangle_{\text{Pt}}$ directions. The nearest-neighbor distance amounts to $a_{(111)} = 2.7748 \text{ \AA}$ with a layer spacing of $\Delta z_{\text{step}} = 2.2632 \text{ \AA}$. The step edges divide into two microfacets in thermodynamic equilibrium, namely $\langle 110 \rangle / \{100\}$ and $\langle 110 \rangle / \{111\}$. Figure 1.4 provides a schematic view of the Pt(111) crystal surface indicating the high symmetry directions.

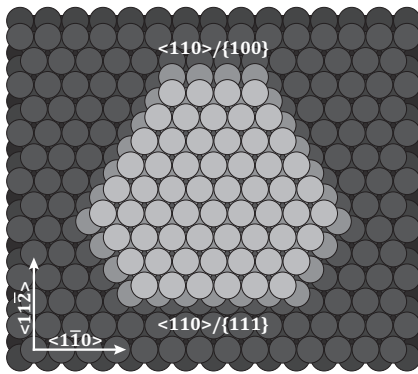


Figure 1.4: Schematic View of the Pt(111)

Crystal Surface. (111) surface of the platinum crystal with a two layer high adatom island of two layer. The nearest-neighbor distance of the hexagonal surface is $a_{(111)} = 2.7748 \text{ \AA}$, the step height is $\Delta z_{\text{step}} = 2.2632 \text{ \AA}$.

Thermal Stability

While water crystallizes at $0 \text{ }^\circ\text{C}$ by definition at atmospheric pressure, the platinum substrate has to be significantly cooled in UHV: For temperatures around $-120 \text{ }^\circ\text{C}$ (153 K) a stable crystalline layer can be observed. At higher temperatures the layer transforms into a liquid-like phase with no crystalline order even in infrared adsorption spectroscopy (IRAS) [79]. Beyond 170 K the water layer has fully desorbed, as seen in thermal desorption spectroscopy (TDS) measurements: $T_{\text{peak}}(\text{monolayer}) = 171 \text{ K}$ [11]. For temperatures much lower than 100 K , on the other hand, the mobility of water molecules on the platinum surface is significantly reduced. This prevents the formation of a continuous wetting layer in favor of finite size clusters. Below $15 \dots 20 \text{ K}$ only water monomers have been observed, as they cannot overcome the monomer diffusion barrier ($E_{\text{diff, monomer}} = 30 \dots 50 \text{ meV}$). [80, 81] A detailed view on this temperature window is given in Figure 1.5(a).

Furthermore, water molecules are more strongly bound to the metal substrate than in a bulk ice crystal. This is clearly shown in the TDS data recorded by A. Picolin, see Figure 1.6, as the multilayer desorption peak [labeled (A2)] occurs at lower temperatures compared to one of the monolayer [labeled (B), $T_{\text{des, multilayer}} = 158 \text{ K}$] [11], characteristic for a wetting surface (cf. non-wetting behaviour exemplary shown for Cu(111) in Figure

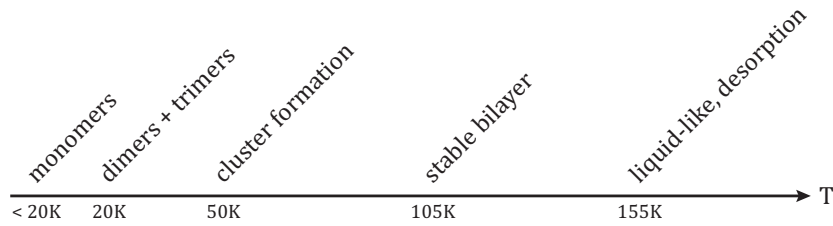


Figure 1.5: Sample Temperature Dependence of the Water Layer while Dosing (Sub-ML Coverage). Dimer formation requires temperatures around 20 K to allow for monomer diffusion. From 50 K on cluster formation is observed. A stable bilayer only grows above 105 K, which loses its crystallinity in favor of a liquid-like layer beyond 155 K [79].

2.2 of reference [3]). In consequence, the sample temperature should be kept above $T_{\text{ads}} = 140$ K while dosing to suppress second layer nucleation.

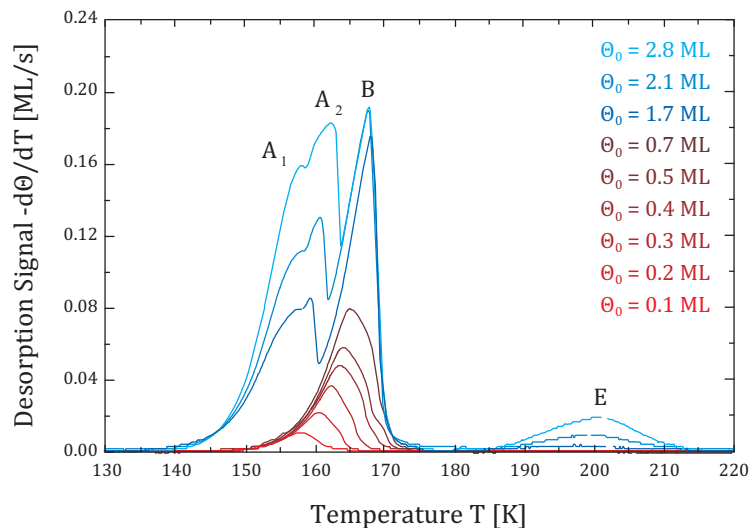


Figure 1.6: Thermal Desorption Spectroscopy Data of H₂O Adsorbed on Pt(111). Coverage dependent H₂O spectra show the formation of a wetting layer [peak (B)] and subsequent growth of multilayer ice [peak (A₂)] with zero order desorption kinetics. The signal of peak (A₁) is addressed to a structural transition from amorphous to crystalline ice. Peak (E) can be explained by desorption of molecules from the sample surroundings (sample holder, etc.). Redrawn from [82].

Structures of the Wetting Layer: H₂O/Pt(111)

As mentioned before, the system H₂O/Pt(111) develops a variety of structures in the interplay of lateral forces and chemisorption. Ogasawara *et al.* [9] applied X-ray photo-

electron spectroscopy (XPS) to determine the arrangement of adsorbed water molecules on the surface. From the intensity change of the split Pt_{4f} signal (surface state \rightarrow bulk state) they derive a fraction of two thirds of the surface atoms to be directly bound to water molecules. As this value corresponds to a full coverage dense layer, the bilayer character of the model shown before has to be re-evaluated.

In particular, these findings require a modification of the role and arrangement of the molecules in the upper part of the bilayer to interact more strongly with the substrate. Further spectra obtained by X-ray adsorption spectroscopy (XAS) fit best to an H-down model, in which all molecules point with their free hydrogen atom towards the metal surface. Whether this is accompanied by the formation of a Pt-HO bond, as in case of Ru [61, 83–86], and/or contain dissociated species, is heavily debated in literature. [9, 13, 75, 87] The H-down geometry results in a reduced buckling of the bilayer ($\Delta h = 0.92 \text{ \AA} \searrow 0.25 \text{ \AA}$), so that the terms "bilayer" and "monolayer" are used synonymously.

The Simple Commensurate Structure: $\sqrt{3} \times \sqrt{3} \text{ R}30^\circ$

The simple commensurate structure of $\text{H}_2\text{O}/\text{Pt}(111)$ relates to the previously introduced $\sqrt{3}$ bilayer. The lattice constant of the $\sqrt{3}$ layer is $a_{\text{H}_2\text{O}} = 4.8061 \text{ \AA}$ which makes for a lattice mismatch of +6.1% in the bilayer but only +0.9% for the H-down model. This $\sqrt{3}$ is also observed for Rh(111) ($a_{(111)} = 2.6870 \text{ \AA}$) and Ru(0001) ($a_{(0001)} = 2.7059 \text{ \AA}$) [88–93], for example. In case of platinum this adlayer was shown to be but an artifact of an electron induced rearrangement. [94] Unfortunately, these studies could not clarify whether the resulting layer is still intact or incorporates fragments of dissociated molecules: The scattering cross section for individual hydrogen atoms is simply too small in low energy electron diffraction (LEED).

Electron induced restructuring of the water adlayer will be discussed in Section 3.4.

A reduction of the electron dose in LEED unveils two more, high order commensurate (HOC) superstructures that are both transferred into the simple commensurate adlayer under prolonged exposure. [10] These are $\sqrt{37} \times \sqrt{37} \text{ R}25.3^\circ$ and $\sqrt{39} \times \sqrt{39} \text{ R}16.1^\circ$ which have been observed first by helium atom scattering (HAS) [12].

Submonolayer Coverage: $\sqrt{37} \times \sqrt{37} \text{ R}25.3^\circ$ (cf. [51])

The advantage of HAS compared to LEED studies is the prevention of charge induced effects (e.g. dissociation) as the helium atoms are neutral. Due to their much higher mass they possess less energy for the same de-Broglie wavelength. In a classical picture the reflection of the helium atoms occurs three to four Ångström above the surface,

avoiding multiple scattering events and interaction with the underlying substrate. Thus, the resulting reflexes are generally sharper.

The working group of A. Menzel and J. P. Toennies implemented this technique to study a partially water covered platinum substrate. Their work revealed the existence of a complex HOC superstructure with a $\sqrt{37} \times \sqrt{37}$ R25.3° unit cell. Based on the $\sqrt{3}$ adlayer they proposed a structural model with a rotation of the dense-packed $\langle 11\bar{2}0 \rangle_{\text{H}_2\text{O}}$ rows by approximately 12° from the high symmetry directions of platinum. The $\sqrt{37}$ unit cell contains 26 molecules resulting in a saturation coverage of $\Theta_{\text{sat}} = 0.70$ ML [12].

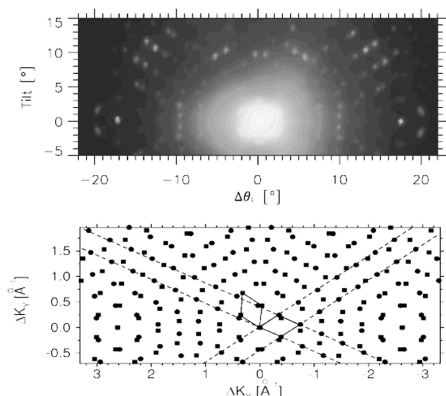


Figure 1.7: Observation of a $\sqrt{37}$ Wetting Layer. Results of HAS on a partially covered water layer: (top) experimental data, (bottom) reciprocal space reconstruction. The $\sqrt{37} \times \sqrt{37}$ R25.3° unit cell is highlighted. Reprinted with permission from [12]. Copyright 1997, American Institute of Physics.

For doing so they had to rely on common assumptions including a reduction of the lattice mismatch to strengthen the lateral interaction. Due to the large unit cell and the relatively weak intermolecular interactions, theoretical *ab initio* studies were not able to offer sound results in agreement with these data.

Recently these diffraction studies have been complemented by real space measurements using scanning tunneling microscopy. [95, 96] Already in the first of these studies unusual features of the first water layer on Pt(111) became evident [see Figure 1.8(a)]: The water layer is composed out of different structural motifs, where the main one - containing the majority of the molecules - is an incomplete honeycomb lattice, but with $\langle 11\bar{2}0 \rangle_{\text{H}_2\text{O}}$ nearly parallel to $\langle 1\bar{1}0 \rangle_{\text{Pt}}$ (the exact angle is 5°) and not rotated by almost 30° as in the $\sqrt{3}$ adlayer.

A minority of the water molecules forms a second structural motif, imaged as triangular depressions in STM. Based on DFT calculations and the apparent depth of the depressions below the matrix this motif was interpreted as single hexagons of flat-lying water molecules in the $\sqrt{3}$ orientation attached to the molecular matrix by squeezed hydrogen bonds, as shown in Figure 1.8(b). Due to the rotational misalignment a "575757" type reconstruction is formed in its surrounding as illustrated in Figure 1.8(c). [96] The pro-

posed structural model contains 24 molecules per unit cell which leads to a saturation coverage of $\Theta_{\text{sat}} = 0.65 \text{ ML}$.

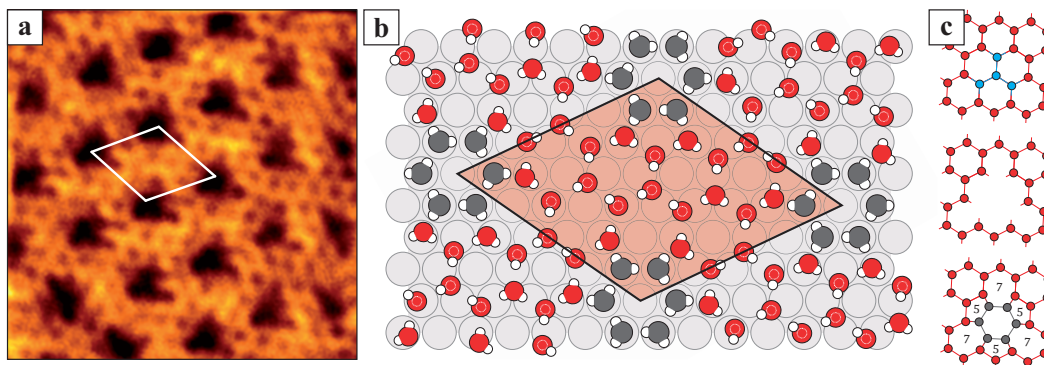


Figure 1.8: Structure of the $\sqrt{37}$ Wetting Layer. (a) Topographic image of the $\sqrt{37}$ adlayer obtained by STM. The unit cell is composed of two distinct structural motifs readily identifiable by their different apparent height. While the structure of the triangular depressions remains unclear, hexagonal ice rings can be identified in the surrounding matrix. Image width: 95 \AA . Reprinted from [97]. (b) Proposed structural model obtained by DFT, showing the depressions to incorporate a hexagon in planar configuration (grey). The molecules attributed to the matrix (red) prefer an H-down configuration. (c) Formation of the "575757" reconstruction surrounding the depression. Redrawn from [96].

The planar hexagons play a crucial role to the stability of the wetting layer [98] as they take on-top adsorption sites and, thus, are most strongly bound to the platinum substrate, as discussed before. However, the planar geometry results in an imbalance of hydrogen donors and acceptors, i.e. violation of the ice-rules, and cannot be continued periodically forming a defect-free network. Similar molecular arrangements have already been observed for water adsorption on Pd(111), resulting in the formation of finite size clusters. [90] However, as presented in this study, the self-limiting growth can be overcome, when placing nonflat molecules at the bridging sites of adjacent hexagons. These molecules offer two hydrogen acceptors, thereby facilitating growth of a (semi-)continuous wetting layer.

In the case of Pt(111) the bridging molecules form a matrix with a characteristic neck width of one molecular ring, embedding the planar hexagons in a trigonal lattice. This threefold symmetry derives from the "575757" type reconstruction at the planar/non-planar molecule interface introduced earlier. Note, that the bridging molecules also prefer an H-down configuration [see Figure 1.8(b)].

Full Coverage: $\sqrt{39} \times \sqrt{39}$ R16.1°

An increase of the water coverage to the full monolayer causes a restructuring of the entire layer. An evaluation of the corresponding HAS diffraction patterns [see Figure 1.9] reveals a $\sqrt{39} \times \sqrt{39}$ R16.1° superstructure. The proposed structural model (aiming on a minimized lattice mismatch) contains 32 molecules per unit cell which translates into a saturation coverage of $\Theta_{\text{sat}} = 0.82$ ML. Here again the lattice mismatch was minimized to lower the free energy of the system. [99]

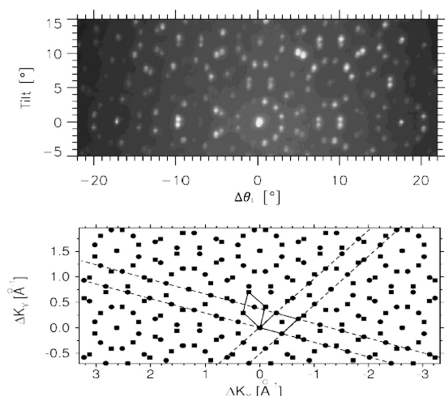


Figure 1.9: Observation of a $\sqrt{39}$ Wetting Layer. Results of HAS on a fully covered water layer: (top) experimental data, (bottom) reciprocal space reconstruction. The $\sqrt{39} \times \sqrt{39}$ R16.1° unit cell is highlighted. Reprinted with permission from [12]. Copyright 1997, American Institute of Physics.

The $\sqrt{39}$ superstructure has also recently been observed by means of STM [Figure 1.10(a)] and subsequently optimized via DFT calculations [Figure 1.10(b)]. As in case of the $\sqrt{37}$ the adlayer is composed by a partially filled matrix (mainly H-down orientation) surrounding single hexagons of planar molecules ($\sqrt{3}$ arrangement).

Compared to the $\sqrt{37}$ adlayer the dense packed $\langle 11\bar{2}0 \rangle_{\text{H}_2\text{O}}$ rows are even stronger aligned to the $\langle 1\bar{1}0 \rangle_{\text{Pt}}$ direction (the exact angle is 2°). Despite a different arrangement of the matrix and embedded hexamers, the superstructure unit cell shows a third structural element: Second layer decoration. The additional molecule resides on the particular site in the unit cell where the underlying matrix molecule is located in an on-top site, adopting the planar arrangement. Based on DFT [96], this gives rise to dangling bonds in its surrounding which saturate by a second layer molecule, as shown in Figure 1.10(b). All in all, the proposed structural model contains 27 molecules per unit cell. The saturation coverage amounts to $\Theta_{\text{sat}} = 0.69$ ML.

The structure of the HOC superstructures will be investigated in Section 3.2, including a full analysis of the phase diagram. In Section 3.3 we will study the interaction of the water layer with foreign molecule species. Finally, in Section 3.5, we will collect our findings and give a proof of the structural model obtained via DFT.

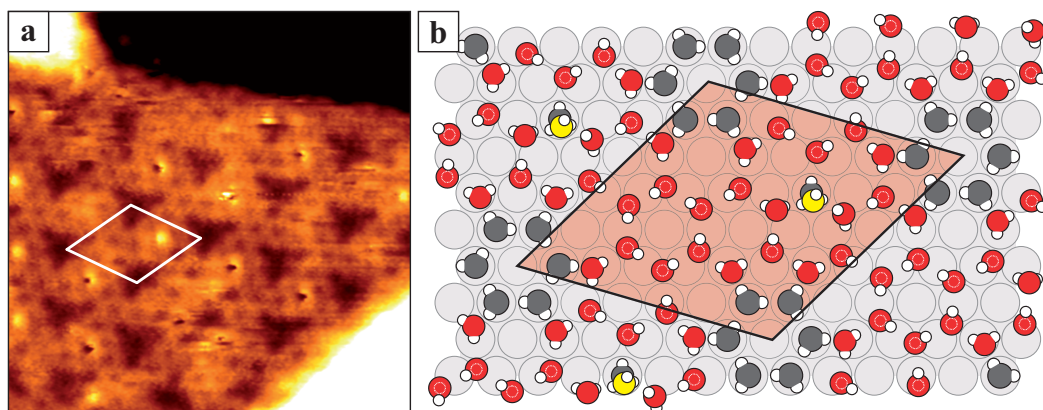


Figure 1.10: Structure of the $\sqrt{39}$ Wetting Layer. (a) Topographic image of the $\sqrt{39}$ adlayer obtained by STM. The unit cell is composed of two distinct structural motifs readily identifiable by their different apparent height. While the structure of the triangular depressions remains unclear, hexagonal ice rings can be identified in the surrounding matrix. Image width: 86 Å. Reprinted from [97]. (b) Proposed structural model obtained by DFT, showing the depressions to incorporate a hexagon in planar configuration (grey) and the second layer decoration (yellow). Redrawn from [96].

The Disordered Layer

Besides the high order commensurate superstructures reported in various studies, an additional disordered layer has been observed in STM studies. [97]

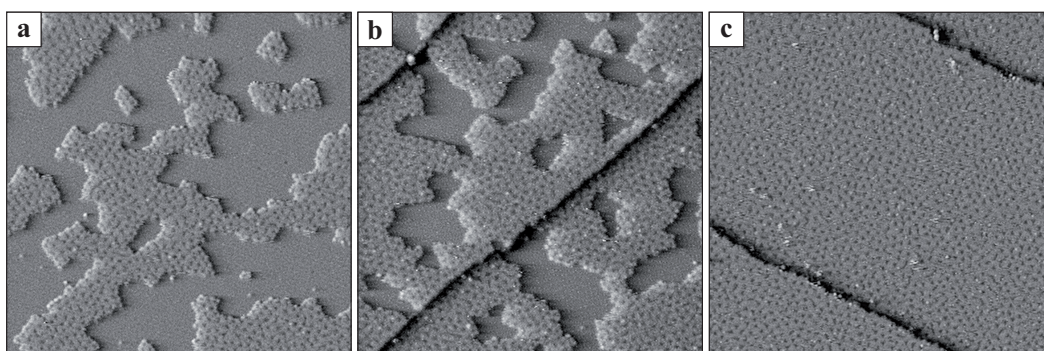


Figure 1.11: Disordered Layer of H₂O Adsorbed on Pt(111). Topographic images of the disordered adlayer adsorbed at 140 K. The layer is composed of the two structural motifs used as building blocks in both the $\sqrt{37}$ and the $\sqrt{39}$ wetting layer. The coverage amounts to (a) $\Theta = 0.48$ ML, (b) $\Theta = 0.73$ ML, (c) $\Theta = 1.00$ ML. Image width: (a-c) 700 Å. Reprinted from [97].

While the structural elements are in line with the HOC superstructures (a continuous adlayer of uniform height surrounding triangular depressions), the long range order of the structure is significantly reduced, see Figure 1.11.

Enhancement of the long range order of the water adlayer will be discussed in Section 3.1.

Multilayer Growth

Although this work deals with the structure of the wetting layer preferentially, a few words should be spent on the multilayer growth mode of ice on Pt(111). The TDS data given in Figure 1.5(b) clearly shows that the water molecules of the wetting layer are more strongly bound to the platinum substrate than to neighboring molecules in a bulk ice crystal.

In the course of their HAS experiments, Glebov *et al.* found that the growth mode of crystalline ice films is not layer-by-layer [100]. Optimizing the technique of TDS with coadsorbates, Kimmel *et al.* could show, that - while the first monolayer wets Pt(111) in the above mentioned temperature range - additional water layers do not wet the monolayer for $T_{\text{ads}} > 135$ K [101]. They conclude, that the wetting layer itself is hydrophobic and that "the nonwetting growth of 3D crystallites on the water monolayer is thermodynamically favored." [101] In 2008 Thürmer and Bartelt were able to image multilayer ice by means of STM: When dosing water at 140 K onto the substrate they observed the formation of individual crystallites embedded in a one layer thick wetting layer, proving the above conclusions [102]. DFT calculations on the wetting layer structures shown in Figures 1.8 and 1.10 agree with the hydrophobic character of the monolayer, as they find no dangling bonds which allow for multilayer nucleation.

1.4 Water Adsorption on Ir(111)

In contrast to Pt(111) the interaction of water molecules with an iridium substrate is barely studied. In fact, it is not even considered in the work of Hodgson and Haq [3]. From a simple point of view, one can expect Ir(111) to resemble the system of H₂O/Pt(111) due to the familiarities of the neighboring elements in the periodic system: Monocrystalline iridium also features a face-centered cubic crystal structure. The lattice constant of $a = b = c = 3.839$ Å is roughly two percent smaller than for platinum. However, the (111) surface is also hexagonal and dense-packed along the $\langle 1\bar{1}0 \rangle_{\text{Ir}}$ directions. The nearest-neighbor distance amounts to $a_{(111)} = 2.7145$ Å with a layer spacing of $\Delta z_{\text{step}} = 2.214$ Å.

In 2011, Pan *et al.* [103] performed TDS measurements which proof the formation of a wetting layer, see Figure 1.12(a). Furthermore, the authors observed a fraction of the molecules to dissociate in contact with the iridium substrate, which clearly separates this system from $\text{H}_2\text{O}/\text{Pt}(111)$. This low temperature water dissociation ($T < 200\text{ K}$) is estimated to increase with decreasing water coverage ($p_{\text{max}} = 0.016 \pm 0.015$ for $\Theta = 0.34\text{ ML}$), shown in Figure 1.12(b), and can be artificially enhanced when dosing at high temperatures (note the use of isotopically labeled D_2O to avoid perturbing effects of background H_2 signal).

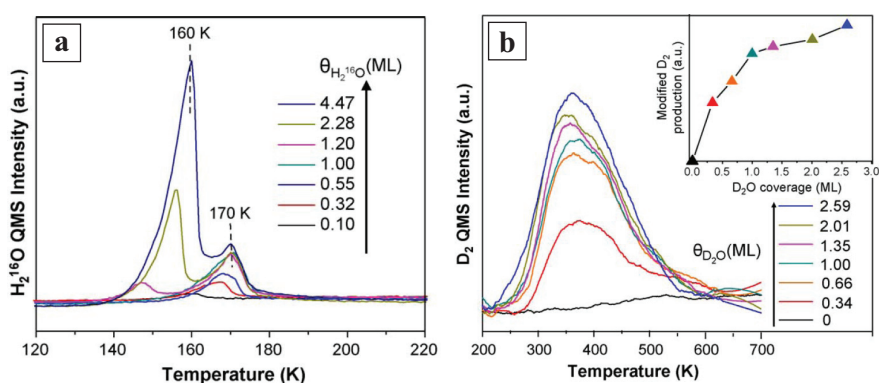


Figure 1.12: Thermal Desorption Spectroscopy Data of H_2O and D_2O Adsorbed on Ir(111). (a) Coverage dependent H_2O spectra unveil the formation of a wetting layer with zero order desorption and a maximum peak temperature of 170 K. The multilayer is more weakly bound. (b) D_2 desorption signal in dependence on the initial D_2O coverage. The modified D_2 production saturates for $\Theta > 1\text{ ML}$, indicating molecule dissociation in contact with the substrate. Reprinted from [103], Copyright 2011, with permission from Elsevier.

The wetting behaviour of Ir(111) will be discussed in Section 4.1. The structure of adsorbed water on the metal substrate will be given in Section 4.2.

1.5 Water Adsorption on Graphene

The interaction of water molecules with graphene is fundamentally different to most of the metal substrates discussed above. This is due to the uniqueness of the crystal structure which will be introduced in the following.

Graphene

Graphene is a two-dimensional crystal, composed of sp^2 -hybridized carbon atoms arranged in a hexagonal lattice with a lattice constant of $a_{\text{Gr}} = 2.46 \text{ \AA}$. The unit cell contains two carbon atoms at a distance of $a_{\text{nn}} = 1.42 \text{ \AA}$ which results in a honeycomb structure. Graphene's peculiar electronic properties are related to the touching points of the valence and conduction band at the K points of the Brillouin zone, shown in Figure 1.13. In their vicinity the electrons obey a linear dispersion and can be described by the Dirac equation for massless particles. [18] Note that this is a fundamental property of graphene, which arises from the special lattice symmetry together with its unique monoatomic thickness. [104] Due to the vanishing electron density at the Fermi level, graphene is often referred to as zero-bandgap semiconductor.

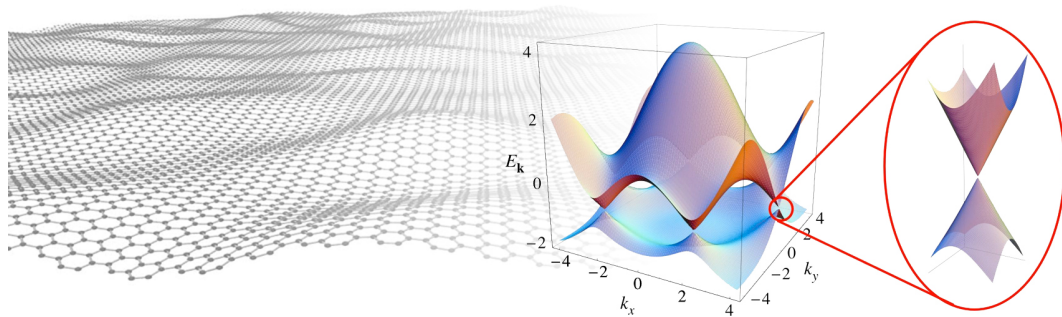


Figure 1.13: Introduction to Graphene. Artistic sketch and calculated band-structure of (free-standing) graphene. The linear dispersion at the K-points is enlarged. For details see text. Sketch by J. Meyer. Bandstructure reprinted with permission from [18]. Copyright 2009 by the American Physical Society.

Graphene can be grown epitaxially on various surfaces including SiC [105, 106] and metal substrates [46, 47, 107–109]. However, graphene grown on Ir(111) is found to be of exceptional structural quality. Using thermal decomposition of hydrocarbon precursor molecules, an epitaxial layer of unmatched structural coherency is formed [44], see Figure 1.14(a), which grows easily across step edges [45, 46]. The lattice mismatch of graphene and the iridium substrate results in an incommensurate $(10.3 \times 10.3)_{\text{Gr}} / (9.3 \times 9.3)_{\text{Ir}}$ superstructure with a moiré periodicity of $a_{\text{moiré}} = 25.3 \text{ \AA}$ [44] schematically drawn in Figure 1.14(b) [110].

Within the moiré unit cell the positions of the carbon atoms with respect to the metal substrate change and give rise to three different high-symmetry regions: TOP, FCC and HCP. The notation is derived from the position of the carbon ring on the substrate: In the TOP region, the carbon ring is centered above an atom of the metal surface, whereas

in the HCP (FCC) region, the center of the ring is situated above a threefold hollow site of hcp (fcc) type. This varying geometry also leads to differences in binding between the carbon layer and the metal substrate (weaker in the TOP regions, stronger in the HCP/FCC regions [110]), resulting in electron density modulations which are visible in the STM topographs. Note that the modulation observed in STM may vary on tunneling parameters and tip state [44]. Hence, the TOP-regions either appear as bright dots in a dark sea - topographic contrast - or as dark dots in a bright sea - reverse contrast, as indicated in Figure 1.14(a).

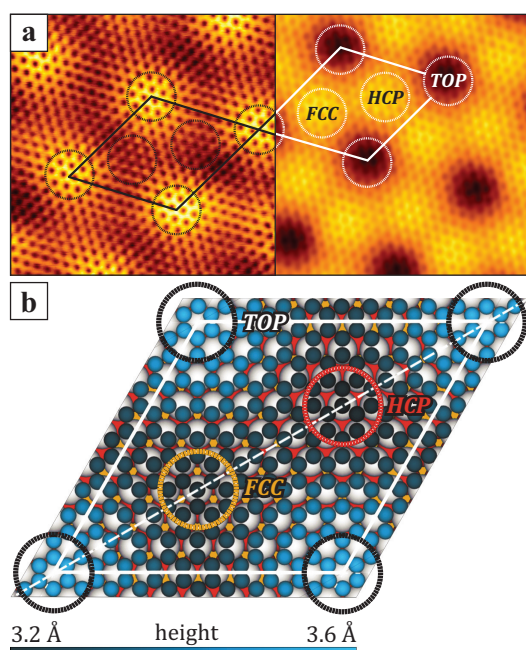


Figure 1.14: Structure of Graphene on Ir(111). (a) Atomic resolution STM topograph of graphene grown on Ir(111) via thermal decomposition of ethylene. The moiré unit cell contains three high-symmetry regions as highlighted. The two different contrast modes are visible. Image width: 59 + 59 Å. (b) DFT simulation of the (commensurate) $10 \times 10/9 \times 9$ Gr/Ir(111) moiré unit cell. Redrawn with permission from [110–112]. Copyright 2011+2012 by the American Physical Society.

Adsorption Energy and Wetting Behaviour

DFT calculations of individual water molecules adsorbed on a freestanding graphene layer (1 H₂O per 32 carbon atoms) predict H₂O to adsorb at a distance of 3..4 Å above the carbon layer. [113] The adsorption energy of this purely physisorbed state is estimated to be less than 50 meV, with no preferential adsorption site. [114] Newer calculations on water clusters (up to 5 H₂O molecules per 32 carbon atoms) show, that the adsorption energy per molecules decreases with increasing cluster size. [115] The very same study could also show that the average lateral binding energy per molecule is roughly one order of magnitude larger than the adsorption energy and furthermore increases with increasing cluster size. [115] These results strongly indicate that water molecules will always form clusters when adsorbed on a graphene sheet. Thus, graphene is hydrophobic.

The graphene sheet inherits this property from its mother-material graphite, which is known for its large contact angle to water droplets of approximately 90° [116, 117]. Contrary to these findings, Kimmel *et al.* [118] observed the formation of a crystalline, hydrophobic, two-layer high ice structure upon water adsorption on graphene on Pt(111) at 125 K. The proposed structural models, obtained via molecular dynamics (MD) simulations, show a nontetrahedral bonding geometry and a rotational alignment with the underlying graphene sheet. The authors furthermore state that this particular adlayer is metastable with respect to bulk ice and reconstructs for higher temperatures and higher water coverages. It should be noted that in 2010 Rafiee *et al.* [116] were able to control the wetting of graphene layers by tuning the corrugation of the films on μm scale.

The wetting behaviour of graphene will be discussed in Section 5.1. The structure of adsorbed water on supported graphene will be given in Section 5.2.

When unsaturated carbon bonds are introduced into the graphene layer (e.g. a monoatomic carbon vacancy), the adsorption energy of water molecules is considerably enhanced, as predicted by Cabrera-Sanfeliix and Darling [114]: Right on top of a carbon vacancy, the adsorption energy accumulates to $E_{\text{ads}} = 210 \text{ meV}$. Yet the water molecule remains in a physisorbed state. However, when the molecule is "pushed" closer towards the vacancy in the graphene surface it may dissociate. This requires an overcoming of the dissociation barrier of $E_{\text{diss}} \approx 900 \text{ meV}$ (700 meV with respect to a molecule in vacuum), the H and O fragments are strongly chemisorbed with a binding energy larger than $E_{\text{ads}} = 3.4 \text{ eV}$. Here, all three broken carbon bonds are saturated with O and H species. [114] Similar saturation of carbon bonds is expected to occur along edges of graphene nanostructures. [119]

Influence of Adsorbed Water on the Graphene Sheet

While water on graphene resides in a purely physisorbed state, it is found to have influence on the crystalline and electronic structure of the carbon sheet.

According to various calculations [28, 115, 120, 121], a crystalline, proton-ordered water cluster of several layers in height causes doping of graphene via the crystals dipole moment. They state: "In the limit of a large concentration of water molecules such that icelike structures can be formed, the dipole moments of the different molecules accumulate instead of averaging out, leading to an appreciable total dipole moment that will have an influence on the electronic properties of graphene." [115]

Scherer *et al.* [122] recently observed a structural splitting of graphene [grown on 6H-SiC(0001)] in the vicinity of step edges, when the carbon layer is exposed to water

molecules. However, this is in contradiction to the results of Seitsonen *et al.*, who claim that the system free energy of water saturating carbon edges is always positive, "meaning that [free-standing] graphene would not spontaneously break to form edges in a water atmosphere." [119]

1.6 Manipulation of the Wetting Layer

In section 1.3 the sensitivity of the wetting layer towards electron induced damaging was mentioned, when Harnett *et al.* [94] observed that the $\sqrt{3}$ adlayer was a result of prolonged irradiation under LEED. Similar effects were seen in STM [7, 123, 124], where the scanning tip and the tunneling current showed to have strong impact on the water adlayers.

Mehlhorn *et al.* [124] were the first to study this process in detail. Their measurements on $\text{H}_2\text{O}/\text{Cu}(111)$, depicted in Figure 1.15, show a strong asymmetry of electron induced damage in dependence on the tunneling voltage which they suppose to originate from electronic excitations.

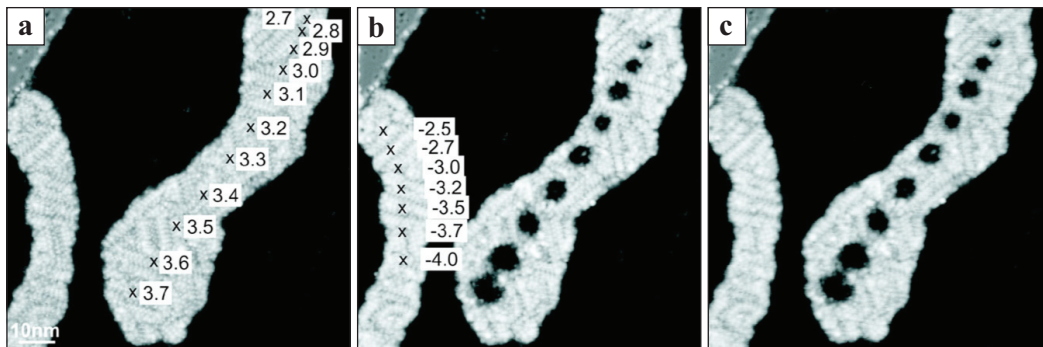


Figure 1.15: Manipulation of the Wetting Layer. (a-c) Series of STM topographic images on the manipulation of the wetting layer of $\text{H}_2\text{O}/\text{Cu}(111)$ via inelastic electron tunneling (IET, for details see [124]). The depicted numbers indicate the bias voltage used in the respective manipulation event. Redrawn with permission from [124]. Copyright 2008 by the American Physical Society.

Their assumption is supported by the high threshold energies required for manipulation (positive sample bias: $U \approx 3 \text{ V}$, negative bias $U > 4 \text{ V}$). This excludes the excitation of vibrational modes as these occur for energies in the range of several meV already. They conclude that manipulation takes place when the anti-bonding (bonding) states or bands of the water layer are (de-)populated which results in the dissociation of the molecules.

A detailed look on electron induced restructuring of the water adlayer will be given in Section 3.4.

CHAPTER 2

Experimental

In this chapter the experimental setup is introduced, including various stages for sample preparation and analysis. Of major importance for the experiments described in this thesis are the water inlet system, the scanning tunneling microscope, the tools used for thermal desorption spectroscopy and the procedures for data evaluation. Furthermore the sample cleaning and water dosing will be discussed, focussing on the critical parameters to achieve contamination-free water adlayers.

2.1 The Scanning Tunneling Apparatus TuMA II

All experiments on water adsorption were performed at "TuMA II" which denotes an ultrahigh vacuum (UHV) chamber equipped with several components for sample cleaning, preparation and analysis. A sketch of the setup is shown in Figure 2.1.

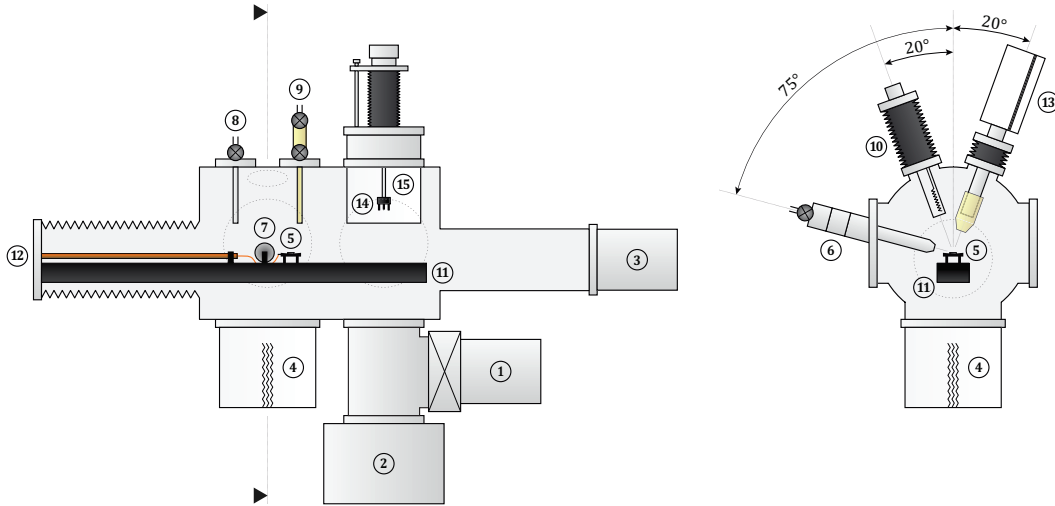


Figure 2.1: Sketch of the UHV Chamber. Side view (left) and cross section (right) at the position marked by arrows. For details see text.

The base pressure in the chamber is in the range of 10^{-11} mbar. The main pump capacity is obtained by the use of a turbomolecular pump (1), an ion getter pump (2) and a (passive) SAES getter pump (3) directly attached to the chamber. An additional titanium sublimation pump is provided embedded into a cooling trap (4) which is used to compensate the loss of pumping power during measurements.

The various sample crystals (5) used in this thesis were preliminary cleaned by ion bombardment via a differentially pumped ion gun (6), mounted 75° with respect to the surface normal (the experiments on Pt(111) were performed in a different setup which allowed for a variation of the ion incidence angle $\vartheta = 75^\circ \dots 90^\circ$). The ion dose was calibrated using a Faraday cup (7). A detailed analysis of this process will be given in section 8.2. The setup furthermore provides a gas inlet system (8) as well as a water reservoir (9) for controlled dosing. Note, that an electron beam evaporator (10) is mounted 20° off normal, but not used in this work. The sample holder is situated on a movable manipulator (11) to access the various stages of sample preparation. The sample can be heated up to 1500 K via electron beam heating and cooled down to 20 K (100 K) using liquid helium (nitrogen) in a continuous flow cryostat (12) which is connected to the sample holder via a copper braid to avoid transmission of vibrations. The temperature is measured by a type

K [Ni₉₀Cr₁₀/Ni₉₅(Al,Si,Mn)₅] thermocouple. Temperature calibration down to 20 K was done via noble gas desorption as discussed in appendix A.2 of reference [125].

The chamber is equipped with a quadropole mass spectrometer (QMS, 13) for residual gas analysis and thermal desorption spectroscopy (cf. section 2.3) as well as a variable temperature scanning tunneling microscope (STM, 14) to study the sample morphology. The STM itself is housed in a second cooling trap (15) used for precooling of the microscope in low temperature experiments.

2.2 Scanning Tunneling Microscopy

The scanning tunneling microscope is of the *inverted beetle design*. It is equipped with three piezo elements for movement on the ramps surrounding the sample, and one positioned on top of the sample, equipped with the tunneling wire and homemade Ir tip, for image recording. A detailed description of this geometry is given in [126].

The principle of data recording in STM is based on the quantum mechanical tunneling effect: When a bias voltage U is applied between the sample and a conductive probe, i.e. the STM tip, a current flow can be measured even without mechanical contact of the two electrodes. The current I is highly distance sensitive as the probability for electron tunneling faces exponential damping with an increasing width of the vacuum barrier. Therefore tip and sample are brought in close contact (several Ångstrom). The tunneling current is basically dependent on the electron density of states, the work function, and the distance of the two electrodes. Taking all this into account, the resulting image can be understood as a combination of the sample topography and the local electron density of states. A more detailed description of the chamber and the STM can be found in [125].

In this work two different imaging modes were used for data recording: (1) the topographic mode, and (2) the differential mode. In topographic mode the height information directly relates to the voltage applied to the scanning piezo regulating the z-distance between tip and sample. Provided a linear gray scale, bright areas are in general higher than dark ones. In differential mode an additional RC element is introduced in the measurement input. As a consequence ascending structures in the scanning direction appear bright while descending structures are imaged dark. The entire image thus appears illuminated from the left side. The advantage of the differential mode resides in imaging highly corrugated surfaces, as every single height change may use the entire gray level range. Thus the image provides a much higher contrast, when compared to one recorded in topographic mode. Note that the gain in contrast involves a loss of the absolute height information.

2.3 Thermal Desorption Spectroscopy

To study the binding and desorption characteristics thermal desorption spectroscopy (TDS) studies are carried out. This technique provides information on the desorption kinetics and the associated desorption order. While a detailed description of this process is given in [82, 127], an introduction to the main parameters and analysis tools is given here.

When a particle receives enough thermal energy $k_B T$ to overcome the binding to the substrate and to neighbouring adsorbates it will desorb from the surface. This thermally activated process can be described by an Arrhenius-type law: The desorption rate R is understood as the (negative) change of the adsorbed particle number N_{ads} in time and depends on the coverage $\Theta = N_{\text{ads}}/N_0$ (N_0 denotes the number of adsorption sites), a frequency factor ν_0 , the desorption energy E_{des} , and the sample temperature T .

$$\text{Wigner-Polanyi equation} \quad R = -\frac{d\Theta}{dt} = \Theta^m \cdot \nu_{0,m} \cdot \exp\left(-\frac{E_{\text{des}}}{k_B T}\right), \quad (2.1)$$

where m is a parameter which will be discussed in the next-but-one paragraph. Note that the desorption energy does not directly link to the adsorption energy as it may result from a complex interplay of different adsorbate stages during desorption.

In all experiments a linear temperature ramp $T(t) = T_0 + \beta(t - t_0)$ is applied in favor of recording the isothermal desorption. Substituting $dT = \beta dt$ results in:

$$\text{desorption rate} \quad -\frac{d\Theta}{dT} = \Theta^m \cdot \frac{\nu_{0,m}}{\beta} \cdot \exp\left(-\frac{E_{\text{des}}}{k_B T}\right). \quad (2.2)$$

An important parameter in here is the desorption order m , determining the dependence of the desorption rate on the residual sample coverage, i.e. the degree of the differential equation. This parameter can be understood in terms of desorption characteristics as shown in the following:

- **Zero Order Desorption**, $m = 0$, describes the desorption of multilayer films [see Figure 2.3(a)] or of an equilibrium of a two-dimensional adsorbate gas with its dense phase [see Figure 2.3(b)]. Consequently, the desorption rate is independent on the current sample coverage, thus all spectra show a common leading edge. The desorption ends abrupt when $N_{\text{ads}} \propto \Theta = 0$.
- **Fractional Order Desorption**, $m = 1/2$, develops when an adsorbate has to overcome a threshold to leave the dense phase and subsequently desorbs individually, i.e. when the detachment denotes the rate limiting step [Figure 2.3(c)]. The desorption rate is proportional to the particle number on the island boundaries: $\Theta^{1/2}$.

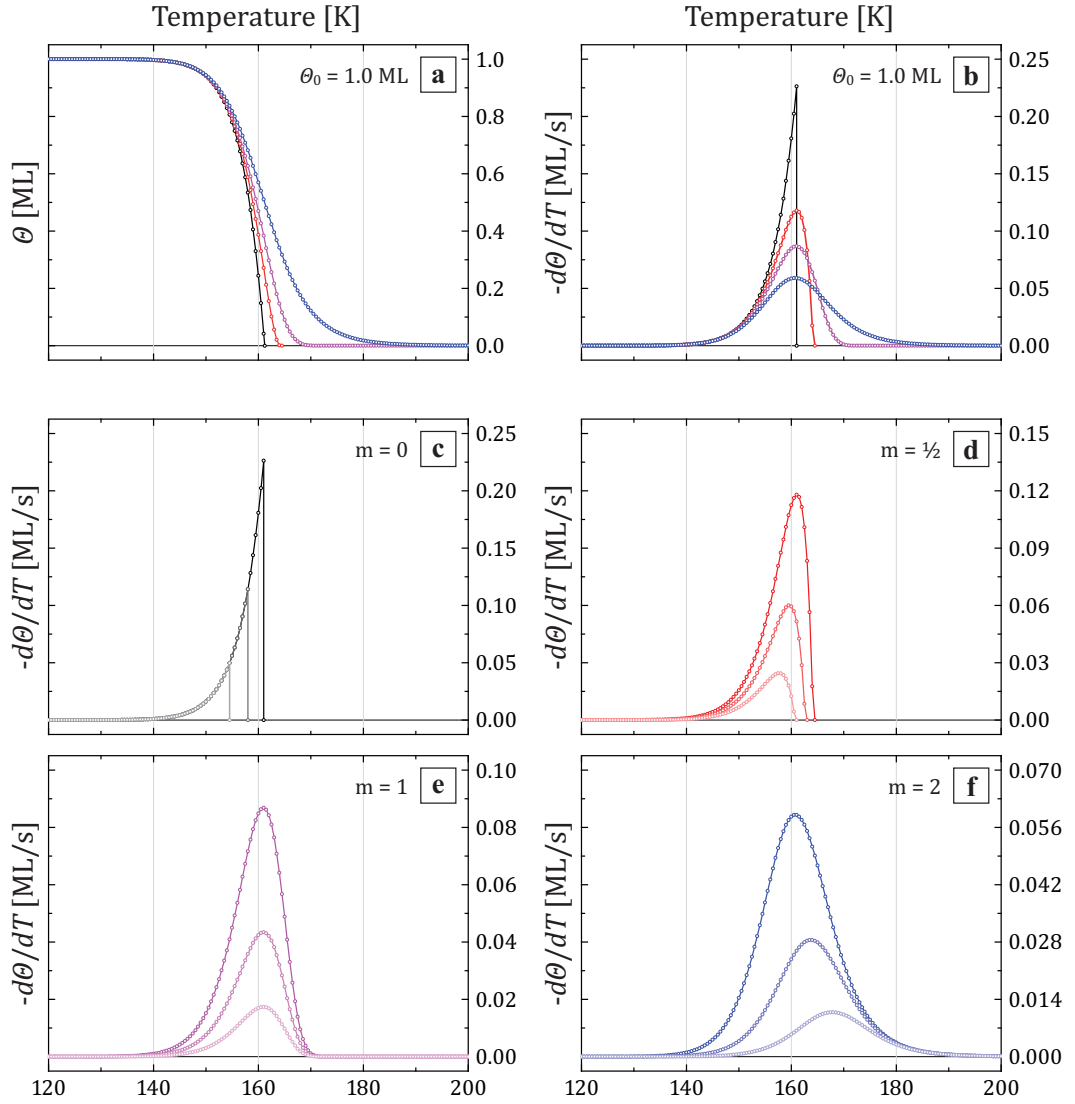


Figure 2.2: Calculated TDS Spectra. (a) Residual coverage and (b) desorption signal against sample temperature during heating ($\beta = 1 \text{ K/s}$) for the different desorption orders: (black) $m = 0$, (red) $m = 1/2$, (purple) $m = 1$, (blue) $m = 2$. Desorption parameters were set as $E_{\text{des}} = 500 \text{ meV}$, $\nu_0 = 1 \cdot 10^{15} \text{ s}^{-1}$. (c-f) Sample TDS spectra of various initial coverages ($\Theta_0 = 1.0 \text{ ML}$, 0.5 ML , and 0.2 ML) for different desorption order.

- Mobile and/or immobile, weakly interacting adsorbates are found to desorb linear in coverage, leading to **First Order Desorption**, $m = 1$ [Figure 2.3(d)]. The peak positions of the recorded spectra are typically independent on the initial coverage.
- **Second Order Desorption**, $m = 2$, occurs for pairwise desorption of individual adsorbates [Figure 2.3(e)]. This is the case for recombination of molecules like e.g. oxygen on Pt(111), which faces dissociation upon adsorption. The resulting desorption rate depends quadratically on the coverage: Θ^2 .

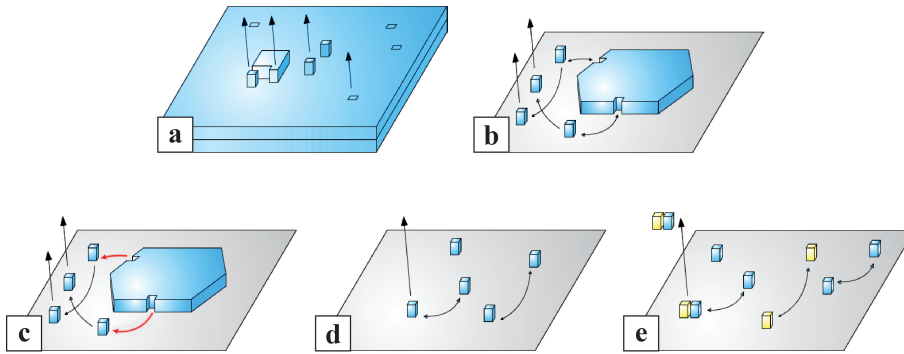


Figure 2.3: Sketch of the Desorption Kinetics. Desorption of (a) thick films, (b) an equilibrium of an adsorbate gas and its dense phase, (c) from island borders, (d) individual adsorbates, (e) recombining species.

For these most common order parameters analytic solutions are available and can be fitted to the recorded spectra. However, various approximative methods are used case-sensitive: For zero order desorption a linear fit of an Arrhenius plot allows for the determination of the desorption energy (slope) and the frequency factor (y-intercept). The method of Redhead [128] is used in case of first order desorption, where the peak temperature T_{\max} is independent of the initial coverage. The so-called Redhead formula is accurate to 1.5% for $\beta = 1 \dots 1000 \text{ K/s}$ (assuming $\nu_{0,1} = 10^{13} \text{ s}^{-1}$ for lattice vibrational modes):

$$\text{Redhead formula} \quad E_{\text{des}} = k_{\text{B}} T_{\max} \left[\ln \left(\frac{\nu_{0,1} \cdot T_{\max}}{\beta} \right) - 3.64 \right]. \quad (2.3)$$

In King's method [129] both the desorption energy and frequency factor can be coverage dependent. For various initial coverages, the desorption rate and temperature for a freely chosen residual coverage are plotted in an Arrhenius diagram and fitted linearly, generalizing the above mentioned zero order technique for more complex desorption kinetics.

Details on the experimental procedure, data processing and spectra evaluation applied in this work are given in section 2.5.

2.4 Sample Preparation

The cleaning and preparation of the various crystal surfaces obey the following routines. The values given are typical values and vary slightly for individual experiments.

Cleaning of Platinum(111) (cf. [125])

For Pt(111) the experimental procedure can be described as follows: Sample cleaning is accomplished by ion bombardment at room temperature with 5 keV Ar⁺ ions. An ion flux of 5.8×10^{16} ions/m²s and an ion fluence of 14 MLE is used (MLE = monolayer equivalent; 1 MLE corresponds to the surface atomic density of Pt(111), i.e. 1 MLE = 1.50×10^{19} particles/m²). Afterwards the sample is flash annealed to 1273 K. If previous experiments showed small traces of carbon impurities on the sample, the sample is additionally treated under an oxygen atmosphere of roughly 1×10^{-6} mbar for a duration of 5 minutes at a sample temperature of 773 K, followed by a second flash annealing to 1273 K.

Cleaning of Iridium(111)

For Ir(111) the experimental procedure can be described as follows: A clean surface is prepared by prolonged ion bombardment [5 keV Xe⁺, $F = 35$ MLE (here, 1 MLE corresponds to the surface atomic density of Ir(111), i.e. 1 MLE = 1.57×10^{19} particles/m²), $T = 300$ K] and subsequent flash annealing to 1473 K. If necessary, the sample is additionally cleaned by repeated cycles of oxygen etching of residual carbon impurities ($p_{\text{O}_2} = 1 \times 10^{-7}$ mbar, $\Delta t = 5$ min, $T = 1073$ K) and high temperature sputtering (5 keV Xe⁺, $F = 15$ MLE, $T = 1073$ K). The extended cleaning procedure is completed with a final flash annealing to 1473 K.

Growth of Graphene/Iridium(111)

Provided a clean iridium surface, a graphene layer can be grown on-top by the well established combined method of room temperature adsorption of ethylene (C₂H₄) to full coverage and consecutive thermal decomposition at 1373 K (hereinafter referred to as *temperature programmed growth*, TPG) followed by continuous ethylene dosing of $p_{\text{C}_2\text{H}_4} = 2 \times 10^{-8}$ mbar at $T = 1123 \dots 1420$ K for 600 s (*chemical vapor deposition*, CVD) [130]. While in most experiments a full coverage graphene layer was used, sub-monolayer films can be achieved by reducing the time of the CVD process or by the use of one to several TPG steps only.

2.5 Preparation of H₂O Adsorbate Layers

All experiments were performed using Ultrapur[®] water (Merck KGaA). It was filled into a glass bulb and scoured with Argon gas overnight, to clean the water from residual gases, that may contaminate the measurements. The incorporation of Argon can be neglected, as the noble gas particles start to desorb from noble metal surfaces below 100 K [131, 132], which is well below the adsorption temperature needed for growing a continuous H₂O adsorbate layer.

Following this procedure the water reservoir is flanged onto the chamber and pumped via an external pumping stage till freezing. This additional step is needed for residual gases that were not removed by argon scouring and contribute to the vapor pressure of approximately 30 mbar (room temperature). Those parts of the water volume still containing impurities have a lower melting point, thereby stay longer in liquid phase upon cooling, will eventually dominate the vapor pressure around 0°C and can thus be efficiently pumped. Nonvolatile impurities such as dissolved salts and metals do not contribute to the vapor pressure significantly and do not have to be treated at large.

The Water Inlet System

For water dosing a reservoir is mounted in between the glass bulb and the chamber that will be filled with water vapor. Its inner walls are gold coated to prevent the molecules from dissociating at the stainless steel housing [2]. For the very same reason a non filament-based gas friction vacuum gauge [133] is used for pressure measurement inside the reservoir. The total volume of the reservoir is $V = (31,8 \pm 0,2) \text{ cm}^3$. The amount N of water molecules in the reservoir and by this the dose of molecules directed onto the sample can be approximated by means of the ideal gas law:

$$\text{number of dosed particles} \quad N = \frac{(p_f - p_i) \cdot V}{k_B T} = \Delta p \cdot 7,7 \times 10^{17} \text{ mbar}^{-1}, \quad (2.4)$$

where p_f and p_i denote the pressure in the reservoir before and after water dosing. A full coverage water layer in the $\sqrt{3}$ structure ($N_{\sqrt{3}} = 2,83 \times 10^{14}$) thereby requires a pressure decrease of approximately $\Delta p = 3.6 \times 10^{-4} \text{ mbar}$, assuming a sticking coefficient of $S \approx 1$, which is justified experimentally over a wide temperature range [10, 134].

In the experiments at TuMA II all molecules are guided directly onto the sample via a glass tube with a diameter of $\varnothing_1 = 3 \text{ mm}$, ending $\Delta z = 20 \text{ mm}$ above the sample surface. Based on these parameters A. Picolin was able to determine the particle flux profile at the sample surface [82] which is plotted in Figure 2.4 (black curve).

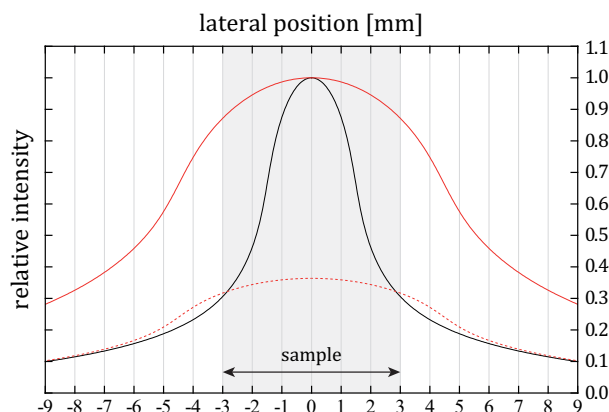


Figure 2.4: Water Dosing Profile. Calculated particle flux intensity for a tube diameter of $\varnothing_1 = 3$ mm (grey) and $\varnothing_2 = 9$ mm (red, solid) versus lateral position. The dashed red line gives the relative intensity for \varnothing_2 in scale with \varnothing_1 . The length of the tube is $L = 185$ mm. The distance between tube and sample is $\Delta t = 20$ mm. The size of the sample $\varnothing_{\text{sample}} = 6$ mm is indicated by a grey shading. Reprinted from [82].

While this setup allows for an exposure of the sample only ($\varnothing_{\text{sample}} = 6$ mm, gray shading), the profile is highly inhomogeneous over mm distances which affects non-localized measurements such as TDS. In the course of this thesis the glass tube was replaced by a (gold coated) steel tube with a significantly larger diameter: $\varnothing_2 = 9$ mm. The particle flux profile for the new setup is shown in red in Figure 2.4. At the expense of a less focussed dosing the sample surface is covered much more homogeneous. In consequence the simple formula introduced before can no longer be used to approximate the amount of particles on the surface. An alternative method to calibrate the water dose, however, is to perform TDS measurements of the mono-/multilayer transition, which has already been studied for the case of Pt(111) [11] and Ir(111) [103].

Water Dosing

As discussed in sections 1.3 and 1.4, the sample has to be cooled below 150 K for water island nucleation but also has to be kept well above 100 K to avoid growth of amorphous ice layers. Right before water dosing, the platinum (iridium) crystal has to be flash annealed to $T = 560$ K (630 K) to desorb particles captured during cooling. CO molecules are of major importance here as they are able to saturate the metal step edges even at low partial pressures ($p = 10^{-10}$ mbar). This decoration was shown to play an important role in the growth and energetics of water layers. [11] The temperatures given here are chosen to guarantee CO desorption even from step edges. [135, 136]

Another ansatz to reduce the influence of CO molecules is to purposefully increase the step edge concentration, which finds a use in section 3.1. Therefore an additional stage of ion bombardment is introduced prior to sample cooling. The parameters are as follows: Pt: $\vartheta = 83^\circ$, $F = 0.5 \dots 3.0$ MLE, $T = 730$ K; Ir: $\vartheta = 75^\circ$, $F = 3.0$ MLE, $T = 750$ K.

Thermal Desorption Spectroscopy

To perform TDS measurements of the water covered surfaces, the sample is positioned in front of the mass spectrometer [(13) in Figure 2.1]. As the QMS is not sensitive to desorbing particles from the sample alone (e.g. attendant desorption of molecules upon warming of the sample holder, cryostat, heating wires...) and features only a small ionisation volume, it is equipped with a Feulner-Cup [137] to increase the sensitivity of the measurement.

As introduced in section 2.3 the sample is heated on a linear ramp. $\beta = 1$ K/s is chosen as heating rate to ensure a high resolution of the spectra. For lower values, the relative error of the control circuit has an increasing impact on the measurement. To suppress the transient oscillation of the ramp controller the filament current of 4.7 A, required to reach 300 K as the final temperature, is applied first. In the beginning this heating provides $\beta \geq 1$ K/s [red curve in Figure 2.5(a)]. When the heating rate drops to 1 K/s, the control unit and the high voltage are switched on [marked by an arrow in Figure 2.5(a)]. Note that the initial temperature overshoot happens well below the desorption temperature and thus has no effect on the actual measurement.

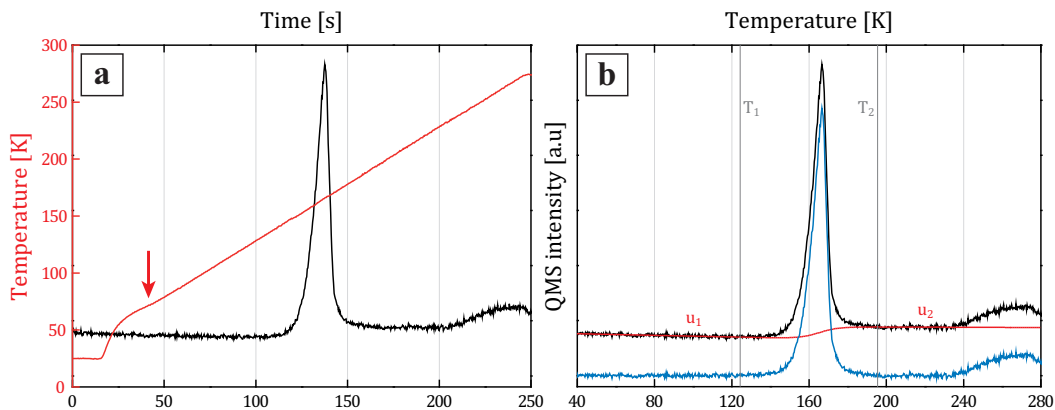


Figure 2.5: Sample TDS Spectrum. (a) Experimental raw data of sample temperature (red curve) and QMS signal (black curve) plotted against time. (b) QMS signal plotted against sample temperature (black curve), background correction (red curve) and final spectrum (blue curve). For details see text.

For data analysis according to section 2.3 the sample temperature is fitted linearly against time to compensate for errors of digitalization in the temperature measurement. Furthermore the background of the spectrum has to be removed [red curve in Figure 2.5(b)]. While $u_1(T)$ ($u_2(T)$) denotes the background before (after) the main desorption feature, the transition between these two is complex. Here the Fermi function is chosen to approximate the background via:

$$\text{background} \quad U(T) = u_1(T) + \frac{u_2(T) - u_1(T)}{\exp(-\Delta \cdot (T - T_c)) + 1}, \quad (2.5)$$

$$\text{where } \lim_{T \rightarrow 0} U(T) = u_1(T) \quad \text{and} \quad \lim_{T \rightarrow \infty} U(T) = u_2(T).$$

The parameter $T_c = 1/2 \cdot (T_1 + T_2)$ marks the arithmetic mean of the onset- and end-temperature of the main desorption feature, T_1/T_2 , while the width of the transition is set to $\Delta = 8 \cdot (T_2 - T_1)^{-1}$ to ensure that the transition takes place right at the desorption features. The resulting spectrum, suitable for further analysis, is shown in blue in Figure 2.5(b).

Scanning Tunneling Microscopy

Scanning tunneling microscopy studies of the adsorbed water layers were performed at $T_{\text{scan}} = 20$ K, if not stated otherwise. In the experiments presented in Chapter 3 the bias voltage is applied to the sample. Yet the value is given with respect to a grounded sample (bias voltage applied to the tip) to match the experimental procedure in all remaining chapters.

Dosing of Gases

Dosing of CO and Xe was performed at $T = 20 \dots 190$ K by backfilling the chamber to $p = 1 \cdot 10^{-9} \dots 2 \cdot 10^{-8}$ mbar. The exposure is given in Langmuir ($1 \text{ L} = 1 \cdot 10^{-6}$ torr s).

CHAPTER 3

Water Adsorption on Pt(111)

*The results in this chapter are published in Physical Review B **82**, 161412(R) (2010) [138] and Journal of Physics: Condensed Matter **24**, 124103 (2012) [51].*

The experiments were planned by Thomas Michely, Carsten Busse, and by myself. I carried out all experiments and performed the data analysis with support of Carsten Busse. All authors of the publications were involved in the discussion of the data and their interpretation. I prepared the drafts of the manuscripts including all figures. Markus Morgenstern, Thomas Michely, and Carsten Busse were involved in editing and finalization of the publications. The following reflects in large parts the published work but is extended in some paragraphs. For experimental details the reader is referred to Chapter 2.

In this chapter, we address several open questions regarding the structure of the first wetting layer on Pt(111), its interaction with foreign molecular species and its sensitivity towards electron irradiation. We present a route towards the formation of ordered adlayers which have been previously observed in diffraction studies, see Section 3.1, and study their thermodynamic behaviour in Section 3.2. As the results obtained in that analysis expand our insight into the first water layer, we go a step further and investigate its interaction with foreign molecular species in Section 3.3. An experimental problem is that the structures are very sensitive and are transformed by prolonged electron exposure. Section 3.4 thus deals with the stability of water molecules against tunneling electrons. In the last part, Section 3.5, we present the key elements of the molecular structures and give an experimental proof of the wetting layer phases as introduced by Nie *et al.* [96]

3.1 Influence of the Step Edge Density on the Structure of the Adlayer

In the following section we investigate the reasons for the fragility of the HOC superstructures as apparent in the poor long-range order obtained in previous STM studies [6, 7, 96]. Here we address this question in more detail and show that the step edges of the substrate have great influence on the layer quality.

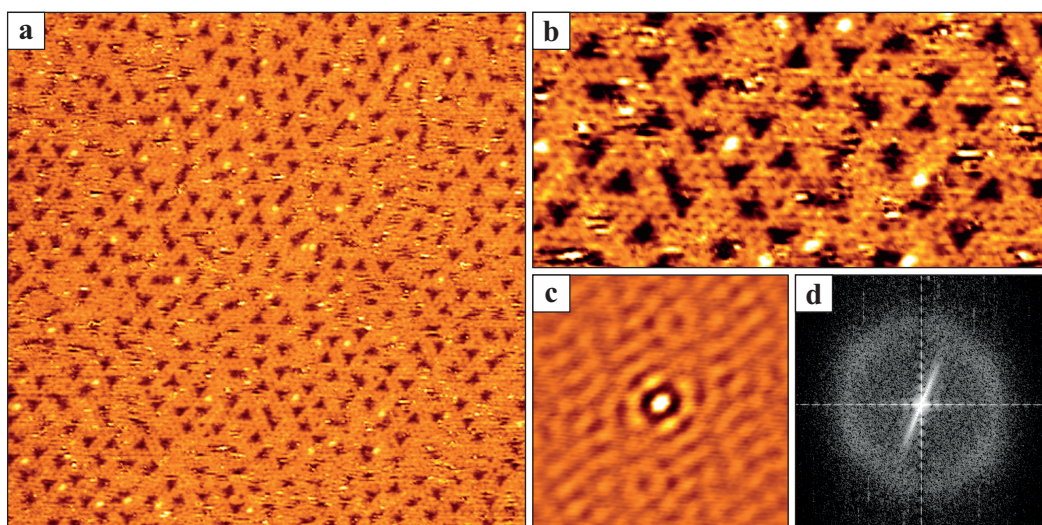


Figure 3.1: STM Topographs of the H₂O Chemisorbed Layer Formed by Adsorption at 140 K on a Flat Surface. (a) On a surface with low step density only low order is visible, i.e. an irregular arrangement of depressions. (b) Molecularly resolved image of the disordered structure showing the triangular depressions embedded in the molecularly ordered matrix and some second layer decoration. (c) Self-correlation image showing a pronounced, sixfold symmetric central peak and almost featureless surrounding. (d) Fourier transform of the disordered structure featuring a pronounced, slightly hexagonal ring. Image width: (a) 325 Å, (b) 151 Å, (c) 152 Å, (d) 0.22 Å⁻¹; Imaging parameters: (a) $U = -1.0$ V, $I = 200$ pA, (b) $U = -1.0$ V, $I = 200$ pA.

Figure 3.1(a) shows the complete chemisorbed layer of H₂O on Pt(111) ($T_{\text{ads}} = 140$ K) as typically observed on a surface with extended terraces, i.e. a low step density. The water adlayer displays an irregular pattern of depressions with triangular shape embedded into a molecularly ordered matrix, which is visible in the enlarged view of Figure 3.1(b), thus resembling the structural elements introduced in chapter 1.3. The apparent height of the molecularly ordered matrix is (1.32 ± 0.03) Å at $U = -1$ V, $I = 200$ pA, while the height

of the depressions is only $(0.7 \pm 0.1) \text{ \AA}$. A closer look in the molecular resolved topograph unveils a rotation of $\langle 11\bar{2}0 \rangle_{\text{H}_2\text{O}}$ in the matrix of $\beta = \pm 5^\circ$ with respect to $\langle 1\bar{1}0 \rangle_{\text{Pt}}$. Figures 3.1(c) and (d) show a self-correlation image and a Fourier transform of this structure. The self-correlation image indicates the irregular structure by a pronounced central peak and an almost featureless surrounding beyond nearest neighbor distance, i.e. short-range order but long-range disorder. The sixfold symmetric shape of the central peak is due to the hexagonal arrangement of molecules in the molecular matrix. It is surrounded by a black ring indicating the formation of depressions with a typical matrix spacing of one ice-ring. The first order peak reflects the spacing of triangles and is already blurred due to their disordered arrangement. The Fourier transform corresponding to this structure is a hexagon with rounded corners. The lattice constants of the disordered layer can therefore be calculated to $(18 \pm 2) \text{ \AA}$ both for the self-correlation and the Fourier transform.

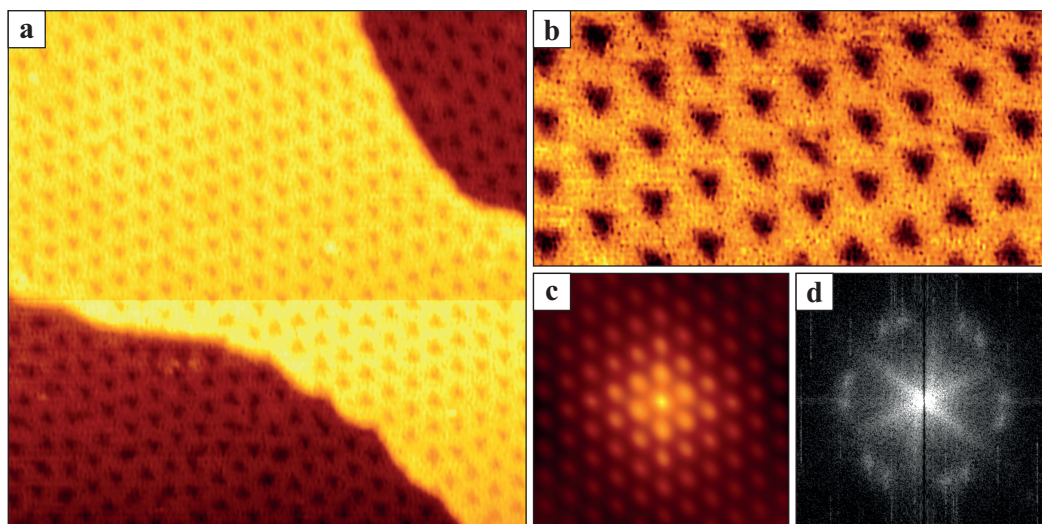


Figure 3.2: STM Topographs of the H_2O Chemisorbed Layer Formed by Adsorption at 140 K on a Stepped Surface. (a) A regular arrangement of depressions characteristic for the $\sqrt{37}$ structure is visible on a surface with an increased step density. (b) Molecularly resolved image of the ordered structure showing the triangular depressions within a molecularly ordered matrix. (c) Self-correlation image of the first wetting layer. (d) Fourier transform of the ordered structure showing sharp reflexes of high intensity. Image width: (a) 325 \AA , (b) 97 \AA , (c) 152 \AA , (d) 0.22 \AA^{-1} ; Imaging parameters: (a) $U = -0.5 \text{ V}$, $I = 110 \text{ pA}$, (b) $U = -0.5 \text{ V}$, $I = 110 \text{ pA}$.

Figure 3.2(a) shows the complete chemisorbed layer of H_2O on $\text{Pt}(111)$ ($T_{\text{ads}} = 140 \text{ K}$) as typically observed on a surface with an increased step density. The steps were produced purposefully by 5 keV Ar^+ bombardment as described in the experimental section, 2.5.

An ion fluence of $F = 3$ MLE leads to a morphology with an average terrace width of ≈ 250 Å. The water adlayer is found in the $\sqrt{37}$ structure (see also [138]) now showing a regular lattice of triangular shaped depressions [Figure 3.2(b)] embedded into a molecularly ordered matrix. The matrix has an apparent height of (1.34 ± 0.03) Å (measured at $U = -0.5$ V, $I = 110$ pA) while the height of the triangular regions is (0.7 ± 0.1) Å. We observed domain sizes between $2 \cdot 10^4$ Å² and $1.5 \cdot 10^5$ Å². A more detailed analysis of this adlayer including molecularly resolved topographs will be given in section 3.2.

The high degree of order is also visualized in the periodic pattern of the self-correlation [Figure 3.2(c)] and sharp spots of the Fourier transform [Figure 3.2(d)]. Note that there are two sets of spots in the Fourier transform due to the presence of two rotational domains. The lattice constant of the ordered adlayer is (17.1 ± 0.9) Å with one depression per unit cell. The depression density is (39 ± 2) Pt surface atoms/depression which satisfies the expected 1:37 ratio within the limits of error. We observe no correlation between the degree of order and the distance to the nearest step of the Pt(111) substrate.

Note that the molecular matrix of this particular height and rotation as well as the depressions are common in both the $\sqrt{37}$ adlayer and on extended terraces. While the matrix is still in perfect molecular order in the latter case, the positioning of triangular depressions in this matrix is disordered in orientation and displays also distance variation. Nevertheless, the depression density again is determined to (39 ± 2) Pt surface atoms/depression. Due to these familiarities the structure on extended terraces is hereinafter referred to as $\sqrt{37}$ -like disordered.

To understand how the step edges affect the order of the first water layer we again studied water adsorption on a surface with a high step density, but treated the steps with CO prior to exposure to H₂O. The intention is that CO passivates the step edge as it is known from thermal desorption spectroscopy measurements that CO molecules are more strongly bound to Pt step edges than the H₂O molecules [11].

Figure 3.3(a) shows the resulting layer of H₂O adsorbed on a CO precovered surface with a high step density [$D(\text{CO}) = 18$ L]. Dosing was performed at $T_{\text{ads}}(\text{CO}) = 400$ K to enhance mobility of the CO molecules and saturate the step edges, i.e. their favorite adsorption site [136]. On the right hand side of Figure 3.3 (a) an extended CO island is visible. The CO molecules are arranged in a $\sqrt{3} \times \sqrt{3}$ R30° pattern with respect to Pt(111), see also Figure 3.9. The presence of CO also on the terrace confirms the saturation of the substrate steps. The islands are surrounded by a closed water layer with crystalline order. The molecularly resolved close-up in Figure 3.3(b) again shows no long-range order of tri-

angular depressions and therefore a reduced order of the entire chemisorbed water layer, confirmed by the blurred appearance of both self-correlation (c) and Fourier transform (d). Note that the density of triangular depressions now is considerably increased by about 15 %, i.e. (33 ± 2) Pt surface atoms/depression.

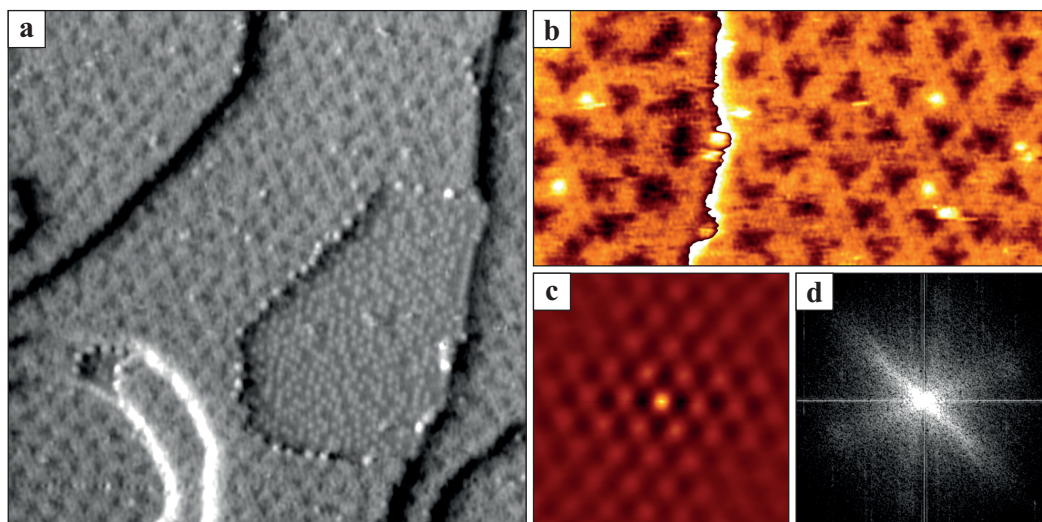


Figure 3.3: Passivation of Step Edges. STM topographs of the H_2O chemisorbed layer formed by adsorption at 140 K on a stepped surface previously exposed to $D = 18\text{L}$ of CO at 400 K. (a) Coexistence of water and CO islands, confirming the saturation of the step edges. The water layer shows poor long-range order. (b) Molecularly resolved image of the water structure showing the disordered arrangement of triangular depressions. Cyclic color shading to enhance contrast on both sides of the substrate step edge (center). (c) Self-correlation image of the structure with a pronounced central peak and blurred surroundings indicating the loss of crystalline order for long distances. (d) Fourier transform of the first wetting layer showing weakened reflex intensity and sharpness. Image width: (a) 325 \AA , (b) 136 \AA , (c) 152 \AA , (d) 0.22 \AA^{-1} ; Imaging parameters: (a) $U = -0.5 \text{ V}$, $I = 160 \text{ pA}$, (b) $U = -0.5 \text{ V}$, $I = 160 \text{ pA}$.

In our STM studies we do observe a superstructural phase found in HAS and LEED measurements on a surface with an increased amount of step edges only. On surfaces with a low step density we always observed a more disordered arrangement of molecules. Since for the stepped surface there are also ordered domains of water not in direct contact with a step, we can rule out a promotion of order by a specific interaction between the step edge atoms and H_2O molecules. However, it is well known that step edge atoms are a sink for several impurities, including H and CO, as these species preferentially bind to steps [136, 139]. Even minute amounts of impurities are able to significantly alter the

structure of an adlayer if a specific interaction mechanism is present [140]. We therefore propose that an increased amount of surface steps effectively binds impurities and consequently reduces their influence on the structure of the water layer on the terrace. This proposal is corroborated by the observation that the order is reduced once the steps are passivated before water adsorption.

The residual gas in our system contains H_2 as the most prominent species, followed by CO (ratio of the respective signals in the mass spectrometer is $\approx 20 : 1$). These species are therefore the most likely candidates for the deterioration of order. In case of hydrogen, it is well known that coadsorption of H_2 and H_2O on Pt surfaces leads to the formation of water-hydronium complexes, i.e. structural units of the form H_5O_2^+ and H_7O_3^+ [141]. The hydronium moiety (H_3O^+) of these complexes has to donate 3 hydrogen bonds in order to achieve the highest degree of binding. This, however is neither possible in the equilibrium structures of water on Pt(111) originally proposed by Glebov *et al.* [12] nor in the structural models introduced in Figures 1.8 and 1.10 where all molecules donate and accept only two hydrogen atoms. Therefore, the hydronium ion cannot be fitted into these structures and consequently may induce disorder. We refrain here from speculations on possible binding patterns of H_3O^+ in a disordered layer due to the lack of experimental data. For the case of CO the situation is more complex (see also the discussion in [2]). Clearly, CO blocks the most favorable adsorption sites for H_2O [68] and can by this mechanism change the structure of the water layer. However, the amount of CO that can be incorporated into the water layer is obviously limited as in Figure 3.3 an island of precipitated CO is visible. Hence, without further experiments aimed at the influence of specific impurities, the species which is responsible for the disorder cannot be identified.

Following our line of reasoning it is not surprising that Harnett *et al.* [94] were able to observe sharp LEED patterns of the $\sqrt{37}$ and $\sqrt{39}$ on a platinum crystal misoriented by 0.3° . This tilting corresponds to terrace widths of only 400 Å, which is a comparable terrace width we find for our irradiated surfaces.

The identical structural elements as well as the similar apparent height and lattice constants indicate the close relationship between the ordered and the disordered structure. The molecularly resolved topographs unveil that both adlayers feature the same structure, i.e. triangular depression and closely related low-lying structures embedded into an ordered molecular matrix, but with a different arrangement of triangular shaped depressions. Based on this analysis we conclude that the $\sqrt{37}$ -like disordered layer and the $\sqrt{37}$ show very similar behavior for spatially integrating experimental methods.

3.2 The Ordered Structures and their Phase Diagram

Figure 3.4(a) shows the ordered superstructure (appearing as a lattice of depressions) observed after water adsorption at $T_{\text{ads}} = 140\text{ K}$, cf. Figure 3.2. While here a full coverage wetting layer is shown, this structure also appears for the entire range of submonolayer coverage. The water layer has an apparent height of $(1.4 \pm 0.1)\text{ \AA}$ [measured with respect to the uncovered Pt(111) surface still visible for submonolayer coverage] which varies smoothly with tunneling voltage (from $1.3\text{--}2.4\text{ \AA}$). For a clean tip it shows no contrast inversion as observed in reference [142]. The Fourier transform of the superstructure displays 12 peaks due to two rotational domains of the hexagonal superstructure. The angle $\alpha = (52 \pm 2)^\circ$ between rotational domains and the periodicity of $(17.1 \pm 0.9)\text{ \AA}$ ($a_{\sqrt{37}} = 16.9\text{ \AA}$) indicate that we observe the $\sqrt{37} \times \sqrt{37}\text{ R}25.3^\circ$ superstructure in real space [equivalent matrix notation $M_{\sqrt{37},\text{Pt}(111)} = (7\ 4, -4\ 3)$ with respect to the substrate]. In Figure 3.4(b), the molecular structure of the $\sqrt{37}$ is resolved. The triangular depressions have an apparent depth between 0.6 \AA and 1.0 \AA with a mean value of $(0.7 \pm 0.1)\text{ \AA}$, the error is mainly given by the varying sharpness of the tip. They are separated by a continuous matrix containing dark spots. The dark spots are part of a hexagonal lattice with primitive translations $\mathbf{a}_1, \mathbf{a}_2$. The dense packed rows of this lattice enclose an angle $\beta = 5^\circ$ with the ones of Pt(111). With respect to \mathbf{a}_1 and \mathbf{a}_2 the superstructure has a matrix $M_{\sqrt{37},\text{H}_2\text{O}} = (4\ 2, -2\ 2)$. We interpret the dark spots as centers of hexagonal ice rings. The structural model proposed in [12] does not comply with these observations.

For lower $T_{\text{ads}} = 130\text{ K}$ a second superstructure forms with prominent protrusions [Figure 3.4(d)]. The Fourier transform shows two rotational domains with $\alpha = (32 \pm 2)^\circ$. The measured periodicity is $(18.0 \pm 0.5)\text{ \AA}$. We identify this structure with the second HOC superstructure: $\sqrt{39} \times \sqrt{39}\text{ R}16.1^\circ$ ($a_{\sqrt{39}} = 17.3\text{ \AA}$) or $M_{\sqrt{39},\text{Pt}(111)} = (7\ 5, -5\ 2)$. Figure 3.4(f) shows that also the $\sqrt{39}$ builds from an ordered arrangement of triangular shaped depressions, but with additional small bright protrusions imaged on the surrounding matrix with an apparent height above the water layer of $(0.9 \pm 0.1)\text{ \AA}$. For the superstructure we derive $M_{\sqrt{39},\text{H}_2\text{O}} = (4\ 3, -3\ 1)$, with $\beta = 2^\circ$.

Preparation of a submonolayer film (adsorption of only 0.55 molecules per site) at 130 K leads to islands of the $\sqrt{37}$ wetting layer.

The proposed arrangement of the H_2O lattice (forming the matrix) with respect to the substrate is backed by the evaluation of the spot intensities found in previous studies [10, 12, 78], as will be shown in the following paragraph.

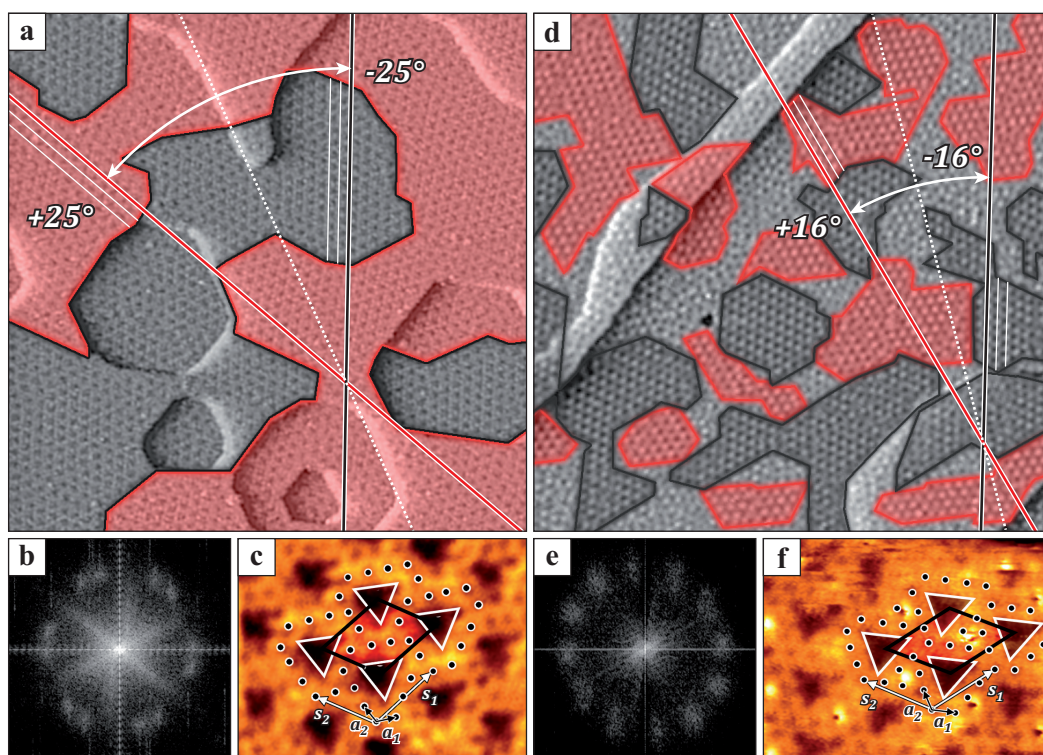


Figure 3.4: Analysis of the Superstructural Domains. (a) STM topograph of the H₂O wetting layer on Pt(111) formed by adsorption at 140 K ($\sqrt{37} \times \sqrt{37}$ R25.3°). The superstructure is characterized by a lattice of depressions spaced by 17 Å. Shading in false colors (dark grey, red) indicates two rotational domains (domain boundaries marked by black and red lines). The lines in the respective colors are parallel to rows of depressions in the appropriate domain (also indicated by parallel thin lines). The angle bisector (white line) is parallel to the step edges of Pt vacancy islands, i.e. parallel to the dense packed $\langle 1\bar{1}0 \rangle$ -direction. (b) Corresponding Fourier transform. (c) Molecularly resolved STM image of the $\sqrt{37}$ with the supercell marked by a rhombus and associated supercell vectors $\mathbf{s}_1, \mathbf{s}_2$. Triangular depressions are marked by white triangles and lattice points associated with the dark spots are indicated by black dots. Primitive translations of the lattice partly populated by the dark spots are \mathbf{a}_1 and \mathbf{a}_2 . (d) STM topograph of the H₂O wetting layer on Pt(111) formed by adsorption at 130 K ($\sqrt{39} \times \sqrt{39}$ R16.1°). The superstructure is characterized by a lattice of depressions and additional protrusions. Color coding and construction of lines as in (a). (e) Corresponding Fourier transform. (f) Molecularly resolved STM image of the $\sqrt{39}$ showing a periodic second layer decoration (white spots). Markings as in (b). Image width: (a,d) 710 Å, (b,e) 1.26 Å⁻¹, (c) 81 Å, (f) 68 Å; Imaging parameters: (a) $U = 0.5$ V, $I = 60$ pA, (c) $U = 0.5$ V, $I = 100$ pA, (d) $U = 0.5$ V, $I = 160$ pA, (f) $U = 0.2$ V, $I = 300$ pA.

Evaluation of HAS Studies

The diffraction spots in the HAS diffraction patterns of the $\sqrt{37}$ and the $\sqrt{39}$ [12] show strongly varying brightness as reproduced in Figure 3.5(b,e). Without a complete analysis of diffracted intensities, we discuss in the following whether these brightness differences corroborated the structural motives for the wetting layer proposed either by us or by Glebov *et al.* [12]. The structural motives for the wetting layer proposed by Glebov *et al.* are reproduced in Figure 3.5(a) and (d). We may associate with these molecular structures a 2D Bravais lattice, with each lattice point sitting in a center of an ice ring (or on every second molecule). We calculate the positions of the diffraction spots for this 2D-lattice from the simple rule [143]:

$$\begin{pmatrix} \mathbf{a}_1^* \\ \mathbf{a}_2^* \end{pmatrix} = (M^{-1})^T \begin{pmatrix} \mathbf{s}_1^* \\ \mathbf{s}_2^* \end{pmatrix}.$$

Here M is the matrix that describes the relation of the superstructure with respect to the ice lattice in real space, \mathbf{a}_1^* and \mathbf{a}_2^* are primitive translations of the ice lattice in reciprocal space (so any linear combination of these two describes a reflex in diffraction), and \mathbf{s}_1^* and \mathbf{s}_2^* are the primitive translations of the superstructure in reciprocal space where the linear combination create all spots depicted in Figure 3.5. The respective matrices according to the model proposed by Glebov *et al.* [12] are given by

$$M_{\sqrt{37}}^{\text{HAS}} = \begin{pmatrix} 4 & 3 \\ -3 & 1 \end{pmatrix}; \quad M_{\sqrt{39}}^{\text{HAS}} = \begin{pmatrix} 4 & 4 \\ -4 & 0 \end{pmatrix}.$$

The result of this calculation is visualized in Figure 3.5 (blue symbols). Due to the existence of two rotational domains we obtain two unit cells in reciprocal space. The resulting locations in reciprocal space are circled in the experimental data in Figure 3.5(b,c) and (e,f) (blue circles). One would expect these spots to be bright within the full superstructure diffraction pattern due to the coherent addition of contributions from molecules associated with these lattice points within the entire superstructure unit cell. In fact, they are only of low or mediocre intensity. As a remark of caution we note that in proceeding like this we neglect the additional distortions in the wetting layer which contribute to the superstructure. Furthermore also structure factor effects caused by the fact that two molecules are associated to each point of our two 2D-lattices or associated with the orientation of individual molecules are neglected.

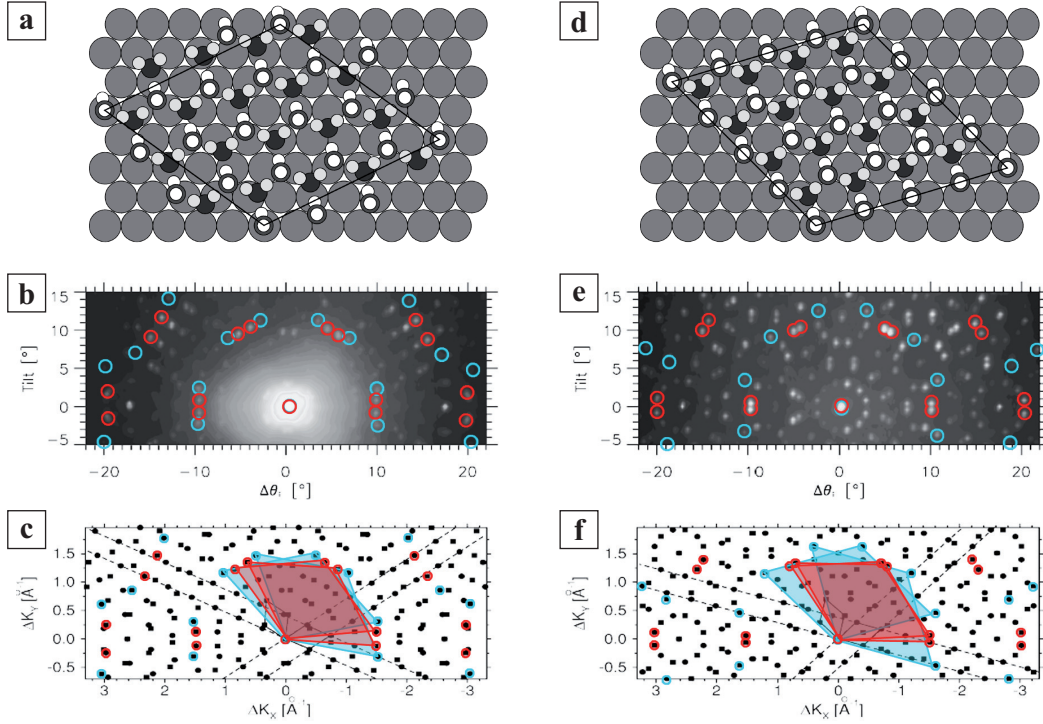


Figure 3.5: Evaluation of the HAS Diffraction Patterns. (a) Sketch of the molecular arrangement of the $\sqrt{37}$ wetting layer suggested in [12] on basis of HAS data. (b,c) HAS data and schematic construction of the $\sqrt{37}$ diffraction patterns originally published in [12]. The overlayer (colored circles) indicate where reflexes that are expected to be of high intensity according to our simplified approach should be found (see text): Glebov model (blue) and structure observed in STM (red). The unit cells related by mirror symmetry are indicated by colored rhombs for each model. (d-f) Same as (a-c), but for the $\sqrt{39}$ wetting layer. Redrawn from [12].

Next we consider our structural models based on the experimental data shown in Figure 3.4 (c) and (f). One may also associate a 2D Bravais lattice to the matrix phase of the $\sqrt{37}$ and the $\sqrt{39}$ by associating a lattice point to each center of an ice ring and extending these points into the space with the $\sqrt{3}$ motive. This lattice only partly represents the full wetting layer structure, but still most of the water molecules can be linked to this lattice. Here the respective matrices are

$$M_{\sqrt{37}}^{\text{STM}} = \begin{pmatrix} 4 & 2 \\ -2 & 2 \end{pmatrix}; \quad M_{\sqrt{39}}^{\text{STM}} = \begin{pmatrix} 4 & 3 \\ -3 & 1 \end{pmatrix}.$$

Again we calculate the diffraction spots for this 2D Bravais lattice [Figure 3.5(c) and (f), red symbols] and circle them red in Figure 3.5(b) and (e). The spots are among the

brightest spots in the entire diffraction pattern. This fact lends additional credit to the structural motive proposed by us for the matrix phase.

Evaluation of LEED Studies

As with the HAS data, one can analyze LEED patterns of the two phases in terms of molecular reflexes of the water layer alone. At this point one has to take into account that the spot intensity may vary upon voltage changes (*IV* LEED). Due to the fact that we do not have access to an extended set of data beyond the published one, we can consider only single frames. Nevertheless, the compliance described for HAS data remains valid for all LEED pictures shown in Figure 3.6. The molecular reflexes of the lattice forming the matrix structure (red circles) appear significantly brighter than the estimated reflexes of the Glebov-model [12] (blue circles), both for the $\sqrt{37}$ and the $\sqrt{39}$ structure and electron energies of 23 eV, 27 eV (for the $\sqrt{37}$ phase), 15 eV and 29 eV (for the $\sqrt{39}$ wetting layer).

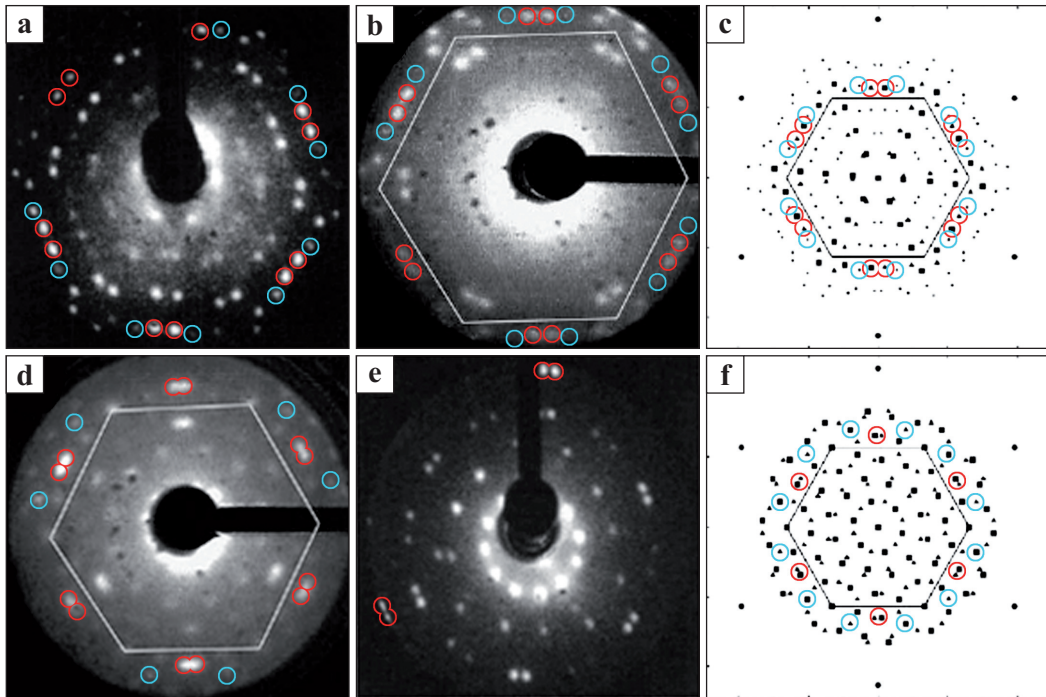


Figure 3.6: Evaluation of the LEED Patterns. Experimental data and corresponding pattern generated from the reciprocal lattice of the two rotational domains (squares, circles) of (a-c) the $\sqrt{37}$ and (d-f) the $\sqrt{39}$ as originally published in [94] and [78]. The blue circles mark the calculated spots of the reciprocal lattice (two rotational domains) formed by the water molecules alone according to the model in [12] whereas red circles are expected for the structures proposed by us. Electron energies: 27 eV (a), 23 eV (b), 29 eV (d), 15 eV (e). Redrawn from [78, 94].

In conclusion one can state: The spots with the highest intensities in the diffraction studies coincide with the reciprocal lattice points calculated from the partly populated black dot lattice in our model. Notably this is not the case for the structure proposed originally by Glebov *et al.* [12].

Phase Transition

The $\sqrt{37}$ and $\sqrt{39}$ can be reversibly transformed into each other through adsorption or desorption of molecules. One direction of this transformation can be induced by heating the $\sqrt{39}$ to 140 K. In Figure 3.7 the angle between two rotational domains changes from $\alpha = (32 \pm 2)^\circ$ to $\alpha = (52 \pm 2)^\circ$ by heating (lines and arrows to guide the eye). Simultaneously, the protrusions of the $\sqrt{39}$ disappear. Together these observations indicate that the $\sqrt{39}$ has a higher density than the $\sqrt{37}$.

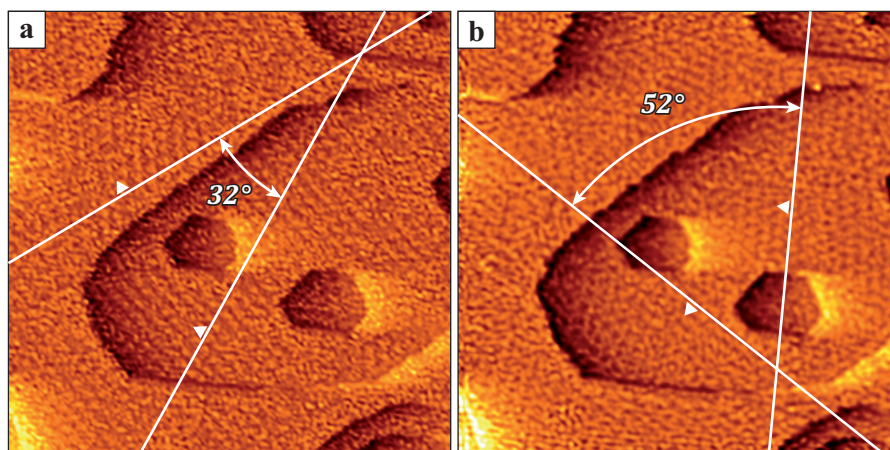


Figure 3.7: Phase Transition. Structural transition from (a) $T = 138$ K, $\sqrt{39} \times \sqrt{39}$ R16.1° symmetry to (b) $T = 140$ K, $\sqrt{37} \times \sqrt{37}$ R25.3° symmetry within 8 minutes. The white dots vanish, enabling the water layer to reorganize as indicated by the change of the orientation of the superstructure. Image width 820 Å; Imaging parameters: $U = 0.5$ V, $I = 160$ pA.

Once the $\sqrt{37}$ is formed, it is preserved upon cooling. The wetting layer can only be re-transformed from the $\sqrt{37}$ to the $\sqrt{39}$ by subsequent exposure at 130 K. The reversible transformations indicate that both are equilibrium phases of the wetting layer on Pt(111). The higher thermal stability of the $\sqrt{37}$ implies a higher binding energy per molecule. Moreover, the fact that we never prepared the $\sqrt{39}$ without protrusions shows that they are an integral part of the $\sqrt{39}$.

3.3 Probing the Molecular Structure via Coadsorption

As we now have an insight into the structure of the wetting layer, we investigate its interaction with foreign molecular species. Here we focus on the coadsorption of Xe and CO, as they provided important pieces of evidence for the nature of the triangular depressions presented in section 3.2. Moreover the interaction of Xe and CO with H₂O is most diverse. The dominant interaction for the case of noble gases is caused by the comparably weak van-der-Waals force. The strong dependence of this interaction on the polarizability in the vicinity of noble gas atom can be exploited to probe the structure of (multiple) water layers in thermal desorption spectroscopy [144]: The noble gas is most strongly bound to the bare metal surface and its bonding strength decreases monotonously with the thickness of the underlying water layer. We therefore expect Xe to provide further information about the structure, i.e. the height distribution, of the water layer.

Dealing with CO, on the contrary, is a matter of catalysis. The catalytic creation of water on a platinum electrode is possibly the most important reaction in electrochemistry, see e.g. [145–147]. But the reaction product itself acts as a catalyst: Bergeld *et al.* [148] demonstrated that H₂O [in contact with the Pt(111) surface] promotes the oxidation of CO. Further adsorption studies showed that it is possible to adsorb > 0.3 ML of CO into a full layer of H₂O/Pt(111), indicating displacement of water molecules by CO species [149]. Our real space measurements now provide insight into the mechanism of CO adsorption on a water covered surface.

Xenon Adsorption

Figure 3.8 shows the Pt(111) surface covered by a complete $\sqrt{37}$ -like disordered water monolayer [$T_{\text{ads}}(\text{H}_2\text{O}) = 140 \text{ K}$], which has been additionally exposed to $D(\text{Xe}) = 5 \text{ L}$ of Xe at $T_{\text{ads}}(\text{Xe}) = 87 \text{ K}$. Xe is imaged as an adlayer with an apparent height of 1.25 \AA above the first water layer at typical tunneling conditions (see Figure 3.8). It forms ramified islands which show a slight height modulation on roughly the same lengthscale as the underlying structure. Also the root mean square (RMS) roughness of the Xe (0.22 \AA) and the water layer (0.18 \AA) are similar. The islands contain several defects such as single vacancies and missing chains visible in the close-up. Xe is arranged in a hexagonal lattice with a lattice constant of $a_{\text{Xe}} = (4.4 \pm 0.2) \text{ \AA}$ [see Figure 3.8(b)]. Two rotational domains can be observed (marked by white lines), where the dense packed $\langle 1\bar{1}0 \rangle_{\text{Xe}}$ directions of the Xe adlayer have an angle of $\beta = \pm 25^\circ$ with respect to the dense packed $\langle 1\bar{1}0 \rangle_{\text{Pt}}$ rows of the substrate. The boundaries between the rotational domains are rather coherent.

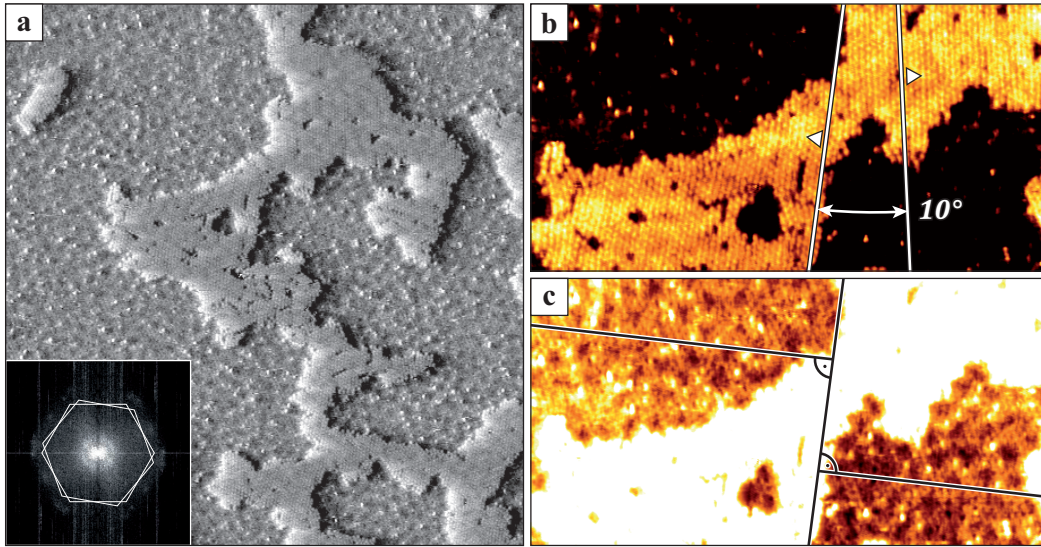


Figure 3.8: Xenon Adsorption. (a) Xe, adsorbed at 87 K on a fully water covered surface, forms ramified islands on top of the water layer. The Fourier transform inset displays two rotational domains. (b) Enlarged view of (a) with contrast enhancement on the Xe layer. White lines indicate the dense packed rows of the different rotational domains, enclosing an angle of approximately 10° . (c) Enlarged view of (a) with contrast enhancement on the water layer. The black lines indicates the $\langle 1\bar{1}0 \rangle$ direction of the particular water layer domain. Image width: (a) 535 \AA , (inset) 0.77 \AA^{-1} , (b,c) 320 \AA ; Imaging parameters: (a) $U = 0.1 \text{ V}$, $I = 180 \text{ pA}$, (b,c) $U = 0.1 \text{ V}$, $I = 180 \text{ pA}$.

Xe is found on top of the $\sqrt{37}$ -like disordered water layer in two rotational domains with the dense-packed direction $\langle 1\bar{1}0 \rangle_{\text{Xe}}$ under an angle of $\beta = \pm 25^\circ$ with respect to $\langle 1\bar{1}0 \rangle_{\text{Pt}}$. The $\sqrt{37}$ has the dense packed water rows $\langle 11\bar{2}0 \rangle_{\sqrt{37}}$ under an angle of $\beta = \pm 5^\circ$ to $\langle 1\bar{1}0 \rangle_{\text{Pt}}$. It is reasonable to assume that the Xe adlayer orients with respect to the water layer underneath and consequently the $+25^\circ$ -domain of Xe is aligned with the -5° -domain of the $\sqrt{37}$ and the -25° -domain of Xe is aligned with the $+5^\circ$ -domain of the $\sqrt{37}$. In this model, $\langle 1\bar{1}0 \rangle_{\text{Xe}}$ runs perpendicular to $\langle 11\bar{2}0 \rangle_{\sqrt{37}}$ as indicated by the black lines in figure 3.8(c) (the second rotational water domain is not visible in this topograph). The ratio $a_{\text{Xe}}/a_{\sqrt{37}} = 0.88 \pm 0.04$ ($a_{\sqrt{37}}$ is the distance between adjacent water hexagons) corresponds to $\sqrt{3}/2 = 0.87$. Therefore the most reasonable model for the structure of Xe on top of water is a commensurate $\sqrt{3} \times \sqrt{3}R30^\circ$ structure with four Xe atoms per unit cell, see Figure 3.8(c). This structure can form easily as by chance there is a good match between the nearest-neighbor distance of solid Xe (4.39 \AA) and the Xe-Xe distance of $(4.4 \pm 0.2) \text{ \AA}$ found here. We cannot make out a preference of the Xe to bind to specific regions of

the water adlayer (i.e. the ice matrix or the triangular depressions). The formation of (ramified) islands seems to be preferred over the adsorption of individual molecules in specific binding sites on top of the water layer.

Carbon Monoxide Adsorption

In order to extend the studies of coadsorption of CO and H₂O mentioned above [94, 148] by real space measurements, we dosed CO on a closed $\sqrt{37}$ water layer grown at $T_{\text{ads}}(\text{H}_2\text{O}) = 140$ K. The CO dose was set to $D = 1$ L at an adsorption temperature of $T_{\text{ads}}(\text{CO}) = 90$ K. This preparation leads to an arrangement of widely spaced islands of varying size and shape inside the water layer with a low apparent height under regular tunneling conditions [see Figure 3.9(a)]. The island spacing is evenly distributed on extended terraces. They have a $\sqrt{3} \times \sqrt{3}R30^\circ$ structure [depicted in Figure 3.9(b)] as well as the more dense $c(4 \times 2) - 2$ CO structure along the edges [see Figure 3.9(c)], both known for the adsorption of CO on bare Pt(111) [136, 150, 151].

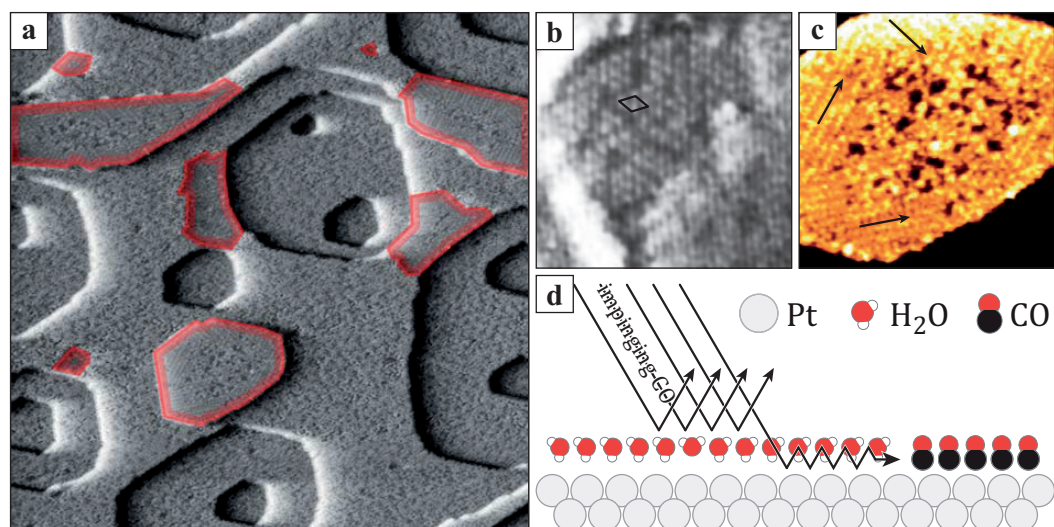


Figure 3.9: CO Adsorption. STM topographs of the closed water layer adsorbed at 140 K and subsequent dosing of 1 L CO at 90 K (a) The CO molecules form islands of manifold shape and spacing, marked by red contours. (b) Molecularly resolved image of a CO island demonstrating the $\sqrt{3} \times \sqrt{3}R30^\circ$ structure (black rhomb marks the unit cell). (c) Close-up of a CO island showing the three $c(4 \times 2) - 2$ CO superstructural rotational domains as highlighted by black arrows. (d) Schematic view of the CO adsorption on the water layer described in the text. Image width: (a) 750 Å, (b) 222 Å, (c) 190 Å; Imaging parameters: (a,c) $U = -0.25$ V, $I = 90$ pA, (b) $U = -0.1$ V, $I = 150$ pA.

After exposing the fully H₂O covered Pt(111) surface to CO we observe the formation of individual CO islands, that can be addressed to molecules binding directly to the bare platinum substrate. The islands are found either in the $\sqrt{3} \times \sqrt{3}R30^\circ$ -structure or the $c(4 \times 2) - 2\text{CO}$ -structure with a total covered fraction of 0.06 .. 0.13 ML, depending on the step edge density. This value is in fair agreement with the data by Kinne *et al.*, who obtained a covered fraction of $\Theta = 0.09$ ML after exposure of 1 L CO (estimated by linear interpolation of their uptake curves) [149]. We interpret the adsorption mechanism as CO displacing the water molecules. This interpretation is well reasoned in the high chemisorption energy of CO on the Pt(111) surface, $E_{\text{B,CO}} \approx 1100$ meV/molecule, in contrast to the relatively weak water-metal bond, $E_{\text{B,H}_2\text{O}} \approx 200$ meV/molecule [135]. A rough estimate of the sticking coefficient of CO on the water layer based on our STM images yields a value of 0.1 .. 0.2, i.e. a strong reduction of the CO sticking coefficient of 0.8 found for clean Pt(111) [152], in agreement with earlier work [149, 153]. We propose a pathway for CO island formation as schematically depicted in Figure 3.9(d): While the majority of CO impinging on the water layer from the gas phase is reflected, a minority is able to penetrate the water layer. The sticking coefficient, albeit reduced, is still too large to be due to penetration at defects only. Therefore we propose that CO is able to adsorb even through the intact water layer. As the C1s peak in x-ray photoemission spectra taken during adsorption only show components characteristic for CO directly bound to Pt(111) [149], adsorption on top of the water layer is improbable. Yet we cannot exclude this mechanism due to the short timescale of the diffusion process. The formation of separated islands evidences that CO is able to diffuse inside the water layer at the temperature of our experiment. Finally, the fact that CO forms close packed islands although the CO-CO interaction is repulsive indicates that there cannot be a substantial number of favorable CO binding sites inside the water layer.

3.4 Manipulation of the Wetting Layer

Electron irradiation effects have previously been observed in LEED studies [10, 77, 94], desorption spectroscopy [154] and STM [123, 124]. Mehlhorn *et al.* claim that "STM imaging of ice is challenging, because the water molecules are easily disturbed by the scanning process due to their large dipole moment and the low energy of a single hydrogen bond. Furthermore, inelastically tunneling electrons starting from approximately 200 mV might easily excite molecular vibrations triggering molecule reorientation" [124]. We studied these phenomena, trying to separate the different effects. By this we are able to present

models for both types of manipulation and conclusively explain the sensitivity of the chemisorbed water layer towards tunneling electrons.

STM topographs presented above were obtained under *normal* tunneling conditions, i.e. bias voltages in the range of $|U| \leq 1.0$ V and tunneling currents below $I \leq 200$ pA. Values higher than these may cause irreversible structural transformations as they were observed in many studies [94, 124]. These damages are caused by (1) electron induced desorption [154] or (2) dissociation of molecules or both of them. To study these mechanisms we investigated the influence of bias voltage and tunneling current independently. As we will detail below, high voltage induces dissociation of molecules and a low-lying mixed H₂O-OH layer in $\sqrt{3}$ symmetry is formed, whereas high currents induce a different, H₂O-only $\sqrt{3}$ structure with the same apparent height as the $\sqrt{37}$. If not stated otherwise, these experiments were performed at $T = 20$ K, to inhibit thermally activated side effects.

Voltage Dependent Manipulation

Figure 3.10 presents the effect of bias voltage on the $\sqrt{37}$ water layer. Figure 3.10(a) shows a topograph of the partially covered substrate ($T_{\text{ads}} = 140$ K, $\Theta = 0.7$ ML) obtained with $U = +0.5$ V, $I = 190$ pA. The water layer seems unaffected by the scanning process. When changing the scanning parameters to $U = +0.5$ V, $I = 190$ pA, the water layer shows strong reaction on the scanning process [see Figure 3.10(b)]. The resulting layer obtained under initial tunneling conditions is depicted in Figure 3.10(c). The structure of the water layer has drastically changed. Note that this process seems to be initiated by an increase of the tunneling voltage only.

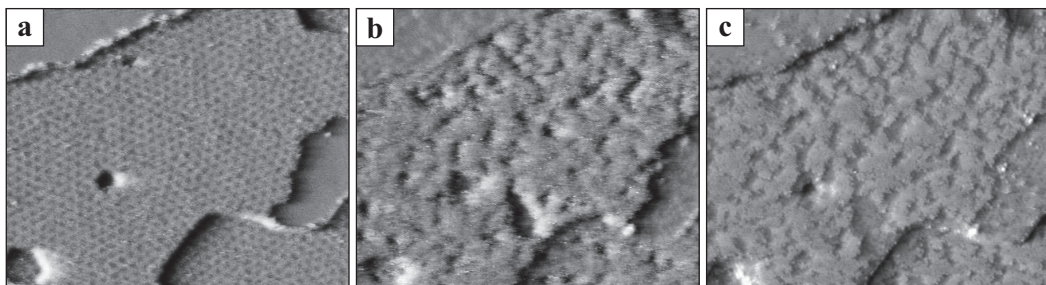


Figure 3.10: Tip Induced Damage of the Water Layer. (a) Chemisorbed water layer ($\Theta = 0.7$ ML, $T_{\text{ads}} = 140$ K) as seen under normal tunneling conditions, $U = 0.5$ V, $I = 190$ pA. (b) Topograph of the water layer when scanning at $U = 5.0$ V, $I = 190$ pA. (c) Resulting layer obtained with $U = 0.5$ V, $I = 190$ pA. Image width: (a-c) 670 Å.

To study the effect of energetic tunneling electrons in more detail we performed measurements with stepwise increasing bias voltage, depicted in Figures 3.11(a) and (b). Starting from $|U| = 0.5\text{ V}$ up to $|U| = 5\text{ V}$ (for both bias polarities) the voltage was increased by 0.5 V in-between each measurement, keeping the current at a fixed value of $I = 190\text{ pA}$.

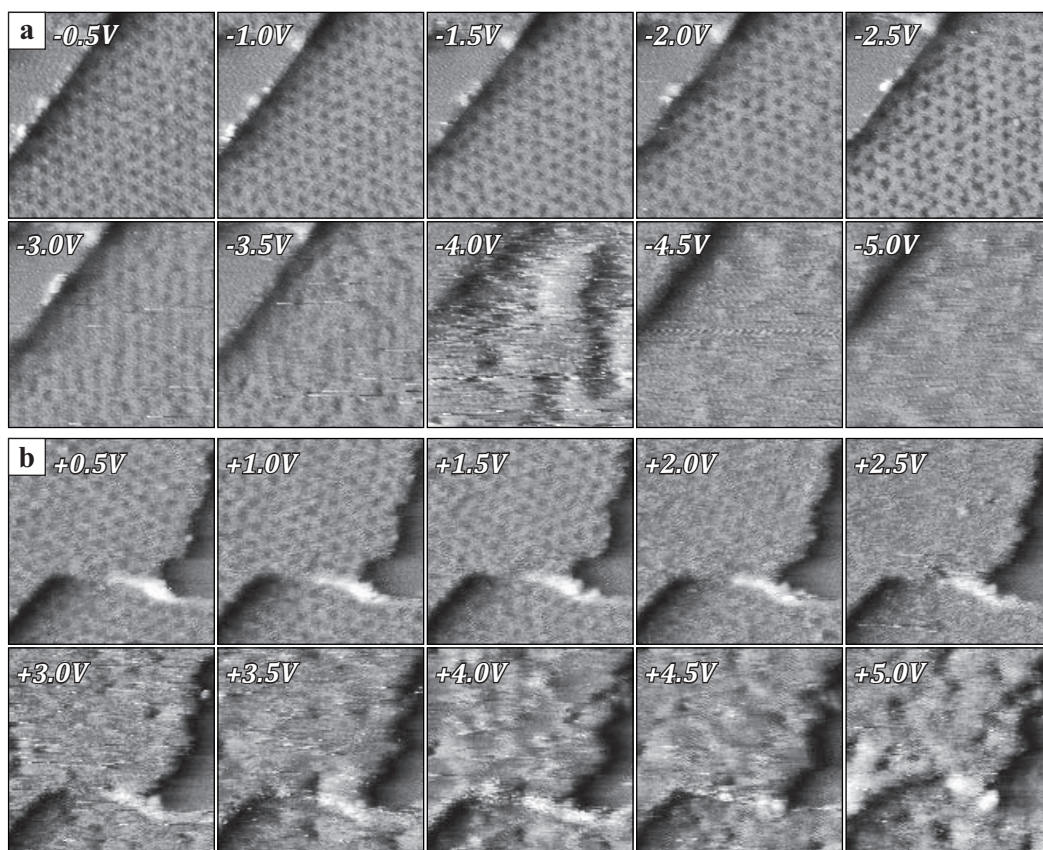


Figure 3.11: Voltage Dependence of the Water Layer Manipulation. STM topographs of the fully covered $\sqrt{37}$ chemisorbed water layer recorded with varying bias voltages at 20 K. (a) Series of measurements at 20 K with stepwise increasing negative bias voltage $U = -0.5.. -5.0\text{ V}$ ($\Delta U = 0.5\text{ V}$). The appearance of the water layer remains unchanged below $U < 4.0\text{ V}$. Passing this threshold results in dissolving the water layer, as the periodic pattern disappears. We observe the formation of grooves exposing the underlying substrate. (b) Series of measurements at 20 K with stepwise increasing positive bias voltage $U = 0.5..5.0\text{ V}$. Structural transitions can be observed already at $U \approx 2.5\text{ V}$. Image width: (a,b) 200 \AA ; Imaging parameters: (a,b) $I = 190\text{ pA}$, U depicted in image.

For negative bias voltages the prominent periodic arrangement of depressions can still be identified at $U = -3.5\text{ V}$, despite occasional tip changes which we address to single molecules being picked up by the STM tip. This means in effect that the extended water

layer remains unaffected of voltages below $U = -4\text{ V}$. When crossing this threshold the superstructure of the water layer dissolves and irregular grooves are observed (running from the top of the image to the bottom) exposing the underlying platinum substrate. The case is similar for positive bias voltages as shown in Figure 3.11(b), though a significant reduction of the layer roughness occurs already at $U \approx 2.5\text{ V}$. The grooves observed for negative voltages also occur here though in smaller amount, which might be due to the more stable tip we had during this series.

Figures 3.12(a) and (b) show a topograph of the partially covered substrate ($T_{\text{ads}} = 140\text{ K}$, $\Theta = 0.7\text{ ML}$) obtained with $U = -0.5\text{ V}$, $I = 190\text{ pA}$, before and after manipulation. The white rectangle in (a) indicates the area purposefully scanned with an increased bias voltage $U = +5.0\text{ V}$. In agreement with the previously shown data, the water layer is clearly affected by the applied high voltage in the range of the afore-mentioned scanning area.

A more detailed analysis of the manipulated area proves the reorganization within the layer: Figure 3.12(c) shows the transition from an unmodified water layer (on the right hand side) to the exposed platinum substrate (left hand side). In between both structures a newly formed adlayer with a lower apparent height is visible. This particular height reduction is conclusively presented in the height profiles in Figure 3.12(d) which displays an average over all scanlines (red curve) of Figure 3.12(c). Showing three distinct height levels, the pristine water layer is imaged 1.3 \AA above the platinum substrate, while the apparent height of the structure obtained by manipulation is 0.7 \AA ($U = -0.5\text{ V}$, $I = 190\text{ pA}$), which means a height reduction of 0.6 \AA with respect to the unaffected water layer. Note that small dips on the right hand side are due to the triangular depressions in the water layer, whereas the protrusions on the left hand side can be addressed to single adsorbates on the platinum surface. Instead of the two height levels observed before (depressions, matrix), the structure after manipulation only has one height level, the one of the depressions, as indicated by arrows in the individual linescan (black curve).

The molecularly resolved topograph in Figure 3.12(e) shows this structure with larger spatial extent (achieved by faster scanning with $U = 5.0\text{ V}$) recorded at $U = -0.5\text{ V}$. It contains spots of bare platinum (dark patches) incorporated in an ordered arrangement of molecules in a $\sqrt{3} \times \sqrt{3}\text{ R}30^\circ$ superstructure. The corresponding unit cell is marked by a rhombus. The apparent height of this layer again is measured to 0.7 \AA ($U = -0.3\text{ V}$, $I = 220\text{ pA}$). Due to the $\sqrt{3}$ arrangement and the low apparent height the structure will be referred to as low- $\sqrt{3}$ in the following.

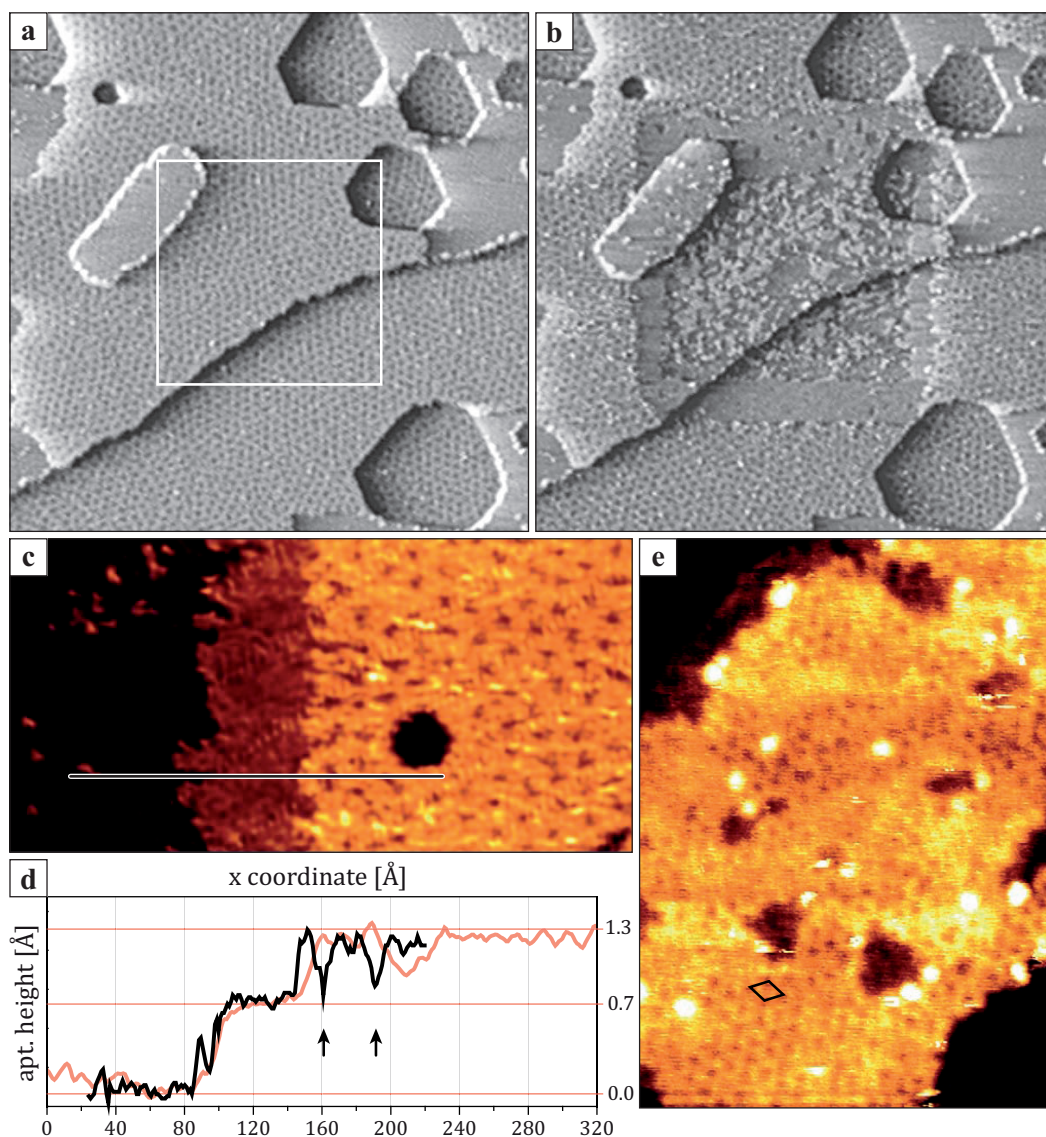


Figure 3.12: Analysis of the Water Layer after Manipulation. (a) STM topographs of the $\sqrt{37}$ water layer ($\Theta = 0.7\text{ML}$, $T_{\text{ads}} = 140\text{K}$) before manipulation. The rectangle marks the area subsequently undergoing a scanning cycle with $U = 5.0\text{V}$. (b) Topograph of the resulting layer after manipulation. (c) Transition between pristine water layer (r.h.s.) and clean platinum substrate (l.h.s.) showing a newly formed flattened layer bridging these two structures. (d) y -average height profile (red) and individual linescan (black line) of (c) display three different height levels at 1.3\AA and 0.7\AA above the platinum ground line. Arrows indicate the location of triangular depressions in the topograph. (e) Molecular resolved topograph after manipulation showing the $\sqrt{3} \times \sqrt{3} R30^\circ$ structure of the flattened layer. The corresponding unit cell is marked. The new layer also shows some second layer decoration (white dots) and dark patches due to exposed platinum substrate. Please note the different color shading and contrast of figures (c) and (e). Image width: (a,b) 900\AA , (c) 320\AA , (e) 140\AA ; Imaging parameters: (a,b) $U = -0.5\text{V}$, $I = 190\text{pA}$, (c) $U = -0.5\text{V}$, $I = 190\text{pA}$, (e) $U = -0.3\text{V}$, $I = 220\text{pA}$.

Temperature Induced Mixing

A closer look at the data unveils that the manipulation exceeds the mere scanning area, meaning that structural transformations also take place in the vicinity to the actual manipulation event. A comparison of the highlighted area in figures 3.12(a) and (b) clearly shows parts of the low $\sqrt{3}$ exceeding the former scanning area by about 50 Å. Nevertheless we observe distinct boundaries between the low $\sqrt{3}$ and the pristine water structures at $T_{\text{scan}} = 20$ K. This observation changes when elevated temperatures ($T_{\text{scan}} \approx 140$ K) are considered: Figure 3.13(a) shows the variety of structures present after manipulating a $\sqrt{37}$ water layer with $U = -5$ V. While the low $\sqrt{3}$ is still observed in the center, the transition towards the regular water layer is heavily blurred for several hundred angstrom. This results in a maze-like structure, indicating intermixing of the two structures. A direct comparison between the high and low temperature regime is shown in Figures 3.12(b) and (c), respectively. The white line marks the left-hand limit of the former scanning area. Note the different image sizes.

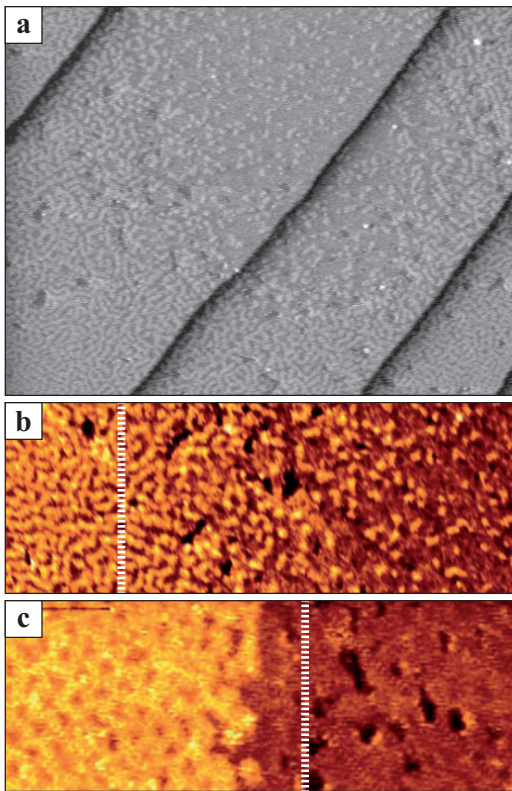


Figure 3.13: Temperature Dependence of the Transition Regime. STM topographs of the chemisorbed water layer after manipulation by $U = 5.0$ V. (a) At 140 K the resulting adlayer gives rise to a maze-like structure, also visible in the enlarged view (b). The dotted line marks the left-hand limit of the previously manipulated area. (c) Transition between the flattened and pristine water layer at 20 K. The mixing of the two structures is drastically inhibited. Image width: (a) 1450 Å, (b) 1000 Å, (c) 330 Å; Imaging parameters: (a) $U = -1.0$ V, $I = 40$ pA, (b) $U = -1.0$ V, $I = 40$ pA, (c) $U = -1.0$ V, $I = 170$ pA.

Our experiments prove that the bias voltages applied in STM do affect the water layer. The high onset voltage provides an indication of the mechanism behind this effect: As the influence on the closed layer starts at $U \approx 2.5$ V or -4.0 V, respectively, we can exclude mechanical perturbation such as phononic excitations which are settled around several meV. It is more likely that tunneling through bonding or anti-bonding orbitals takes place, that finally leads to a dissociation of the molecules. This interpretation is supported by X-ray adsorption spectroscopy (XAS) and X-ray emission spectroscopy (XES) data obtained by Ogasawara *et al.* [9], who measured the DOS of the O-H bond along the p_z component. From the spectra presented in their work the bonding states can be determined at 4 eV below the Fermi edge, and the antibonding states 2 eV above the Fermi edge, in excellent agreement with the disintegration thresholds of -4 V and $+2.5$ V measured in our experiments. Crossing the threshold voltage therefore either extracts electrons from bonding orbitals or injects electrons into anti-bonding orbitals and subsequently causes dissociation of the molecules. The water layer changes its structure in order to be able to incorporate both intact H_2O molecules as well as OH-fragments, resulting in the low $\sqrt{3}$. Further support for the dissociation model can be found in the work of Clay *et al.* [155], who studied mixed OH + H_2O overlayers adsorbed on Pt(111). Due to the reduced number of hydrogen atoms the ice rules can easily be satisfied, leading to a $\sqrt{3}$ -like arrangement in which the water molecules are adsorbed with their molecular plane parallel to the surface, i.e. a low adlayer. [147] Both the $\sqrt{3}$ -like structure and the low apparent height could now be observed in real space in our studies.

The fact that the restructuring of the water layer extends several nm beyond the range of tip motion (see Figures 3.12 and 3.13) even at 20 K can be attributed to hole (electron) transport in the (anti-)bonding molecular bands. This electron transport was previously observed for water adsorbed on Cu(111) [124]. Increasing the temperature during manipulation blurs the transition regime. Thermal diffusion results in an intermixing of the two structures leading to a nonuniform, maze-like structure with both height levels still distinguishable, which resemble the structures observed by Völkening in the intermediate state in the oxidation of hydroxide to water [4]. Our results complement these catalysis studies as we now are able to investigate the decomposition of the reaction product from H_2O via OH fragments to single oxygen adatoms.

We speculate that the mechanism of restructuring following electron-induced dissociation is also responsible for the initial difficulties in observing the equilibrium structures of the first water layer in LEED [77], which only became possible after significant reduction of the electron dose [10, 94]. Though dissociation may still take place at any electron energy

accessible in LEED, the amount of electrons is sufficiently low to avoid reorganisation on a decent timescale.

Current Induced Manipulation

Not only high bias voltages, but also high tunneling currents affect the order (and structure) of the water layer. Figure 3.14(a) shows the $\sqrt{37}$ -like disordered first wetting layer after continued scanning with $U = -0.6$ V, $I = 400$ pA at $T_{\text{scan}} = 140$ K. The scanning process causes a reorganization of the entire layer which results in an adlayer with a $\sqrt{3}$ superstructure. The structural coherency of this layer is high as shown by the self-correlation image and intense reflexes in the Fourier transform [see Figures 3.14(b) and (c), respectively]. Nevertheless it contains several defect structures visible as sixfold symmetric depressions.

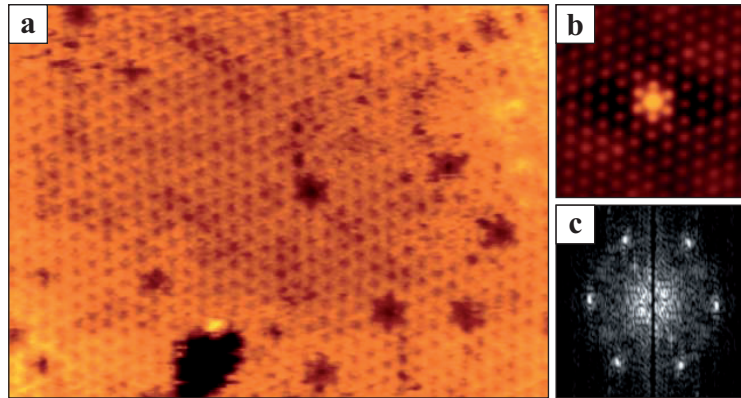


Figure 3.14: Structure of the Adsorbed Layer upon Current Induced Manipulation. STM topograph of the fully covered water layer ($T_{\text{ads}} = 140$ K) to investigate the effect of tunneling electrons on the layer. (a) By continued scanning with $U = -0.6$ V, $I = 300$ pA the water layer is transferred into a $\sqrt{3}$ structure with an (unchanged) apparent height of 1.3 Å. The resulting adlayer shows several defects whereof sixfold symmetric depressions are the most abundant ones. (b) Self-correlation image of the $\sqrt{3}$ structure created by manipulation at high currents showing the high structural coherency in a periodic dot pattern. (c) Fourier transform of the $\sqrt{3}$ structure created by manipulation at high currents emphasizing the high order of the layer by sharp and intense reflexes. Image width: (a) 145 Å, (b) 50 Å, (c) 0.72 Å $^{-1}$.

In contrast to manipulation at high voltages, the apparent height of the new adlayer remains unchanged at 1.3 Å with respect to the platinum substrate. We also observed coexistence of both the high $\sqrt{3}$ and the $\sqrt{37}$ adlayer structures, shown in Figure 3.15(a).

Due to the inherent disorder caused by the misorientation of the dense packed rows, the coexistence areas inhabit a rich variety of defects with different shape, such as rhombs and trapezoids, encircled white in Figure 3.15(a). Sometimes also the known triangles (b) and sixfold symmetric stars (c) are incorporated into the layer. On large $\sqrt{3}$ domains we occasionally observed periodic defect patterns with a typical spacing of 80 \AA as shown in Figure 3.15(d).

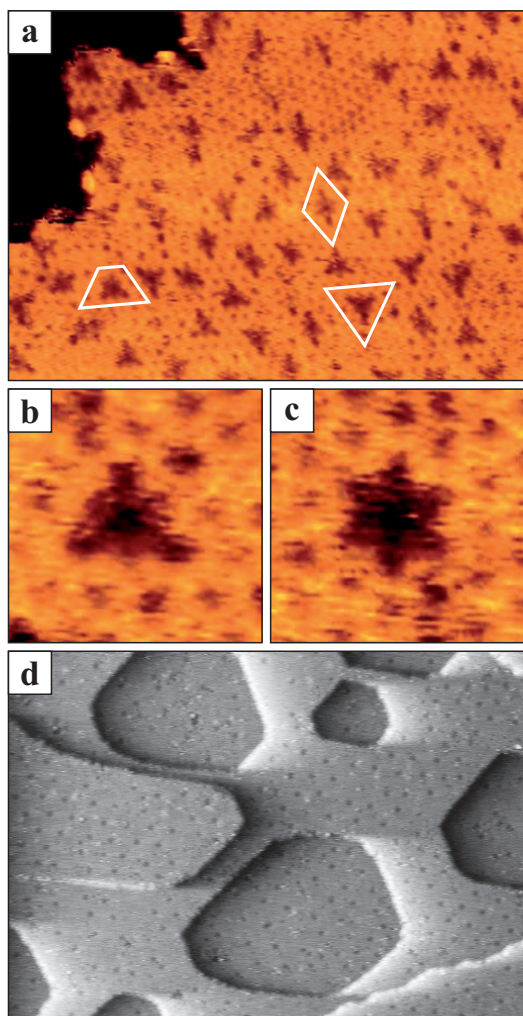


Figure 3.15: Disorder in the Adsorbed Layer upon Current Induced Manipulation. STM topograph of the fully covered water layer ($T_{\text{ads}} = 140 \text{ K}$). (a) Water island formed by coexistence of the $\sqrt{37}$ -like disordered and $\sqrt{3}$ (top center *inter alia*) structures. Various defect structures (rhombs and trapezoids, highlighted) are visible despite triangular (b) and sixfold symmetric (c) depressions. (d) Periodic pattern of sixfold symmetric depressions. The average spacing is 80 \AA . Image width: (a) 190 \AA , (b,c) 24 \AA , (d) 710 \AA ; Imaging parameters: (a-c) $U = -0.6 \text{ V}$, $I = 300 \text{ pA}$, (d) $U = -0.4 \text{ V}$, $I = 300 \text{ pA}$.

The mechanism behind manipulation at high current must be different to the one in the case of high voltages presented above, as the molecules in the affected region in fact have reorganized but the apparent height of the layer remains unchanged, i.e. on the level of the initial $\sqrt{37}$ -like disordered arrangement. The manipulation results in an adlayer with a $\sqrt{3} \times \sqrt{3} R30^\circ$ superstructure. The persisting structural familiarity is expressed in the coexistence of the high $\sqrt{3}$ and the $\sqrt{37}$ -like disordered layer. We observe no further intermixing between the structures, once the tunneling parameters have been changed to a non-manipulative set. Note there is no threshold in bias voltage that has to be exceeded

to perform manipulation. Therefore we rule out dissociation of molecules and suppose that the molecular species in the adlayer has not changed. But how can we affect the chemisorbed water layer on a large scale, if not by dissociation? One possibility is that high electric currents excite vibrations of the molecules, causing the breaking of bonds and a reorganization of the water molecules on the platinum surface. Nevertheless it is still not understood, why the $\sqrt{3}$ is stable, as the lattice constant increases. In fact, an ideal $\sqrt{3}$ layer requires a stretching of all hydrogen bonds of +6.1%. Thus it should be energetically unfavoured and retransform into the initial first wetting layer. A possible explanation of the stability is the existence of defects. Their most common appearance is a sixfold symmetric star, strikingly similar to the triangular depressions observed in the $\sqrt{37}$ and $\sqrt{39}$ superstructures. Assuming they are built from flat hexamers as proposed by Nie *et al.* [96], (periodically) incorporated in the surrounding layer, the hydrogen bonding network experiences slight relaxation. In case of a $\sqrt{3}$ adlayer the defect should be of sixfold symmetric shape, clearly visible in Figure 3.15(f), whereas more complex shapes can easily be explained by the particular arrangement of the surrounding molecules. After all, the $\sqrt{3}$ structure formed here can only be a metastable structure. We speculate that the newly formed layer cannot transform back into the $\sqrt{37}$ arrangement as the molecular density of the $\sqrt{3}$ is slightly lower, i.e., H₂O has to be added again in order to go back to the equilibrium.

Finally we note that following adsorption of impure water, i.e. water not regularly purified or insufficiently treated by Ar bubbling, we obtained irregular structures featuring the aforementioned structural elements. This finding offers a reasonable explanation why the structure of the first layer of H₂O on Pt(111) was addressed for a long time to obey a $\sqrt{3}$ arrangement.

3.5 Experimental Proof of the Structural Model

Hitherto we studied the formation of the ordered wetting layer, its interaction with foreign molecular species and sensitivity towards tunneling electrons. However, the molecular arrangement of these structures was not discussed in detail. We have shown that all (pristine) water layers are formed out of the same structural elements: (1) Triangular shaped depressions embedded in (2) a continuous matrix of uniform height with (3) second layer decoration (in case of the $\sqrt{39}$ wetting layer only). Their molecular structure is yet unclear. In chapter 1.3 a structural model was introduced, proposed by Nie *et al.* [96], which relies on results of DFT calculations: They find the depressions to be built from a

molecular hexamer in flat geometry, rotated by approximately 30° against the surrounding matrix, which for its part is composed of water molecules in an H-down geometry. Several examples of an inhomogeneous appearance of an H_2O wetting layer have been reported. In [6, 7] the structure was interpreted as a moiré-pattern, i.e. an interference pattern arising when two similar grids are superimposed. However, this effect can be ruled out here as it cannot explain the different appearance of neighboring depressions, their rather large depth, or the sharp edges of these pits. Another possible explanation is that the depressions are molecular vacancy clusters, similar to the lace structure reported for sub-monolayer coverages of H_2O on Pd(111) [90], which indeed bears a striking resemblance to the structures observed here. Geometrically, in such a flat hexagonal structure an imbalance between hydrogen bond donors and acceptors arises which leads to the appearance of holes in the water film. In the following we analyze the nature of the depressions as the common structural element based on the findings of this chapter, and give an experimental proof of the proposed model.

Manipulation of the Water Layer

In the previous section we demonstrated that the wetting layer can be modified by prolonged scanning with $|U| \geq 4 \text{ V}$. The structure of this modified layer gives important clues on the structure of the intact layer: At the edge of water-free areas [cf. Figure 3.12(c)] a transition from the Pt surface via the dissociated $\sqrt{3}$ adlayer to the intact $\sqrt{37}$ water layer can be observed. Three associated height levels can be determined in respective line profile (black curve): For $U = 0.5 \text{ V}$, the dissociated phase has an apparent height of $(0.7 \pm 0.1) \text{ \AA}$, whereas we measure $(1.4 \pm 0.1) \text{ \AA}$ for the $\sqrt{37}$. As discussed above, the established model for the equilibrium structure of a 1:1 mixed $\sqrt{3} \times \sqrt{3} \text{ R}30^\circ \text{ OH}+\text{H}_2\text{O}$ adlayer is composed of molecules in uniform height above the surface with their molecular planes oriented parallel to the surface, i.e. a flat-lying geometry [147], which agrees with our findings. We point out that the bottom of triangular depressions in the intact water layer has approximately the same height as the partially dissociated $\sqrt{3}$ structure.

Molecule Coadsorption

When dosing xenon on the fully water covered platinum surface no change in the appearance of the triangular depressions was observed, cf. Figure 3.8(c). To be more specific, we analyze the assumption that the flat hexagon is a preferred adsorption site for rare gas ions [98]. We observe Xe at the kink positions at the edges of Xe islands, but never an isolated Xe atom on top of the flat-laying water hexagon. Using the assumption that at

the temperature of Xe deposition [$T_{\text{ads}}(\text{Xe}) = 87 \text{ K}$] the Xe adatom gas was in equilibrium with the Xe islands we can give an upper bond for the binding energy $E_{\text{hex,Xe}}$ of the Xe to the water hexamer: In thermal equilibrium, the ratio between the probability for finding Xe at a kink site P_{kink} and the probability of finding Xe on top of a flat hexamer P_{hex} is given by a Boltzmann distribution:

$$\text{relative population} \quad \frac{P_{\text{kink}}}{P_{\text{hex}}} = \exp\left(\frac{E_{\text{kink}} - E_{\text{hex}}}{k_{\text{B}}T}\right), \quad (3.1)$$

where $E_{\text{B,kink}} = 80 \text{ meV}$ [156] is the energy gain by adding a Xe atom to a kink site of an island (which is here simply assumed to be equivalent to the cohesive energy of solid Xe). Using as an upper bond $\frac{P_{\text{kink}}}{P_{\text{hex}}} \geq 1000$ this leads to $E_{\text{hex}} \leq 26 \text{ meV}$. For the closely related rare gas Kr, a shoulder in the desorption spectra from the first monolayer was interpreted as gas atoms desorbing from the the flat-lying hexamer [98]. Following this interpretation, one can determine an extra binding energy $E_{\text{hex,Kr}} = 25 \text{ meV}$, which is around the upper limit given by our experiments. Therefore, unfortunately, we can neither support nor contradict the revised interpretation of the Kr desorption spectra.

In case of carbon monoxide, it is reported that about 5% of the saturation coverage of CO adsorbs to the $\sqrt{39}$ and only a two layer thick ice film has a zero sticking probability for CO. [94] Does this observation corroborate the hole-model? We tested this by dosing CO on a closed water layer, cf. Figure 3.9. However, the appearance of the triangular depressions did not change even upon exposure in excess of 1 MLE CO. Specifically, in our STM images we see no evidence for CO adsorption inside the flat hexamer as speculated in [98] as can be seen in Figure 3.16(a). Instead, widely spaced islands of the CO $\sqrt{3} \times \sqrt{3}$ - or $c(4 \times 2)$ -structure [157] appeared inside the water layer indicating that CO is able to partly break up the H₂O layer here.

During the CO-experiments occasionally an inverted contrast STM imaging mode was encountered. We tentatively attribute this imaging mode to a CO molecule adsorbed to the PtIr tip. In inverted contrast mode the triangular depressions are imaged as protrusions with their triangular envelope rotated by 30°, see Figure 3.16(b). The other parts of the wetting layer and CO-islands are imaged 0.8 Å lower than the protrusions. Prolonged scanning in the inverted contrast mode causes the triangular protrusions in the wetting layer to grow to a connected pattern of the $\sqrt{3}$ [Figure 3.16 (c)], which displays the same height as the original protrusions. Apparently, the triangular protrusions are nuclei of the $\sqrt{3}$.

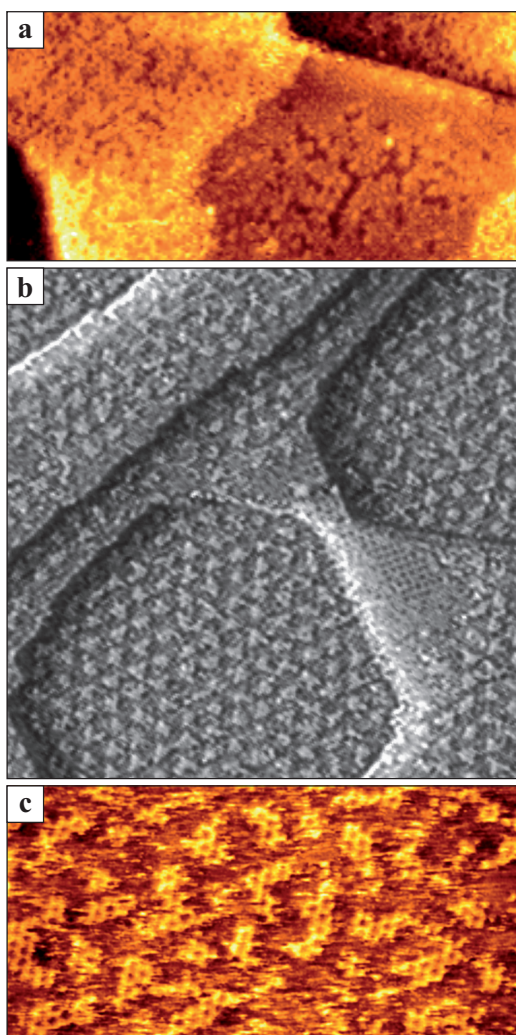


Figure 3.16: Structure Conservation and Contrast Inversion upon CO Dosing.

STM topographs of the closed water layer adsorbed at 140 K and subsequent dosing of 1 L CO at 90 K. (a) Structure of the water layer in close vicinity to a $c(4 \times 2) - 2 \text{ CO}$ island. Triangular depressions are still visible on the left hand side. (b) Topograph in inverted contrast imaging mode (see text). The triangular depressions are now imaged as triangular protrusions rotated by 30° . (c) With the triangular protrusions as nuclei the $\sqrt{3}$ structure grows by prolonged scanning in the inverted contrast mode. Image width: (a) 300 \AA , (b) 310 \AA , (c) 180 \AA ; Imaging parameters: (a) $U = -0.25 \text{ V}$, $I = 90 \text{ pA}$, (b,c) $U = 0.5 \text{ V}$, $I = 150 \text{ pA}$.

Conclusion

Based on the experimental results we suggest the following elements for the $\sqrt{37}$ and $\sqrt{39}$ as shown in Figure 3.17:

(1) The matrix phase of the superstructures consist of a hexagonal network of ice molecules derived from the lattice generated by the primitive translations \mathbf{a}_1 and \mathbf{a}_2 in Figure 3.4. Each lattice point visible as a dark spot in Figures 3.4(c) and (f) is surrounded by an ice ring. Consistent with previous results the matrix phase of the intact wetting layer are assumed to consist of a structure according to the H-down model [7, 9, 10, 154]. Previous work rules out that a significant number of dangling hydrogen bonds points into the vacuum, which makes the first water layer hydrophobic, exemplified by three-dimensional ice growth on top. Consequently, we propose that the molecules in the ridges are arranged similar to the H-down model. However, as the position of the hydrogen atoms cannot be

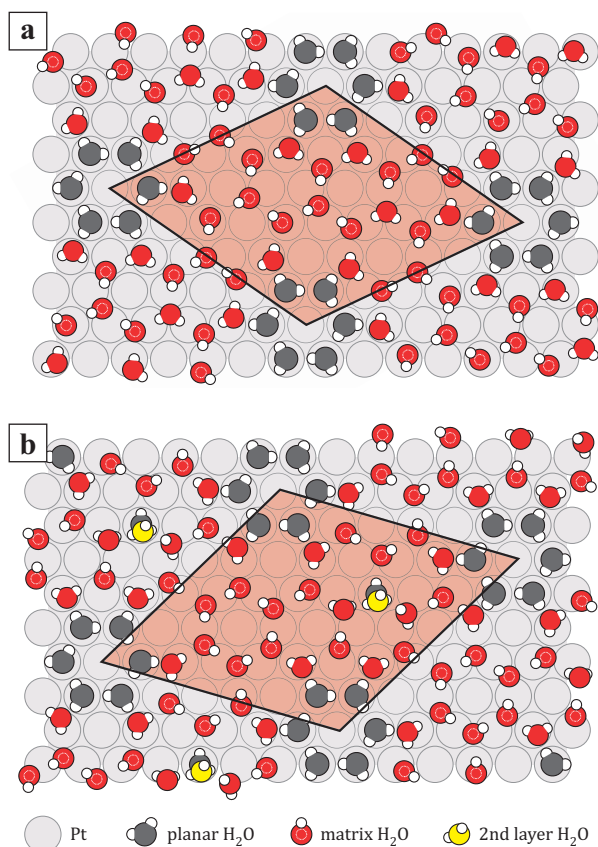


Figure 3.17: Structural Model of the Wetting Layer. (a) Ball model of the $\sqrt{37}$ wetting layer as described in the text. (b) Ball model of the $\sqrt{39}$ wetting layer as described in the text. Positioning of the hydrogen atoms according to reference [96].

determined using STM we made no attempt to propose an orientation of individual water molecules but rely on the findings of reference [96]. Furthermore, we made no attempt to relax the molecular positions. In the resulting $\sqrt{37}$ ($\sqrt{39}$), the hydrogen bond length of the molecules in the matrix phase is extended by only 0.7% (1.8%) compared to the one in bulk ice even if one neglects possible relaxations through the presence of the depressions.

(2) The triangular depressions are filled with water molecules forming the basic building block of the $\sqrt{3}$. As the triangular depressions are not empty, have the same height as the dissociated partially $\sqrt{3}$ adlayer under regular imaging conditions and act as their nuclei they are most probably filled with flat-lying molecules and/or flat-lying fragments in a $\sqrt{3}$ geometry. It has to be noted that a small flat-lying segment does not have to contain dissociated H₂O in order to avoid the occurrence of frustrated hydrogen bonds. If a complete hexagon of a nondissociated $\sqrt{3}$ phase is placed inside the depression one arrives at the structures proposed in [96].

(3) In addition, to the $\sqrt{39}$ in each unit cell a second layer water molecule is adsorbed, thereby saturating dangling bonds and thus lowering the energy [158]. This provides a simple explanation for the bright protrusions observed in Figure 3.4(d) and (f). We assume that the protrusions are formed by a single water molecule, as we infrequently observed

protrusions consisting of two or three dots (of uniform size) which are most probably composed out of two or three water molecules.

Based on the structural models shown in Figure 3.17 we can calculate the coverage to 0.70 (0.75) molecules/site for the $\sqrt{37}$ ($\sqrt{39}$), in fair agreement with uptake measurements [155] for the $\sqrt{39}$. The ease of the phase transformation can be rationalized by the similarity of the two structures, the almost identical length of the O \cdots H bonds and the similar orientation of the dense-packed molecular rows. Note that the $\sqrt{37}$ is most probably identical to phase II in reference [6] whereas phase I from this reference could not be reproduced.

CHAPTER 4

Water Adsorption on Ir(111)

All experiments discussed in the following chapter were carried out by myself. They were planned and interpreted with support of Carsten Busse. For experimental details the reader is referred to Chapter 2.

In this chapter, we present experimental data regarding the wetting behaviour and structure formation of water on Ir(111). In Section 4.1 we study the thermodynamics of water adsorption and point out the possibility to form a wetting layer, suitable for analysis via STM. Based on these results we perform a coverage dependent study of the structure of the wetting layer, see Section 4.2. Here, we apply the findings we obtained for water adsorption on Pt(111) and, furthermore, shortly address the stability of water molecules against tunneling electrons.

4.1 Thermodynamics of Water Adsorption on Ir(111)

In the following section we investigate the energetics and growth of H₂O on Ir(111) via thermal desorption spectroscopy. The focus of this study is on the temperature dependence and formation of a wetting layer on the metal substrate.

Figure 4.1 shows the TDS data (a) for water adsorption in the sub-ML regime and the temperature dependence of the coverage (b) extracted from these curves by integration. The adsorption temperature was $T_{\text{ads}} = 125$ K, the temperature ramp in the spectra was set to $\beta = 1$ K/s.

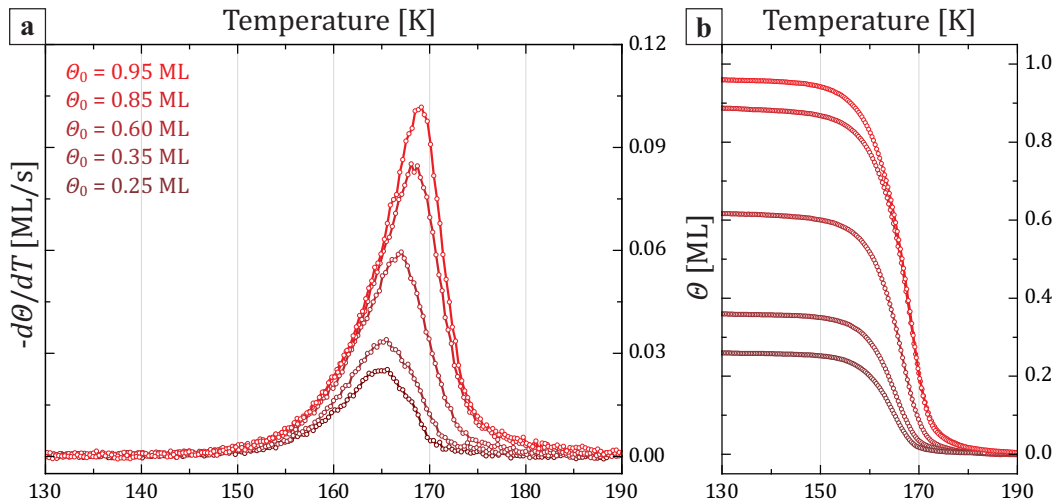


Figure 4.1: Thermal Desorption Spectroscopy of sub-ML Coverage. (a) TDS spectra of H₂O (recorded mass: 18) adsorbed on Ir(111) at $T_{\text{ads}} = 125$ K. The temperature ramp while recording was set to 1 K/s. $\Theta_0 = 0.25 \dots 0.95$ ML, as indicated in the diagram. (b) Corresponding coverage obtained via integration of the spectra shown in (a).

For the lowest coverages For $\Theta_0 > 0.35$ ML the desorbing species shows a single peak with common leading edge which indicates zero order desorption kinetics, cf. section 2.3 and references therein. Note that the non-steep flank of the peaks towards higher temperature can be addressed to the finite pumping speed of our setup in combination with the use of a Feulner-Cup [137] to enhance the signal intensity.

When increasing the coverage further, the previously observed desorption peak [labeled peak (A)] saturates in intensity and a low temperature shoulder emerges, see Figure 4.2(a). The shoulder develops into a distinct second peak [labeled peak (C)] for initial coverages $\Theta_0 > 2.0$ ML. Simultaneously a feature arises [labeled (B)] which resides in between the

two main peaks. As for the low coverage regime, the second peak shows a common leading edge, indicating zero order desorption.

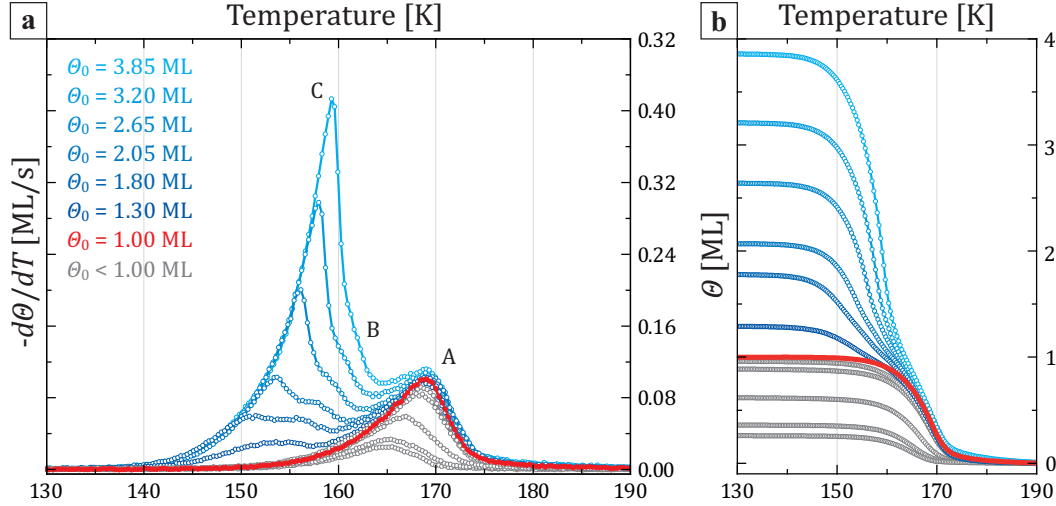


Figure 4.2: Thermal Desorption Spectroscopy of Multilayer Coverage. (a) TDS spectra of H_2O adsorbed on Ir(111) at $T_{\text{ads}} = 125$ K. The temperature ramp while recording was set to 1 K/s. $\Theta_0 = 1.30 \dots 3.85$ ML, as indicated in the diagram. Sub-ML spectra from Figure 4.1 are printed in grey. (b) Corresponding coverage obtained via integration of the spectra shown in (a).

Further support for zero order desorption kinetics of both structures is found in the evaluation of the desorption peak temperature T_{peak} in dependence of the initial coverage. For peak (A) T_{peak} shifts to higher values with increasing Θ_0 , as depicted in Figure 4.3 (red curve). It saturates at $T_{\text{peak}} = (169.1 \pm 0.4)$ K with completion of the monolayer. For peak (C) T_{peak} increases with the initial coverage [blue curve in Figure 4.3] and shows no saturation up to $\Theta_0 = 5.2$ ML.

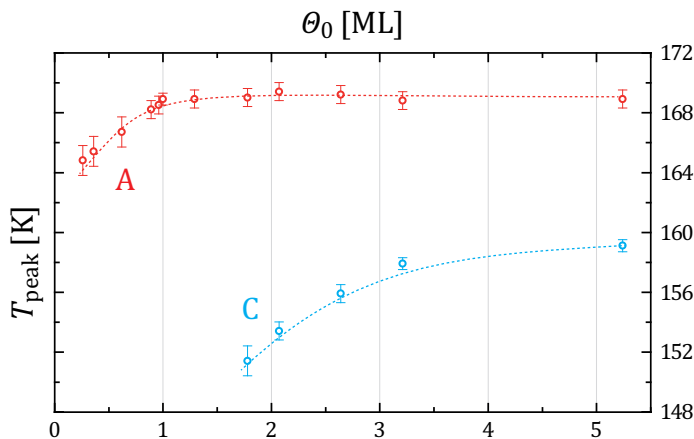


Figure 4.3: Peak Temperature Shift. Desorption peak temperature T_{peak} in dependence of the initial coverage Θ_0 for (A) sub-ML and (C) the high coverage regime. Lines to guide the eye.

For thick water films ($\Theta_0 \gg 10$ ML) we do observe yet another structural transition. The corresponding thermal desorption spectroscopy measurements are depicted in Figure 4.4. Here, we deposited up to 40 ML of water onto the metal substrate at $T_{\text{ads}} = 125$ K. The desorption spectra of these ice films show a newly emerged peak structure which consists of a dominant desorption signal [labeled (X1)] and a low-temperature shoulder [labeled (X2)]. For $\Theta_0 < 20$ ML monolayer desorption can still be identified in the spectra. Notably, the leading edge of these spectra does not coincide with the one of the 3 – 4 ML high adlayer (blue curve in Figure 4.4).

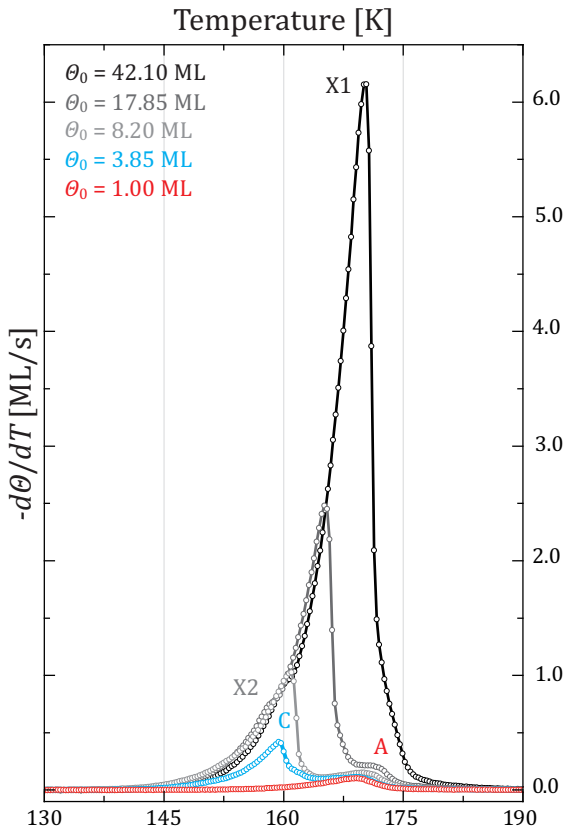


Figure 4.4: TDS of Thick Ice Films. (a) TDS spectra of H_2O adsorbed on Ir(111) at $T_{\text{ads}} = 125$ K. The temperature ramp was set to $\beta = 1$ K/s. $\Theta_0 = 8.20, 17.85,$ and 42.10 ML, as indicated in the diagram. The monolayer spectrum is printed in red. The multilayer desorption signal, $\Theta_0 = 3.82$ ML, is shown in blue.

To quantitatively evaluate the desorption spectra we make use of the approximative methods described in section 2.3: For zero order desorption the desorption energy E_{des} and the frequency factor ν_0 can be determined via a linear fit of the leading edge in the Arrhenius plot. The signal of $\Theta_0 \leq 0.35$ ML was fitted separately to take the deviation from the leading edge into account. Values for the entire coverage range are collected in table 4.1. There also the resulting values of the frequency factors are listed.

Comparing our results to similar measurements performed on different noble metal substrates [3, 10, 11] we can confirm the formation of a chemisorbed wetting layer on Ir(111), as the low coverage water layer is energetically favoured over thin water films. By

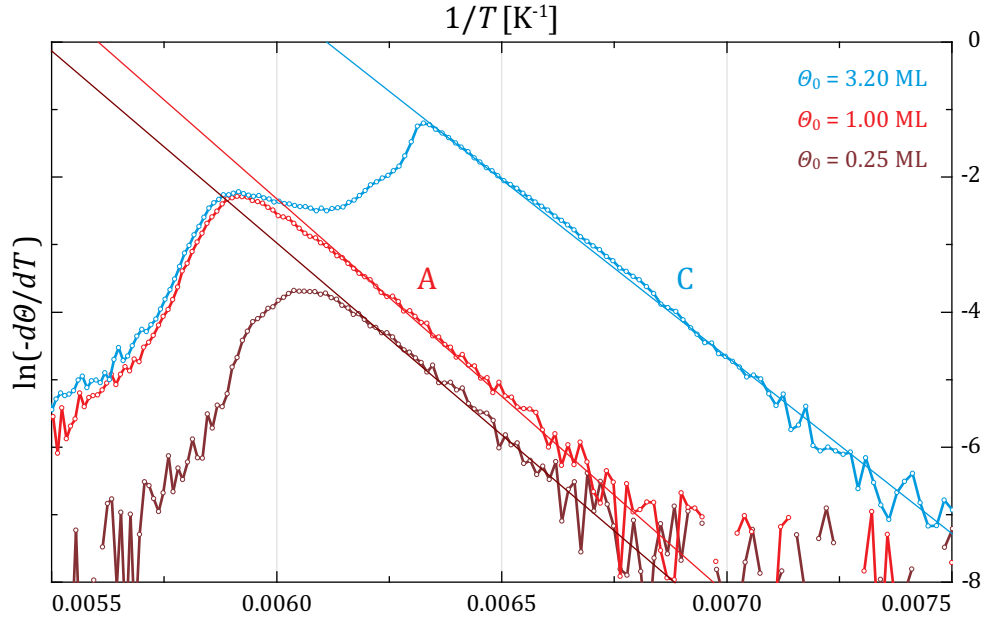


Figure 4.5: Arrhenius Plot Analysis. Logarithmic representation of the desorption signal $\ln(-d\Theta/dT)$ versus the reciprocal sample temperature $1/T$ for $\Theta_0 = 0.25$ ML, 1.0 ML and 3.2 ML. The linear fit of the leading edge is delineated.

Table 4.1: Experimentally Determined Desorption Parameters. Calculated desorption energy E_{des} and frequency factor ν_0 via Arrhenius plot analysis for the different desorption peaks studied. Literature values for Pt(111) [10, 11, 53] are given for comparison.

structure	assignment	E_{des} [meV]	E_{des} [kJ/mol]	ν_0 [1/s]
(A), $\Theta \leq 0.35$ ML	monolayer	490 ± 10	47.3 ± 1.0	$(0.3 \pm 0.2) \cdot 10^{14}$
(A), $\Theta > 0.35$ ML	monolayer	511 ± 12	49.3 ± 1.1	$(2.9 \pm 2.0) \cdot 10^{14}$
(C), $\Theta > 2.0$ ML	few layer	485 ± 6	46.8 ± 0.6	$(9.9 \pm 3.8) \cdot 10^{14}$
(X1), $\Theta \gg 10$ ML	bulk ice	531 ± 2	51.3 ± 0.2	$(4.0 \pm 0.5) \cdot 10^{16}$
(X2), $\Theta \gg 10$ ML	amorphous water	517 ± 2	49.8 ± 0.2	$(1.8 \pm 0.2) \cdot 10^{16}$
	monolayer Pt(111) [11]	550 ± 40	53 ± 4	$3.1 \cdot 10^{15 \pm 1.3}$
	monolayer Pt(111) [10]	539	52	–
	multilayer Pt(111) [11]	500 ± 30	48 ± 3	$3.1 \cdot 10^{15 \pm 1.3}$
	multilayer Pt(111) [10]	518	50	–
	bulk ice [53]	530	51	–

analogy with literature data, we can now associate the peaks to the desorption of the wetting layer [peak (A), $E_{\text{des}}^{\text{A}} = (511 \pm 12) \text{ meV}$] and the few layer ice film [peak (C), $E_{\text{des}}^{\text{B}} = (485 \pm 6) \text{ meV}$]. While the monolayer desorption energy agrees well with typical literature values of a chemisorbed water layer (cf. section 1.2) the desorption energy of the multilayer deviates substantially from the literature value for bulk ice sublimation, $E_{\text{subl}} = 530 \text{ meV}$. At this point of the analysis one can only speculate on the reason for this behaviour. The occurrence of an intermediate feature (B) - which is present right in the beginning of multilayer growth - indicates that the binding of excess water molecules to the wetting layer is more complex than in a simple layer-by-layer growth mode. For Pt(111) it was shown that the growth mode of crystalline ice films clearly deviates from this picture [100]. In fact, the wetting layer itself is hydrophobic [101] and the growth of 3D crystallites is thermodynamically favored [102]. In consequence, the water molecules have to face various boundary effects, like e.g. lower coordination than in the bulk, which lowers the overall desorption energy. Assuming a similar geometry for Ir(111) offers a sound explanation for our observation, that the desorption energy of a (only) 3 – 4 ML high adlayer has not yet reached the value for bulk ice sublimation.

From the results obtained by fitting peak X1 [$E_{\text{des}}^{\text{X1}} = (531 \pm 2) \text{ meV}$] we can state that the water layer has finally taken its equilibrium bulk structure for $\Theta_0 > 10 \text{ ML}$. The low temperature shoulder X2 [$E_{\text{des}}^{\text{X2}} = (517 \pm 2) \text{ meV}$] can be attributed to a preceding crystallization of an amorphous solid water and/or non-wetting ice film which is a result of the finite adsorption temperature.

While these measurements support our assumption of a non-wetting multilayer growth, we yet have no direct proof of the hydrophobicity of the wetting layer. It is therefore of utmost importance to gain information on the spatial arrangement of the monolayer. As discussed before, the wetting characteristics of H_2O adsorbed on Ir(111) allows for analysis of the wetting layer (cf. platinum) up to full saturation when adsorbed above $T > 130 \text{ K}$. An experimental proof of this procedure is given by the solid red curve of Figure 4.2: Here, water was adsorbed at $T = 140 \text{ K}$ to a nominal coverage of $\Theta = 1.5 \text{ ML}$. The TDS data however shows only a monolayer desorption signal.

4.2 Structure and Stability of the Wetting Layer

In the previous section we could show that water adsorbed on Ir(111) forms a wetting layer which is energetically favoured over the bulk ice structure, in agreement with reference [103]. Based on these results we study the structure of the wetting layer in the following section in form of a coverage dependent analysis.

Low Coverage Regime and Island Growth

Figure 4.6 shows the chemisorbed water layer of H₂O on Ir(111) with a coverage of $\Theta = 0.14$ ML (a) and 0.25 ML (b) ($T_{\text{ads}} = 120$ K). In the topographic images one can make out individual adsorbate islands with an average size of $(400 \pm 40) \text{ \AA}^2$ ($380 \pm 30 \text{ \AA}^2$) and an average spacing of 50 \AA (35 \AA) for (a) and (b), respectively. The island size translates into finite size clusters consisting of 30 to 40 molecules at most. The apparent height of these clusters is 1.0 \AA at $U = -1.0$ V, $I = 50$ pA. While the self-correlation image (inset) does not show any long range order for the lowest coverage (a), the more dense arrangement of clusters in Figure 4.6(b) gives rise to some amount of order at nearest neighbour distance [first order maxima in the self-correlation image, cf. Figure 3.1(d)]. Further increasing the coverage to $\Theta = 0.43$ ML results in a dense arrangement of clusters showing the same narrow size distribution as before, see Figure 4.6(c). At this point of the coverage dependence series nucleation of islands sets in. For $\Theta = 0.56$ ML the water islands start to form a continuous network, covering large parts of the iridium substrate. However, individual clusters can still be distinguished in between the island adlayer.

Having a closer look at the substrate steps, we observe only individual adsorbates populating the upper step edges. The topographic images furthermore show that the water clusters seem to be repelled by them, showing a separation of roughly 20 \AA up to high coverages. Contrary, on lower step edges water clusters accumulate and promote the growth of larger adsorbate islands. In the island phase lower step edges are almost completely populated.

Figure 4.6(a,b) and the related size information in the previous paragraph clearly show that, while the cluster density increases with increasing coverage, the cluster size does not. In fact, we do not observe coalescence of individual clusters below $\Theta = 0.43$ ML. In the respective topograph a dense arrangement of clusters with predominantly triangular shape is visible. Consequently, this adsorbate phase consists of well-defined structures.

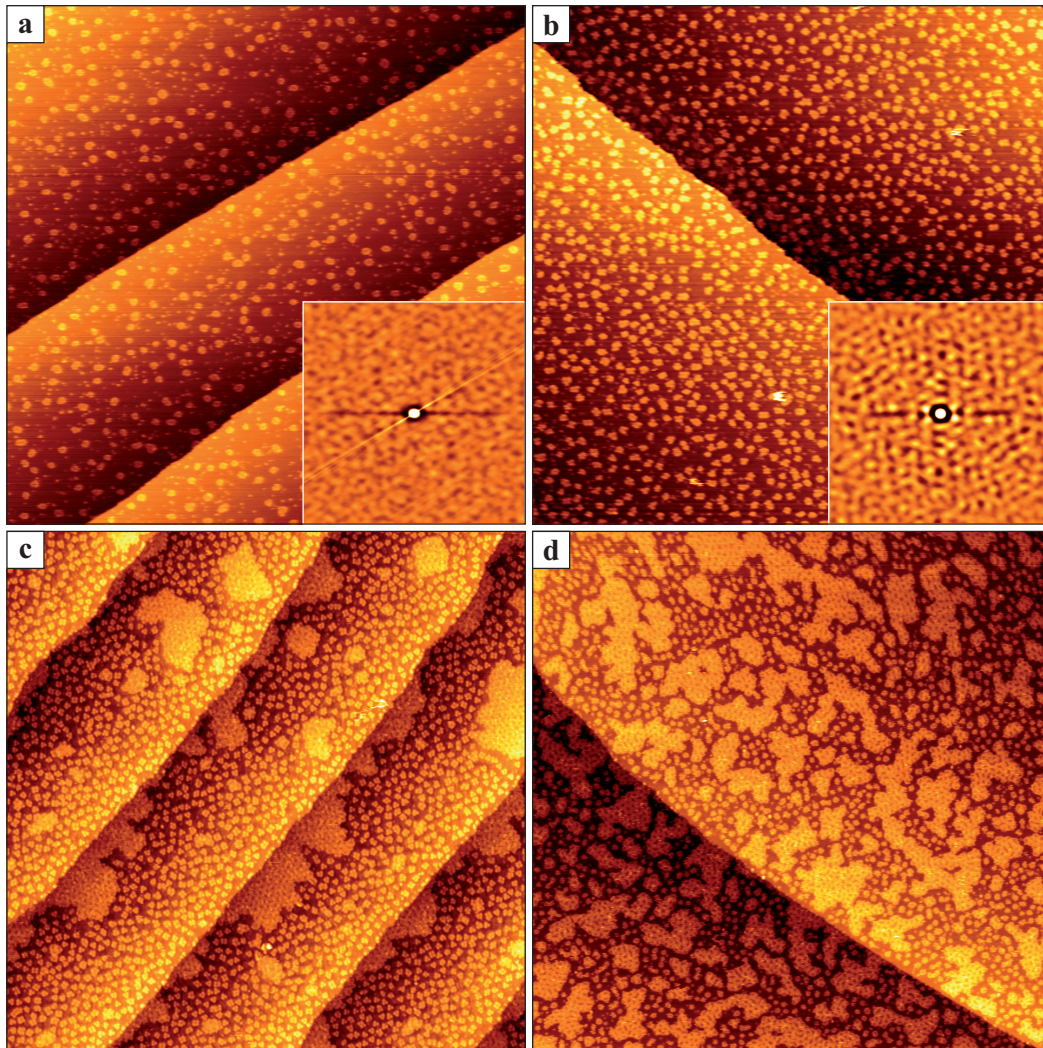


Figure 4.6: Coverage Dependence of the Chemisorbed Water Layer on Ir(111). STM topographic images for water coverages of (a) $\Theta = 0.14$ ML, (b) 0.25 ML, (c) 0.43 ML, and (d) 0.56 ML. The adsorption temperature was set to $T_{\text{ads}} = 120$ K. Insets show the self-correlation image of the respective structures. The molecules form individual clusters upon adsorption. The cluster phase grows in density with increasing coverage and is present on the surface for the entire coverage range studied. We additionally observe the formation of an island network for $\Theta \geq 0.43$ ML. Image width: (a-d) 1500 Å, (insets) 700 Å; Imaging parameters: (a) $U = -1.0$ V, $I = 50$ pA, (b) $U = 0.2$ V, $I = 30$ pA, (c) $U = -0.2$ V, $I = 50$ pA, (d) $U = -1.4$ V, $I = 160$ pA.

In the close-up topograph of Figure 4.7(a) the intrinsic structure of the clusters becomes obvious. As indicated before, most of the clusters obey a triangular shape also visible in the detail view of Figure 4.7(b). The clusters show three distinct height levels: While the apparent height of the structure reaches $h = (1.3 \pm 0.1) \text{ \AA}$ at the edges (imaged at $U = -0.2 \text{ V}$, $I = 30 \text{ pA}$), the central base of the cluster is imaged significantly lower, $h = (0.7 \pm 0.1) \text{ \AA}$. Note that the very center of the cluster shows a depression down to only $h \approx 0.2 \text{ \AA}$. Sometimes we observe also different cluster geometries [cf. Figure 4.7(c) and (d)] but the structural properties - bright edges, dark imaged centers - are common for all these structures.

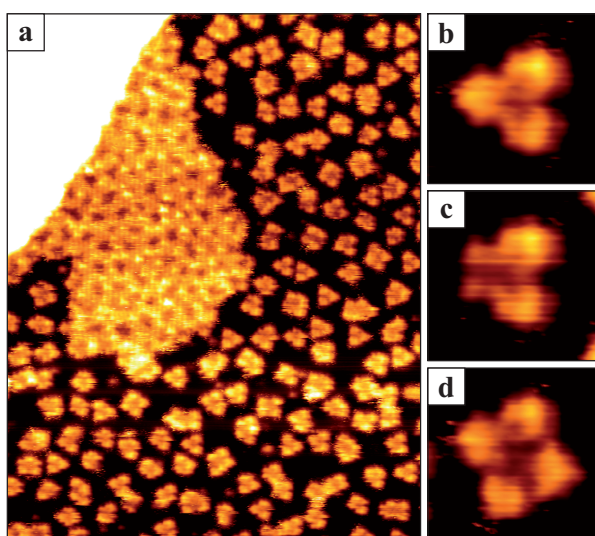


Figure 4.7: Close-up Topographs of the Cluster Phase.

(a) Overview, (b) triangular shaped cluster, (c,d) asymmetric adsorbate clusters. Image width: (a) 320 \AA , (b-d) 24 \AA ; Imaging parameters: (a-d) $U = -0.2 \text{ V}$, $I = 50 \text{ pA}$.

Based on our knowledge obtained by studying the wetting layer of H_2O on $\text{Pt}(111)$ we are able to propose a structural model for the triangular (most common) clusters, shown in Figure 4.8. As discussed in section 1.3, a $\sqrt{3} \times \sqrt{3} \text{ R}30^\circ$ arrangement of molecules is energetically favoured as they take on-top adsorption sites and thus are most strongly bound to the metal substrate. We expect this arrangement to be stable also for $\text{Ir}(111)$ as the lattice mismatch is only -1.5% . Accordingly we address the main structural motif to be a hexagonal ice ring in planar geometry [O colored grey in Figure 4.8(a)]. This geometry results in a violation of the ice-rules and cannot be continued periodically. Consequently we place molecules in an H-down geometry in the bridging sites [O colored red in Figure 4.8(a)], forming a pentagon ice ring. Note, the model is closely related to the structural motif used in the triangular depressions of the continuous layer of $\text{H}_2\text{O}/\text{Pt}(111)$.

The proposed structural model is able to rationalize the overall triangular shape of the cluster and its spatial extent, as indicated in the overlay of Figure 4.8(b): The low apparent height of the base and the center dip agree with the planar geometry of a central ice ring,

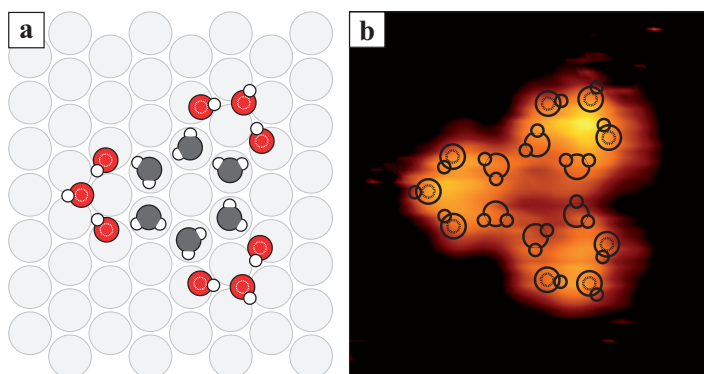


Figure 4.8: Structural Model of the Water Cluster. (a) Proposed structural model for the water cluster shown in Figure 4.7(b), based on a hexagonal ice ring in planar arrangement (oxygen colored grey). The dangling bonds of the $\sqrt{3}$ motif are saturated by bridging molecules in H-down geometry (oxygen colored red). (b) Schematic view of the proposed model superimposing a topographic image of the water cluster. Model and experimental data in scale. Angular alignment obtained via atomically resolved images of the metal substrate.

whereas the increase in height fits to the upright geometry of the bridging molecules and the (possible) dangling hydrogen bond located at the cluster edges.

The structural model also explains different cluster structures as exemplary shown in Figure 4.9. Here, a single molecule of a pentagon ice ring was stripped off and the fragments were arranged into the planar geometry [In fact, we observe a tip-induced transformation of the water clusters of triangular shape into the arrangement shown in Figure 4.7(c). The strong tip-sample interaction is easily visible by horizontal lines and noise in the topographic images. Continued scanning sometimes causes further disassembling of the structures. Details of this process will be given in section 4.2.]. As for the triangular cluster, the model fits well to the experimental data. Note that more complex cluster geometries may require the incorporation of more planar molecules. Based on the dissociative adsorption observed by Pan *et al.* [103] the clusters may even be comprised of molecular fragments (OH groups) which give rise to a variety of possible structures. However, the fact that we predominantly observe clusters in a well defined triangular geometry agrees with their findings, that only a small fraction of molecules dissociates in contact with the iridium substrate.

With the information given here, we are able to explain the observed wetting behaviour of H_2O on Ir(111). According to the structural model, the cluster edges terminate in upright molecules, pointing away from the center of the cluster with (at least) one hydrogen atom.

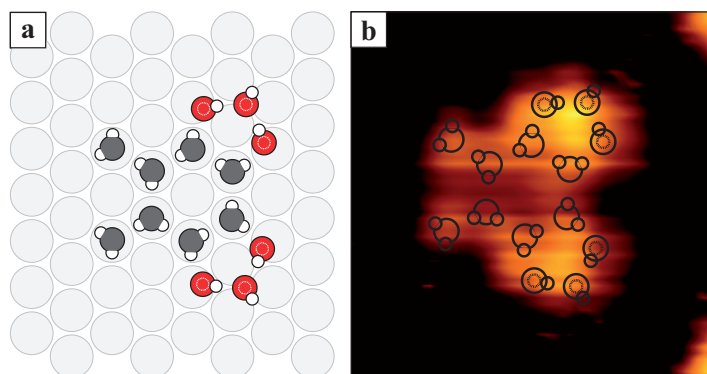


Figure 4.9: Structural Model of an Asymmetric Water Cluster. (a) Proposed structural model of the cluster with one of the pentagon molecules being stripped off, cf. Figure 4.8. (b) Schematic view of the proposed model superimposing a topographic image of the water cluster shown in Figure 4.7(c). Model and experimental data in scale. Angular alignment obtained via atomically resolved images of the metal substrate.

This results in a dipole moment with the positive charge accumulating at the hydrogen atoms, as introduced in the very beginning of this work (Figure 1.1, the effective charge transfer of a molecule in the cluster compound may be different from the isolated case due to its chemical environment). While an individual cluster has a large fraction of molecules residing in the energetically favourable on-top adsorption site, neighbouring clusters face a repulsive force according to the Coulomb potential which prevents the clusters from coalescing and stabilizes the cluster phase. With increasing coverage a characteristic cluster spacing develops, in agreement with the self-correlation images presented in Figure 4.6. With the dipole moment of the frontmost molecule acting on neighboring clusters the energy barrier between them amounts to 10 meV (50 meV) at a cluster spacing of 10 Å (5 Å) already, which effectively prevents the clusters from coalescence. Note, that here a polarity of the water molecule according to Figure 1.1 is assumed, which is but a meager approximation of the charge distribution within a water cluster due to neglected binding. For $\Theta = 0.43$ ML and higher values we observe the formation and subsequent growth of water islands within the disperse cluster phase. We assume that the islands make for a second minimum in the Gibbs free energy at high coverages. As the coordination of the molecules is weaker in the cluster phase (dangling bonds) and the above mentioned Coulomb energy penalty has to be paid with increasing coverage, the formation of a continuous wetting layer is energetically favoured. Consequently a phase coexistence between both structures develops with the equilibrium shifted towards the island phase for high coverage.

Note, that the polarity of the water clusters also explains the decoration of surface steps: According to Smoluchowski electron density accumulates at lower step edges whereas upper step edges show an electron deficiency. [76] The resulting dipole interacts with the polar clusters and prevents them from populating upper step edges. At lower step edges on the other hand the clusters feel an attractive force and may form a continuous decoration. In line with this, we observe the lower step edges to be preferred source for nucleation of the island phase. This observation offers additional support for our structural model.

Hitherto the structure of the water islands was not discussed. Based on our findings of island nucleation out of the cluster phase it is likely that the structural elements of the water clusters persist in the continuous layer. In fact, the islands show two distinct height levels with a regular arrangement of depressions embedded into a almost uniform matrix. A detailed discussion of this structure will be given in the next paragraph.

Continuous Wetting Layer

Figure 4.10 shows the resulting structure of H₂O adsorbed on Ir(111) at $T_{\text{ads}} = 120$ K. The coverage is $\Theta = 0.85$ ML. When compared to lower coverage topographs, the water adlayer now forms a continuous wetting layer on the iridium surface terraces. It displays a pattern of depressions embedded in a continuous matrix.

While the arrangement of the depressions appears periodic on larger scale, Figure 4.10(a), this observation is proven wrong in the enlarged view of Figure 4.10(b). Although the depressions show a uniform apparent height of $h = (0.7 \pm 0.1) \text{ \AA}$ (measured at $U = -0.3$ V, $I = 37$ pA) we observe various different geometries for the depressions, such as triangles, diamonds and even elongated structures. All of these depressions are embedded into a molecularly ordered matrix with a height of $h = (1.3 \pm 0.1) \text{ \AA}$. The matrix contains dark spots which we interpret as centers of ice rings. A closer look at the molecularly resolved topograph unveils that the $\langle 11\bar{2}0 \rangle_{\text{H}_2\text{O}}$ rows in the matrix are parallel to the $\langle 1\bar{1}0 \rangle_{\text{Ir}}$ directions of the metal substrate (The error of this value is in the order of 2° . However, we do not observe rotational domains.). The matrix shows a characteristic neck width of one ice ring which results in a comparably well-ordered self-correlation image [Figure 4.10(c)]. The periodicity of this structure is $(17.3 \pm 0.1) \text{ \AA}$. Note that the water layer incorporates vacancy islands and does not populate upper step edges.

Both the shape and the apparent height of the structural elements observed in the continuous layer agree with the related structures found in the cluster phase. As in the case of Pt(111) [96] the triangular depressions can be rationalized by a flat hexamer in a

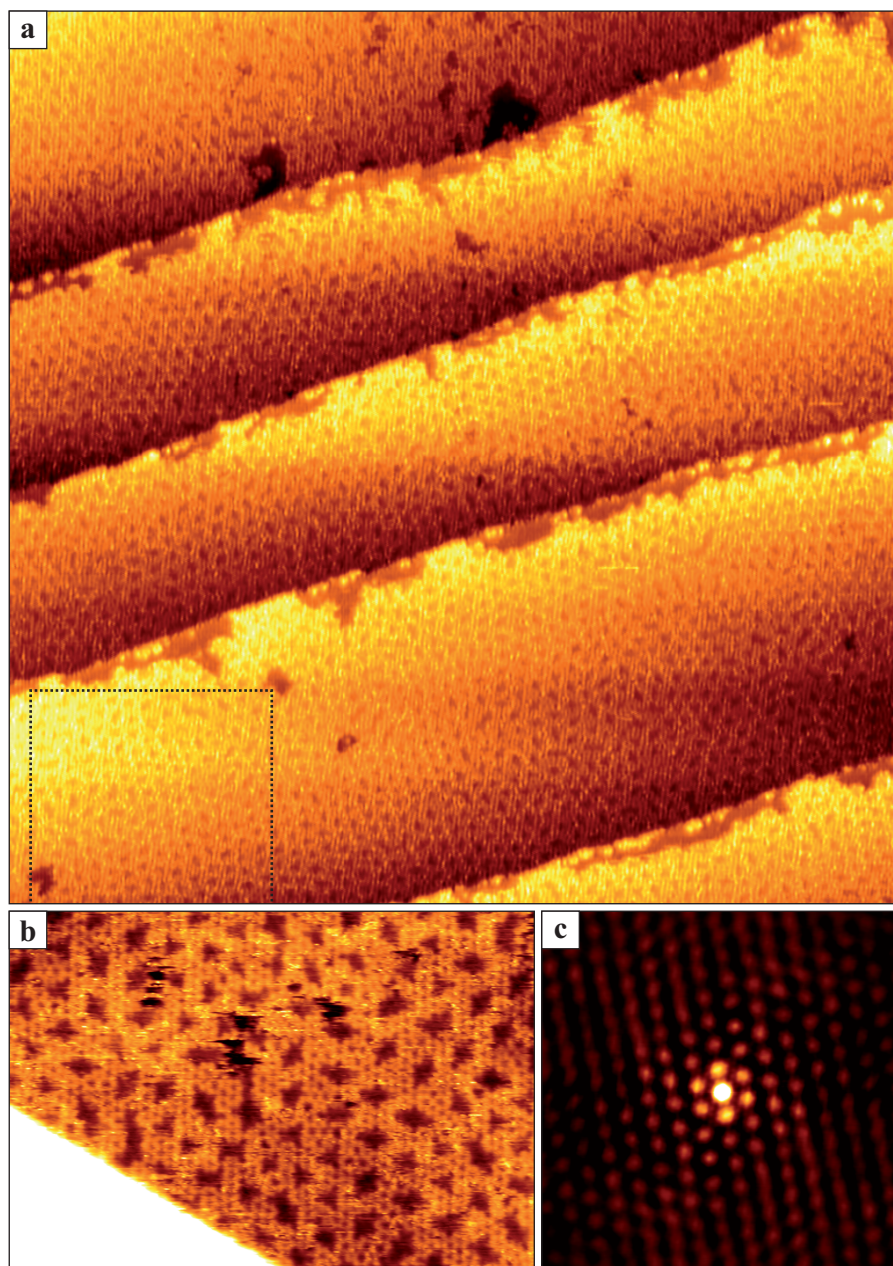


Figure 4.10: Continuous Wetting Layer. (a) Topographic STM image of the wetting layer upon adsorption of $\Theta = 0.85$ ML of H_2O on Ir(111) at $T_{\text{ads}} = 120$ K. A pattern of depressions is visible, embedded in a continuous matrix. (b) Molecularly resolved topograph, showing a disordered arrangement of depressions of uniform height but various shapes. (c) Self-correlation image of the area highlighted in (a). The image unveils a periodic structure of (17.3 ± 0.1) Å. Image width: (a) 820 Å, (b) 220 Å, (c) 225 Å; Imaging parameters: (a-c) $U = -0.3$ V, $I = 37$ pA.

$\sqrt{3}$ on-top arrangement, surrounded by molecules in an upright geometry resembling the continuous matrix. This model agrees with the above finding that the continuous layer nucleates out of the cluster phase, as the particular structure can easily be continued by adding further bridging molecules to the cluster. A triangular cluster pointing into a certain direction would then result in a triangular depression pointing to the opposite direction (cf. formation of a 575757 reconstruction, shown in Figure 1.8). According to the manifold structures observed in the cluster phase, we also understand the formation of differently shaped depressions in the wetting layer.

As we did not observe significant long range order in our experiments at this point - even on a surface with an artificially increased step edge density - one has to deduce the perfectly ordered structure from the quasi-ordered structure observed in experiment. In the discussion of water adsorption on Pt(111) we could show, that the disordered layer carries the same structural elements as the ordered adlayer. Hence it is most likely, that a periodic water structure on Ir(111) would be composed of triangular depressions (which make for the most common type of depression observed) embedded into a matrix with a characteristic width of one ice ring. This results in a $\sqrt{37} \times \sqrt{37} R25.3^\circ$ superstructure, well-known for the platinum substrate. The proposed structural model is depicted in Figure 4.11. The periodicity of this structure is $a_{\sqrt{37}} = 16.5 \text{ \AA}$. The difference of this value to the measured periodicity of the observed adlayer, $a_{\text{dis}} = (17.3 \pm 0.1) \text{ \AA}$, can be reasonably explained by the intrinsic disorder of this layer: Here, we do observe matrices of different widths and manifold, particularly larger depressions. Altogether, these variations account for an increase of the superlattice unit cell, compared to the ideal dense arrangement used in the $\sqrt{37}$ structural model.

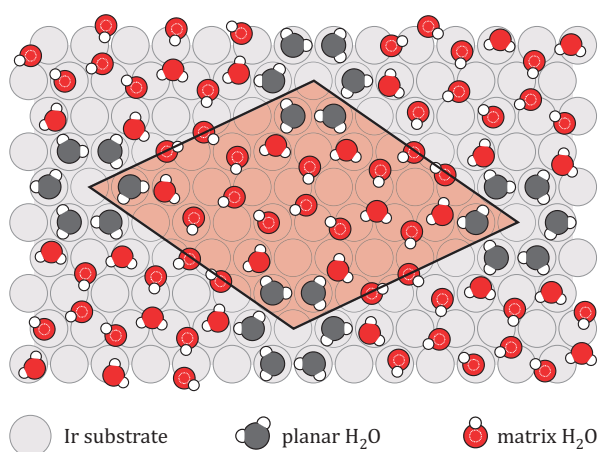


Figure 4.11: Proposed Structure of the Wetting Layer of $\text{H}_2\text{O}/\text{Ir}(111)$. The superstructure unit cell features a planar hexamer of molecules surrounded by a molecularly ordered matrix of one ice-ring width. In a dense arrangement this results in a $\sqrt{37} \times \sqrt{37} R25.3^\circ$ unit cell. For details see text.

In fact, the molecular arrangement in the $\sqrt{37}$ unit cell makes for a hydrophobic wetting layer, as discussed in case of Pt(111) [100–102]. Accordingly, the model offers a sound

explanation for the low desorption energy of thin water films (see Table 4.1) compared to the bulk ice value.

Manipulation of the Wetting Layer

As already mentioned in the discussion of the cluster phase, the adsorbed water layer is very sensitive to electron induced damage. A similar behaviour is observed for the system $\text{H}_2\text{O}/\text{Pt}(111)$, as discussed in detail in section 3.4 and references therein. The (controlled) manipulation of the water layer by the STM tip has been studied by the group of K. Morgenstern. [123, 124]

The effects of continued scanning on the chemisorbed water layer on $\text{Ir}(111)$ is best seen in the low coverage regime, where the iridium substrate is predominantly covered by individual water clusters. An example of the transformation of water clusters is given in Figure 4.12, showing successively obtained images of an isolated cluster.

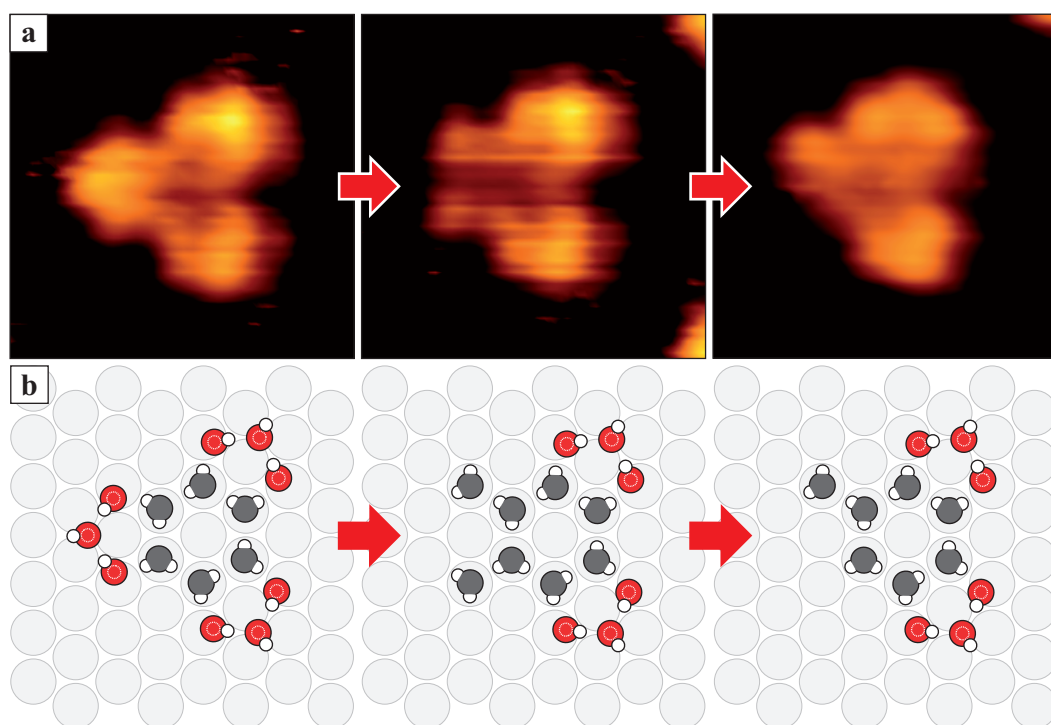


Figure 4.12: Tip-Induced Transformation of Water Clusters. Series of STM topographs (a) and corresponding models (b) illustrating the disassembling of a triangular cluster (left) into different cluster fragments (center, right) upon continued scanning. Image width: 24 Å; Imaging parameters: $U = -0.2\text{ V}$, $I = 50\text{ pA}$.

In the topographic images the transformation of the water cluster is clearly visible. Beginning with a triangular shape (left) the cluster size is reduced within each scanning

process. In the end only a fragment of the cluster remains on the surface (right) which lacks two water molecules when compared to the initial state [see Figure 4.12(b)].

We attribute this structural changes to a tip-induced transformation of the water cluster, as the triangularly shaped cluster is the dominant species and ubiquitously present on the sample, whereas many different cluster geometries emerge after scanning only. This is supported by the strong tip-sample interaction visible as noise in the topographic images. We furthermore deal with serious tip changes (not shown), even at low tunneling currents.

Another aspect of tip-induced manipulation of the wetting layer is related to the applied bias voltage, cf. Section 3.4. Figure 4.13(a) shows the water layer after executing a voltage pulse ($U = +5\text{ V}$, $\Delta t = 0.2\text{ s}$) in close vicinity to the site marked by an \times . One can easily see that the water layer has been completely removed in an area surrounding the manipulation site, exposing the underlying iridium substrate. The affected region has a diameter of approximately 200 \AA and is encircled by a newly formed structure which extends 250 \AA further from the manipulation site. Moving away from the center we observe a complex transition between the newly formed adlayer and the pristine water structure. At a distance of roughly 400 \AA the pristine water layer is fully recovered, showing the characteristic (disordered) arrangement of depressions. Note, the tip-induced manipulation also affects the water layer on neighbouring terraces.

A close-up topograph of the manipulation site with a atomic-scale resolution is shown in Figure 4.13(b). The contrast of the image is enhanced to offer insight into the structure of the newly formed adlayer. It shows a honeycomb lattice of $a = (4.7 \pm 0.1)\text{ \AA}$ periodicity with the dense packed rows rotated by 30° against the $\langle 1\bar{1}0 \rangle_{\text{Ir}}$ directions of the metal substrate. The apparent height of the adlayer is $h = 0.7\text{ \AA}$ with a variation of less than 0.1 \AA (apart from the black dots at the center of the honeycomb lattice).

In the Fourier transform of this topograph [Figure 4.13(c)] six intensity maxima are visible at first sight which confirm the sixfold symmetry of the adlayer. Having a closer look at these maxima unveils a more complex structure, redrawn in Figure 4.13(d) for better visibility: Each of the maxima in the Fourier transform splits into three spots (black dots). By their arrangement each group of spots can be interpreted as satellite spots surrounding a central reflex (red circles) located at $a = (4.7 \pm 0.1)\text{ \AA}$, in agreement with the real space measurements.

Our experiments prove that the bias voltages applied in STM affect the chemisorbed water layer on Ir(111), as has been previously discussed for $\text{H}_2\text{O}/\text{Pt}(111)$. In agreement with these findings, we can address the voltage pulse to cause dissociation of water molecules.

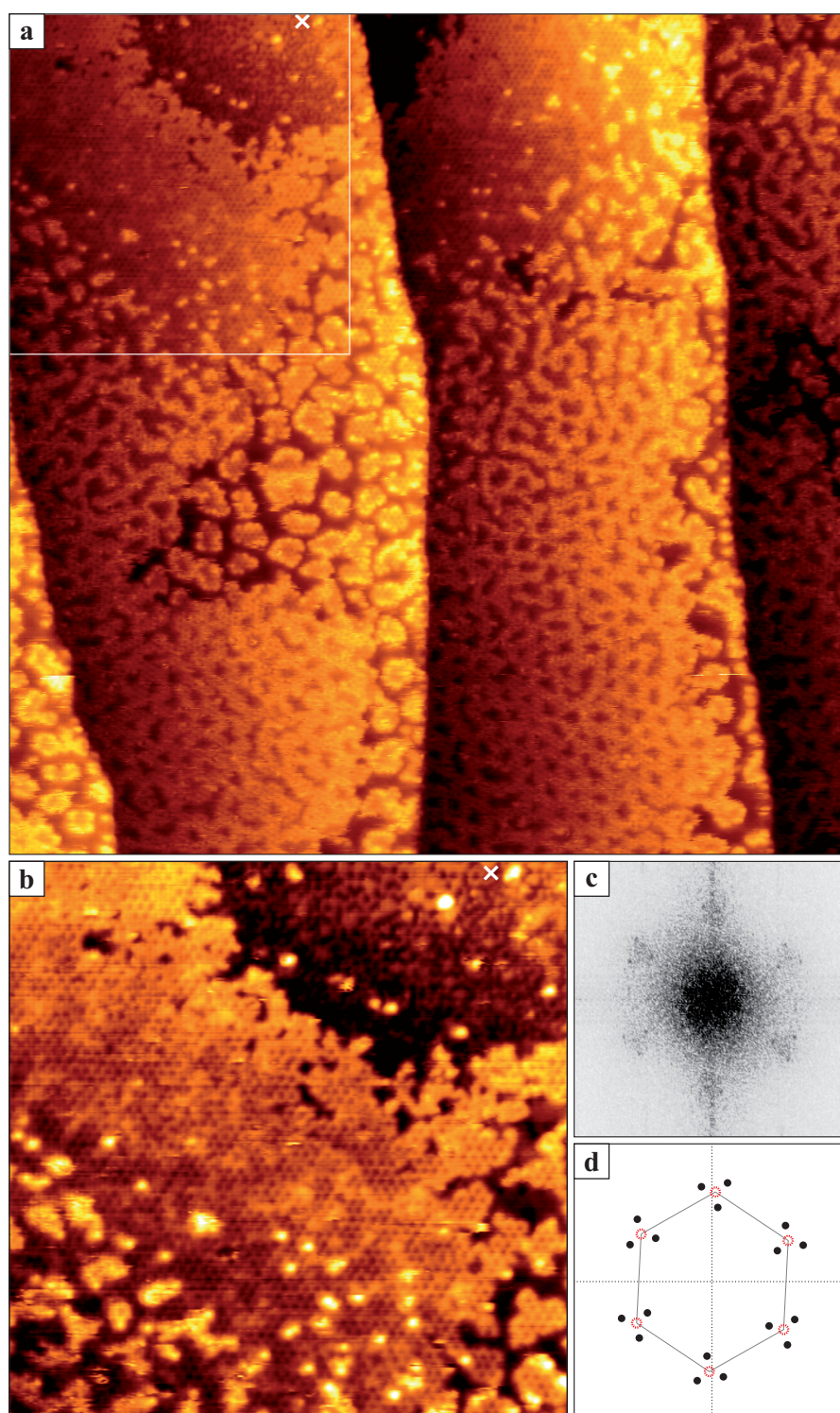


Figure 4.13: Manipulation of the Water Layer by Voltage Pulses. (a) STM topographic image of the adlayer after executing a voltage pulse ($U = +5$ V, $\Delta t = 0.2$ s) in close vicinity to the site marked by an \times . (b) Close-up topograph of the area marked in (a). The contrast of the image is enhanced to offer insight into the structure of the newly formed adlayer. (c,d) Fourier transform and schematic representation of (b). Image width: (a) 600 Å, (b) 245 Å, (c,d) 0.781/Å; Imaging parameters: (a,b) $U = -0.1$ V, $I = 110$ pA.

Due to the reduced number of hydrogen atoms after dissociation the ice rules can easily be satisfied and allow for a planar arrangement of molecules (water molecule fragments). Accordingly we observe the formation of a hexagonal adlayer with a reduced apparent height. Based on this low apparent height [$h = (0.7 \pm 0.1) \text{ \AA}$] and the measured lattice constant [$a = (4.7 \pm 0.1) \text{ \AA}$] we identify the resulting adlayer to form a $\sqrt{3} \times \sqrt{3} \text{R}30^\circ$ structure composed of water molecule fragments that are adsorbed with their molecular plane parallel to the surface. The satellite spots visible in the Fourier transform can be attributed to a moiré superstructure arising from the slight height modulation visible in the topographic images. In the transition regime ($\sqrt{3}$ adlayer \rightarrow pristine water layer) a complex, maze-like structure develops, in agreement with mixed OH + H₂O adlayers studied by Völkening *et al.* [4]. The fact that the restructuring of the water layer extends several nm away from the actual manipulation site can be attributed to hole (electron) transport in the (anti-)bonding molecular bands (cf. section 3.4 and reference [124]).

CHAPTER 5

Water Adsorption on Graphene

All experiments discussed in the following chapter were carried out by myself. They were planned and interpreted with support of Carsten Busse and Thomas Michely. For experimental details the reader is referred to Chapter 2.

In this chapter, we present experimental data regarding the wetting behaviour and structure formation of water on a graphene covered Ir(111) surface. The analysis starts with a discussion of the thermodynamics of water adsorption via thermal desorption spectroscopy, see Section 5.1. Of particular interest in this study is the question, whether water molecules form a wetting layer on graphene or not. In the second part of this chapter, Section 5.2, we complement these findings by real space measurements utilizing scanning tunneling microscopy.

5.1 Thermodynamics of Water Adsorption on Graphene

In the following section we investigate the energetics and growth of H₂O on a graphene covered Ir(111) surface via thermal desorption spectroscopy. This study mainly focusses on the wetting behaviour and the dependence of the adsorbed water structure on the adsorption temperature.

Figure 5.1 shows the TDS data (a) and extracted coverage (b) for water adsorption in the investigated coverage regime, $\Theta_0 \approx 1.0 \dots 7.0$ ML (coverages are given with respect to the wetting layer on an Ir(111) substrate). The adsorption temperature was $T_{\text{ads}} = 20$ K, the temperature ramp in the spectra was set to $\beta = 1$ K/s.

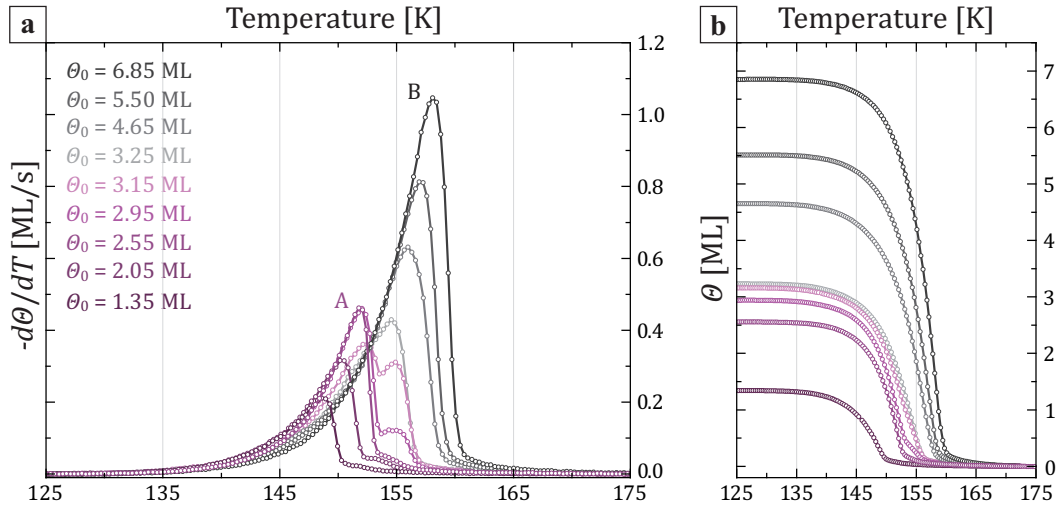


Figure 5.1: Thermal Desorption Spectroscopy of H₂O/Graphene. (a) TDS spectra of H₂O adsorbed on a graphene covered Ir(111) surface at $T_{\text{ads}} = 20$ K. The temperature ramp while recording was set to 1 K/s. $\Theta_0 = 1.35 \dots 6.85$ ML, as indicated in the diagram. (b) Corresponding coverage obtained via integration of the spectra shown in (a).

For $\Theta_0 < 2.5$ ML the desorbing species shows a single peak [labeled peak (A)] with a common leading edge for all coverages. As discussed in section 2.3 this is attributed to zero order desorption kinetics. Accordingly, the peak temperature shifts to higher values with increasing initial coverage, as depicted in Figure 5.2 (purple curve). Increasing the initial coverage results in saturation of peak (A). Simultaneously a shoulder emerges located at $T_{\text{peak}} \approx 155$ K, as can be seen in comparison of the TDS data for $\Theta_0 = 2.55$ ML and 2.95 ML. This high temperature shoulder keeps growing upon increasing the coverage, while the initial peak structure loses intensity, see $\Theta_0 = 3.15$ ML. For $\Theta_0 > 3.25$ ML, peak (A) is totally suppressed and the high temperature shoulder develops into a separate

peak [labeled peak (B)] which also shows characteristics of zero order desorption kinetics. The shift of the peak temperature with increasing coverage is shown in figure 5.2.

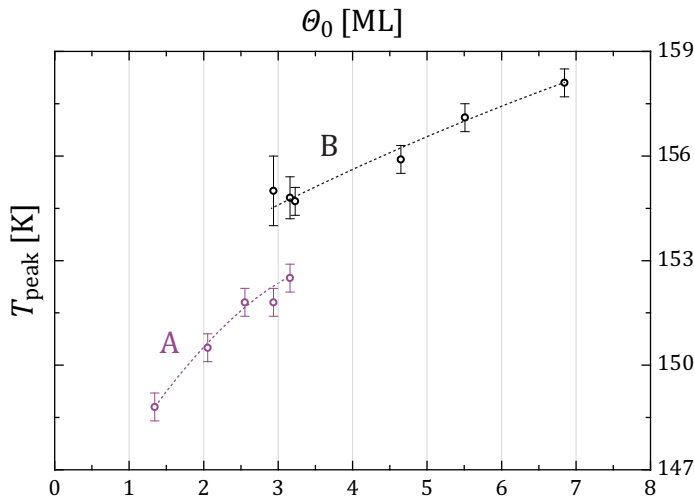


Figure 5.2: Peak Temperature Shift. Desorption peak temperature T_{peak} in dependence on the initial coverage Θ_0 for (A) the low and (B) the high coverage regime. Lines to guide the eye.

Note, that we do observe another structural transformation for very high coverages ($\Theta_0 = 42.80$ ML), see Figure 5.3. As in the case of a clean Ir(111) substrate, the desorption spectrum consists of a single peak [hereinafter referred to as (X)] which is further shifted to higher temperatures.

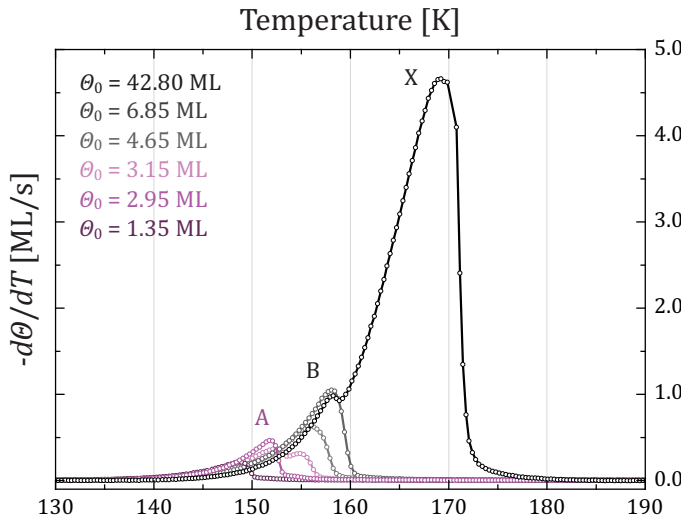


Figure 5.3: TDS of Thick Ice Films. (a) TDS spectra of $\Theta_0 = 42.80$ ML of H_2O adsorbed on a graphene covered Ir(111) surface at $T_{\text{ads}} = 20$ K. The temperature ramp was set to $\beta = 1$ K/s. Selected spectra from Figure 5.1 are printed for comparison.

To quantitatively evaluate the desorption spectra we again make use of the approximative methods described in section 2.3: For zero order desorption the desorption energy E_{des} and the frequency factor ν_0 can be determined via a linear fit of the leading edge in the Arrhenius plot. The analysis results in desorption energies of $E_{\text{des}}^{\text{A}} = (424 \pm 2)$ meV, $E_{\text{des}}^{\text{B}} = (466 \pm 2)$ meV, and $E_{\text{des}}^{\text{X}} = (525 \pm 2)$ meV for the respective peaks, also listed in table 5.1 together with the corresponding values of the frequency factors. The data obtained in probing the water adsorption on a clean Ir(111) surface are given for comparison.

Table 5.1: Experimentally Determined Desorption Parameters. Calculated desorption energy E_{des} and frequency factor ν_0 via Arrhenius plot analysis for the different desorption peaks studied. Values for Ir(111) are given for comparison.

structure	assignment	E_{des} [meV]	E_{des} [kJ/mol]	ν_0 [1/s]
(A), $\Theta \leq 3$ ML	droplets	424 ± 2	40.9 ± 0.2	$(0.6 \pm 0.1) \cdot 10^{14}$
(B), $\Theta > 3$ ML	few layer	466 ± 2	45.0 ± 0.2	$(8.8 \pm 1.5) \cdot 10^{14}$
(X), $\Theta \gg 10$ ML	bulk ice	525 ± 2	50.6 ± 0.2	$(3.9 \pm 0.7) \cdot 10^{16}$
	monolayer H ₂ O/Ir(111)	511 ± 12	49.3 ± 1.1	$(2.9 \pm 2.0) \cdot 10^{14}$
	few layer H ₂ O/Ir(111)	485 ± 6	46.8 ± 0.6	$(9.9 \pm 3.8) \cdot 10^{14}$
	bulk ice	530 ± 2	51.3 ± 0.2	$(4.0 \pm 0.5) \cdot 10^{16}$

The calculated desorption energy for water adsorbed on graphene is significantly lower than for the adsorption on a clean iridium substrate. For low water coverages, the desorption energy is comparable to the literature value of an extended hydrogen bridge bonding network, $E_{\text{O...H}} \approx 450 \text{ meV/H}_2\text{O}$ [53]. On the other hand, this means the graphene substrate interacts with the water molecules via van-der-Waals forces only [113–115]. These considerations even hold in case the hydrogen bridge bonding network is highly disordered and/or of small spatial extent, which might lower the average lateral binding energy due to lower coordination. Furthermore, the fact that we do observe a structural transition (A \rightarrow B) to higher binding energies with increasing coverage clearly shows that water is able to gain energy when extending its bonding network. That this energy gain is related to a restructuring at the water/graphene interface is very unlikely, as the transition occurs for $\Theta_0 = \Theta_0^{\text{Ir}} \approx 3$ ML, where we typically expect all substrate adsorption sites to be occupied. While the energy gain is relative small, $\Delta E_{\text{des}} \approx 40$ meV, the structural transition occurs within $\Delta\Theta \approx 0.3$ ML only (thus being far from continuous) and completely suppresses the initial adlayer structure. We come to the conclusion that water does not wet the graphene covered substrate, i.e. graphene is hydrophobic [115].

According to the low desorption energy, $E_{\text{des}} \approx 425$ meV, it is highly improbable, that the initial structure is composed of crystalline water layers, but can rather be described as low-coordinated water droplets, in agreement with previous findings and predictions regarding graphene’s mother material graphite [115, 116]. This structure is metastable and completely rearranges when reaching a critical value. Yet, even the few layer water structure on graphene, $E_{\text{des}} \approx 465$ meV, does not reach the desorption energy value of the ice multilayer adsorbed on Ir(111) ($E_{\text{des}} \approx 485$ meV, see Table 5.1), which hints at an amorphous nature of the adlayer (cf. Reference [11]).

We may ask now: Why does the water adlayer not take its preferred structure right from the beginning? This question arises particularly with regard to our observation that the graphene substrate has only weak contribution to the adlayer binding. The answer might be the low adsorption temperature of $T_{\text{ads}} = 20$ K, i.e. a kinetic stunting of the adlayer growth. To examine this idea, we adsorbed a fixed amount of water well below the transition regime ($\Theta \approx 2.15$ ML) at different temperatures ($T_{\text{ads}} = 20 \dots 130$ K) and probed the desorption kinetics of the adlayer, as depicted in Figure 5.4.

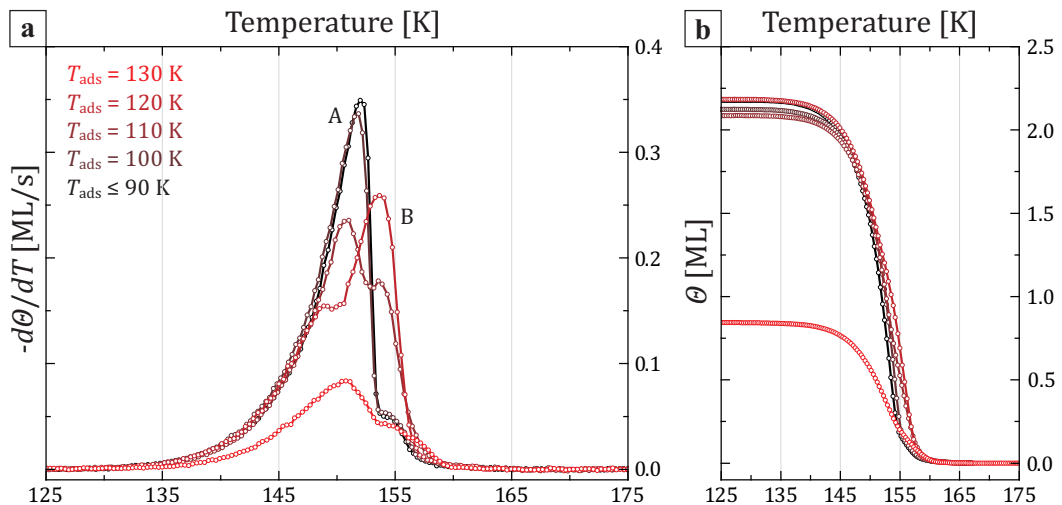


Figure 5.4: Thermal Desorption Spectroscopy of H₂O/Graphene. (a) TDS spectra of 2.15 ML H₂O adsorbed on a graphene covered Ir(111) surface at variable adsorption temperature. The temperature ramp while recording was set to 1 K/s. $T_{\text{ads}} = 20 \dots 130$ K, as indicated in the diagram. (b) Corresponding coverage obtained via integration of the spectra shown in (a).

For $T_{\text{ads}} \leq 100$ K the TDS spectra (black and brown curve) show the well-known characteristics discussed in Figure 5.1: A single peak (A) with a high temperature tail around 155 K. Water adsorption at $T_{\text{ads}} = 110$ K results in a distinct change of the desorption spectrum, as the intensity of peak (A) is reduced in favor of the high temperature shoulder [peak (B)]. This intensity shift continues at $T_{\text{ads}} = 120$ K. Here the dominant fraction of the water adsorbates is present in the stronger bound structural arrangement. Further increasing the adsorption temperature to $T_{\text{ads}} = 130$ K finally leads to competing water desorption. Accordingly, the coverage of the water adlayer is strongly reduced.

Our measurement on the structure of the water adlayer in dependence of the adsorption temperature clearly shows, that the low-coverage adsorbate structure is but a metastable state of H₂O/graphene. Increasing the adsorption temperature to $T_{\text{ads}} \approx 110$ K initiates

a transition of the adsorbate structure into the (more) stable state, previously observed for higher coverages only. Thus, the TDS data presented in Figure 5.4(a) proves our above idea: The growth of the adlayer is kinetically stunted. The reason for this may be traced back to the H₂O/graphene interface. While the graphene substrate has almost no contribution to the water binding energy [113, 115] it may still suppress the diffusion of the droplets. It is therefore of utmost importance to gain information on the spatial arrangement of the adlayer.

5.2 Structure of the Water Adlayer

In the previous section we could show that water adsorbed on a graphene layer does not form a wetting layer. Instead graphene is hydrophobic and - according to theoretical predictions [113, 115] - allows for a weak physisorption of the water molecules only. However, the desorption spectra clearly show that the adlayer reorganizes for water coverages around 3 ML and adopts a more stable structure.

Imaging the Water Adlayer

The main task in imaging the water adlayer im STM is to find stable (i.e. noninvasive) tunneling parameters, as the water structure is very sensitive to the scanning process. In fact, we found the water adsorbates to be heavily distorted even at tunneling currents $I < 10$ pA. The distortion ranges from picking up single molecules as far as displacement of the entire adsorbate layer across the sample surface. An example of the tip-induced restructuring of the sample surface can be seen in Figure 5.5 which shows subsequently recorded topographs of the same sample area after deposition of approximately 4.0 ML at $T_{\text{ads}} = 20$ K. The water amount was chosen to investigate the (presumably) stable adlayer structure. Scanning was performed at $T_{\text{scan}} = 20$ K with $U = 170$ mV and $I = 15$ pA. To enhance the visibility the water adsorbates are colored in the previously used black-red-yellow-white palette, whereas the substrate is shown in gray scale. This assignment is possible because the water adsorbate structure is imaged as elevation in STM with an apparent height of $h = (2.2 \pm 0.1)$ Å above the iridium surface. Furthermore, it shows an intrinsic corrugation with a periodicity of $a = (25 \pm 2)$ Å. According to the rotational alignment, this pattern can be attributed to the underlying graphene moiré. When comparing subfigures (a) and (b) one can easily see that a large fraction of the adsorbate structure has been removed from the surface/shifted out of the scanning area.

In fact, the strong tip-sample interaction is omnipresent in the scanning process, visible as horizontal lines in the topographs.

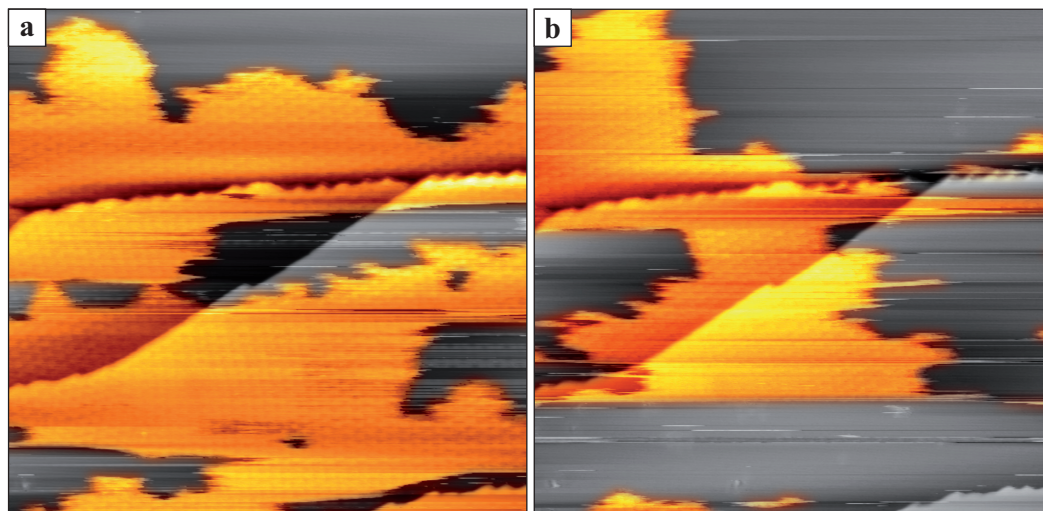


Figure 5.5: Issues in Imaging of the Water Adlayer. (a,b) Subsequently recorded STM topographs of approximately 4.0 ML H_2O adsorbed on graphene at $T_{\text{ads}} = 20$ K and 60 s annealing at 80 K. For clarity reasons, the water adsorbates are colored in the previously used palette, whereas the substrate is shown in gray scale. Image width: (a,b) 1000 Å; Imaging parameters: (a,b) $U = 170$ mV, $I = 15$ pA.

The strong influence of the scanning tip on the structure of the adlayer can be reasonably explained by the weak interaction of the water adlayer and the graphene substrate. As shown in the previous section, the stability of the water adsorbates is a result of intermolecular bonds whereas the substrate has almost no contribution to it. Consequently, the STM tip may affect the water adlayer and shift the adsorbate islands as a whole - even at 20 K. Another aspect to consider despite the overall weak binding is the factual lack of chemical bonds between water molecules and the graphene layer. In case of a metal substrate, these chemical bonds are responsible for the good imaging conditions of the wetting layer, whereas a lack of them results in an insulating adlayer [cf. multilayer ice on Pt(111) [102]]. Given these considerations, the apparent height of the water adlayer presented in the previous paragraph has to be considered with caution.

For tunneling currents down to $I = 3$ pA and applied bias voltages in the range of $U = -4.. + 4$ V we were not able to find scanning parameters, that guarantee a non-destructive imaging of the adsorbate structure. While we were occasionally able to obtain STM topographs by chance, only a few of these images are suitable for further analysis due to a lack of resolution or earlier manipulation.

Low Coverage Regime

Figure 5.6 shows the surface topography after dosing of 2.0 ML H_2O on graphene at $T_{\text{ads}} = 20\text{ K}$ and subsequent annealing at $T_{\text{anneal}} = 80\text{ K}$ for 60 s.

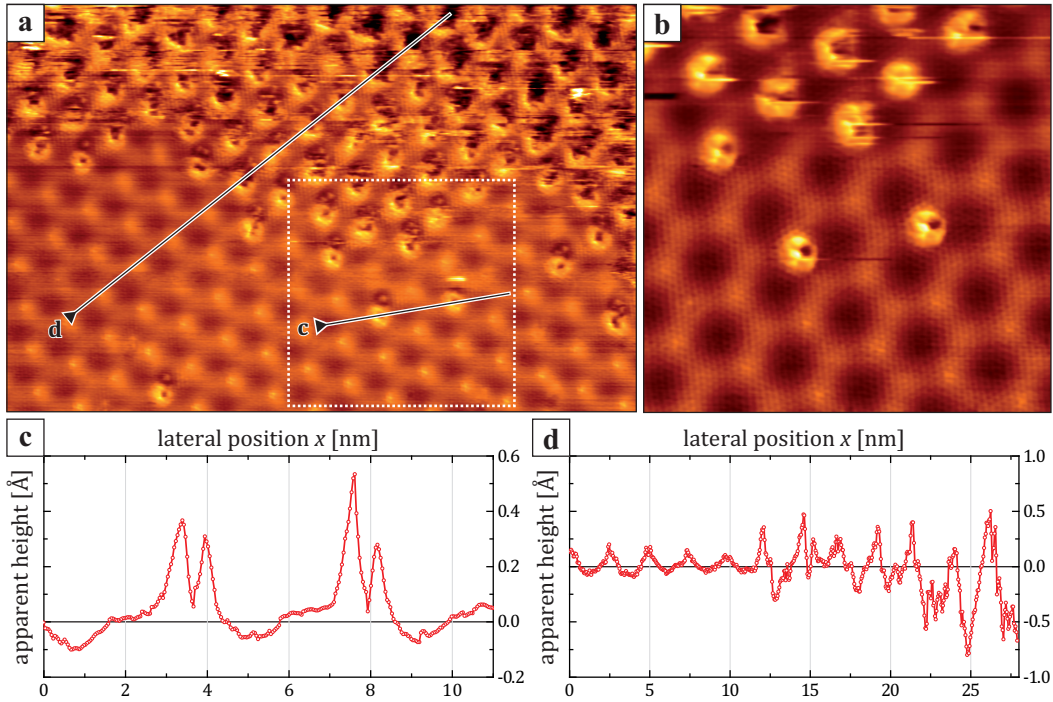


Figure 5.6: Cluster Formation. (a) STM topograph of approximately 2.0 ML H_2O adsorbed on graphene at $T_{\text{ads}} = 20\text{ K}$ and 60 s annealing at 80 K. One can make out a dense arrangement of individual clusters following the graphene/Ir(111) moiré periodicity. (b) Close-up topograph of the area highlighted in (a) in atomic resolution. (c,d) Height profiles along the lines indicated in (a). Image width: (a) 360 Å, (b) 135 Å; Imaging parameters: (a,b) $U = 1.0\text{ V}$, $I = 25\text{ pA}$.

In (a) the upper part of the depicted surface area is fully covered by water adsorbates. In the lower half the clean graphene substrate is visible, featuring the well-known graphene/iridium moiré pattern (reverse contrast, cf. section 1.5). At first sight one can make out a somewhat ordered arrangement of adsorbates following the moiré periodicity. In fact the water adsorbates tend to form individual clusters and align in the moiré pattern. Based on our findings obtained in the TDS experiments, we can now associate the low coverage structure, $\Theta < 3.0\text{ ML}$, with the cluster phase observed in STM. However, their appearance is highly non-uniform showing a complex structure and various sizes.

A close-up topograph of the smaller water clusters is given in (b) [according to the area highlighted in (a)]. Each of the clusters shows a characteristic O-shaped structure. The

maximum apparent height of the rim above the graphene layer is $h = (0.6 \pm 0.1) \text{ \AA}$, whereas the central dip reaches down to the substrate. This is also illustrated in the line profile of the two central clusters, Figure 5.6(c), where the zero level was set to match the graphene substrate. The larger the clusters grow the more dark they are imaged, i.e. their central dip gains in size with the apparent height dropping below the substrate, cf. right hand side of Figure 5.6(d). This behaviour hints at the formation of an insulation (or, at least, polar) adsorbate structure, in agreement with the imaging difficulties discussed before.

At this early stage of analysis we can already confirm that water dewets graphene: Molecule adsorption does not result in a continuous adlayer. Instead water molecules show a strong preference for clustering, which agrees with theoretical predictions of water adsorption on free-standing graphene [115, 117]. In this simple model one would expect the formation of large water clusters which continue to grow in size with further dosing. Nevertheless, it does not explain our observation of a dense, periodic arrangement of finite size clusters.

Provided atomic resolution on the graphene layer the aforementioned alignment of water clusters to the moiré pattern becomes obvious. We find them located in the HCP region, which is also known as preferred nucleation site for metal clusters [159]. In case of these metal adsorbates the particular cluster formation is related to a local rehybridization of the graphene sheet, $sp^2 \rightarrow sp^3$, and the chemical binding of the metal cluster to the carbon atoms in the HCP region. Whether a similar mechanism is responsible for the formation of water clusters can not be determined from STM data alone. But in fact, the formation of (strong) chemical bonds between the water molecules and the graphene substrate can be ruled out, as we do not see any signature of these in TDS experiments. The low desorption energy of the cluster phase, $E_{\text{des}} = (424 \pm 20) \text{ meV}$, strongly indicates van-der-Waals interaction only and does not allow for major contribution from the substrate. Hence, we can only speculate about the driving force of the cluster formation: It is known that a corrugated surface, like e.g. the graphene moiré, acts as a potential landscape. According to the model of heterogeneous nucleation [160, 161] the HCP regions can be viewed as preferential adsorption sites which facilitate nucleation of the water droplet. In the case of metal adsorption on graphene this landscape further stabilizes the clusters as they sense a diffusion barrier. This barrier amounts to approximately 10 % of the adsorption energy value ($E_{\text{diff}} \approx 0.4 \text{ eV}$, $E_{\text{ads}} \approx 5 \text{ eV}$) for the most stable clusters [162]. While the adsorption energy for a water molecule is severely lower, the diffusion barrier may still stabilize individual clusters. In conclusion we can state that the potential

landscape of the graphene moiré specifies the nucleation sites, which clearly separates this system from graphite and/or free-standing graphene sheets used in theoretical works. From the deposited amount of water $\Theta = 2.0 \text{ ML}_{\text{Ir}}$ we can calculate the average size of the water clusters to $n = 61$ molecules/cluster (based on a $\sqrt{37} \text{ H}_2\text{O}/\text{Ir}(111)$ wetting layer, $n = 0.7$ molecules/Ir). Admittedly, as we now understand the formation of individual clusters, we can offer no explanation for the inhomogeneous coverage. While we may speculate about some sort of cluster-cluster-interaction - probably even via the graphene substrate - it might as well be possible that the clusters were covering the entire surface but were picked up by the STM tip in the scanning process. In consequence, we can make no statement on this topic without further theoretical support.

High Coverage Regime

Increasing the coverage to $\Theta = 3.0 \text{ ML}$ ($T_{\text{ads}} = 20 \text{ K}$, 60 s annealing at $T_{\text{anneal}} = 80 \text{ K}$) leads to a water adlayer shown in Figure 5.7. According to the TDS data presented in Section 5.1, we expect this layer to resemble the situation right at the structural transition $A \rightarrow B$.

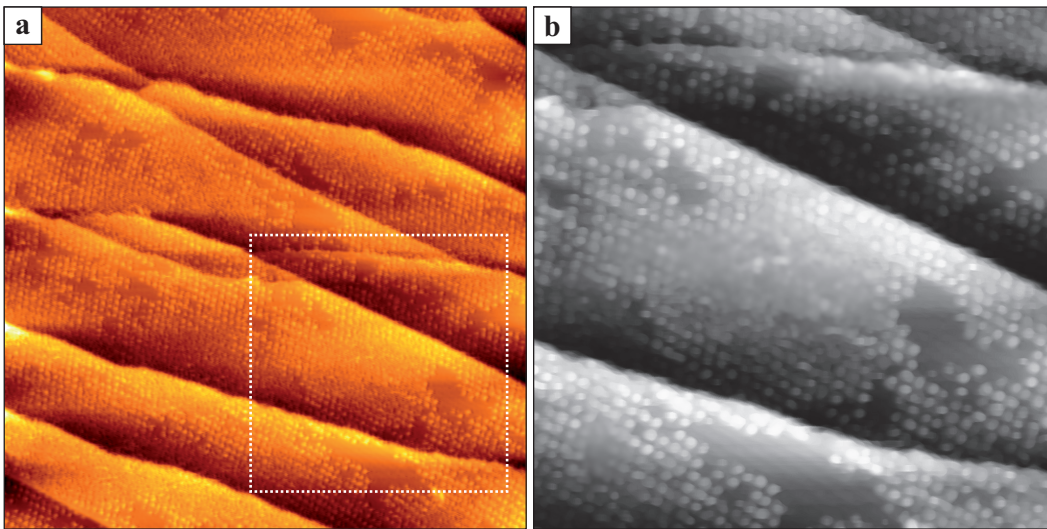


Figure 5.7: Formation of a Continuous Adlayer. (a) STM topograph of approximately 3.0 ML H_2O adsorbed on graphene at $T_{\text{ads}} = 20 \text{ K}$ followed by 60 s annealing at 80 K. (b) Close-up topograph of the area highlighted in (a). The image has been blurred to enhance visibility. Image width: (a) 1250 Å, (b) 800 Å; Imaging parameters: (a,b) $U = 3.0 \text{ V}$, $I = 3 \text{ pA}$.

At first sight, the adlayer structure appears very inhomogeneous, best to see in the close-up of Figure 5.7(b). Note that the image has been low-pass filtered to get rid of noise

and thereby enhance visibility. While water clusters make for the predominant species, some patches still reveal the uncovered graphene surface (e.g. in the bottom part of the image). In contrast with that a significant fraction of the surface is covered by a continuous adlayer (center) which has a slightly lower apparent height.

The experiment reveals that these islands are always surrounded by water clusters which makes it highly probable, that they originate from the cluster phase. As stated in the beginning of this section, we were not able to image continuous adlayers in reliable quality. Nevertheless, we may attribute this structure to the second peak (B) in the desorption spectra.

In the last part of this analysis, we link the STM data to the results obtained in section 5.1. The first finding we address is the structural transition $A \rightarrow B$ - which occurs either by increasing the coverage above $\Theta \geq 3.0$ MLE or by increasing the adsorption temperature to $T \approx 110$ K. Our STM analysis assigns the two structures as distinct phases, namely water clusters (A) and a continuous water adlayer (B). We argue there are different mechanisms responsible for the phase transition: While an increase of the water coverage will ultimately result in the coalescence of neighboring clusters due to the finite size of the moiré unit cell, the temperature induced shift of the desorption signal is attributed to cluster ripening. Due to the low binding strength of the hydrogen bridge bonds ($E_{O...H} \approx 0.2$ eV [53]) it is most likely that cluster ripening at $T_{\text{ads}} \approx 110$ K is provided via evaporation of individual molecules and reincorporation at different sites (bond reorganization) toward a continuous adlayer. This process agrees with the model of Ostwald ripening [163] and is substantiated by the observed zero order desorption kinetics, cf. Section 2.3 and Figure 2.3.

Furthermore we address the difference in binding energy of the two structures. Therefore we calculate the surface energy cost by changing the number of molecules in each structure: As water on graphitic surfaces shows a contact angle close to 90° [115, 116], we approximate water clusters as hemispherical droplets (surface area $A = 2\pi r^2$). The basal plane can be neglected in our consideration as the water-graphene interface is a common feature of both adlayer structures and thus will cause no difference. We assume this droplet to be throughout amorphous (due to the low adsorption temperature) and to consist of n water molecules with a characteristic volume of $v = 3.0 \times 10^{-29}$ m³ per

molecule (density equals liquid water). The total surface energy of the droplet can be calculated via:

$$\text{surface energy} \quad E_s(n) = \sigma \cdot A(n) = \sigma \cdot 2\pi \left(\frac{3nv}{2\pi} \right)^{2/3}, \quad (5.1)$$

where $\sigma \approx 0.1 \text{ N/m}$ denotes the surface tension of water at 120 K, where we observe water desorption. The energy cost to change the number of atoms from the surface of the droplet is thus:

$$\text{energy cost} \quad \frac{dE_s}{dn} = 2\sigma \left(\frac{2\pi v^2}{3n} \right)^{1/3}. \quad (5.2)$$

Note that $dE_s/dn \rightarrow 0$ for an extended droplet/layer, as no surface is created when removing a single molecule. For a cluster consisting of 50-60 molecules, on the other hand, the cluster gains energy as the surface area is effectively reduced. The value calculates to $dE_s/dn \approx 40 \text{ meV}$, which is in fair agreement with the desorption energy difference of the two structures presented in Table 5.1.

According to its finite size the surface of the water droplet is strongly curved. This curvature causes an increase of the internal pressure of the cluster according to Laplace. The removal of a molecule is thereby promoted when compared to an extended layer and, in consequence, lowers the desorption energy of the cluster. Note that this continuum approximation may be lacking in accuracy when describing atomic scale structures. However, our model gives a first impression on the relevant energy scale.

Our STM findings also offer a sound explanation for the dependence of the adsorbate structure on the adsorption temperature: Dosing H_2O at low temperatures, the molecules will stick at their adsorption site and take their favored adsorption site within the moiré unit cell. A diffusion between neighbouring unit cells is impeded due to the low thermal energy and the moiré potential landscape. When the adsorption temperature is increased above 100 K the clusters finally get mobile on the surface and may coalesce with neighbouring water clusters. Accordingly, the high-coverage structure is promoted over the cluster phase which gives rise to a shift of the peak intensity $A \rightarrow B$ in thermal desorption spectroscopy. In agreement with the measurements performed on Ir(111) the occurrence of peak X for highest coverages can easily be explained by the transformation of a thick water film into the bulk ice structure.

CHAPTER 6

Comparison

Up to now, we have discussed the wetting behaviour and adsorption structure of water on graphene (Chapter 5), Ir(111) (Chapter 4), and Pt(111) (Chapter 3) individually. The results obtained in each of these chapters will now be compared. We will discuss the common characteristics, and point out the differences we observed in the course of our experiments, giving an insight into the physical diversity of wetting and non-wetting surfaces.

Wetting Behaviour

For both platinum and iridium surfaces water adsorption shows typical wetting behaviour, as it is known for many other hexagonal transition metal surfaces [3]. That is, the water monolayer structure is more strongly bound to the surface than subsequent layers to the monolayer. This conclusion is justified by thermal desorption spectroscopy, which shows well-separated peaks for both structures (see Figures 1.6 and 4.2), with the monolayer energetically favored (see Table 6.1). The reason for this is the formation of certain bonding geometries at the water-metal interface [9, 13, 75, 87, 98], which are energetically stronger than the hydrogen bridge bonds between adjacent molecules.

The absence of these bonds on a graphene covered surface causes a fundamental difference in the wetting behaviour. As water molecules interact with the graphene sheet via van-der-Waals forces only [113–115], the molecules do not preferentially form a wetting layer, i.e. water dewets graphene. Instead, we observe the formation of a metastable low coverage structure, which is transferred into a more stable arrangement when the coverage reaches 3 ML_{Ir} or when the adsorption temperature is increased to 120 K (cf. Figures 5.1 and 5.4). However, the desorption energy of the low coverage structure is lower than the one obtained for desorption of thin water films from metal surfaces. This can be assigned to a low coordination of the water molecules in the adlayer structure.

The discrepancy in the desorption energy of a thin water film on a metal surface and of bulk ice can be explained by the hydrophobicity of the wetting layer on both Pt(111) and Ir(111) [100–102]. Consequently, the ice multilayer fully crystallizes upon heating during the desorption process only (see Figures 1.6 and 4.4). In fact, the desorption energy of thick water films ($\Theta \gg 10$ ML) is independent on the substrate and in agreement with bulk ice sublimation.

Table 6.1: Experimentally Determined Desorption Energies. Measured desorption energy E_{des} in meV for the different water adlayer structures studied. Values for Pt(111) are taken from references [10, 53] and [11].

structure	coverage	E_{des} [meV]		
		Pt(111)	Ir(111)	Graphene
monolayer	$\Theta \leq 1$ ML	550 ± 40	511 ± 12	–
few layer	$\Theta > 1$ ML	500 ± 30	485 ± 6	–
low coverage (clusters)	$\Theta \leq 3$ ML	–	–	424 ± 2
high coverage (islands)	$\Theta > 3$ ML	–	–	466 ± 2
bulk	$\Theta \gg 10$ ML	530	531 ± 2	525 ± 2

It should be noted that we generally obtain slightly lower values for water desorption from Ir(111) than those for Pt(111) presented in the work of Picolin *et al.* [11]. While the desorption energy does not directly link to the adsorption energy it is most likely that (for these two consimilar systems) this discrepancy does result from differences in the adsorption strength. As was shown in Section 1.2 the adsorption of water molecules on metal surfaces takes place via the H₂O lone-pair orbitals interacting with the unoccupied states of the metal substrate close to the Fermi level. In fact, the 5d states of Pt and Ir show a different filling which translates into (slightly) different energetic positions and affects the binding strength. Yet we cannot derive quantitative results from this consideration without a more detailed theoretical analysis.

Structure of the Adlayer

While the formation of a wetting layer on Pt(111) has been known for years, the structure of this layer has been widely discussed. In this work, we could show, that both superstructure phases unveiled by Glebov *et al.* [12] - (1) the $\sqrt{37} \times \sqrt{37}$ R25.3°, and (2) the $\sqrt{39} \times \sqrt{39}$ R16.1° - consist of a common set of structural elements. That is, a hexagonal ice ring in planar geometry, surrounded by a dense matrix of molecules in an H-down arrangement, and - for the $\sqrt{39}$ wetting layer only - second layer decoration (see Figures 3.4 and 3.16). Feibelman *et al.* [98] showed that the planar hexamer is responsible for the wetting behaviour of water on Pt(111) as the molecules within are able to take their favoured on-top adsorption site. In agreement with these results, an ordered adlayer develops for the entire range of submonolayer coverage. However, we found that the formation of a long range order of both the $\sqrt{37}$ and $\sqrt{39}$ wetting layer is strongly limited by the presence of impurities on the surface (cf. Figures 3.2 and 3.3). While these impurities ultimately prevent the formation of any long range order, the structural elements remain the same for all structures and coverages.

We observe closely related structural elements for extended water islands grown on Ir(111) (Figure 4.10). For both metal substrates, the proposed structural models of the wetting layer agree with the findings, that the monolayer itself is hydrophobic [101, 102]. Yet, in case of Ir(111), we did not observe a significant long range order of the wetting layer. This holds even though we carefully took our findings from water adsorption on Pt(111) into account and prepared a surface with an enhanced step edge density to efficiently trap impurities at the steps. Moreover we found the adsorbate islands to be surrounded by water clusters in a dense arrangement (see Figures 4.6 and 4.7). This observation clearly separates Ir(111) from Pt(111), where we never observed any such finite size structures.

We relate this dissimilarity to the slightly smaller lattice constant of the Ir(111) surface and to the (partial) dissociative adsorption of water molecules, which has recently been observed by Pan *et al.* [103]. Both aspects indicate that the planar $\sqrt{3}$ motif is preferred over the matrix phase, which offers a sound explanation for the formation and for the polar structure of the clusters, as shown in Figures 4.8 and 4.9. As discussed in the section 4.2, the coexistence of clusters and islands can then be attributed to a balance of Coulomb repulsion and enhanced lateral binding.

Except for cluster formation, the overall similarity of Pt(111) and Ir(111) is not surprising, as the neighbouring elements in the periodic system share many physical properties and show striking resemblance in their wetting behaviour.

In contrast to this the system $\text{H}_2\text{O}/\text{graphene}$ is different: TDS data rules out the existence of a wetting layer. Instead, we observe the formation of three-dimensional water clusters aligned in the graphene/Ir(111) moiré (see Figure 5.6). The strong variation in their apparent height indicates that the clusters are electronically decoupled from the substrate and possess a polar character. The inherent potential landscape of the moiré pattern specifies the nucleation sites for cluster formation (heterogeneous nucleation), but also limits the cluster size: For $\Theta = 3.0$ ML the clusters start to coalesce and form a quasi-continuous, most probably amorphous ice structure of several layers height (cf. Figure 5.7). The cluster formation is in agreement with theoretical predictions obtained for free-standing graphene [113–115], whereas their metastable character and the transition to a continuous layer is a unique property of graphene/Ir(111).

Stability towards Imaging

All systems studied in this part of the thesis have in common, that they are very sensitive to the STM tip (pick up), the applied bias voltage (dissociation) and the amount of tunneling electrons (vibrational excitation and rearrangement of molecules). While any of these mechanisms causes an irreversible structure transformation, we were able to create mixed OH/ H_2O adlayer structures on both metal substrate via controlled dissociation of molecules (cf. Figures 3.13 and 4.13). Note, that manipulation is most severe in case of graphene support which agrees with the previous findings of a well-decoupled water adlayer.

PART III

Ion Induced Defect Formation on Graphene and Noble Metal Surfaces

CHAPTER 7

Fundamentals: Ion Surface Interaction and Defect Production

Several paragraphs of this chapter are adopted within their meaning or literally taken from the work of Alex Redinger [125] and Charlotte Herbig [164], as indicated in the respective section headings. I do not claim intellectual property on any of the results presented in this chapter.

The following chapter introduces the physics of ion bombardment, with a strong focus on the interaction of charged particles in the keV range with a solid target. Firstly, the energy transfer of binary collisions is discussed in Section 7.1, followed by a description of the concomitant defect formation and thermally activated diffusion processes, Section 7.2. To motivate the experimental setup, the ion-surface interaction in case of grazing incidence is considered separately in Section 7.3. Finally, in Section 7.4 defects in graphene are introduced, giving an outlook to ion-induced, artificial patterning of the graphene layer in form of a nanomesh.

7.1 Ion Bombardment

The interaction of an energetic ion with a target material can be described in a classical scattering picture. When the ion and the target get into collisional contact the projectile experiences an energy loss and decelerates. This is due to a transfer of its kinetic energy to the target material, which can be assigned to three mechanisms: Displacement of the target nuclei, excitation of the target electronic system, and initiation of nuclear reactions within the target atoms. Thus, the stopping power $S(E)$ of a material can be written as:

$$\text{stopping power} \quad N \cdot S(E) = - \left(\frac{dE}{dx} \right)_d - \left(\frac{dE}{dx} \right)_e - \left(\frac{dE}{dx} \right)_n, \quad (7.1)$$

where dE/dx describes the energy loss per unit path length in each term and N the number density of substrate atoms. While nuclear stopping (displacement, index d) denotes elastic scattering, electronic stopping (index e) and nuclear reactions (index n) resemble inelastic scattering processes.

Nuclear reactions have to be considered only at very high projectile energies, $E_{\text{ion}} \gg 1$ MeV and will therefore not be discussed further. For intermediate energies (MeV range) electronic stopping gains importance, while on the laboratory scale, $E_{\text{ion}} < 100$ keV, scattering with the target nucleus is the dominant process. Thus, the interaction of the scattered particles with the target material can be approximated by using the Coulomb potential:

$$\text{scattering potential} \quad V(r) = \frac{Z_1 Z_2 e^2}{r} \cdot \chi(r). \quad (7.2)$$

While the fractional term describes the case of classical Rutherford scattering of swift particles (MeV regime), for low energetic ions a correction of the Coulomb potential $\chi(r)$ due to electron screening of the core has to be implemented. For very high ion energies relativistic corrections have to be considered.

Energy Transfer (cf. [125, 164])

The energy transfer of a keV ion onto a target atom can be calculated from a two body scattering event (illustrated in Figure 7.1): The primary particle (1) with mass M_1 , atomic number Z_1 , and velocity \vec{v}_1 collides with a target atom (2) (mass M_2 , atomic number Z_2) at rest, $v_2 = 0$. Upon scattering, the primary ion is deflected by α_1 and faces an energy transfer $E_1 \rightarrow E_1^* + E_2^*$ (velocities \vec{v}_1^* , \vec{v}_2^*):

$$\text{energy transfer} \quad E_1^* = E_1 \cdot \frac{\left(\cos \alpha_1 \pm \left(\left(\frac{M_2}{M_1} \right)^2 - \sin^2 \alpha_1 \right)^{\frac{1}{2}} \right)^2}{\left(1 + \frac{M_2}{M_1} \right)^2}. \quad (7.3)$$

According to Winter *et al.* [165] for small scattering angles of the projectile, $\alpha_1 \rightarrow 0$, the energy transfer of a single binary collision can be approximated via:

$$\text{small angle scattering} \quad \Delta E = E_1 - E_1^* \approx \frac{M_1}{M_2} \cdot E_1 \cdot \alpha_1^2 . \quad (7.4)$$

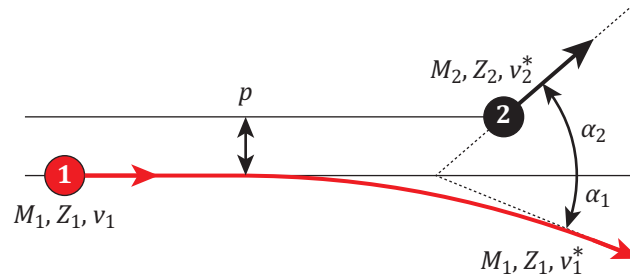


Figure 7.1: Schematic View of a Two Body Scattering Event. An energetic particle [(1), mass M_1 , atomic number Z_1 , velocity \vec{v}_1] is approaching a target at rest [(2), $M_2, Z_2, v_2 = 0$] with impact parameter p . Upon scattering, the projectile loses energy to the target atom and faces deflection by α_1 . In the aftermath of the scattering event, the particle velocities amount to \vec{v}_1^* and \vec{v}_2^* .

Shadow Cone (cf. [125])

The deflection of incident particles via Coulomb repulsion leads to the formation of a shadow cone behind the rest atom as shown in Figure 7.2. Considering many trajectories of uniform energy E , the cone visualizes a forbidden zone which the impinging ion is not able to enter. Its radius R_{sc} at distance d from the target atom can be calculated via:

$$\text{shadow cone radius} \quad R_{sc} = 2\sqrt{\frac{Z_1 Z_2 e^2}{4\pi\epsilon_0 E}} \cdot d . \quad (7.5)$$

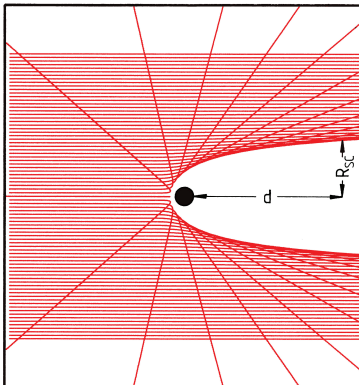


Figure 7.2: Formation of a Shadow Cone. Energetic particles (red trajectories, starting on the left) hitting a target atom (black circle) at rest. The cone is parameterized by its radius R_{sc} at a certain distance d from the rest atom. Redrawn from [165], Copyright 2002, with permission from Elsevier.

Here, an unscreened Coulomb potential is considered. A universal expression for the shadow cone has been deduced by O. S. Oen [166]. Having a closer look at Figure 7.2, one can see that the density of trajectories increases at the rim of the shadow cone, which is called *focussing effect*.

7.2 Defect Production and Evolution

So far, only isolated target atoms are considered. In a crystalline target material more complex scattering events have to be taken into account. Thus the defect production is not only influenced by the target density but also by the target crystal structure.

Collision Cascade (cf. [125, 164])

When an ion hits a crystalline target, a primary knock-on atom (PKA) is produced by the transfer of kinetic energy. In case that the energy deposited by the impinging ion just exceeds the displacement threshold E_d to release an atom from its regular lattice site, a vacancy-interstitial (Frenkel) pair develops ($E_d = 15..40$ eV in case of metals and semiconductor materials [167]). Defect production according to this model in the *near-threshold-regime* can be applied for light ions (H^+ , He^+) with keV energy and heavy ions in the eV range. For heavy ions with higher projectile energies the deposited energy is sufficient to cause more severe damage: The PKA itself can undergo collisions with the surrounding lattice atoms, thereby causing secondary (tertiary, etc.) recoils. Thus, the ion initiates a collision cascade, shown in Figure 7.3. As a result, temporary or permanent displacement occurs, where the latter forms bulk defects (vacancies, interstitials) as well as surface vacancies and adatoms. Temporary displacement occurs, when the Frenkel pair is not well separated, i.e. if the vacancy and the interstitial remain within their spontaneous recombination volume [168] and will anneal in time. In most cases, the primary ion creates several PKAs and is finally implanted into the bulk.

At this stage of our discussion, the damage production process can be divided into a linear and a non-linear regime. In the linear regime, the collisions can be considered as a sequence of independent binary collisions and explained by the above approximation. Yet this picture fails for heavy ions, higher particle energies, and denser target materials: Here the collision events occur in close vicinity to each other and cannot be described as individual events. A many-body collision takes place that requires molecular dynamics (MD) methods for an accurate description of the process. Moreover, electronic excitations of the target material will appear, that are not discussed in this simple picture.

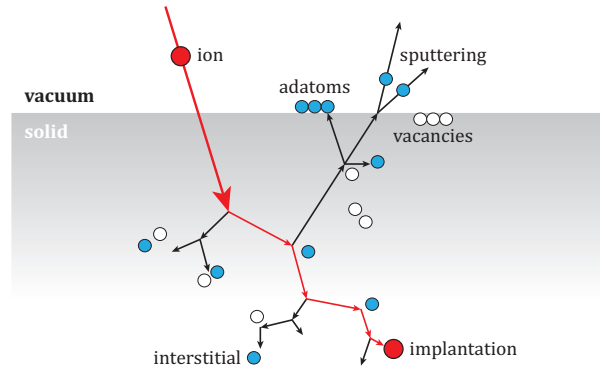


Figure 7.3: Sketch of an Ion Induced Collision Cascade. The impinging ion causes production of Frenkel pairs, surface adatoms, and sputtering of target atoms. Vacancies are shown in white, target atoms removed from a regular lattice site are shown in blue. The path of the impinging is printed in red. Redrawn from [125].

For heavy, high energetic ions (keV regime) the collision cascade terminates in a liquid like zone, the thermal spike, and is followed by a recovery phase. The entire process occurs in a time interval of picoseconds and will be discussed in more detail in the following.

Within the first 0.1 – 0.3 ps the PKA faces sequent recoils and produces several branches of collision cascades until the energy of all moving atoms has dropped below E_d . In the course of this sequence, the distance between two collisions decreases. In the end ($t \approx 0.25$ ps), the energy is deposited in such a small volume that a collective motion of the atoms leads to a *thermal spike*. This name derives from simulations which predict the temperature in the spike region to reach a multiple of the melting temperature [169] according to equation 7.6:

$$\text{thermal energy} \quad E = \frac{3}{2}k_B T = \frac{1}{2}m\bar{v}^2. \quad (7.6)$$

In this liquid-like zone all atoms are in motion. At the same time, the local atomic density in that region is reduced by up to 20% and compressed material is found in the surrounding. In the subsequent cooling phase, which durates approximately 3 ps, stable interstitials are produced outside the molten zone. The center of the molten region itself cools down via phonos, solidifies and recrystallizes after about 10 ps. While several vacancies are able to recombine with nearby interstitials a great part of them remains and forms a depletion zone [167].

The morphology of graphene and metal substrates following impacts of keV ions with various fluences will be discussed in Sections 9.1, 9.2, and 10.1.

Thermal Evolution (cf. [164])

Since all experiments are carried out at finite temperature, diffusion processes have to be considered and will, therefore, be briefly addressed in the following. Defect evolution is a temperature activated process that is mainly governed by mobilities of interstitials and vacancies. Therefore, it obeys an Arrhenius law:

$$\text{diffusion} \quad D_{\max} = D_0 \cdot \exp\left(-\frac{E_m}{k_B T}\right), \quad (7.7)$$

where D_0 denotes a pre-exponential factor and E_m the migration energy. In general, interstitial mobility sets in at lower temperatures than vacancy mobility. In the bulk, both species will agglomerate into defect clusters to reduce their free energy. At high temperatures these clusters will dissociate and/or recombine right after creation (e.g. in case of high temperature ion bombardment). As the surface displays an energy sink for unsaturated bonds bulk defects will diffuse towards it, forming vacancy or adatom islands. Further increasing the sample temperature will cause these islands to diffuse at the surface and finally attach to step edges.

The evolution of point defects and adatom clusters in graphene and metal surfaces upon thermal treatment will be discussed in Sections 9.3 and 10.1.

Sputtering Yield (cf. [125, 164])

When the collision cascade intersects the surface with the momentum of particles in the surface-near region directed towards the vacuum sputtering occurs: In case an atom gains enough kinetic energy to exceed the surface binding energy it can be ejected from the surface. Usually, only atoms originating from the first three layers [170] can gain enough kinetic energy to be pushed towards the crystal surface. Here, the characteristic parameter is the sputtering yield which describes the average number of removed atoms per incident ion:

$$\text{sputtering yield} \quad Y = \frac{\text{number of removed atoms}}{\text{number of incident ions}}. \quad (7.8)$$

The sputtering yield is proportional to the stopping power $S_d(E)$ for atom displacement and inversely proportional to the surface binding energy U_0 . For an amorphous target, this leads to a first approximation of the sputtering yield [171]:

$$\text{sputtering yield} \quad Y = \frac{0.042 \cdot \phi(\vartheta) \cdot S_d(E)}{U_0}. \quad (7.9)$$

Here, ϕ denotes a function of the angle of incidence ϑ . An increase of ϑ , measured with respect to the surface normal, leads to an increase of the sputtering yield, as the ion penetration depth decreases with more energy being deposited in the near-surface region:

$$\text{angular dependence} \quad Y(\vartheta) \approx \frac{Y(\vartheta = 0^\circ)}{\cos \vartheta}. \quad (7.10)$$

This approximation breaks down for large incidence angles, since the reflection probability increases, which can be visualized in the shadow-cone model introduced earlier (see Figure 7.4): While the impinging ion is able to penetrate the crystal in a wide angular range, the shadow cones of the surface atoms start to overlap at a certain angle [Figure 7.4(b)], causing reflection. However, sputtering still occurs, as the ions face large angle scattering and thus transfer a significant amount of energy to the topmost layer (terrace erosion). Further increasing ϑ finally leads to specular reflection and minimized erosion [Figure 7.4(c)]. Depending on the experimental parameters ion energy and projectile/target mass ratio, the maximum of the sputtering yield ranges between 60° and 80° , measured from the surface normal. For grazing incidence ions the sputtering yield drops sharply [172].

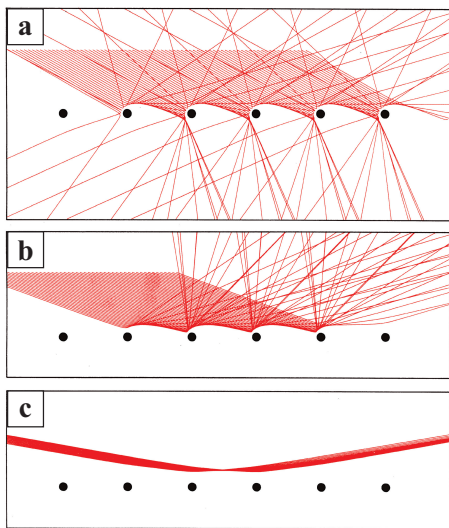


Figure 7.4: Angular Dependence of Ion Scattering for 1 keV Argon Bombardment on Aluminium. (a) For $\vartheta = 60^\circ$ the ions (red trajectories) are able to penetrate the surface layer (black circles). (b) For $\vartheta = 70^\circ$ the shadow cones largely overlap causing reflection of the impinging ions. The scattering trajectories are spread over a wide range of angles. (c) At $\vartheta = 80^\circ$ specular reflection occurs. Reprinted from [165], Copyright 2002, with permission from Elsevier.

Another aspect, which has to be considered for single crystal targets, is the crystallographic orientation of the target material. When an ion enters the crystal along a low index direction, it may be focussed in between the crystal planes. In this channeling motion the importance of nuclear stopping $(dE/dx)_d$ is strongly reduced. The main stopping power is then provided by electronic contributions $(dE/dx)_e$ and the ion penetration depth increases. Consequently, the intersection of the collision cascade with the surface shrinks, which results in less sputtering.

A more detailed survey on fundamental ion-surface interactions is given in e.g. [125, 167, 168] and references therein.

7.3 Grazing Incidence

When the angle of incidence ϑ between the ion and the surface approaches 90° , the deposited energy per ion drops since the reflection coefficient increases. As shown in Figure 7.4, total reflection occurs for angles larger than ϑ_{tot} , with a corresponding energy transfer $E_{\perp} = E_o \cos^2 \vartheta_{\text{tot}}$. The lack of large angle scattering events in this geometry results in surface channeling, i.e. a focussing of the ion trajectory parallel to the target surface (cf. Figure 7.2). Large angle scattering processes do only occur at surface imperfections like adsorbates and preexisting steps, from which follows that ions impinging at grazing incidence are very surface sensitive. This effect can be used to study the morphology (and/or growth) of single crystals by means of grazing incidence ions.

Subsurface Channeling (cf. [125, 164])

A new, remarkable feature arises, when grazing incidence ions are able to penetrate the topmost crystal layers along a low index direction. Given that case, a projectile will move almost parallel to the strings or planes of the surface atoms. The ion is effectively trapped in the open space between two layers where only small angle binary collisions occur. The energy loss per unit length is strongly reduced compared to direct impacts, which leads to an extended, oscillatory motion of the particle below the surface - *subsurface channeling*. As a result, surface vacancies and adatoms are formed along the ion path, where the projectile hits the topmost crystal layer from below. Due to the low coordination of surface atoms, the energy threshold for damage formation is reduced by roughly one order of magnitude compared to bulk channeling. Redinger *et al.* [173, 174] observed continuous surface vacancy trenches for Xe bombardment which effectively unveil the trajectory of the channeled particles - shown in Figure 7.5.

Note that the probability for subsurface channeling is enhanced, when an ion hits an ascending step edge. As this geometry resembles the case of normal incidence, the projectiles are easily able to enter the crystal.

A mechanism closely related to subsurface channeling will be introduced in Section 9.1.

As we now have an understanding of the defect formation in bulk materials (amorphous as well as crystalline), we will apply this knowledge to the case of graphene. Due to the

peculiar structural properties of this 2D material, cf. Section 1.5, the following section is dedicated to intrinsic defects in the carbon layer as well as the possibility of artificial patterning of the graphene sheet via electron and ion beams.

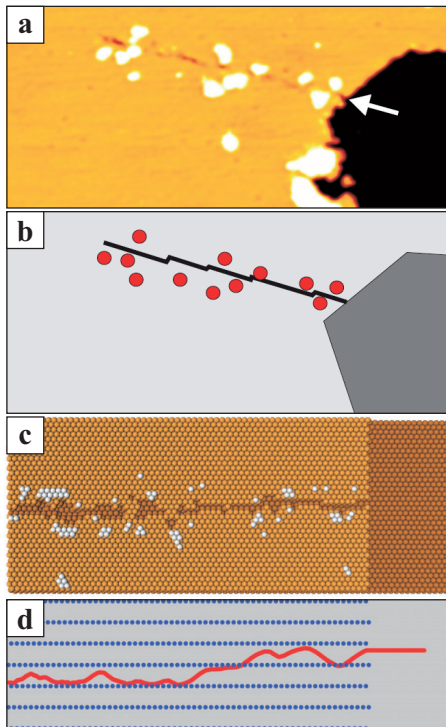


Figure 7.5: Subsurface Channeling. (a) Scanning tunneling microscopy (STM) topograph of a 5 keV Xe^+ single-ion impact on a preexisting metal step edge. The ion is impinging parallel to the $[1\bar{1}0]$ direction (arrow). Image width: 400 Å. (b) Sketch of the above situation highlighting the positions of the surface trench and the adatom clusters. (c) Top view ball model obtained by MD simulation damage for a corresponding event. (d) Top view of the same MD simulation event with the ion trajectory (red curve) performing channel switching. Blue dots mark the positions of atoms on the upper terrace. The scale in the direction normal to the initial ion direction is expanded by a factor of three to enhance visibility. Reprinted from [174]. ©IOP Publishing Ltd and Deutsche Physikalische Gesellschaft. Published under a CC BY-NC-SA licence.

7.4 Defects in Graphene

The outstanding electronic and structural properties of graphene, introduced earlier in section 1.5, make this material a promising candidate for post-CMOS technology. However, many envisioned applications require to tailor these properties. Here a controlled introduction of defects into the two-dimensional lattice comes into play, as they are able to alter the macroscopic properties by modifications on the atomic scale.

This section will introduce various kinds of structural defects found in graphene, deal with defect configurations in the presence of a substrate, and introduce a way to tune these structures experimentally.

Structural Classification

In the discussion of intrinsic graphene defects, two different mechanisms have to be considered: Ejection of carbon atoms and bond rotation. While the threshold energy for displacement amounts to $E_d = 18..22$ eV [175, 176], bond rotation is energetically lower in cost. In the simplest case, i.e. the rotation of one carbon bond by 90° , the four adjacent hexagon rings are transformed into two pairs of pentagons and heptagons. The resulting Stone-Wales defect [SW(5775), see Figure 7.6] has a formation energy of $E_f \approx 5$ eV, with a kinetic barrier of roughly 10 eV, when the transformation is realized through an in-plane rotation [177]. Thus once formed, this type of defect is stable at all temperatures typically accessible in experiments. Note that in this configuration no dangling bonds are formed.

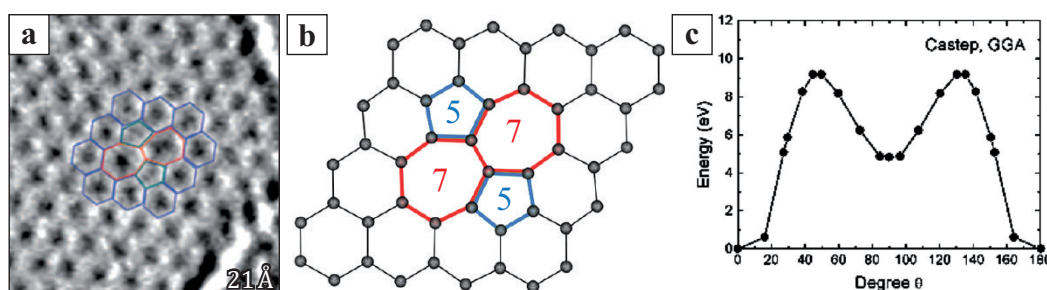


Figure 7.6: Stone-Wales Defect. (a,b) Atomic scale transmission electron microscopy (TEM) image of a Stone-Wales defect SW(5775) and corresponding atomic structure obtained via density functional theory (DFT) calculations. (c) Calculated energy barrier for bond rotation. Reprinted (adapted) with permission from [176]. Copyright 2011 American Chemical Society.

When the threshold energy for displacement is overcome (e.g. via ion or electron impacts) vacancies start to form. The removal of one carbon atom results in three dangling bonds, which are energetically very unstable and thus very reactive towards bond reorganisation. To lower the total energy of the single vacancy (SV) a pentagon-nonagon pair develops [$V_1(5-9)$ defect], illustrated in Figure 7.7(a,b). As there is still an undercoordinated atom, the formation energy $E_f \approx 7.5$ eV [178] is much higher than the vacancy formation energies in e.g. Si (4.0 eV [179]) and most metals (< 3 eV [180]). The dangling bonds excess electron resides in the π system, directly at the Fermi level. Microscopic studies have proven that the defect carries an enhanced density of states and is found to disturb the electronic structure in its surrounding, see Figure 7.7(c). [48] The migration energy amounts to 1.3 eV. [178] Hence, single vacancies are mobile even at moderate temperatures of several hundred K.

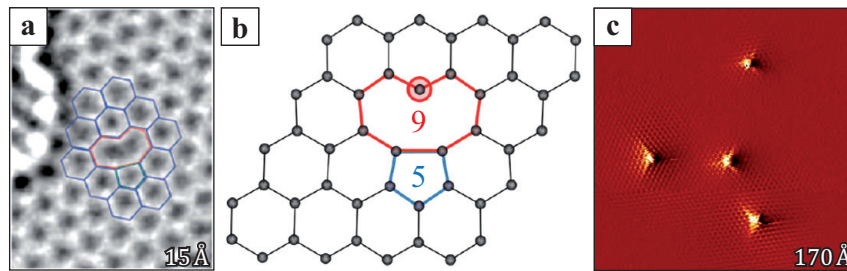


Figure 7.7: Single Vacancy. (a,b) Atomic scale TEM image of a single vacancy in graphene $V_1(5-9)$ and corresponding atomic structure obtained via DFT calculations. Reprinted (adapted) with permission from [176]. Copyright 2011 American Chemical Society. (c) STM topographic image showing single vacancies sitting on different sublattices of highly ordered pyrolytic graphite (HOPG) ($U_{\text{bias}} = 270$ mV, $I = 1$ nA). The vacancy appears bright in STM images due to an increase in the local density of states at the Fermi level. Reprinted with permission from [48]. Copyright 2010 by the American Physical Society.

When two SVs agglomerate or in case two neighbouring carbon atoms are removed directly, a divacancy (DV) is formed. As shown in Figure 7.8(a,b), the system reconstructs in plane by forming a structure out of two pentagons and one octagon [$V_2(5-8-5)$ defect]. By this, all bonds are saturated. The formation energy $E_f \approx 7.5$ eV [176] is similar to the one of SVs. In consequence, the energy per missing atom is much lower. The STM signature of such a defect structure is depicted in Figure 7.8(c), showing the characteristic two-fold symmetry.

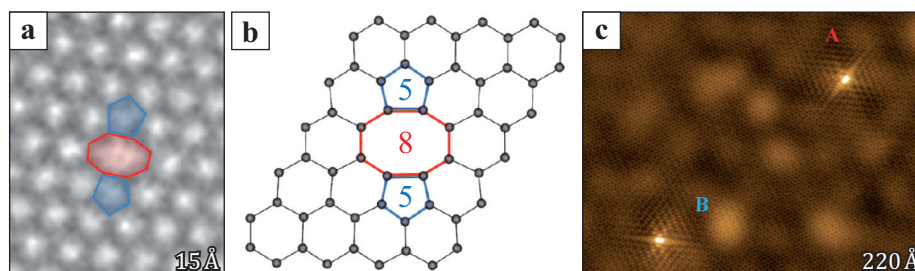


Figure 7.8: Double Vacancy. (a,b) Atomic scale TEM image of a divacancy type defect $V_2(5-8-5)$ and corresponding atomic structure obtained via DFT calculations. Reprinted (adapted) with permission from [176]. Copyright 2011 American Chemical Society. (c) STM topograph showing differently oriented divacancies in 4-5 ML G/SiC(0001) ($U_{\text{bias}} = 280$ mV, I not specified). Reprinted with permission from [50]. Copyright 2012 by the American Physical Society.

More complex defect structures can be produced when a larger amount of atoms is removed at once. Generally, vacancy structures with an even number of missing atoms are energetically favored over those with an odd number, as for the latter case it is not possible to completely saturate all dangling bonds. While large vacancy clusters are rather stable, many nearby holes cause bond reorganization that may lead to amorphization of the entire graphene sheet.

On the other hand, the ejected carbon atoms may stay in contact to the graphene layer. With a migration barrier of only 0.4 eV [181] they are highly mobile even at room temperature. When two adatoms assemble, they can be incorporated into the graphene lattice via an inverse Stone-Wales defect [$I_2(7557)$, Figure 7.9(a,b)].

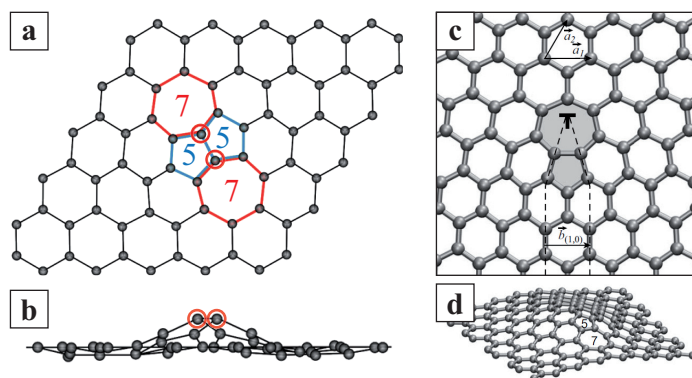


Figure 7.9: Defect Induced Buckling of the Graphene Sheet. (a,b) Formation of an inverse Stone-Wales defect $I_2(7557)$ by incorporation of carbon adatoms (red circles), obtained via DFT calculations. Reprinted (adapted) with permission from [176]. Copyright 2011 American Chemical Society. (c) Step dislocation terminating in a 5-7 defect [type (1,0) dislocation]. (d) The graphene layer faces buckling in close vicinity to the defect site. Atomic structure optimization via DFT calculations. Reprinted with permission from [182]. Copyright 2010 by the American Physical Society.

Once formed ($E_f \approx 5.8$ eV [176]), the embedded dimer is stable and causes local curvature. It resembles a finite size step dislocation which was observed earlier by Coraux *et al.* [45] and theoretically described by Yazyev and Louie [182] [Figure 7.9(c,d)].

Graphene Nanomesh

While all structures introduced up to now affect the properties of graphene on atomic scale only, its macroscopic properties remain as for the pristine layer (except for the mechanical properties which are controlled by the mobility of step dislocations as it is the

case for bulk materials). However, an extended two-dimensional defect structure is able to tune the electronic structure of graphene significantly: a periodic arrangement of holes, called *graphene nanomesh* (GNM). This antidot lattice turns the semimetallic graphene sheet into a semiconductor as the array of strong potential barriers induces a bandgap opening. [36, 183–186]

Using a tight binding description, Pedersen *et al.* demonstrated that the electronic structure is strongly dependent on the antidot lattice parameter and the amount of removed carbon atoms per unit cell. [183] They proposed a bandgap opening:

$$\text{bandgap} \quad E_g = 25 \text{ eV} \cdot \frac{N_{\text{removed}}^{1/2}}{N_{\text{total}}} . \quad (7.11)$$

Here, N_{total} (N_{removed}) denotes the number of (removed) atoms per unit cell. Given a nanomesh in the size of the Gr/Ir(111) moiré, the bandgap amounts to $E_g \leq 1 \text{ eV}$.

A graphene nanomesh with a lattice constant in the order of 100 nm has been realized using reactive ion etching. [187, 188] Subsequently, more methods have been established to realize an antidot lattice like, e.g. lithographic techniques [35, 189, 190], chemical reduction of graphene oxide films [191], templated growth [39], and ion bombardment [192]. An example of the experimental routine to create a GNM is shown in Figure 7.10. [35] The work of Bai *et al.* confirms the dependence of the bandgap and the on-off-ratio on the hole-size and lattice constant. [35]

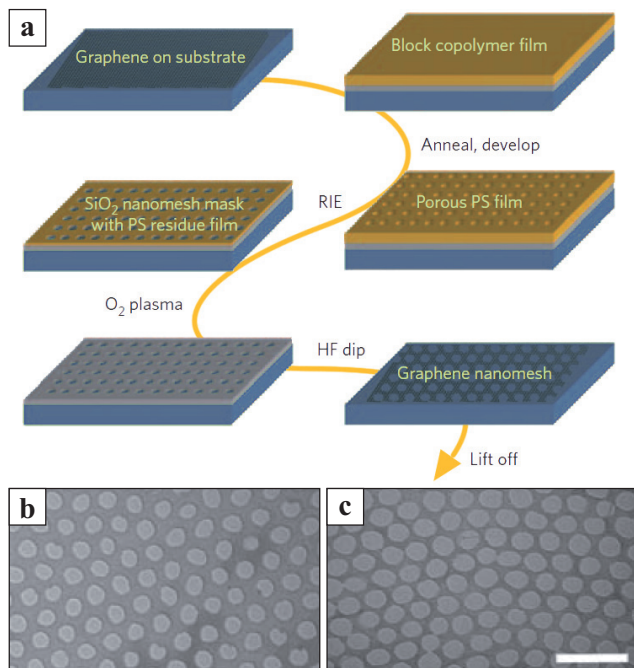


Figure 7.10: Fabrication of a Graphene Nanomesh. (a) Experimental routine of nanomesh fabrication via block copolymer lithography. (b,c) TEM images of various graphene nanomeshes with varying periodicity and neck width. The scale bar is 100 nm. Details on the experimental procedure and mesh characterization can be found in [35]. Reprinted by permission from Macmillan Publishers Ltd: Nature Nanotechnology [35], copyright 2010.

While several of these techniques allow for a large scale synthesis of a GNM with a reproducible quality, several restrictions remain when one tries to downscale the structures to an atomic level. Furthermore, drawbacks arise by the experimental routine, when a substrate comes into play. This aspect will be closer inspected in the next but one section. Yet the geometry of a graphene nanomesh is envisioned to pave the way for a new generation of semiconducting devices, which go beyond the scope of this work.

Beam Induced Defect Formation

As the formation energy for all kinds of defects amounts to several eV, they typically occur under non-equilibrium conditions like (prolonged) exposure towards swift particles only. To fabricate defects in a graphene sheet, several tools are at hand as shown in the previous section. However, ion bombardment and electron irradiation have been proven useful techniques due to their flexibility and scalability. Especially electron beam induced damage is widely studied, as the processes involved are important already during any transmission electron microscopy (TEM) analysis. Given an appropriate electron energy (cf. kinetic barrier for bond rotation) beam driven defect evolution occurs. An example of this process is shown in Figure 7.11. [42]

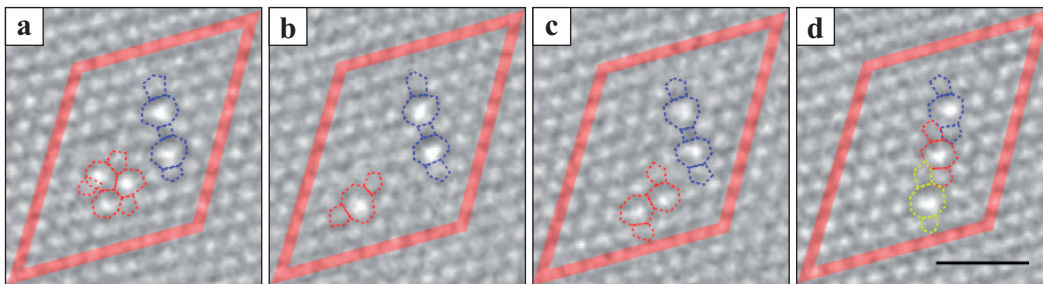


Figure 7.11: Electron Beam Driven Divacancy Migration. Imaging of defects in a suspended graphene sheet using an electron energy of $E_e = 80$ keV. The transformation between individual stages is initiated by bond rotation only. The scale bar is 1 nm. Reprinted with permission from [42]. Copyright 2011 by the American Physical Society.

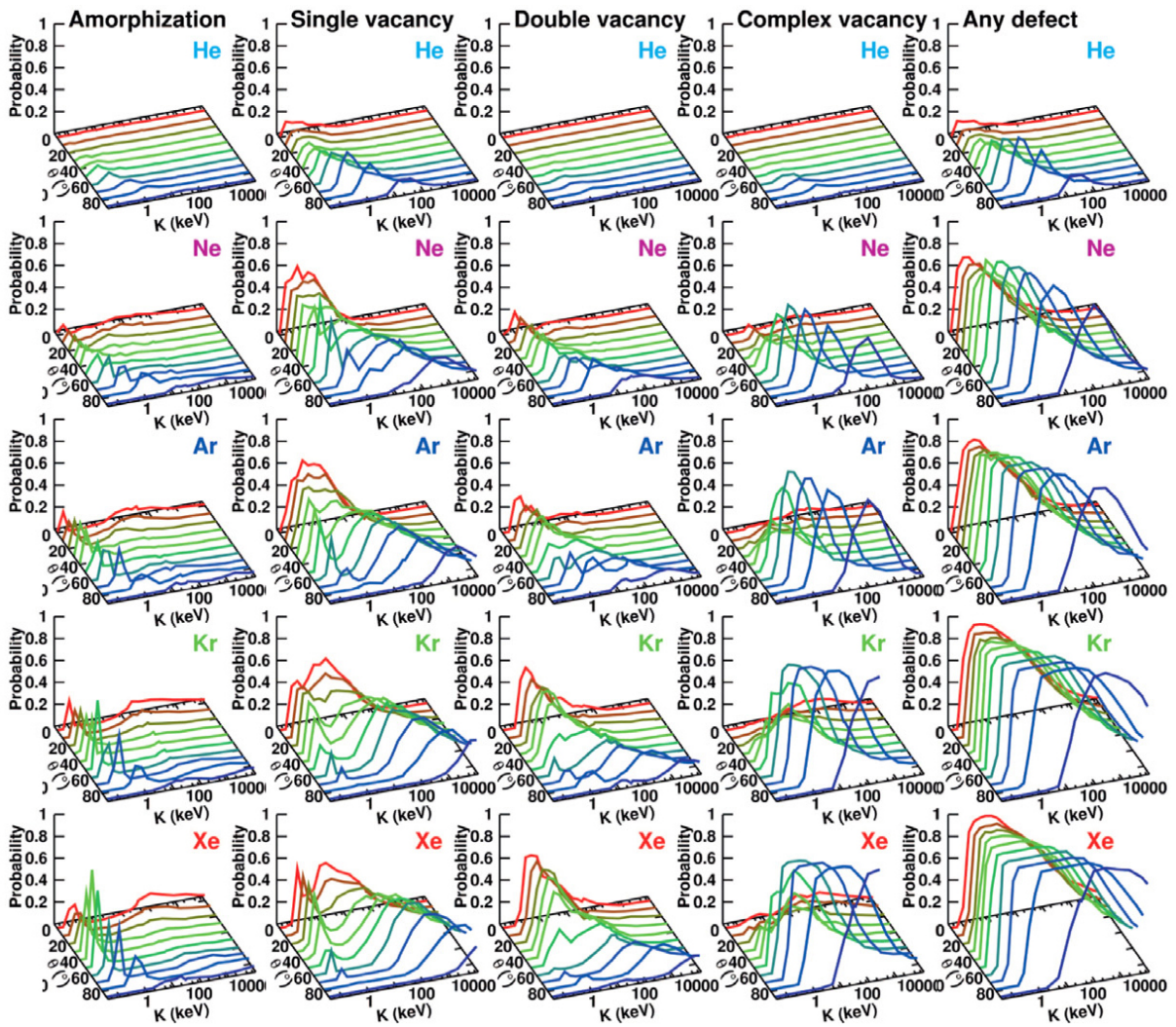


Figure 7.12: Molecular Dynamics Simulation Data of the Defect Production in Free-Standing Graphene. Probabilities of producing single vacancies, double vacancies, complex vacancies, local amorphizations, and any defect (any modification to the pristine structure) in graphene under irradiation of noble gas ions as functions of angle of incidence θ (with respect to the surface normal) and ion energy K . Reprinted from [193]. © IOP Publishing. All rights reserved.

While creation of vacancies requires an electron beam energy of $E \approx 100$ keV [194, 195], the activation threshold for ion irradiation is severely lowered due to a significantly higher cross-section. Figure 7.12 summarizes the results of noble gas ion bombardment in a molecular dynamics approach. The plots [193] give the probabilities for the formation of well-defined defects as well as complex defect structures in dependence of the ion energy K and angle of incidence θ (with respect to the surface normal): Amorphization (via bond rotation) is the dominant process in the near-threshold regime. More swift, low

keV-ions most likely produce single and divacancies, where the latter gain importance with increasing particle mass. For larger incidence angles complex defect structures arise as the projected density of the graphene sheet is substantially increased.

Given the case of normal incidence Ar bombardment, the creation of a single vacancy requires an ion energy of $E_{\text{ion}} \approx 140 \text{ eV}$ [48, 50]. In addition to the previously mentioned studies, more experimental examples of ion induced defect formation can be found in the work of Tapasztó *et al.* [196] and Compagnini *et al.* [197].

The Role of the Substrate

So far, the influence of a substrate on the defect structure was ignored, as most of the studies shown before were carried out on suspended graphene layers. However, when a substrate comes into play, the morphology and electronic signature of the defects are altered. The creation of defects on supported graphene has been studied by Ugeda *et al.* [48–50], who performed normal incidence bombardment using 140 eV Ar^+ ions (which is just above the threshold to create well-defined defects, cf. [198]). Given a weakly interacting system like highly ordered pyrolytic graphite (HOPG) [48] or graphene on SiC [50] single and divacancies resemble the structures shown in figures 7.7(c) and 7.8(c), i.e. the underlying substrate has negligible effect on the defect structures. However, in case of a platinum support the defect appearance has fundamentally changed: The metal substrate stabilizes the vacancy type defects by saturation of the dangling carbon bonds at the Pt surface atoms (Figure 7.13). In consequence, the entire graphene sheet is pulled towards the substrate by 0.08 \AA . [49]

Akcoeltekkin *et al.* [41] observed an even stronger graphene substrate interaction when irradiating a dielectric substrate (SrTiO_3) by swift heavy ions ($E \approx 100 \text{ MeV}$) at grazing incidence angle. In that system ion bombardment causes the formation of hillock-like structures at the surface as a result of electronic excitations which are then transferred to the crystal lattice. In case of graphene coverage these hillocks cause a splitting of the carbon lattice along the ion trail.

Furthermore, Jacobsen *et al.* [199] have demonstrated that the annealing mechanism of defective graphene sheets is substantially different for the case of Ni support as for free-standing graphene. Based on DFT calculations they demonstrate SW-like defects to be energetically benefitted, as the reaction barrier for bond rotation is reduced by the use of an intermediate reaction state involving the Ni substrate.

In Chapter 9 and, in particular, Section 9.4 we will study the structure and interaction of defects in graphene with the underlying metal substrate.

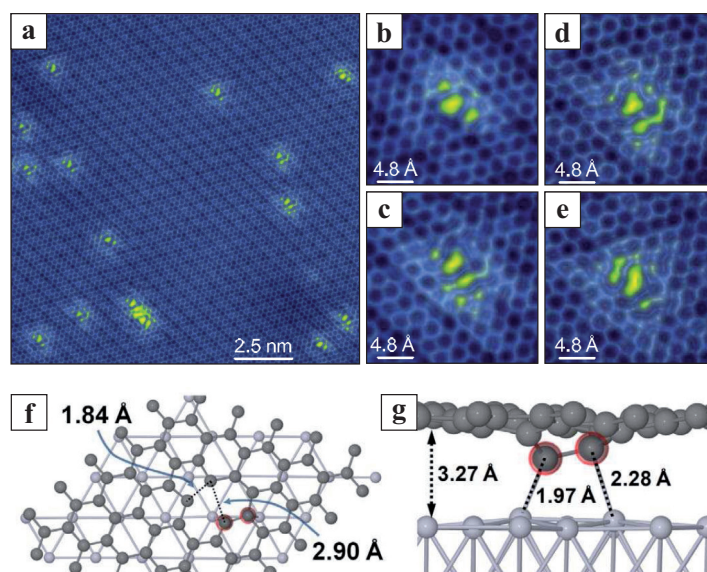


Figure 7.13: Morphology of Single Vacancies on Supported Graphene. (a) STM topographs of graphene/Pt(111) after bombardment with 140 eV Ar^+ ions at normal incidence. The morphology of the defect is complex and non-uniform (b-e) compared to the case of HOPG [see Figure 7.7(c)]. (f,g) Atomistic model obtained by DFT. The single vacancy is found to saturate its dangling bond at the underlying Pt atoms. All figures reprinted with permission from [49]. Copyright 2011 by the American Physical Society.

The approaches outlined here imply the possibility of structuring graphene by making extensive use of the underlying substrate. The presence of a support may not only affect the defect morphology but defect modeling seems possible via guided thermal annealing. In Chapter 10 a new route towards the controlled defect formation and fabrication of a GNM is implemented by ion irradiation of graphene supported by Ir(111).

CHAPTER 8

Experimental

Several paragraphs of this chapter are adopted within their meaning or literally taken from the work of Georgia Lewes-Malandrakis [200], Charlotte Herbig [164], and Ivo Pletikosić et al. [201], as indicated in the respective section headings. The description of ion bombardment, molecular dynamics simulations, and density functional theory calculations are published in Nano Letters [112].

This chapter complements the description of the experimental setup given in detail in Chapter 2. New aspects of the sample preparation will be discussed with a major focus on the calibration of the ion beam, see Sections 8.2 and 8.3. Furthermore, the parameters used in molecular dynamics simulations (Section 8.4) and density functional theory calculations (Section 8.5) are introduced.

8.1 Experimental Setup

All experiments on grazing incidence ion bombardment shown in this thesis were performed at the scanning tunneling apparatus "TuMA II", introduced in Section 2.1. An additional series of experiments addressing the electronic characterisation are carried out at the low temperature UHV setup "TSTM". For a description of this setup, the reader is referred to the work of F. Craes [202]. Bandstructure measurements are performed by angle resolved photoelectron spectroscopy, in collaboration with Marin Petrović and Marko Kralj from the Institut za fizika, Zagreb, Croatia. Differences in the experimental procedure of these experiments are listed in Section 8.3.

8.2 Calibration of the Ion Flux

To determine the ion flux impinging onto the sample during the bombardment a Faraday cup, mounted next to the sample on the manipulator, is used. The cup is composed of a front shield (the "Faraday plate") comprising a hole of 1 mm diameter. This hole marks the entrance to the eponymous Faraday cup. Cup and plate are insulated against each other and can be used for ion flux measurements individually. The cup is constructed in such a way that it prevents particle reflection and efficiently absorbs the particle charge. By this, the ion current is measured as precisely as possible and the contributions from secondary electron emission are kept at a low level. Only the cup is used to determine the ion flux in experiments.

Determination of the Ion Fluence (cf. [164, 200])

With the knowledge of the entrance hole area of the Faraday cup A_{cup} and the measured ion current I_{cup} the particle flux, particle flux density and particle fluence can be determined as follows:

$$\text{particle flux} \quad j_{\text{cup}} = \frac{I_{\text{cup}}}{N \cdot e} \left[\frac{\text{ions}}{\text{s}} \right], \quad (8.1)$$

with the charge of the ion $N \cdot e$ in which e is the elementary charge. Hence, the particle flux density J_{cup} can be calculated via:

$$\text{particle flux density} \quad J_{\text{cup}} = \frac{j_{\text{cup}}}{A_{\text{cup}}} = \frac{I_{\text{cup}}}{A_{\text{cup}} \cdot N \cdot e} \left[\frac{\text{ions}}{\text{m}^2\text{s}} \right]. \quad (8.2)$$

This leads to the following expression for the fluence:

$$\text{fluence } F_{\text{cup}} = J_{\text{cup}} \cdot t \left[\frac{\text{ions}}{\text{m}^2} \right], \quad (8.3)$$

$$\text{fluence (sample) } F = J_{\text{cup}} \cdot t \cdot \cos 75^\circ \left[\frac{\text{ions}}{\text{m}^2} \right]. \quad (8.4)$$

Here, a factor $\cos 75^\circ$ is introduced, as the ion beam hits the sample surface 75° off-normal. Typical values of the quantities F_{cup} and F are in the range of $10^{16} \dots 10^{22}$ ions/m². A more handy way used in this thesis is to give the ion fluence in MLE with respect to the Ir(111) surface, where 1 MLE corresponds to the surface atomic density of Ir(111) of $A^{\text{Ir}(111)} = 1.57 \times 10^{19}$ m²/atom:

$$\text{fluence (sample) } F \text{ [MLE]} = F \left[\frac{\text{ions}}{\text{m}^2} \right] \cdot A^{\text{Ir}(111)} \left[\frac{\text{m}^2}{\text{atom}} \right]. \quad (8.5)$$

A peculiar feature of the setup of TuMA II is that the ions enter the Faraday cup at an angle of 15° . Therefore, a reduction in the ion current might be expected. In order to verify this, the fluence was also determined by counting the number of (well separated) defect patterns under conditions, where each ion leads to significant surface damage. Due to a leakage current from the plate to the cup, which was found evolving in the course of this thesis, the counting was repeated after a certain time interval. Hereinafter all images are provided with the correct (experimentally determined) fluence.

8.3 Sample Preparation

The cleaning of the Ir(111) crystal follows the experimental procedure given in section 2.4, including cycles of prolonged sputtering (5 keV Xe⁺, $F = 35$ MLE, $T = 300$ K) and flash annealing to 1473 K. Graphene films were grown to various coverages up to full monolayer.

Ion Bombardment

Ion bombardment was performed under $(75 \pm 1)^\circ$ with respect to the surface normal along the dense-packed rows of the iridium crystal, i.e. the samples' $[1\bar{1}0]$ crystallographic orientation was aligned parallel with respect to the projection of the ion beam direction which is indicated in the topographic images. The alignment is accurate within $\pm 2^\circ$. The ion energy spread is smaller than 20 eV.

For bombardment the Faraday cup is moved in front of the ion gun to set and monitor the ion current for a period of time. Slight changes in the ion current are corrected by adjusting the gas flux into the ion gun. When a constant value is reached, the ion beam is blanked

and the sample is moved to the ion gun. The blanking is switched off for a well defined time interval, to ensure the desired ion fluence. Occasionally, bombardment takes place at elevated or lowered temperatures. Experiments performed at high temperatures are cooled down to room temperature directly after bombardment. Experiments performed below room temperature are quenched down to 20 K by liquid helium cooling. The ion current is cross checked after bombardment in order to assure that no flux changes occurred.

Scanning Tunneling Spectroscopy

Spectroscopy measurements are performed at the low temperature UHV setup "TSTM". The corresponding sample is grown *in situ* according to the standard routine (cf. 2.4) including growth of a closed graphene layer. After preparation, the sample faces 250 eV Ne⁺ bombardment under normal incidence at room temperature. The measurements are carried out at 5 K.

Angle Resolved Photoelectron Spectroscopy (cf. [201])

Angle resolved photoelectron spectroscopy (ARPES) measurements are performed *in situ* at a UHV setup with a base pressure of $1 \cdot 10^{-9}$ mbar, following sample preparation according to the standard routine (cf. 2.4) including growth of a closed graphene layer and 1 keV Xe⁺ ion bombardment 75° off normal. The spectra have been taken at room temperature by a Scienta SES-100 hemispherical electron analyzer with an energy resolution of 25 meV using 21.22 eV photons from a helium discharge source with a beam spot diameter of about 2 mm. The scans are performed perpendicular to the Γ -K-direction. The azimuthal alignment was checked by low energy electron diffraction (LEED) spot orientation. The parallel momentum is given by the polar angle, which could be adjusted with the precision of $\pm 0.5^\circ$. A precise determination of the ion current in the setup was not possible.

8.4 Molecular Dynamics Simulations

To understand the damage formation of our system in detail, we carried out atomistic simulations at the classical molecular dynamics (MD) level of approximation using the PARCAS code [203]. We approximate the experimental system by conducting the simulations for graphene on a Pt substrate (Ir's neighbor element in the periodic table, with the same fcc crystal structure) as an interatomic potential is available for Pt-C, but not for Ir-C. Due to the similarity of Pt and Ir, the main conclusions drawn from the simulations are expected to be transferable to the Ir-C system. In the simulations, the

Pt-Pt, Pt-C and C-C interactions were modeled using an analytical bond-order potential [204] smoothly joined with the universal repulsive Ziegler-Biersack-Littmark (ZBL) potential [205] at small atom separations. The Xe-Pt and Xe-C interactions were described by the ZBL potential.

As ion energies were quite low, and energy transfer from the projectile to the target atoms was fully governed by nuclear collisions, electronic stopping was not included in the simulations. In reality, the ion loses energy also to the target electrons through inelastic collisions. However, such processes do not alter the geometrical trajectory of the ion, but rather act as frictional forces. Moreover, the electron density in the gap in between the graphene sheet and the platinum substrate, where the ion trajectory mainly resides, is lower than in the bulk, which further reduces the significance of electronic stopping in the experiments at hand.

We used a simulation super cell of 36×79 Pt atoms with a height of 15 layers (42660 Pt atoms in total). On top of this we placed 40×87 graphene unit cells (6960 C atoms), resulting in a commensurate 11-on-10 structure. The graphene lattice constant was set to 0.252 nm, which is the equilibrium value for the employed interatomic potential. Accordingly the Pt lattice constant had to be slightly increased ($\approx 1\%$) from the equilibrium value of the potential. The graphene-substrate distance was set to the experimental value of 0.338 nm [110] for the Ir-C system in order to model the experimental conditions. The long-scale height variation of the moiré-pattern was neglected. The simulations were carried out at 0 K with a total simulation time of 1000 fs, which is adequate for the completion of the collision process. Time scales typical for defect diffusion are unreachable by the MD simulations. Nevertheless, due to relatively high migration barriers, most of the defects created by ion impacts will be stable at room temperature.

A total of 300 simulations were run, where Xe ions with a kinetic energy of 5 keV impacted the target at 75° with respect to the surface normal along the close-packed $[1\bar{1}0]_{\text{Ir}}$ direction, identical to the experimental setup. The impact points were randomly chosen in the simulated supercell. In addition, 200 simulations on a Pt target without the graphene layer were conducted in order to compare sputtering yields.

Statistics on the number and distribution of holes in graphene and adatoms on Ir were gathered by counting their numbers and determining their locations at the end of a simulation.

8.5 Density Functional Theory Calculations

In order to get a microscopic insight into the atomic structure of the (vacancy-type) defects, we carried out first-principles simulations using DFT as implemented in the plane-wave-basis-set VASP [206] code. We used Projector Augmented Wave (PAW) potentials [207] to describe the core electrons and the van der Waals (vdW) VV10 functional [208] for exchange and correlation. The kinetic energy cutoff (400 eV) and \mathbf{k} -point sampling over the Brillouin zone ($3 \times 3 \times 1$ mesh) were chosen to guarantee that defect formation energies are converged within 0.1 eV. This accuracy made it possible to draw all the conclusions, while avoiding excess computational effort. All calculations were carried out for a 200-atom 10×10 graphene supercell on top of a (111) 9×9 Ir slab containing 243 atoms. For the pristine system, we received essentially the same results as in Ref. [110], although the difference between graphene-metal separations in the TOP and HCP/FCC regions was smaller.

STM images were simulated using an approach we used before for modeling STM images of carbon nanotubes with defects [209]. We described the interaction between the surface and STM tip within the tight-binding (TB) approximation. We modeled the STM tip as the final atom of a semi-infinite, one-dimensional chain. All simulations were carried out at zero temperature. Treating tip-sample (graphene) interaction perturbatively (to the first order) and employing the Green's function method, one can write the STM current $I(x,y,z)$ between the tip positioned at the point with the coordinates (x,y,z) and the sample as:

$$\text{current} \quad I(x,y,z) = \frac{2\pi e}{\hbar} \int_{E_F - eU_{\text{bias}}}^{E_F} \sum_i |V_i(x,y,z)|^2 \rho_{\text{tip}}(E) \rho_{\text{graphene}}(i,E) dE, \quad (8.6)$$

where the sum runs over all sites involved in the tip-surface hopping. U_{bias} is the bias voltage applied to the tip-surface interface, $V_i(x,y,z)$ is the tunneling matrix element coupling the tip apex atom to the atom i of graphene, $\rho_{\text{tip}}(E)$ and $\rho_{\text{graphene}}(i,E)$ are the local densities of states (LDOS) of the non-interacting tip and the surface. LDOS of graphene was calculated by projecting DFT results (with account for metal substrate) to carbon atomic sites.

The TB tip-surface hopping parameter V was calculated within the framework of the Bardeen formalism [210]. V is defined as

$$\text{hopping parameter} \quad V = \langle \psi_{\text{graphene}}(i) | H | \psi_{\text{tip}} \rangle, \quad (8.7)$$

where $\{\psi_{\text{graphene}}(i)\}$ are the eigenstates of the TB Hamiltonian, which are the set of Wannier states centered about the lattice sites. We approximated the Wannier states by atomic-like states $\{\phi_i\}$, so that to the first order in perturbation theory the hopping element between the tip apex atom and graphene atom i may be written as follows:

$$\text{hopping element} \quad V_i = \frac{\hbar^2}{2m} \oint_{\mathbf{S}} d\mathbf{S} \{ \phi_i^* \nabla \phi_{\text{tip}} - \phi_{\text{tip}} \nabla \phi_i^* \} \quad (8.8)$$

The tip states were modelled by a $3d_{z^2}$ hydrogen-like wave function, whereas graphene states were approximated by s, $2p_x$, $2p_y$, $2p_z$ atomic orbitals. The integral (Equation 8.8) was evaluated numerically with the integration surface being the infinite plane halfway between the tip and the surface. We simulated a constant height mode of the STM operation. Solving Equation 8.6 for h , we plotted h as a function of the tip position in the (x,y) plane. Other details can be found in [211].

CHAPTER 9

Grazing Incidence Ion Impacts on Graphene

*Part of the results in this chapter are published in Nano Letters **13**, 1948 (2013) [112] and have also been discussed in the work of Georgia Lewes-Malandrakis [200] and Charlotte Herbig [164].*

The STM experiments discussed in the following chapter were planned by Georgia Lewes-Malandrakis, Charlotte Herbig, Carsten Busse, Thomas Michely, and by myself. Georgia Lewes-Malandrakis and me developed the model of interface channeling. The statistical analysis was done by Charlotte Herbig and me. The statistical model to approximate the experimental results was developed by Charlotte Herbig and Carsten Busse. STS measurements were performed by me with great support of Fabian Craes and Sven Runte. MD simulations were provided by Ossi Lehtinen (University of Helsinki), whereas DFT calculations were done by Arkady V. Krashennnikov (Aalto University). All authors of the publication were involved in the discussion of the experimental and theoretical results, and contributed to the text and editing of the manuscript. I prepared all images and wrote the draft of the manuscript. The following reflects in large parts the submitted work but is extended in most paragraphs. For experimental details the reader is referred to Chapter 8.

In this chapter we study defect patterns in graphene on an Ir(111) support created by keV ion bombardment and elucidate the formation mechanism of these patterns using molecular dynamics (MD) simulations, see Section 9.1. We employ noble gas ion irradiation under grazing incidence to maximize the interaction of the ions with graphene. Low fluences are chosen to make the damage patterns of individual ions visible. In Section 9.2 we study the dependence of the defect structure on the bombardment parameters. Furthermore, the thermal stability of defects in Section 9.3 is investigated. Combining experiments and density functional theory (DFT) calculations, we discuss the atomic structure of defects and show that with the onset of vacancy cluster mobility around 800 K, the vacancies sense formation energy differences within the moiré supercell formed by the graphene layer with the incommensurate iridium metal substrate, see Section 9.4.

9.1 Defect Formation via Interface Channeling

Figure 9.1(a) shows a topographic image of the fully graphene covered Ir(111) surface after ion bombardment. The typical moiré superstructure of Gr/Ir(111) [44] is visible as a hexagonal lattice of depressions with a lattice constant of 25.3 Å. It is due to the different registry of the carbon atoms with respect to the substrate inside the incommensurate supercell (as explained in detail in Section 1.5), see Figure 1.14(a) for an atomically resolved image and Figure 1.14(b) for a model. Unless noted otherwise, all STM topographs are in reverse contrast.

The defect patterns visible in Figure 9.1(a) are caused by irradiation with 5 keV Xe⁺ ions impinging 75° off normal. The projection of the primary ion beam is along the close-packed $[1\bar{1}0]_{\text{Ir}}$ -direction of the iridium substrate as indicated by the white arrows. This is also along the $[11\bar{2}0]_{\text{Gr}}$ -direction (zigzag-direction) of the graphene layer due to the epitaxial arrangement, and consequently also parallel to the close-packed direction of the moiré pattern. The fluence was set to $F = 0.8 \times 10^{-4}$ MLE. Individual defect patterns (i.e. structures caused by just one ion) can be distinguished. Each one is marked with an arrow in Figure 9.1(a). Note that sometimes the assignment of individual defect patterns is ambiguous.

The majority of the defect patterns extend in the direction of the incident ions. A single defect pattern consists of a chain of depressions, often accompanied by bright protrusions. We tentatively interpret the depressions as holes in the graphene layer. The apparent depth of the depressions cannot be determined directly as the STM image is a convolution of the sample topography with the STM tip. Line profiles of the three leftmost defect patterns are provided in Figure 9.2 [(b-d), from left to right, x coordinate runs from bottom to top]: In (b) the iridium step height $\Delta z = 2.2$ Å is visible as the line profile runs across a pre-existing step edge. The apparent height of the graphene layer above the iridium substrate is in the range of 2.0..2.5 Å and barely depends on the tunneling parameters [44]. The defect patterns are visible in the line scans as dips with a characteristic profile which vary strongly in depth. These features can be attributed to the finite size of the microscope tip, which has a dominating effect in STM images of small depressions as observed here. Only in case of spatially extended vacancy defects the STM tip is able to reach down to the substrate and then indeed a depth corresponding to the experimentally observed apparent distance between graphene and its substrate is measured. The fact that for small depressions the apparent depth increases with size and no saturation on a

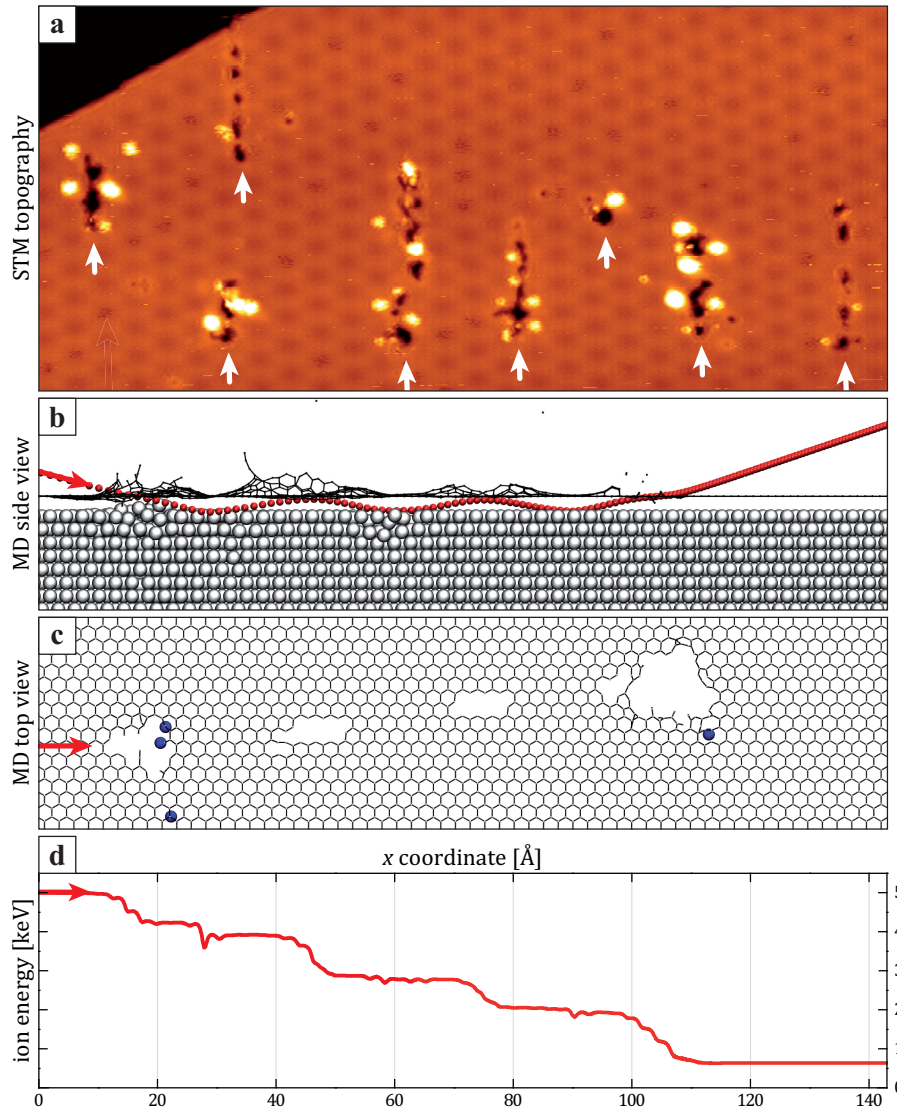


Figure 9.1: Defect Patterns - Experiment and MD Simulation. (a) STM image of the fully graphene covered Ir(111) surface after room temperature irradiation with 5 keV Xe⁺ ions at 75° off normal, fluence $F = 0.8 \times 10^{-4}$ MLE. Individual defect patterns are marked by arrows pointing along the direction of the impinging ions. A pre-existing substrate step is visible in the upper left corner. Image width: 530 Å; Imaging parameters: $U = 12$ mV, $I = 0.9$ nA. (b) Snapshot from an MD simulation showing the side view of a single 5 keV Xe⁺ ion impinging on graphene/Pt(111) at 75° off normal (Xe is impinging from the left). The size of the simulated layer is 87 Å × 220 Å. The time-lapse motion of the ion (red circle) is shown in steps of 2 fs (position of graphene and platinum atoms at fixed simulation time of 170 fs). (c) Top view of the same simulated impact at 1000 fs. For clarity the image shows the resulting graphene layer and metal adatoms (blue spheres) only. (d) Evolution of ion energy during the simulation as the ion travels along the lateral coordinate x for the event shown in (b) and (c).

level lower than the one of the substrate is observed allow us to use the line profiles as indication that the depressions are indeed holes in the graphene layer.

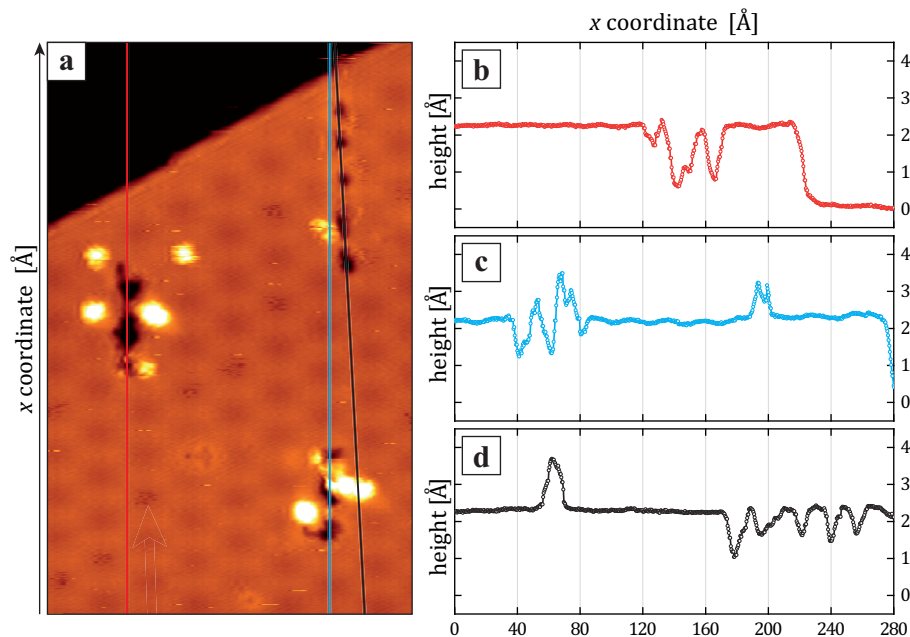


Figure 9.2: Analysis of the Defect Morphology. (a) STM image of the fully graphene covered Ir(111) surface after room temperature irradiation with 5 keV Xe⁺ ions at 75° off normal, fluence $F = 0.8 \times 10^{-4}$ MLE [cf. Figure 9.1(a)]. Image width: 150 Å; Imaging parameters: $U = 12$ mV, $I = 0.9$ nA. (b-d) Line profiles along the prominent defect patterns visible in (a). The locations of the profiles are indicated by colored lines. The profiles read from bottom ($x = 0$ Å) to top ($x = 280$ Å).

To understand the damage formation in detail and to find the appropriate interpretation of the STM images, we carry out atomistic simulations at the classical MD level of approximation, as described in Section 8.4. A total of 300 simulations are run, where Xe ions with a kinetic energy of 5 keV impact the target at 75° with respect to the surface normal along the close-packed $[1\bar{1}0]_{\text{Ir}}$ direction, identical to the experimental setup. The impact points are randomly chosen in the simulated supercell.

An example of the irradiation simulations is presented in Figure 9.1(b) which shows a time-lapse side view of an impact that caused the formation of $N = 4$ holes and extends over a length of $l = 104$ Å. The image illustrates the Xe-ion path (impinging from the left) with red spheres at time intervals of $\Delta t = 2$ fs, revealing an oscillatory motion at the graphene/metal interface: The ion first penetrates the graphene layer after which it is repeatedly reflected at the metal surface and the carbon sheet. The impacts on graphene result in carbon sputtering, causing a track of holes in the graphene layer, clearly visible

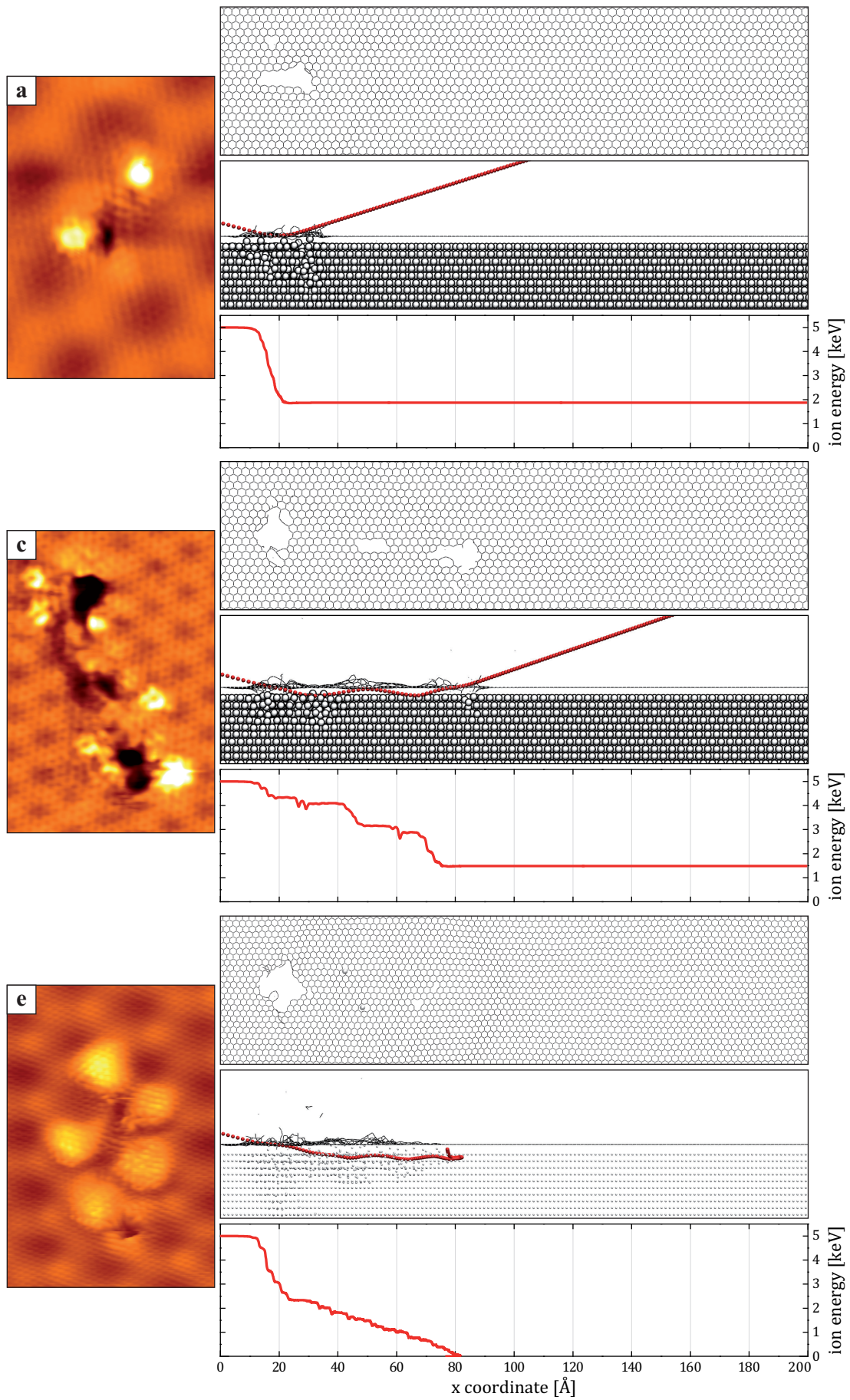
in the top view of the last frame of the simulation [Figure 9.1(c)]. The simulated and the experimental impact patterns show qualitative agreement which justifies our assumption that the depressions observed in experiment are indeed holes in the graphene layer. As is obvious from the plot in Figure 9.1(d), the Xe ion loses remarkably more energy in the encounter of graphene as compared with the collisional contact with the metal surface. This difference originates from a much larger ion to target atom mass ratio for Xe to graphene compared with Xe to the metal substrate.

The guided motion of the ion in the interface region, in the following referred to as *interface channeling*, is analogous to subsurface channeling (cf. Section 7.3) observed earlier for the case of pristine crystal surfaces [173, 212]: For the given ion energy and angle, the projectile penetrates the topmost crystal layer and is guided in between this layer and the one underneath parallel to the surface. Consequently the ion is trapped between the layers until it can dechannel after a comparably unlikely scattering event. Our experiments reveal that such a channeling process is also possible at the interface of two different materials.

Pattern Diversity

As the scattering process and thereby the entire interface channeling event is of stochastic nature, we can easily understand the manifold structures and inhomogeneity of the defect patterns shown in Figure 9.1(a). In the next step we now have a closer look on individual experimentally observed defect patterns and assign them to single impact events obtained by MD simulations, see Figure 9.3.

In (a) the defect consists of a single hole in the graphene sheet (the nature of the surrounding protrusions is still under discussion and will be examined in Section 9.3). According to the MD simulation data, this pattern can be attributed to a reflection of the impinging ion at the graphene sheet upon first impact. Consequently, the energy plot of the ion shows a single drop and the particle escapes into vacuum with a remaining kinetic energy of 2 keV. Note that a single hole might also be attributed to ion implantation into the bulk upon first impact. As the destination of the ion cannot be determined in STM we are unable to distinguish these two cases from experimental data. Hence, for all events discussed in the following it might as well be possible that the ion either is implanted or comes to rest at the interface or is able to escape into vacuum. The defect pattern shown in (b) features two holes, which can be explained by a trajectory in which the impinging ion is able to penetrate the graphene layer, gets reflected on the metal substrate and escapes



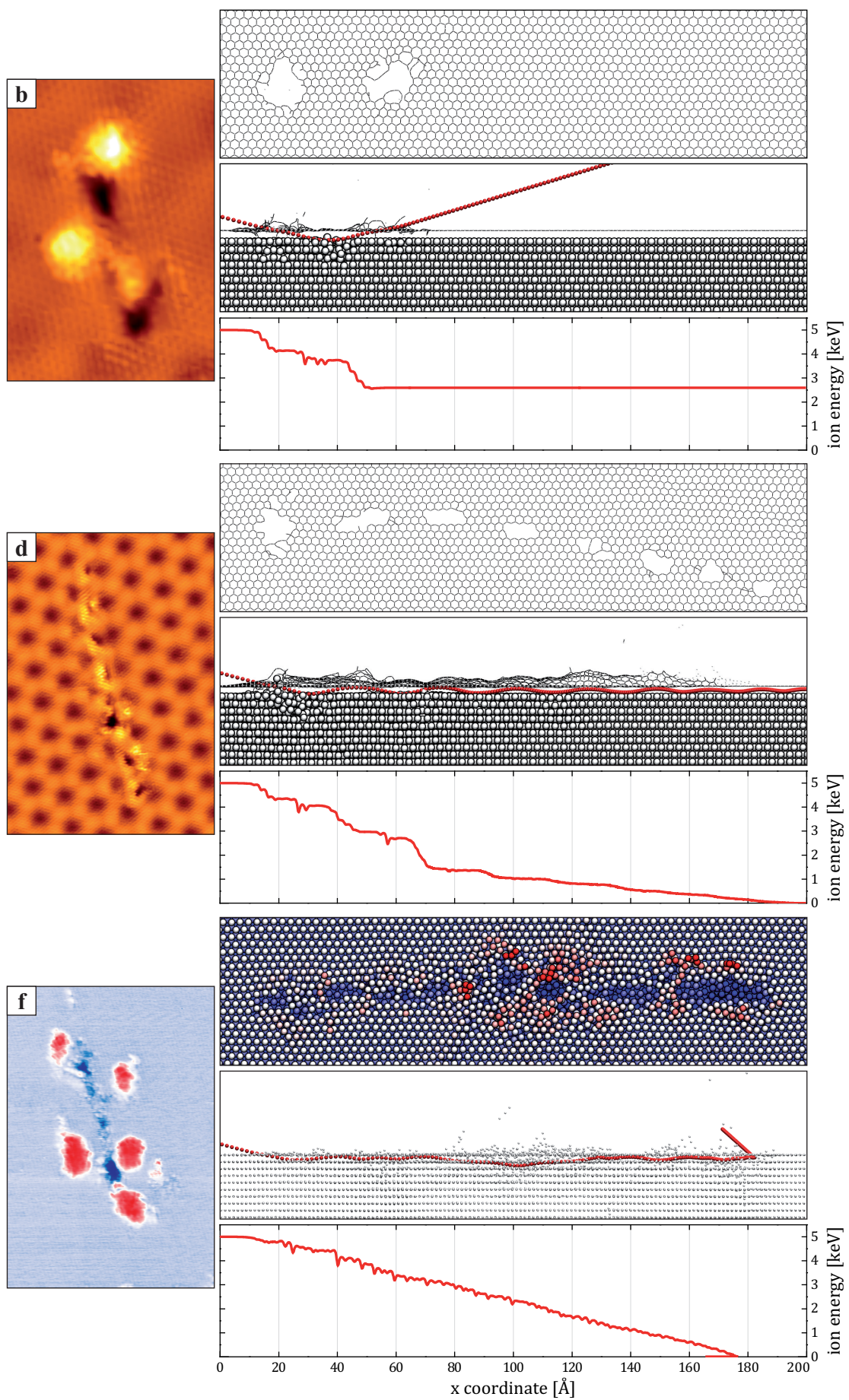


Figure 9.3: Pattern Diversity (Previous Two Pages).

(a-e) Experimentally observed defect patterns created by single ion impacts on a fully graphene covered Ir(111) surface together with their corresponding MD simulation events (top view, side view, evolution of ion energy; image details as in Figure 9.1). In (c) the graphene layer shows a rotational misalignment to the iridium substrate of approximately 11° which results in a $(4 \times 4)_{\text{Gr}}$ moiré unit cell. (f) Experimentally observed surface defect created by a single ion impact on a clean Ir(111) surface. In the top view of the respective MD simulation event the metal atoms are color coded according to their elevation (blue = low, red = high). Image width: (a-c) 60 Å, (d) 160 Å, (e) 80 Å, (f) 135 Å; Imaging parameters: (a) $U = 280$ mV, $I = 2.7$ nA, (b) $U = 100$ mV, $I = 11.0$ nA, (c) $U = 90$ mV, $I = 1.7$ nA, (d) $U = 12$ mV, $I = 11.0$ nA, (e) $U = 25$ mV, $I = 0.7$ nA, (f) $U = 120$ mV, $I = 14.0$ nA.

into vacuum after hitting the graphene layer from below. Note that the kinetic energy of the ion after the entire scattering process is comparable to (a). Following this, elongated patterns can be attributed to multiple reflection events at both layers, see Figure 9.3(c) for a three-hole event and Figure 9.1(b-d) for a pattern consisting of four holes (simulation data only). In case the ion is not able to escape into vacuum, Figure 9.3(d), it will come to rest at the interface with all kinetic energy transferred to the target material.

In addition to interface channeling we also observe subsurface channeling events. An example of this process can be seen in Figure 9.3(e), where the Xe ion is able to enter the topmost crystal layer of the metal substrate. It is evident that the defect pattern differs from the case without subsurface channeling: Mainly one impact hole is visible accompanied by some minor damage in the graphene layer due to sputtered metal atoms, whereas the amount of protrusions is strongly increased. Our experiments reveal subsurface channeling also for the bare metal substrate [Figure 9.3(f)]. As known from Pt(111), the Xe ion effectively sputters the surface atoms from below and causes the formation of a quasi-continuous surface trench, surrounded by adatom clusters. [173, 174] Note that subsurface channeling is less frequently observed for a graphene covered surface than for the bare metal as a result of lateral deflection of the impinging ion at the graphene sheet.

As discussed above, the energy loss of the Xe ion is much larger encountering the graphene sheet than for hitting the metal substrate, in agreement with formula 7.4. In fact, the energy loss of approximately $100 \text{ eV}/\text{\AA}$ observed for reflection on the graphene sheet is almost as large as for an ion hitting bulk graphite in a random direction [213]. However, for a channeling event, which is mainly governed by small angle scattering events, one expects the energy loss to be much smaller than for the bulk. The energy loss during reflection on the iridium substrate is in the range of $10 \text{ eV}/\text{\AA}$, which agrees with the classical channeling model (bulk Ir: $\Delta E/\Delta x \approx 200 \text{ eV}/\text{\AA}$ [213]). We attribute this peculiarity of graphene reflection to the factual geometry of the scattering event. That is, the ion encounters a much denser arrangement of carbon atoms in its traveling direction, when compared to the spacing of different layers in a graphite crystal. Moreover, the overlap of the shadow cones in the graphene layer is much smaller than for the metal substrate due to the low mass of the carbon atoms. This results in smaller impact parameters and thereby an increase of the transferred energy. While the overlap is still sufficient to invert the z component of the projectile momentum, we are close to the limit of the channeling regime for the graphene layer. Note that, once the ion is able to enter the topmost crystal layer, the energy loss per unit length is almost continuous. That is because the channel created by the shadow cones in the metal bulk is much more narrow [125] and with this the small angle scattering events are more uniform.

The events shown here clearly demonstrate the overall agreement between the experimentally observed defect patterns and the simulated data. This validates our model of interface and subsurface channeling for grazing incidence ion bombardment of Gr/Ir(111). The depressions can be identified as being holes in the carbon layer.

Quantitative Analysis

For quantitative analysis several values are defined and evaluated for both the experimental and simulation data set. These are:

- The number of holes N , characterized by separately identified depressions,
- the distance d between subsequent holes,
- the length l of the damage trail, which is measured from the beginning of the first hole up to the ending of the last one,
- and the azimuthal deflection α of the entire ion trail with respect to the $[11\bar{2}0]_{\text{Gr}}$ direction of the graphene lattice, i.e. the direction of the impinging ion.

The statistical evaluation leads to distinct data sets for each quantity according to the evaluation of experimental and simulation data. For each of these quantities a histogram is provided in Figure 9.4 (Note, that we do not give a histogram of the hole distance d , as a different statistical base was used in that particular analysis).

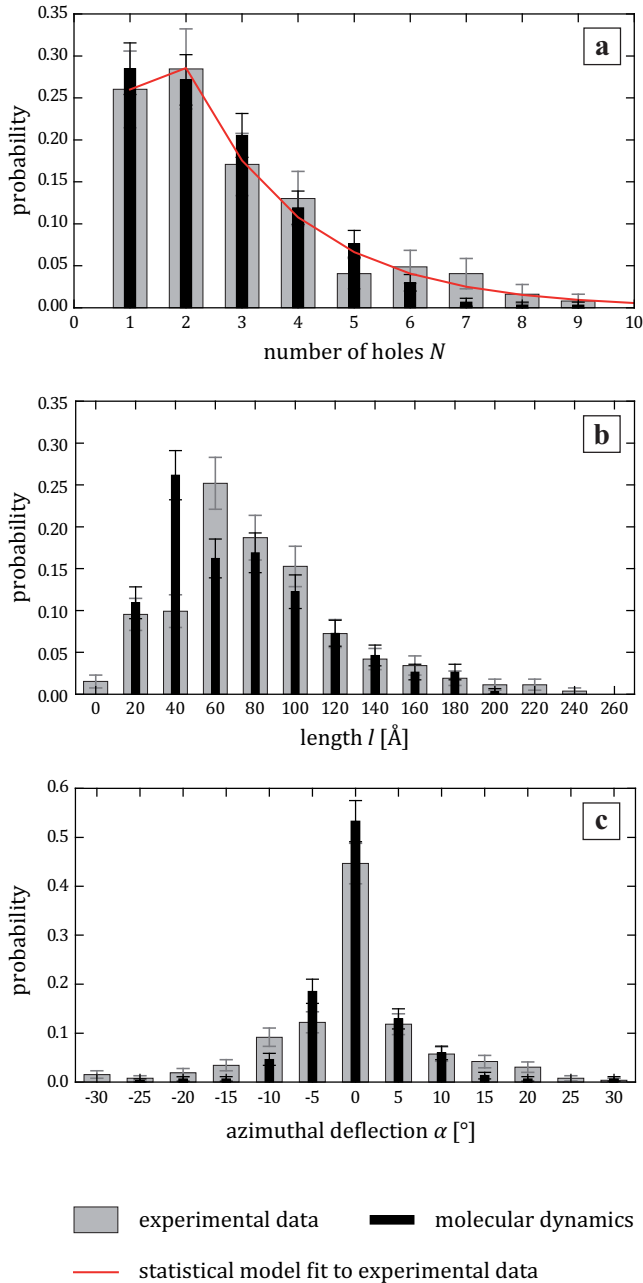


Figure 9.4: Statistical Evaluation of the Defect Patterns.

Histograms of the (a) number of holes N , (b) length l , and (c) azimuthal deflection α of the damage trail, as described in the text. Experimental data is shown in grey bars, results obtained for the MD simulation data set is shown in black. In (a) a statistical model was applied to approximate the experimental data (cf. Figure 9.5, for details see text).

For the experimentally determined number of holes [grey bars in Figure 9.4(a)] we find a dominance for the quantities one and two which translate into single reflection ion trails. The distribution decreases rapidly for larger numbers, with a maximum of nine holes, $N_{\max}(\text{exp}) = 9$. While this drop is less developed in the equivalent analysis carried out on

the basis of MD simulation data [black bars in Figure 9.4(a), $N_{\max}(\text{sim}) = 9$], the two data sets match within the error bars. Note that the analysis was carried out independently without any fitting of the respective data.

The evaluation of the defect pattern length l is depicted in Figure 9.4(b). The histogram (bin width 20 \AA) shows a broad distribution in the range of $50 - 60 \text{ \AA}$. While we observe damage trails with $l \geq 200 \text{ \AA}$ in both experiment and simulation data (note that the length of the simulation cell is limited to 220 \AA with periodic boundary conditions), events with a length of more than 130 \AA are rare. This continuous decrease for extended damage trails shows a great accordance between experiment and simulation and its occurrence is in line with the evaluation of the number of holes seen previously. Note that the determination of the length for events with $N = 1$ strongly depends on the tip state which causes large deviations between the experimental and the simulation data set toward zero extent.

The evaluation of the azimuthal deflection α of the ion trail with respect to the direction of the impinging ions is depicted in Figure 9.4(c). The histogram (bin width 5°) shows a predominance of events with $\alpha = 0^\circ$ and steep flanks toward higher values. Note that this imbalance can be attributed to single hole events which were assumed to have zero deflection as a deviation was not evaluable. Despite the rapid decrease in probability for large angular deflection elongated events with $\alpha > 30^\circ$ have been observed. The distribution is slightly wider for the experimental data compared to the MD simulation data set.

The accordance between experiment and simulation already indicated in the comparison of individual damage patterns is quantitatively verified in this statistical comparison.

Based on the above findings we now aim at giving a rough approximation of the hole distribution as derived from the experimental data. For this we developed a simple statistical model which will be discussed in the following:

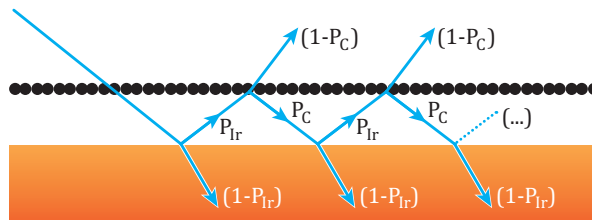


Figure 9.5: Statistical Model. Sketch of an ion impinging on the graphene/metal surface to illustrate the reflection probabilities on the metal substrate P_{Ir} and the graphene sheet P_{Gr} involved in the statistical approximation.

We assume that the ion motion is determined by two probabilities: The probability, that an impinging ion is reflected at the iridium surface P_{Ir} and the probability for ion reflection off the graphene layer from below P_{Gr} , as schematically drawn in Figure 9.5. Each encounter of the graphene sheet will cause hole formation, in fair agreement with the MD simulation data (see Figure 9.3). The probability for the ion to penetrate the graphene sheet upon first impact is assumed to 100%. Thereby, a single hole is achieved only by direct ion implantation into the bulk: $P(N = 1) = (1 - P_{\text{Ir}})$. Note that this assumption is in line with the discussion of the defect patterns presented in Section 9.1. The probabilities for two or more holes can be derived from this model directly:

$$\begin{aligned}
 P(1) &= 1 - P_{\text{Ir}} \\
 P(2) &= P_{\text{Ir}}(1 - P_{\text{Gr}}) + P_{\text{Ir}}P_{\text{Gr}}(1 - P_{\text{Ir}}) = P_{\text{Ir}}(1 - P_{\text{Ir}}P_{\text{Gr}}) \\
 P(3) &= P_{\text{Ir}}P_{\text{Gr}}P_{\text{Ir}}(1 - P_{\text{Gr}}) + P_{\text{Ir}}P_{\text{Gr}}P_{\text{Ir}}P_{\text{Gr}}(1 - P_{\text{Ir}}) = P_{\text{Ir}}^2P_{\text{Gr}}(1 - P_{\text{Ir}}P_{\text{Gr}}) \\
 &\dots \\
 \Rightarrow P(N) &= (P_{\text{Ir}}P_{\text{Gr}})^{N-2}[P_{\text{Ir}}(1 - P_{\text{Gr}}) + P_{\text{Ir}}P_{\text{Gr}}(1 - P_{\text{Ir}})] \quad \text{for } N > 1. \quad (9.1)
 \end{aligned}$$

This model is able to approximate the experimental data for $P_{\text{Gr}} = 0.83$ and $P_{\text{Ir}} = 0.74$ as can be seen in Figure 9.4(a). The criterion used for optimization was the least squares method. For the avoidance of doubt it should be emphasized that this approach is but a crude approximation of the underlying processes.

Due to the stochastic nature of damage formation by ion irradiation the quantities characterizing an individual pattern show a broad distribution around their mean values, see Table 9.1. The longest patterns observed have up to 9 depressions and extend over more than 200 Å. For a fraction of $f_{\text{prot}} = 0.81 \pm 0.02$ of patterns the holes are accompanied by protrusions of approximately 2 Å in height.

The averaged results of the simulations are presented along the experimental ones in Table 9.1, showing a good quantitative agreement without using any fitting parameters. We point out that the experimental and simulation values for the distance between two holes d is in line with a simple geometrical model of the oscillation period which yields $d = 2h \tan 75^\circ = 25.3 \text{ \AA}$, using $h = 3.38 \text{ \AA}$ [110] for the height of the graphene sheet above the metal.

Besides, supporting our interpretation of the experimental results, the MD simulations also offer insight to quantities not directly accessible in STM experiments: We find that 34 % of the ions are reflected into vacuum upon their first impact on graphene, leaving significant damage behind, as shown in Figure 9.3(a). 41 % of the penetrating ions (66 % in

Table 9.1: Quantitative Analysis of Defect Patterns. Comparison of experimental and simulation results for maximum (x_{\max}) and average values (\bar{x}) of several measures for the defect patterns induced by ion irradiation, along with their respective standard deviations (σ_x) and standard errors of the mean ($\sigma_{\bar{x}}$): Number of holes N , that can be associated with a single impact, distance between subsequent holes d , length l of the entire damage patterns defined as the distance between the first and the last hole of a chain, and angle α of the line joining the first and the last hole with respect to the close-packed $[11\bar{2}0]_{\text{Gr}}$ direction.

quantity		experiment				simulation			
x		\bar{x}	σ_x	$\sigma_{\bar{x}}$	x_{\max}	\bar{x}	σ_x	$\sigma_{\bar{x}}$	x_{\max}
N	number of holes	2.7	1.8	0.2	9	2.58	1.51	0.09	9
d	hole distance [nm]	2.3	0.9	–	–	3.09	1.15	0.05	–
l	channeling length [nm]	8.9	4.2	0.3	34.2	7.3	4.0	0.2	20.0
α	azimuthal deflection [deg]	1.3	8.9	0.6	44.7	0.2	6.4	0.4	37.2

total) end up between the graphene and the substrate, while 13.5% are buried in the metal and 45.5% escape into vacuum by penetrating the graphene a second time. Therefore, the probability for the ion to penetrate the graphene sheet from below is significant (22% per impact). In consequence, only an ion encountering a lucky streak can travel in the interface considerably further than average, explaining the broad distribution of the relevant quantities. Subsurface channeling occurs in only 20% of the impacts, as the Ir atoms form perfect strings with respect to the ion beam direction and possess wider shadow cones causing better overlap as compared to the C atoms.

The sputtering yield of metal atoms is decreased in the presence of graphene from $Y_{\text{sub}} = 8.3$ for the pristine surfaces to $Y_{\text{sub}} = 0.65$ (200 simulations on a Pt target without the graphene layer were conducted in order to obtain the former value). The sputtering yield for carbon is $Y_{\text{C}} = 17.0$. For the example shown in Figure 9.1, 27 carbon atoms but zero Pt atoms are sputtered. We also determined the Pt adatom yield by carrying out a subset of simulations over an extended time (20 ps). We then counted all atoms elevated by more than $0.5h$ above the metal surface as adatoms, where h is the interlayer spacing of Pt. The adatom yield determined this way is $Y_{\text{ad}} = 33$. It varies significantly between different impacts and is highest for the 19% of events where subsurface channeling takes place. The difficulty in giving an appropriate value for this quantity is reasoned by the aforementioned total simulation time of $t \approx 20$ ps. While this time span is sufficient to fully describe the ion motion and the scattering mechanism, the system is still far from

equilibrium. Consequently, the graphene sheet is still in motion and the metal adatoms have not yet formed stable clusters. This can easily be seen in Figure 9.6 showing two exemplary sputtering events. For both events two different frames are given, taken at fixed points in time: $t_1 = 1$ ps (left column) and $t_2 = 20$ ps (right column). Note that the first column figures correspond to the regular experiments presented above, while the latter ones illustrate the final sample state of extended simulation events which were used to determine the metal adatom yield. The view is along the close-packed $[1\bar{1}0]_{\text{Ir}}$ -direction of the substrate, i.e. in the direction of the ion beam, parallel to the surface.

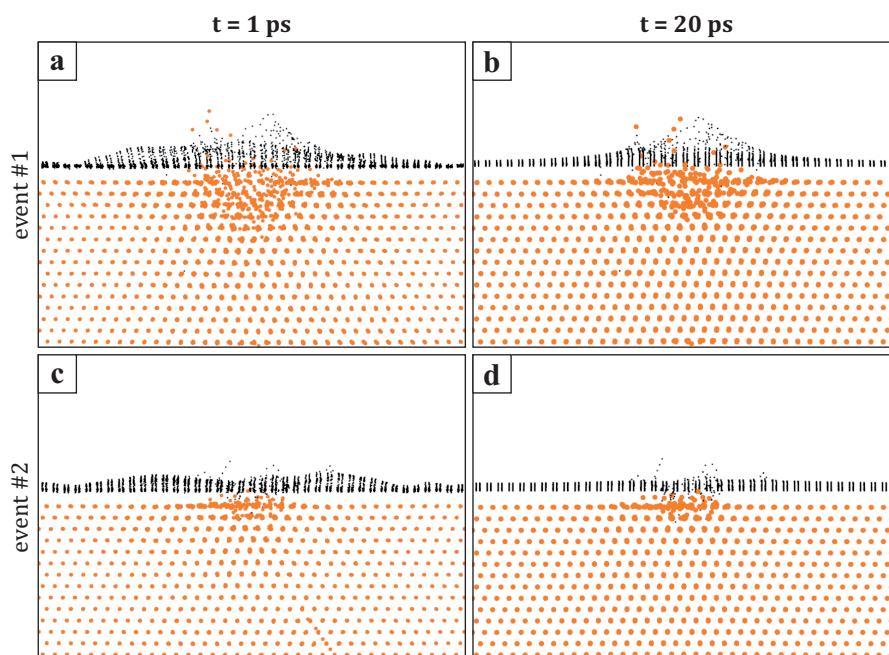


Figure 9.6: MD Simulation Endframe. Sample state after a total simulation time of $t = 1$ ps (a,c) and after further relaxation at $t = 20$ ps (b,d) for two different events. The view is along the close-packed $[1\bar{1}0]_{\text{Ir}}$ -direction of the iridium substrate. The ion is impinging from outside the paper plane.

Comparing the sample states for each event one can see that the graphene sheet is highly corrugated for $t = t_1$, while after $t_2 = 20$ ps it is much closer to a flat geometry. Thus, it has greatly benefitted from the increase of simulation time. Yet one can still make out individual strings and loops of carbon atoms sticking out of the surface towards the vacuum. As for the substrate one can witness the ongoing recrystallization of the topmost layers. Starting from a heavy amorphization at $t = t_1$, deeper crystal layers are almost entirely rebuild after $t_2 = 20$ ps. Nevertheless, the surface region is still heavily disturbed at all times accessible in the simulation. In particular, platinum atoms handing on top of the graphene sheet are bound to carbon atoms which represents a *local* energy minimum.

9.2 Variation of Ion Energy and Species

Based on the findings of 5 keV Xe⁺ bombardment of graphene grown on Ir(111), we now have a qualitative and quantitative understanding on the damage patterns and the relevant formation mechanisms. We now go a step further and ask whether we can control the ion induced defect structure via tuning the bombardment parameters.

In our first approach we study the dependence of the surface defect patterns on the projectile mass. For this, we exposed a fully graphene covered Ir(111) surface to different ion species while keeping the energy and the fluence at a fixed value: $E = 5$ keV, $F = 3.2 \times 10^{-3}$ MLE. To avoid secondary effects due to chemical interaction of the projectile and the target atoms this study is still restricted to noble gases. The resulting sample morphologies after bombardment are shown in Figures 9.7(a-d). All experiments have been analyzed with respect to the density of defect patterns Θ_{pat} and to the maximum channeling length l_{max} (The error bar in determination of the channeling length is approximated to 0.8 nm for all measurements due to limitations of experimental resolution on large-scale images).

While for both argon and xenon the sample morphology shows the previously introduced characteristics of interface channeling [cf. central defect in Figure 9.7(d) and Figure 9.3(b)] the defect pattern appearance changes rapidly with low projectile mass. For both argon and xenon we do observe a broad distribution of the channeling length with a maximum value of $l_{\text{max}} = 22.5(35.0)$ nm for argon (xenon) bombardment [Figure 9.7(e)]. Following neon bombardment [Figure 9.7(b)], the prominent defect pattern consists of pairs of holes only. Consequently, the maximum channeling length is further reduced to $l_{\text{max}} = 13.2$ nm. It should be noted that we did observe only two events with $l > 5$ nm in total. In case of helium bombardment the overall defect morphology has changed to single holes, see Figure 9.7(a), and the maximum channeling length has dropped to zero. Along with that we observe a reduction of the pattern density ($\Theta_{\text{pat}} = (2.1 \pm 0.4) \times 10^{-3}$ MLE) of almost 30 % when compared to xenon bombardment ($\Theta_{\text{pat}} = (3.28 \pm 0.22) \times 10^{-3}$ MLE) [Figure 9.7(e)].

Secondly, we study the dependence of the surface defect patterns on the projectile energy. Based on our experience with xenon bombardment, we separately exposed a fully graphene covered Ir(111) surface to Xe⁺ ions with varying projectile energy $E = 0.5 \dots 15$ keV. Again, the fluence was kept at $F = 3.2 \times 10^{-3}$ MLE. The resulting sample morphologies after bombardment are shown in Figures 9.8(a-d). The ion energy is depicted in the images.

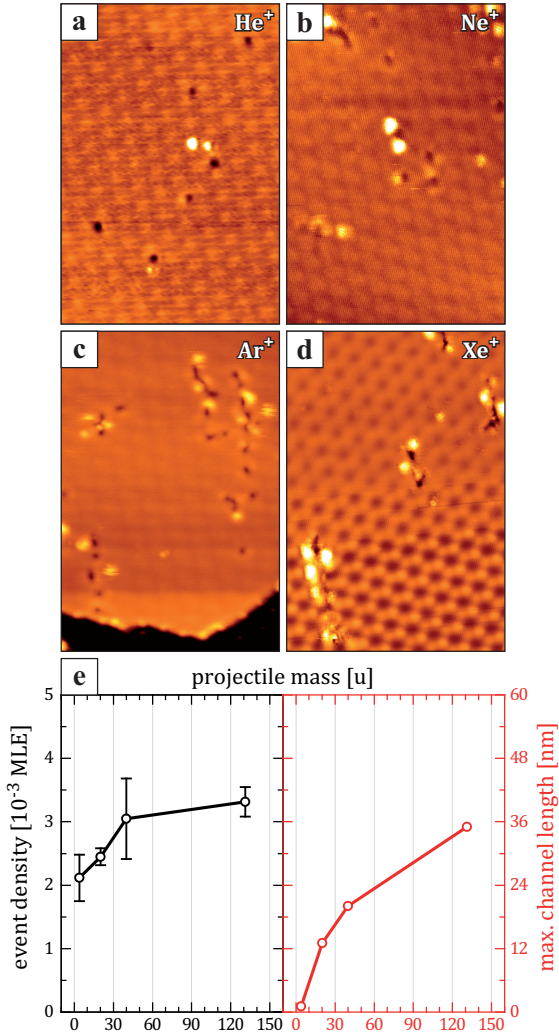


Figure 9.7: Dependence of the Defect Patterns on Ion Mass. STM topographs after $F = 0.0032$ MLE of $E = 5$ keV (a) He⁺, (b) Ne⁺, (c) Ar⁺, (d) Xe⁺ ions impinging the surface 75° off normal. (e) Experimental evaluation of the defect density and maximum channeling lengths plotted against the projectile mass. All image widths: 235 Å; Imaging parameters: (a) $U = 970$ mV, $I = 2.0$ nA, (b) $U = 125$ mV, $I = 2.6$ nA, (c) $U = 1000$ mV, $I = 1.6$ nA, (d) $U = 100$ mV, $I = 1.1$ nA.

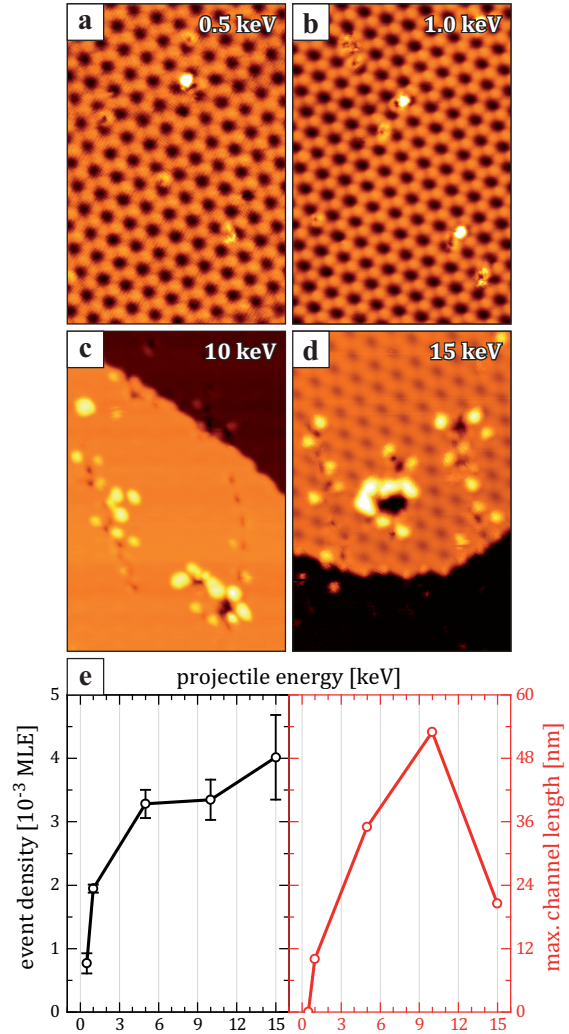


Figure 9.8: Dependence of the Defect Patterns on Ion Energy. STM topographs after $F = 0.0032$ MLE Xe⁺ ions with primary energy E of (a) 0.5 keV, (b) 1.0 keV, (c) 10.0 keV and (d) 15.0 keV impinging the surface 75° off normal. (e) Experimental evaluation of the defect density and maximum channeling lengths plotted against the projectile energy. All image widths: 235 Å; Imaging parameters: (a) $U = 95$ mV, $I = 4.1$ nA, (b) $U = 325$ mV, $I = 2.5$ nA, (c) $U = 8700$ mV, $I = 1.7$ nA, (d) $U = 100$ mV, $I = 5.3$ nA.

For the 5 keV experiment, the reader is referred to Figure 9.7(d). All experiments have been analyzed for the density of defect patterns Θ_{pat} and for the maximum channeling length l_{max} , as shown in Figure 9.8(e).

In the sub-keV regime [Figure 9.8(a)] the defect morphology is dominated by single holes and even smaller lattice distortions in the graphene layer. We do not observe channeling ($l_{\text{max}} = 0$ nm) and the pattern density is much lower than the actual ion fluence, $\Theta_{\text{pat}} = (0.76 \pm 0.16) \times 10^{-3}$ MLE. Increasing the projectile energy to 1 keV [Figure 9.8(b)] leaves the overall defect morphology unchanged. However we do observe paired holes and some elongated defect patterns ($l_{\text{max}} = 11$ nm). Remarkably, the pattern density is increased by 240 %, $\Theta_{\text{pat}} = (1.94 \pm 0.06) \times 10^{-3}$ MLE, yet still lower than the ion fluence. This value is reached for 5 keV ion bombardment, $\Theta_{\text{pat}} = (3.28 \pm 0.22) \times 10^{-3}$ MLE, and does not increase significantly when increasing the projectile energy, see Figure 9.8(e). For 15 keV bombardment the complexity of the defect patterns is highly increased, which can be seen in the example of extended holes [center of Figure 9.8(c)] and expresses in a large error bar of the determined defect density. Contrary, we do observe a strong variation of the maximum channeling length for 5, 10 and 15 keV, respectively, with a maximum of $l_{\text{max}}(10 \text{ keV}) = 53.0$ nm.

The energy dependence of pattern formation can be understood by having a closer look on the scattering cross-sections. As detailed in Section 7.1 the shadow cone radius R_{sc} at a distance d from the target atom can be calculated via

$$R_{\text{sc}} = 2\sqrt{\frac{Z_1 Z_2 e^2}{4\pi\epsilon_0 E}} \cdot d.$$

Hence, for low ion energies the shadow cones largely overlap and the projectile cannot enter the channel through the graphene layer, i.e. it faces reflection. Consequently, we do observe single holes only which we can attribute to individual impact points. The reflection probability decreases for higher energies as the shadow cone radius decreases and the ion may penetrate the graphene layer upon first impact. Losing a severe amount of energy in this process, the particle is trapped at the interface. From $E > 1$ keV on a channeling motion at the interface develops as introduced above. For all these cases we do observe a broad distribution of the characteristic measures. The maximum channeling length increases steadily with a broad maximum in the range of 4 to 14 keV. However, for 15 keV ions we notice a rapid decrease of l_{max} which we attribute to the onset of bulk channeling, i.e. the projectile is able to deeply enter the bulk in between crystal planes of higher order. As side-effects like subsurface and/or carbon sputtering (via

sputtered Ir atoms) are strongly enhanced for higher projectile energies, this also explains the increasing complexity of and large scale holes in the defect patterns.

When it comes to mass dependence a similar approach can be taken as the deposited energy directly relates to the mass ratio of the projectile and the target atom (see Formula 7.3). Moreover, we expect a drastic increase of channeling events in deeper layers for the light elements and, ultimately, ion implantation into the bulk. Thereby, helium and neon particles do create finite size defects only, whereas for argon and xenon the experimental parameters allow the evolution of ion trails via interface channeling.

9.3 Thermal Stability

Hitherto, we were able to identify the depressions as holes in the carbon layer. However, their exact atomic structure cannot be determined due to the complexity of the resulting morphologies. Furthermore, the origin of the protrusions has so far not been solved. In view of the significant adatom yield found in the MD simulations, they are likely to be aggregates of Ir adatoms similar to what has been found for subsurface channeling on Pt(111) [173], which are buried beneath the graphene sheet in our system. Notwithstanding, a priori we cannot exclude that the bright protrusions result from an enhanced density of states due to dangling carbon bonds [48, 49] or from rearranged carbon atoms. In order to clarify these issues, we investigate the thermal stability of the defect patterns next.

We gradually heat an irradiated sample in steps of 150 K (30 s at each temperature). The resulting topographies at selected temperatures are shown in Figure 9.9(a)-(c). The full annealing data set is provided in the diagram of Figure 9.10, showing the coverage of defect patterns Θ_{pat} (black open circles) as well as the fraction of defect patterns accompanied by protrusions f_{prot} (red closed circles) against annealing temperature T .

At room temperature [Figure 9.9(a)], protrusions are present in almost 80 % of the defect patterns. As can be seen in Figure 9.9(d), which shows the area marked in (a) in differential contrast, the graphene lattice is continuous across the protrusions indicating that they arise from the interface area below graphene. After annealing to 600 K, protrusions decrease in number while growing in size [Figure 9.9(g)]. They finally disappear at temperatures close to 750 K.

This annealing behavior is in line with the assumption that the protrusions are due to iridium adatom clusters produced by the ion impact and covered by the graphene sheet:

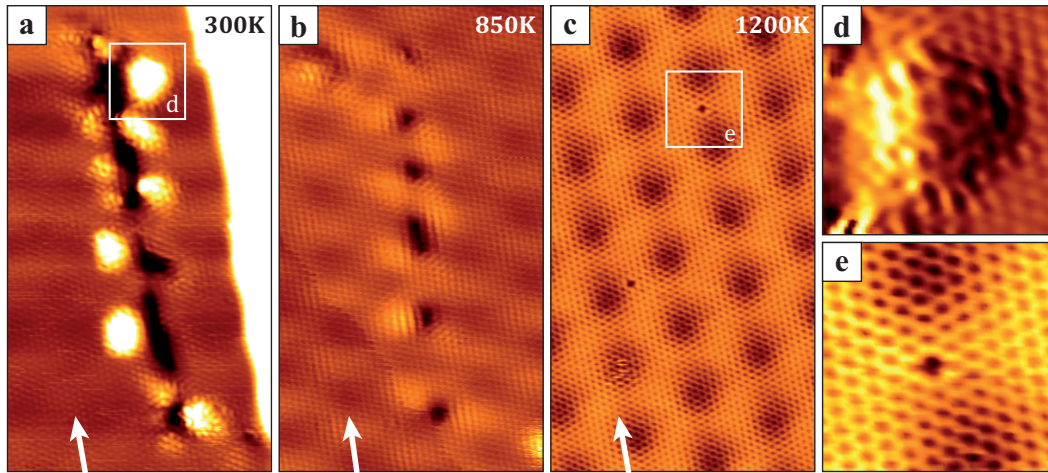


Figure 9.9: Thermal Stability of Defects I. (a) STM image of the graphene covered Ir(111) surface after $E = 5$ keV Xe^+ bombardment with $F = 0.8 \times 10^{-4}$ MLE, recorded at room temperature. A pre-existing substrate step is visible on the right hand side. (b,c) STM topographs after steps of 30 s annealing at $T = 850$ K and 1200 K, respectively [note that (a)-(c) are taken at different locations]. (d) Protrusion [position marked in (a)] in atomic resolution. The image is shown in differential contrast to enhance visibility. (e) Residual defect [position marked in (c)] in atomic resolution. Arrows in (a-c) are pointing along the direction of the impinging ions. Image width: (a-c) 90 \AA , (d,e) 26 \AA ; Imaging parameters: (a,d) $U = 180$ mV, $I = 2.2$ nA, (b) $U = 130$ mV, $I = 1.1$ nA, (c,e) $U = 130$ mV, $I = 5.0$ nA.

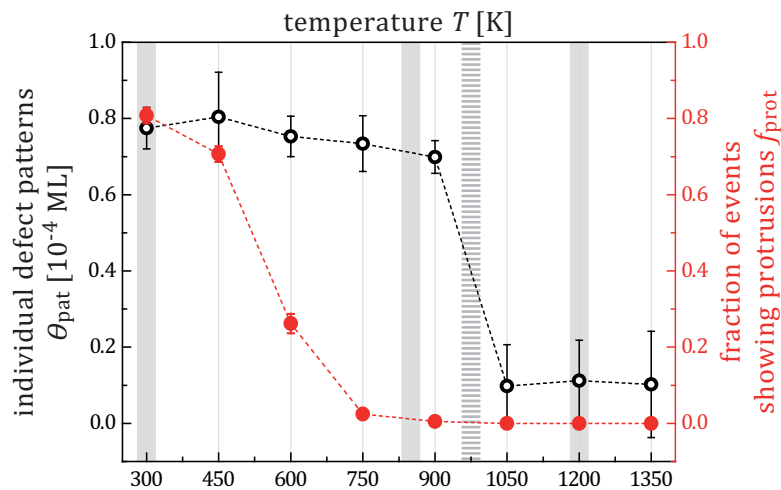


Figure 9.10: Thermal Stability of Defects II. Coverage of defect patterns Θ_{pat} (black open circles) and fraction of patterns showing protrusions f_{prot} (red closed circles) plotted against the annealing temperature T . Temperatures corresponding to (a-c) are shaded gray. The dashed vertical line indicates the temperature of the transition from amorphous carbon to graphene (≈ 970 K[46]).

It is known that adatom clusters larger than $n = 4$ are immobile on a pristine Ir(111) surface at room temperature [214], i.e. the temperature during ion irradiation. We expect that this behaviour does not change drastically for the case of adatom clusters between the metal surface and the weakly interacting graphene sheet. Therefore, larger clusters formed either directly by the impact or by agglomeration of smaller clusters should remain stable during the irradiation experiment. In contrast, even rather large clusters ($n \leq 13$) become mobile at elevated temperatures around $T = 500$ K for the case of pristine iridium. [214] This is the same temperature range where the bright protrusions vanish in the experiment. Assuming that the presence of graphene has only a weak influence on this diffusion process, we can postulate the following mechanism: The clusters diffuse and recombine with the corresponding Ir surface vacancies, leading to their disappearance. Also our MD simulations predict the formation of adatoms at the interface. A remaining discrepancy is the fact that in the simulations the adatoms are mostly found along the ion track, whereas in experiment they are found next to it with a preference for the TOP-regions [see Figure 9.9(a)]. This can be explained by diffusion of adatoms to the pockets between graphene and the substrate in the TOP regions, which occurs at time scales beyond the reach of MD simulations. Note that for the simulation depicted in Figure 9.1(b-d) the adatom yield is low, as no subsurface channeling took place here. The alternative models for the nature of the bright protrusions mentioned above can now be excluded: Disordered, amorphous-like regions of carbon only transform into graphene at much higher temperatures (≈ 970 K [46]). Also unsaturated carbon bonds offer no sound explanation as the appearance of the protrusions are highly non-uniform, when compared to the modulation patterns observed by Ugeda *et al.* [48]. Furthermore, we often observe holes in the graphene layer without extended protrusions.

In contrast to the iridium adatom clusters, the vacancy clusters in the graphene sheet remain present at 850 K [Figure 9.9(b)]. However, their edges do not appear very sharp in STM, the holes rather have the shape of funnels reaching down towards the substrate. Finally, the holes also begin to disappear just around 970 K, which is close to the temperature of the transition from amorphous carbon to graphene [46]. Consequently, at this temperature single vacancies and small vacancy clusters are able to undergo large-scale diffusion. At the highest investigated temperatures [$T \geq 1200$ K, Figure 9.9(c)] the graphene layer appears to be entirely rebuilt on a large scale. Specifically, we do not observe larger vacancy islands as a result of defect agglomeration. A possible pathway to lower the energy of the system without the formation of large holes in the graphene is the edge dislocation climb mechanism recently observed by Warner *et al.* [43] under electron

irradiation of graphene. This process can start with a single vacancy which is transformed into a pair of neighboring, opposing edge dislocations. Note that an edge dislocation is a point defect for the case of a 2D material. These defects can be driven apart by dislocation climb upon the incorporation of further vacancies. The graphene lattice in between the dislocations is structurally coherent, but slightly tensile. This mechanism significantly reduces the defect density and leaves very little residual damage behind, in line with our observations: An example of such a defect (most probably a double vacancy) is given in Figure 9.9(e). The remaining small defect density can not be estimated to great accuracy, resulting in uncertainties for the case of high temperatures.

By means of our annealing series we now have a first understanding of the atomic structure of defects. Whereas the protrusions are caused by iridium adatom clusters buried under the graphene layer, the holes correspond to vacancies in the graphene sheet. While their atomic arrangement is still point of discussion thermal treatment has proven a suitable instrument for isolating defects in the graphene layer while suppressing damage in the iridium substrate. Thereby, we can study the structure of the defective graphene sheet and investigate its interaction with the substrate. As discussed in Section 7.4 little is known about this topic which we will address in the following.

9.4 Structure of Defects

In this section the atomic structure of defects in a supported graphene layer is studied. For this purpose we exposed the a fully graphene covered Ir(111) sample to 5 keV Xe ions at room temperature, $F = 1 \times 10^{-4}$ MLE, and subsequently annealed the system for 30 s to 850 K, see Figure 9.11.

As we could show in the previous section, this preparation guarantees complete annealing of the metal adatom clusters at the interface. Thereby we can study the arrangement of carbon vacancies and their interaction with the Ir substrate on an atomic level without interfering damage in the substrate created during ion bombardment.

Figure 9.11(a) shows a single ion impact after thermal treatment. The moiré superstructure is visible (reverse contrast) as well as the depressions associated with the graphene vacancies. The characteristic damage pattern associated to the ion trail can still be identified, indicating that only the substrate has annealed whereas graphene vacancy agglomeration has not been activated. Interestingly, the edges of the carbon vacancies are imaged smooth in STM and give rise to a funnel-like shape. This is shown for an exemplary defect in the magnified view of Figure 9.11(b). Superimposing a honeycomb lattice

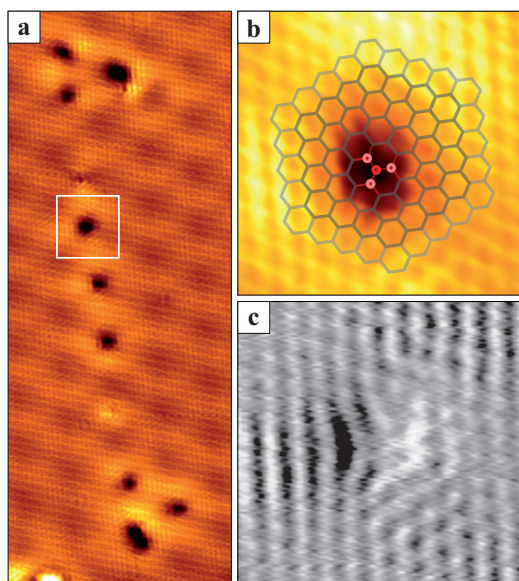


Figure 9.11: Structure of the Defects I. (a) STM topograph of a single 5 keV Xe^+ ion impact on Gr/Ir(111) after 30 s annealing to 850 K. (b) Magnified view of the area highlighted in (a) superimposed by a graphene lattice. The depression covers one to four carbon lattice sites as indicated by colored circles. (c) Differential contrast image on the same area. Image width: (a) 110 Å, (b,c) 25 Å; Imaging parameters: (a-c) $U = 135$ mV, $I = 1.1$ nA.

onto the atomically resolved defect we can verify that only few atoms are missing in the graphene network. This is further substantiated by the differentiated image in Figure 9.11(c) which accentuates the atomic rows. It appears that the carbon atoms rearrange and bend downward to the metal substrate. While this indicates the formation of chemical bonds between the two species, we still have to proof this assumption. Note that the exact atomic structure of the defects may vary. However, the overall funnel-like shape following thermal treatment is a characteristic feature of all defects, as illustrated in the overview of Figure 9.12. Interestingly, several defects show a weak height modulation pattern in their vicinity, cf. [48].

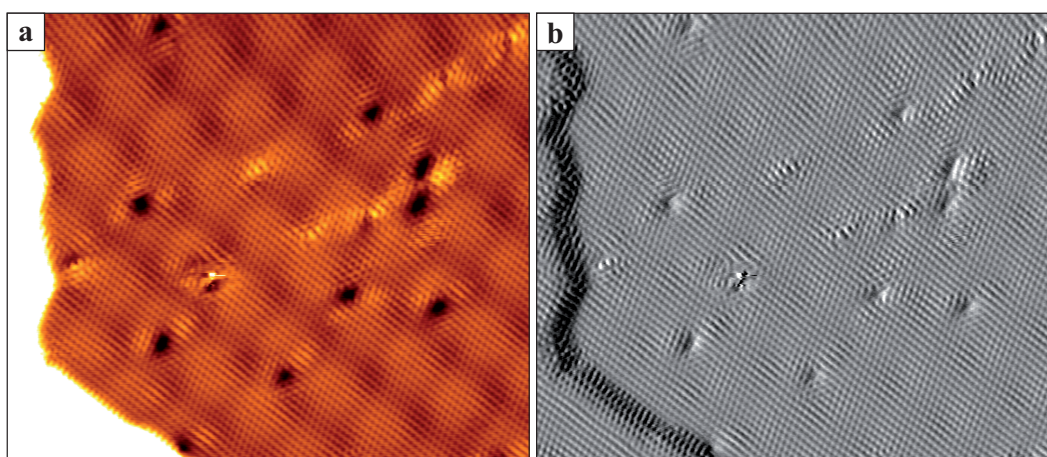


Figure 9.12: Structure of the Defects II. (a) STM topograph of 5 keV Xe^+ ion impacts on Gr/Ir(111) after 30 s annealing to 900 K. (b) Differential contrast image on the same area. Image width: 180 Å; Imaging parameters: $U = 48$ mV, $I = 2.1$ nA.

Scanning Tunneling Spectroscopy

Since the presence of unsaturated bonds can often be verified by the detection of a peak in the density of states at the Fermi energy [48, 50], we perform scanning tunneling spectroscopy (STS) measurements on the funnel-shaped holes [Figure 9.13(a)].

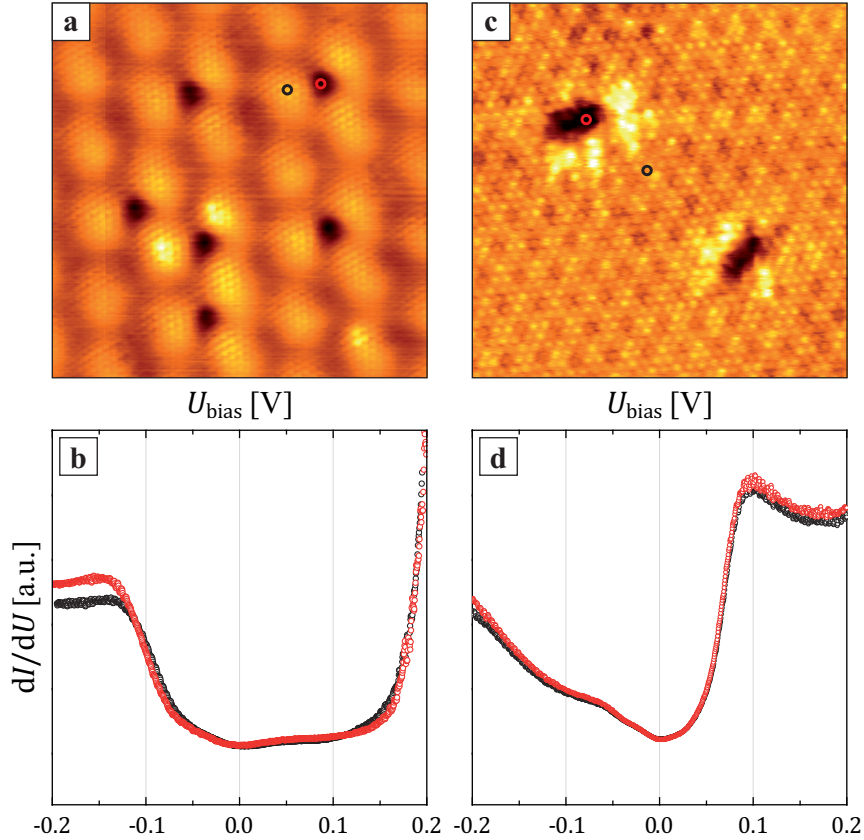


Figure 9.13: Electronic Structure of the Defects. (a) STM topographs of a graphene covered Ir(111) surface after 250 eV Ne^+ irradiation at normal incidence and subsequent annealing to 850 K. Several funnel-shaped defects are visible. (b) Scanning tunneling spectroscopy measurement on (red line) and next to (black line) a hole in the graphene sheet as indicated in the topographic image. (c,d) Same as (a,b) but for a different rotational graphene domain. Image width: (a) 118 Å, (c) 74 Å; Imaging parameters: (a) $U = 475$ mV, $I = 0.5$ nA, (c) $U = 51$ mV, $I = 1.1$ nA.

Note that the ion bombardment has been performed under different experimental conditions than before, as stated in the experimental section. However, the resulting morphologies of individual vacancy sites are almost identical, cf. Figures 9.13(a) and 9.11(a). The spectra recorded on intact graphene (black line) and at the vacancy site (red line) are similar and show a typical shape for graphene on metal surfaces. Specifically, we observe no peak close to the Fermi level ($U_{\text{bias}} = 0$ V) which proves the absence of dangling bonds

in our system, in contrast to previous experiments for Gr/Pt(111) [49]. The identical shape of the spectra is explained by the finite size of the tip, collecting density of states from the surrounding graphene even though located above the vacancy. These findings of funnel-shaped vacancies and the absence of dangling bonds hold for holes of all sizes and shapes - even for different rotational graphene domains as shown in Figure 9.13(c,d).

Density Functional Theory Calculations

In order to get a microscopic insight into the atomic structure of the vacancy-type defects, we carried out first-principles simulations using DFT as introduced in Section 8.5 of the experimental part. All calculations are carried out for a 200-atom 10×10 graphene supercell on top of a 9×9 Ir(111) slab containing 243 atoms. For the pristine system, we receive essentially the same results as in Reference [110].

An exemplary tetravacancy type defect is shown in Figure 9.14. Carbon atoms are colored blue, whereas iridium substrate atoms are shown in a gradient red/white/purple color scale according to their height.

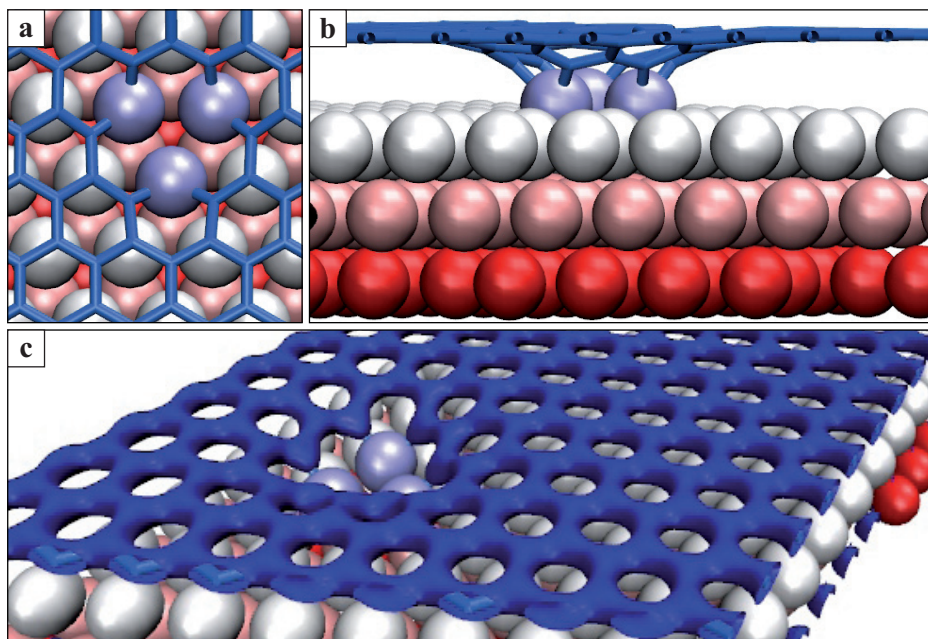


Figure 9.14: Calculated Structure of a Tetravacancy Defect. DFT calculation results for a tetravacancy type defect in iridium supported graphene. (a,b) Atomic model top and side view of the defect. Metal atoms are shown in a red/white/purple color scale according to their height. Carbon atoms are colored blue. (c) Three dimensional view of the simulated sample slab including the electron density of the graphene sheet.

In the side view it becomes evident that the dangling carbon bonds do not rearrange in plane, as expected from defects in a free-standing graphene layer (see Section 7.4). On the contrary, the dangling carbon bonds saturate by connecting with the metal surface underneath. In fact, the interaction between C atoms with dangling bonds and Ir atoms is so strong that the underlying Ir atom is essentially pulled out. This saturation of dangling bonds reasonably explains the funnel-like shape of the vacancies, cf. Figure 9.14, and the absence of localized states close to the Fermi level.

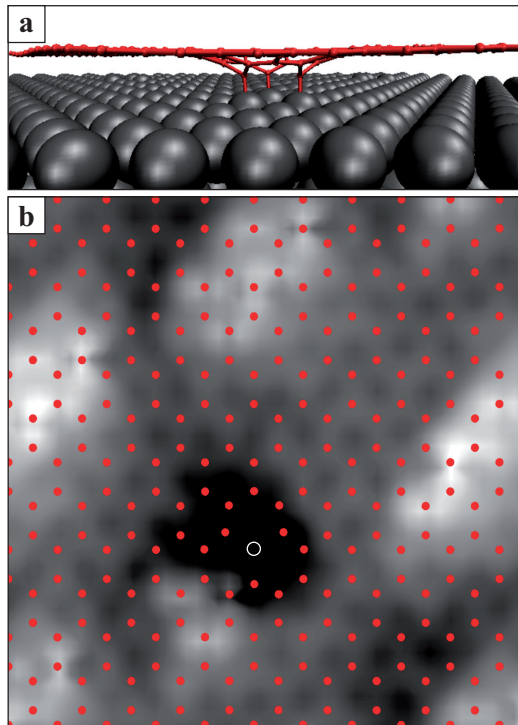


Figure 9.15: Simulated STM Image. Atomic model (a) and simulated STM image of a single vacancy defect in graphene on Ir(111). The red dots represent for the positions of the C atoms, and brighter/darker areas correspond to higher/lower elevation of the STM tip in constant current mode.

In order to allow for a better correspondence between the results of DFT calculations and experimental STM images, we simulated STM images for a representative example of a vacancy in graphene with dangling bond atoms connected to Ir atoms, see Figure 9.15. We stress that the Tersoff-Hamann formalism (the standard DFT-based approach to STM image simulations) cannot be employed due to the very nature of the system, as not only LDOS at the surface (electronic contribution), but also the tunneling matrix element between the tip and the atoms (topography contribution) should be taken into account. The tight binding approach used relies on many approximations, but is expected to give the qualitatively correct picture.

The simulated STM image for a single vacancy is presented in Figure 9.15(b), with an atomic model sideview shown in panel (a). The red dots represent the positions of the carbon atoms, whereas the white circle marks the vacancy site. The height information

(higher/lower elevation of the STM tip in the constant current mode) is given in greyscale. White areas correspond to an elevated position of the STM tip with respect to the sample originating from the electronic effects in the moiré pattern. It is evident that indeed the vacancy gives rise to a funnel-like depression in the STM image complementing the experimental images.

We calculated the equilibrium geometries as well as the formation energies of various vacancy configurations, Figure 9.16 and Table 9.2. It turned out that for the case of graphene/Ir(111) not only the atomic positions of the carbon atoms in the graphene sheet had to be taken into account but also the relative position with respect to the metal atoms underneath. To obtain representative results we studied several defect configurations corresponding to various positions of vacancies in the moiré pattern. As defined above, three prominent regions of the moiré pattern can be identified by correlating the position of the carbon hexagon with the atoms of the metal: The very similar, strongly bound HCP- and FCC-regions and the more weakly bound TOP regions. In the HCP-region, three carbon atoms of one graphene hexagon are found in a top site (HCP-top) and three in an fcc site (HCP-fcc). In a similar manner, other positions can be defined.

As it is evident from Table 9.2, for both single and tetra vacancies, the formation energy varies significantly with the position in the supercell. Single vacancies always prefer to be on top of an Ir atom. For the optimum positions, the energy is lower in the HCP/FCC regions, as compared to TOP regions. The reason for this is obvious from geometrical considerations: The vacancy formation energy in the TOP regions is higher, as there is no good match between the underlying Ir atoms and the C atoms with dangling bonds. Also note that the formation energy of tetra vacancies is only slightly higher than for single vacancies, indicating that vacancies should cluster under heating.

The findings elaborated in this chapter unfold the mechanisms behind defect formation by ion bombardment of graphene on Ir(111). We demonstrate that interface channeling as well as subsurface channeling play a key role in the defect creation mechanism for grazing incidence ions. It is shown that carbon sputtering is activated but simultaneously iridium sputtering is strongly reduced by the blanking graphene sheet, resulting in enhanced adatom production. These iridium substrate defects completely anneal after heating up to 750 K, whereas the resulting graphene defects are thermally stable beyond 900 K. All dangling carbon bonds saturate by connecting to the metal surface. Here, deviations in the formation energies can be found within the moiré cell.

This strongly varying potential landscape for vacancies opens a path for ion beam struc-

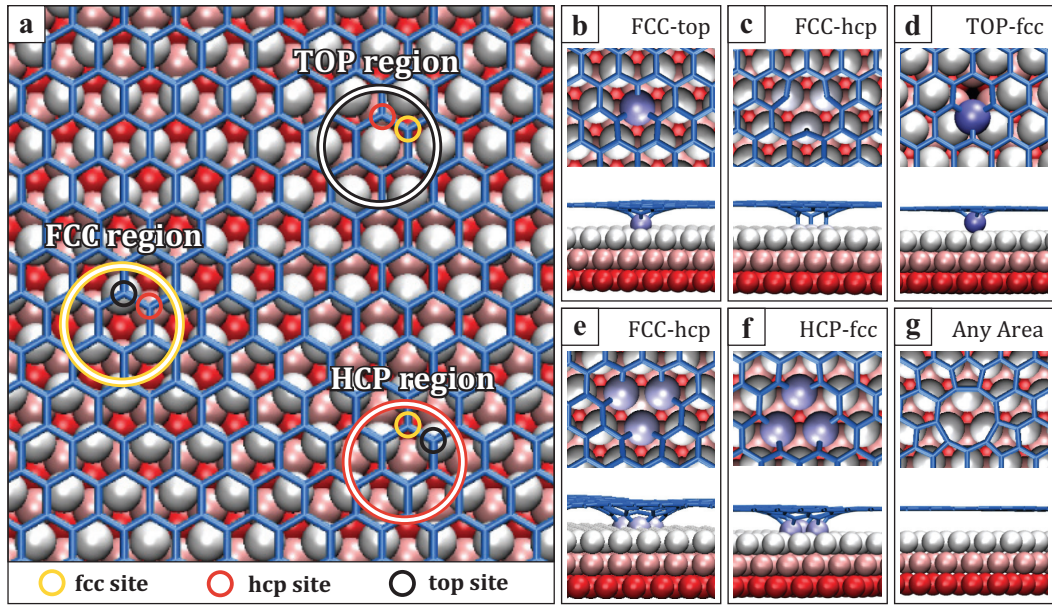


Figure 9.16: Site Dependence of the Defect Structure. Atomic structure of single and tetra-vacancies in graphene on top of Ir (111) surface as obtained in the DFT calculations. (a) Defect-free surface. Regions of high symmetry (HCP, FCC, TOP region) are indicated by large circles. The sites of selected individual carbon atoms are indicated by colored small circles. Ir atoms are colored according to their elevation. (b-d) Top and side views of a single vacancy in different configurations. (e-g) Top and side view of different tetra-vacancy configurations.

Table 9.2: Formation Energies of Vacancy Type Defects. Calculated formation energies $E_{\text{formation}}$ of single and tetra vacancy defects in various areas of the moiré pattern as calculated using the AM05-VV10sol [215] vdW functional. Capital letters denote the region, small ones stand for the position of the missing C atom (the central atom in the case of tetra-vacancies).

Defect Site	$E_{\text{formation}}$ [eV]		Figure	
	single	tetra	single	tetra
non-bonded	7.2	10.6		9.16(g)
TOP-fcc	4.7	12.9	9.16(d)	
TOP-hcp	4.8	≈ 12.7		
FCC-top	4.3	8.8	9.16(b)	
FCC-hcp	5.5	6.8	9.16(c)	9.16(e)
HCP-top	4.2	8.5		
HCP-fcc	5.3	6.9		9.16(f)

turing of graphene on Ir(111): For the right combination of vacancy creation, migration, and annihilation it seems possible to enable vacancy relaxation within one moiré cell, while at the same time avoiding complete vacancy annealing by staying below the onset of intercell diffusion. Thereby one could create a graphene sheet with an ordered array of holes, constituting a graphene nanomesh of 2.53 nm-periodicity. The next chapter is devoted to the experimental realization of this structure.

CHAPTER 10

Pattern Formation in Graphene: Towards a Graphene Nanomesh

*Parts of the results in this chapter are published in Nano Letters **13**, 1948 (2013) [112] and have also been discussed in the work of Charlotte Herbig [164].*

The STM experiments presented in the following chapter were planned by Charlotte Herbig, Carsten Busse, Thomas Michely and by myself. They were carried out by Charlotte Herbig and by myself. The statistical analysis was done by Charlotte Herbig. All authors of the publication have contributed in the discussion of results and writing of the manuscript, while the draft was written by myself. The results on graphene annealing and the temperature dependence of the sputtering yield have been processed by Charlotte Herbig. ARPES measurements were performed in collaboration with Marin Petrović and Marko Kralj from the Institut za fizika, Zagreb, Croatia. For experimental details the reader is referred to Chapter 8.

In order to realize a graphene nanomesh, i.e. a periodic arrangement of defects, by using ion bombardment a transition from isolated damage patterns towards a defect density in the magnitude of one per moiré cell has to be accomplished. This requires large ion fluences which give rise to new phenomena. Therefore, firstly the sample morphology and thermal evolution of the damage patterns following prolonged ion exposure is discussed in Section 10.1. Based on this study we will show that the temperature during bombardment is of great importance to drive carbon vacancies to designated sites of lowest formation energy within the graphene moiré. This allows for an immediate reconstruction of the graphene layer, see Section 10.2. In the third part, Section 10.3, we implement our findings of appropriate parameters for the formation of a high quality graphene nanomesh and give an experimental realization of this structure. Finally, we will investigate the changes of the electronic structure of graphene following ion bombardment in a precursory ARPES study, see Section 10.4.

10.1 Morphology and Thermal Evolution

As manifested in the previous chapter spatially confined defect structures in a supported graphene sheet are obtained by grazing incidence Xe ion irradiation with particle energies around 1 keV. Thereby, a typical ion impact creates a single vacancy site (see Figure 9.8). Simultaneously, the ion fluence has to be increased substantially to satisfy our requirement for a dense nanomesh, i.e. one vacancy agglomerate per moiré unit cell. In the first step, the fluence is set to 0.05 MLE. The resulting sample morphology is shown in Figure 10.1(a).

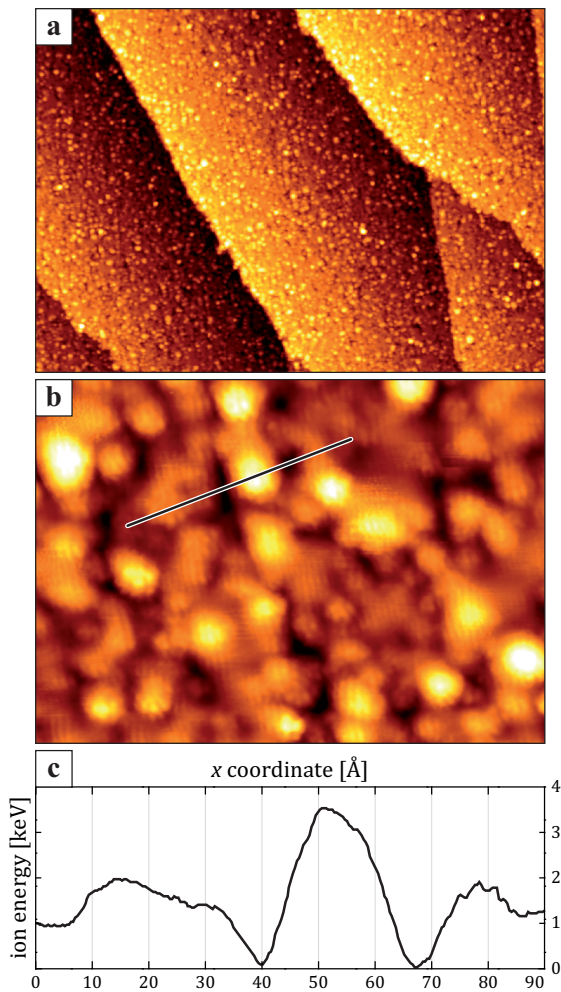


Figure 10.1: Graphene Amorphization Following Prolonged Ion Irradiation. (a) STM topograph of a fully graphene covered Ir(111) sample after 1 keV Xe^+ room temperature bombardment 75° off normal with an ion fluence of $F = 0.05$ MLE. Several preexisting surface steps are visible. (b) Close-up topograph of an extended terrace. (c) Line profile along the line drawn in (b) showing a broad distribution of the height levels. Image width: (a) 1630 \AA , (b) 200 \AA ; Imaging parameters: (a) $U = 800 \text{ mV}$, $I = 0.13 \text{ nA}$, (b) $U = 100 \text{ mV}$, $I = 1.1 \text{ nA}$.

The topographic image shows a strongly damaged surface where no moiré pattern or any other long range order is present. We cannot make out individual ion impacts and conclude that the carbon lattice is quasi-amorphized to a great extent. The profile shown in Figure 10.1(c) is highly non-uniform and does not reveal distinct height levels. Yet one can make out holes in the carbon layer as well as protrusion. A closer look on these reveals

the latter as subsurface irregularities, covered by the remainder of the graphene sheet, see Figure 10.1(b). Based on our insight on single ion impacts, the subsurface distortions can be assigned to metal adatom clusters trapped at the interface of the graphene layer and the iridium surface. The sample corrugation is in fair agreement with the apparent height of buried metal adatom clusters, $\Delta h \approx 2.2 \text{ \AA}$, cf. Section 9.3.

What has proven to be a useful tool to understand the defect morphology is to study its thermal evolution. Thus, we perform an annealing series from which we aim to track the activation temperatures for defect diffusion and bond reorganization. An overview of the sample annealing in steps from 700 K up to 1350 K is given in Figure 10.2. The annealing time intervals are set to 30 s, in line with our experiments on single ion impacts. At first sight one can see that the graphene layer rearranges in the course of this study. Before discussing the ongoing ripening mechanisms we take a look at the prominent surface morphology changes.

Comparing the sample morphology after 700 K annealing [Figure 10.2(a)] to the initial state after room temperature bombardment the surface has become distinctly smoother. The amount of subsurface irregularities has reduced significantly and the graphene layer has redeveloped, discontinued only by vacancy clusters. The number of protrusions does change only little in the temperature range of 800 K [Figure 10.2(b)] to 900 K [Figure 10.2(c)] but individual protrusions gain in both lateral and vertical size. In fact, the apparent height of the remaining protrusions varies strongly between 2.0 \AA and 3.0 \AA . At the same time larger vacancy clusters form. While their shape gives no hint on ordering, their size is sufficient for the STM tip to reach down to the iridium substrate. Besides these vacancy agglomerates also smaller holes remain. After annealing to 1000 K and 1100 K [Figures 10.2(d) and (e), respectively] the vacancies develop into larger vacancy islands and start to configurate according to the dense-packed directions of the moiré, i.e. they form zigzag edges. Simultaneously, also the remaining protrusions begin to rearrange: Occasionally, we observe protrusions of hexagonal shape, depicted in the inset of Figure 10.2(e). With this, their apparent height saturates at approximately 3 \AA . In between these structures the graphene layer seems intact at first sight. Having a closer look one makes out small vacancies that agree with the funnel-shaped vacancies described in the preceding chapter as well as deformations of carbon bonds, giving rise to a strong local buckling. By annealing to 1350 K the vacancy islands have coalesced on large scales and further reshaped. Small depressions in the graphene layer indicate a considerable amount of point defects. Additionally, prominent bright protrusions of elongated shape have emerged displaying the exclusively present protrusions.

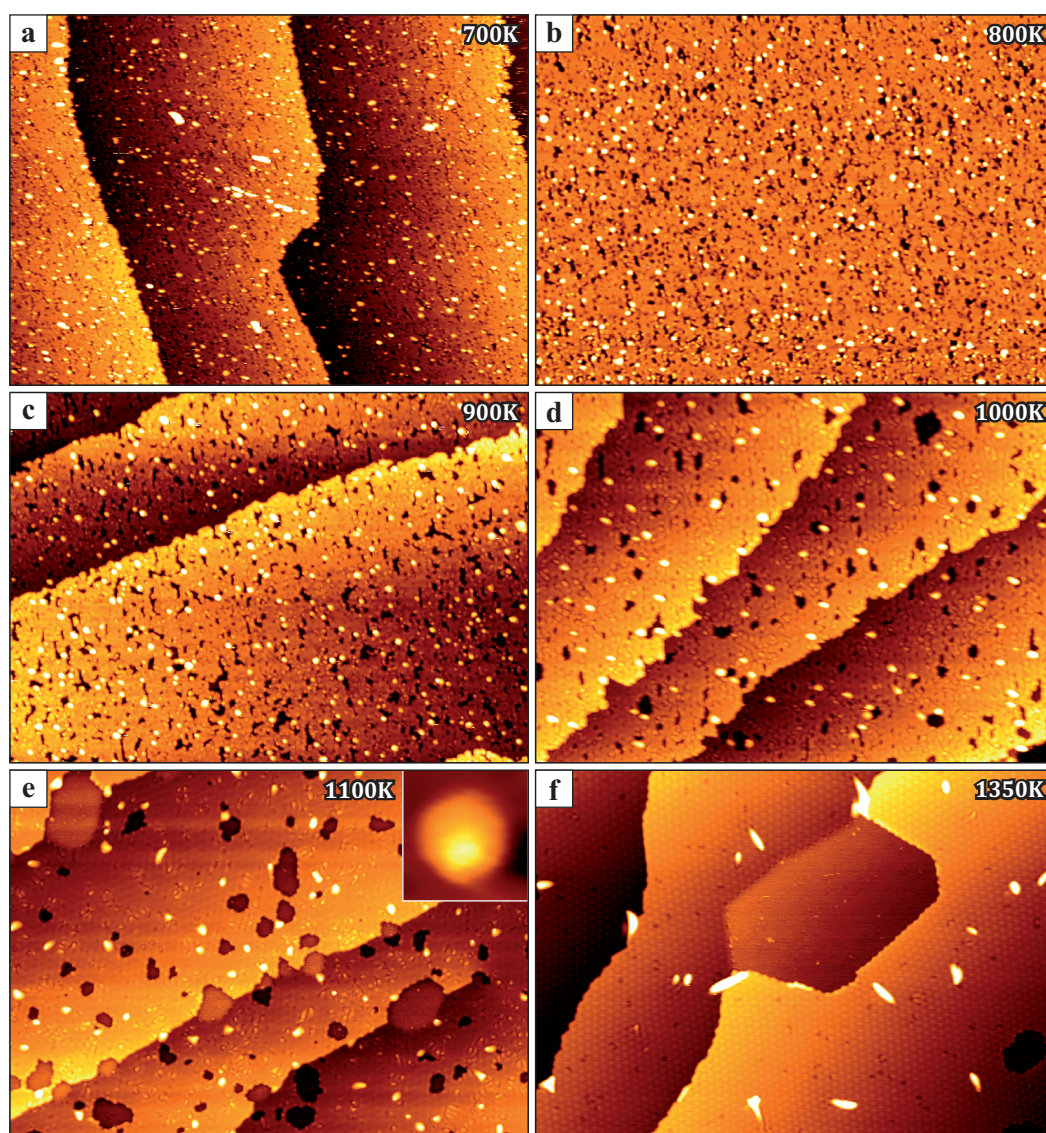


Figure 10.2: Graphene Annealing. STM topographs of a fully graphene covered Ir(111) sample after 1 keV Xe⁺ room temperature bombardment 75° off normal with an ion fluence of $F = 0.05$ MLE, cf. Figure 10.1, and subsequent annealing for 30 s. The annealing temperature was set to (a) 700 K, (b) 800 K, (c) 900 K, (d) 1000 K, (e) 1100 K, and (f) 1350 K, as depicted in the images. Image width: (a-f) 1630 Å, (inset) 30 Å; Imaging parameters: (a) $U = 1.2$ V, $I = 0.16$ nA, (b) $U = 1.1$ V, $I = 0.11$ nA, (c) $U = 1.4$ V, $I = 0.23$ nA, (d) $U = 1.0$ V, $I = 0.13$ nA, (e) $U = -0.2$ V, $I = 1.4$ nA, (f) $U = -0.7$ V, $I = 1.6$ nA.

Based on our knowledge of the annealing behaviour of single ion impacts, the reduction of protrusions upon heating to 700 K can be attributed to a recombination of iridium adatom clusters with segregated vacancies from the bulk. In Section 9.3 we found this process is completed before 750 K. Ergo, the remaining protrusions we observe at elevated temperatures, $T > 800$ K, have to be of different origin. At this point one has to reconsider the parameters used during bombardment. The reduction of the projectile energy does not only affect the lateral dimension of the defects but also the way defects are created: With a reduction of the ion energy to 1 keV Ir adatom production is drastically reduced [174] and the dominating process in defect creation is the displacement of individual carbon atoms upon first impact, which come to rest at the interface. This is supported by the MD simulation data shown in e.g. Figure 9.6, which proof that upon first impact carbon atoms are implanted into the bulk or buried underneath the graphene surface. For that reason, we attribute the remaining protrusions to agglomerates of carbon atoms trapped at the interface. Note that this was hardly ever observed for single ion impacts due to different bombardment parameters. We also expect the increase of ion fluence to have an effect here, as the displacement threshold for undercoordinated carbon atoms (e.g. in a quasi-amorphized layer) is severely lowered [42]. As assumed for iridium adatom clusters in Section 9.3 we expect that the presence of graphene has only a weak influence on the carbon diffusion process and allows for coalescence in this temperature range [46]. Upon further heating, $T > 1000$ K, both the vacancy islands as well as the carbon clusters begin to take a hexagonal shape. While this geometry displays the equilibrium structure featuring the lowest density of broken carbon bonds it denotes the onset of diffusion of carbon atoms along step edges. In consequence, we attribute the ongoing restructuring at the interface to the transformation of carbon clusters into graphene platelets at the interface. The temperature dependence observed in the course of our experiments matches what has previously been observed for the growth of graphene on clean iridium in Reference [46].

The fact that the apparent height of the smallest bilayer graphene platelets is lower than the expected interlayer distance in graphite, $d = 3 \text{ \AA}$, can be explained by strain in the graphene layer: For the formation of (carbon) clusters at the interface the covering graphene sheet has to be lift off the substrate locally. In this process delamination energy has to be paid and strain is induced into the carbon lattice due to the curvature along the edges. The amount of delaminated area is strongly dependent on the size of the interface structure. While for fully developed graphene platelets a large fraction of the blanking graphene sheet is almost relaxed and an interlayer spacing similar to graphite develops, for small clusters the resulting curvature is strongest which exerts pressure on

the interface atoms and reduces the height of the surface structure. A visualization of this effect is given in Figure 10.3. It should be noted that already in the work of Coraux *et al.* [46] similar fluctuations of the apparent height have been found for carbon clusters rather than graphene islands.

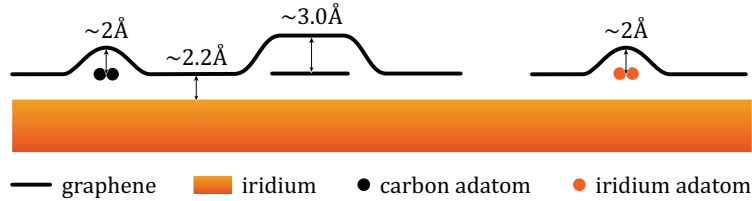


Figure 10.3: Schematic View on the Apparent Height Levels in STM.

The graphene layer on Ir(111) is typically imaged with a height of 2.2 \AA , that is comparable to an iridium step edge. Adatom agglomerates buried underneath the graphene layer show an apparent height in the range of approximately 2 \AA towards the surrounding layer. When a bilayer graphene platelet develops, it displays an elevation of about 3.0 \AA .

A closer look at the sample morphology after annealing to $T = 1100 \text{ K}$ unveils the presence of many grooves, see Figure 10.4(a), which are a well-known feature observed in grain boundaries [inset of Figure 10.4(a)]. Accordingly, we interpret these grooves as chains of pentagon-heptagon pairs [182]. Since our growth method guarantees a high quality graphene layer where rotational misalignment and thus the grain boundary density is minimized [46], we conclude that these grooves are formed under ion irradiation and subsequent annealing solely. This assumption is in line with our findings on the evolution of defects following single ion impacts (see Section 9.3) which is governed by edge dislocation climbing [43]).

While most of the pentagon-heptagon pairs are accumulated in grooves, several of these defects remain isolated and offer a sound explanation for the wrinkle formation upon further annealing: Certain types of defects - including pentagon-heptagon pairs - induce stress in the carbon lattice which results in a curvature of the graphene sheet in close vicinity (see e.g. References [45, 176, 182] and the description given in Section 7.4). This curvature facilitates further delamination on account of stress relaxation. In fact, most of the wrinkles observed after annealing to 1350 K directly link to a step dislocation [Figure 10.4(b)], i.e. a pentagon-heptagon pair. The finite size of these wrinkles is attributed to the high density of stable defects and concomitant stress in the carbon lattice, which contrasts the formation of a continuous wrinkle network in the graphene growth process [162]. While we observe a coexistence of bilayer graphene platelets and dislocation-driven stress

relaxation induced warping of the graphene layer at 1100 K, our STM measurements show an exclusive abundance of wrinkles at 1350 K. We assume that the promoted wrinkle formation can be linked to the diffusion of carbon adatoms and carbon clusters. As we have seen before, these interface structures undergo ripening at the very same temperature range. While the evaporation of carbon atom from the graphene clusters and the formation of a carbon adatom gas at the interface (Ostwald ripening) is assumed to be too slow to contribute to the ripening process on the timescale of seconds due to the strong carbon-carbon bonds [46], most probably entire carbon clusters are set into movement (Smoluchowski ripening). Wrinkles are then formed by the incorporation of mobile carbon at the dislocation, where the delamination energy cost is lowered due to the pre-existing local curvature of the graphene sheet. In addition, also inverse Stone-Wales defects should be considered as sources for local curvature, which may have formed under non-equilibrium conditions during ion bombardment.

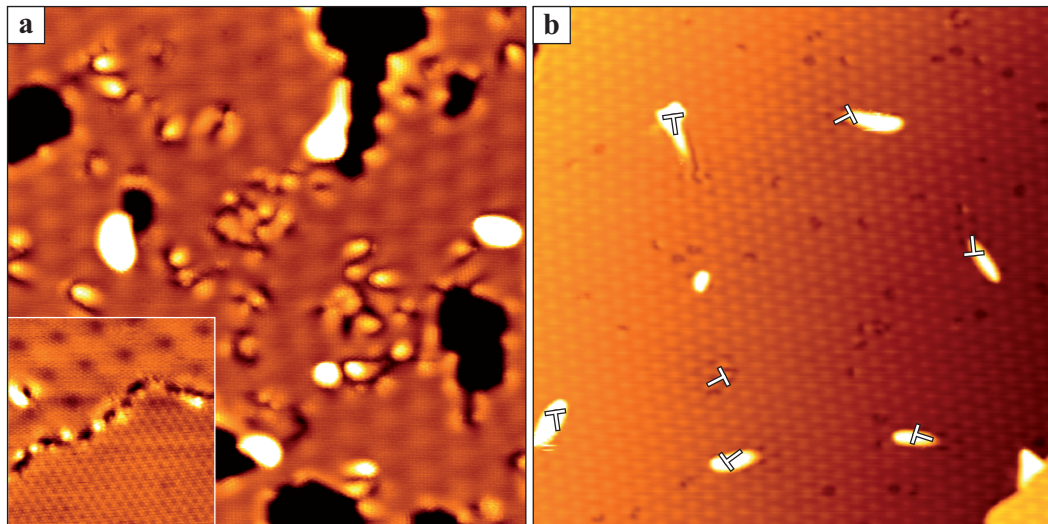


Figure 10.4: Wrinkle Formation upon Annealing. Close up topographs of the sample morphology shown in Figure 10.2(e) and (f). In (a) different rotational domains are visible, surrounded by extended vacancy clusters and finite size grooves. Inset: Coherent grain boundary between different rotational domains in a pristine graphene layer grown via CVD only. In (b) step dislocations are marked by a \perp symbol. Image width: (a) 340 Å, (inset) 140 Å, (b) 725 Å; Imaging parameters: (a) $U = -0.3$ V, $I = 10$ nA, (inset) $U = 0.1$ V, $I = 1.7$ nA, (b) $U = -0.7$ V, $I = 1.6$ nA.

While we now have a qualitative understanding of the damage pattern following high ion fluences and its annealing, the experiment discussed here did not show any hint that the vacancies arrange according to the moiré superstructure as predicted by DFT calculations for single and tetra vacancies in the previous chapter. As for carbon migration

energies of approximately 2 eV the annealing duration might have an effect on the sample morphology in the above temperature range, we also carried out experiments in which the annealing time after bombardment has been extended by a factor of 40 to match the total time of bombardment. Yet the experiments have shown no differences and we can exclude a dependence on annealing duration from further considerations at least on our experimental timescale.

We propose that the lack of defect ordering is reasoned in the room temperature bombardment alone. That is, the graphene lattice was too heavily destroyed to form a moiré superstructure, in agreement with our observations, see Figure 10.1. Consequently, no energetically favored sinks form in the potential landscape that would guide mobile vacancies.

As this result is contrary to our initial intention, in the next section we carry out irradiation experiments at elevated temperatures. These experiments will be contrasted to the annealing series where irradiation was conducted at room temperature. We aim at finding a sample temperature at which the carbon lattice has the chance to rearrange after an impact before subsequent impacts occur in its vicinity. Thereby, the graphene sheet may preserve its superstructure with respect to the Ir substrate and is able to force mobile vacancies to predetermined sites.

10.2 Irradiation at Elevated Temperatures

The results of the preceding chapter have shown that prolonged ion irradiation of the graphene covered Ir(111) surface causes heavy damage to the carbon lattice. Hence, it seems reasonable to expose the graphene covered surface to high fluence experiments at elevated temperatures to allow for an immediate reconstruction of the graphene sheet after each impact. In the following, the previously discussed results of 0.05 MLE 1 keV Xe^+ bombardment at room temperature and subsequent annealing are compared to corresponding experiments with bombardment carried out at the former annealing temperatures: $T = 700$ K, 800 K and 900 K. These values were chosen in the temperature range where vacancy diffusion is thermally activated, see Section 9.3.

The left column of Figure 10.5 offers an overview on the sample morphology shown before, following 1 keV Xe^+ bombardment, $F = 0.05$ MLE, at room temperatures and subsequent annealing for 30 s at $T = 700$ K, 800 K and 900 K (from top to bottom). The right column lists the experiments where ion bombardment was carried out directly at the respective

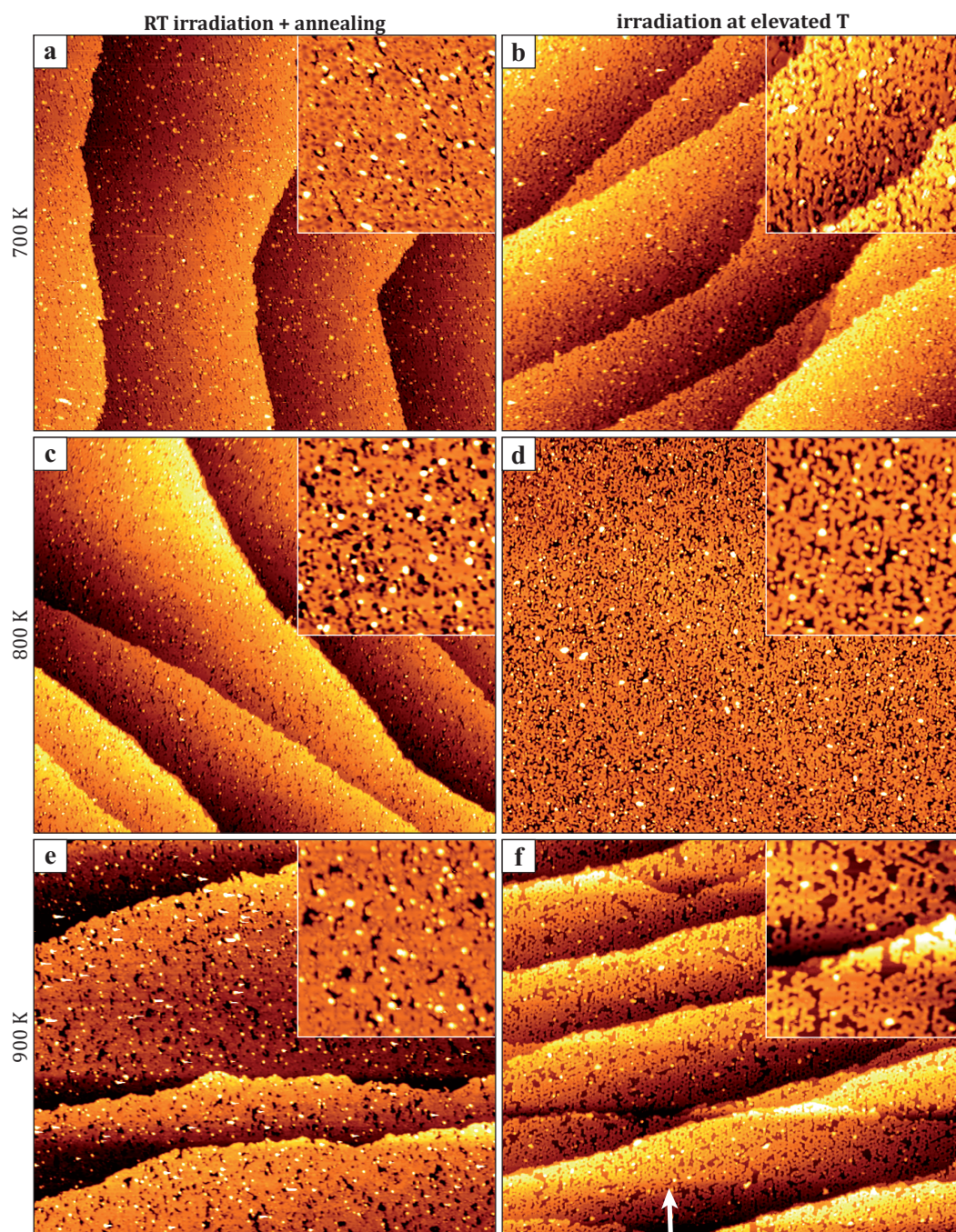


Figure 10.5: Temperature Dependence. STM topographs to compare the sample morphology after prolonged ion bombardment at room temperature and subsequent annealing (left hand side) with ion irradiation at elevated temperatures (right hand side); 1 keV Xe⁺, $F = 0.05$ MLE. The studied temperatures for annealing and bombardment are (a,b) 700 K, (c,d) 800 K, and (e,f) 900 K. Image width: (a-f) 2500 Å, (insets) 500 Å; Imaging parameters: (a) $U = 1.2$ V, $I = 0.16$ nA, (inset) $U = 1.7$ V, $I = 0.16$ nA, (b) $U = 90$ mV, $I = 91$ pA, (c) $U = 1.6$ V, $I = 0.16$ nA, (d) $U = 1.5$ V, $I = 0.11$ nA, (e) $U = 1.4$ V, $I = 0.23$ nA, (inset) $U = 0.9$ V, $I = 0.23$ nA, (f) $U = 0.9$ V, $I = 0.34$ nA, (inset) $U = 0.9$ V, $I = 0.13$ nA.

temperatures. The fluence was set to 0.05 MLE in all experiments. A quantitative analysis of the sample morphology is given in Figure 10.6. Here the surface erosion Θ_{surf} (a) and the protrusion coverage Θ_{prot} (b) are measured for each sample state and plotted against the annealing (black curve) or irradiation (red curve) temperature, respectively.

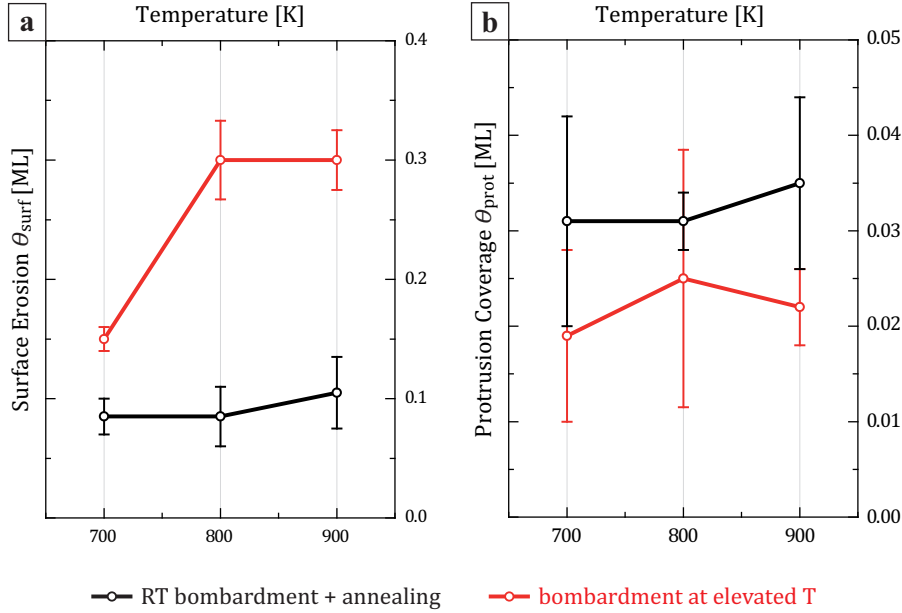


Figure 10.6: Evaluation of the Temperature Dependence. (a) Surface erosion Θ_{surf} and (b) protrusion coverage Θ_{prot} plotted against the sample temperature during annealing (black curve) and for irradiation at the corresponding temperature (red curve). Lines are printed to guide the eye.

Comparing the sample morphologies for each temperature step one can see on first glance, that the surface is eroded to a greater extent for bombardment at elevated temperatures. This impression is substantiated by the data evaluation shown in Figure 10.6(a). It follows that the surface erosion is approximately tripled at temperatures exceeding 700 K. Contrary to these findings, we do observe a (barely observable, yet systematic) reduction of the protrusion coverage for irradiation of a heated sample, $\bar{\Theta}_{\text{prot}}(\text{RT}) = (0.032 \pm 0.005) \text{ ML} \searrow \bar{\Theta}_{\text{prot}}(\text{elev. T}) = (0.022 \pm 0.006) \text{ ML}$, see Figure 10.5(b). While for post-irradiation annealed sample the annealing process does not evolve new structural features in the depicted temperature range, the sample irradiated at 800 K [Figure 10.5(d)] gives a first hint of a vacancies in an hexagonal arrangement. This observation becomes more evident for the sample irradiated at 900 K [Figure 10.5(f)] which gives a first clue for the onset temperature of defect ordering as predicted by DFT. Note that the vacancy clusters are elongated in the direction of the ion beam [arrow in Figure 10.5(f)].

Given the high thermal energy of the system during bombardment at elevated temperatures, we can assign the slight reduction of adatom clusters to an immediate reincorporation of carbon atoms into the graphene layer. To address the higher erosion rate observed in this experimental series we propose that the probability for large angle scattering events is increased for bombardment at elevated temperatures. This increase can be explained by the combination of grazing incidence ions and thermally activated oscillations of the graphene layer with respect to the iridium which reduce the channeling fraction of particles. These assumptions seem reasonable since the graphene sheet is well decoupled from the metal substrate and a temperature dependence of the sputtering yield due to atomic vibrations has been experimentally observed for step edge sputtering through grazing ions on Pt(111) [216].

Furthermore, the onset of carbon vacancy mobilities at temperatures above 800 K may play an important role in surface erosion. As we learned from the experimental data, vacancy clusters start to form in the particular temperature range. These larger vacancies give rise to a different sputtering mechanism, which can be described by a geometrical model developed by Hansen *et al.* [217] and is shown in Figure 10.7.

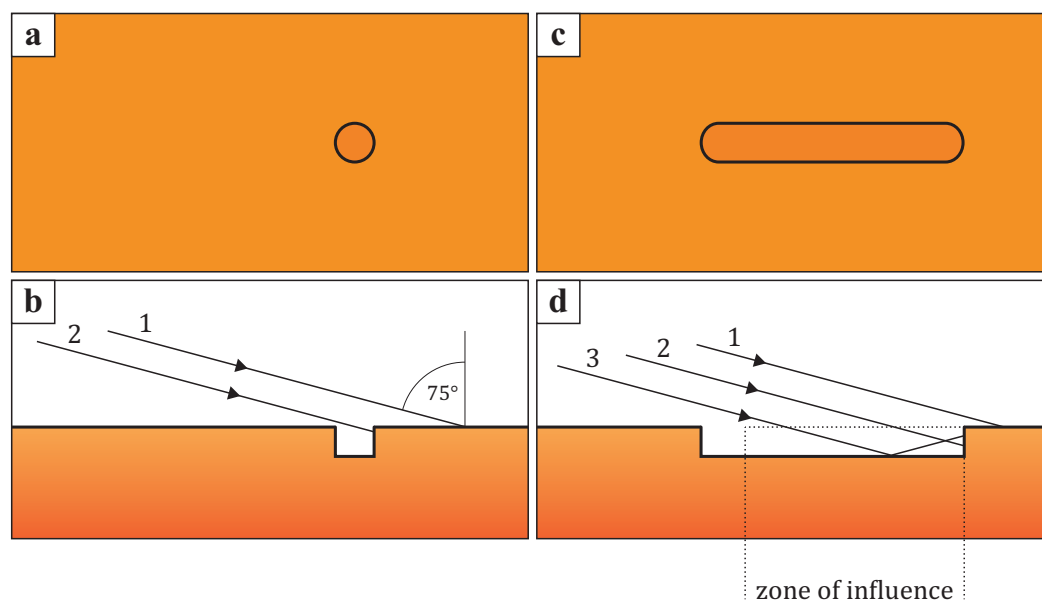


Figure 10.7: Model to Illustrate the Zone of Influence. (a,b) Top and side view of ions impinging on a surface step caused by a point defect. (c,d) Top and side view of ions impinging on a vacancy type defect elongated in the direction of the incident ion beam.

Assuming an ascending step edge of a point defect [Figure 10.7(a,b)] impinging ions can be distinguished into two classes. The first class is assigned to a ions hitting a terrace or

intact graphene sheet (trajectory 1). The second class describes ions hitting the step edge by a direct impact (trajectory 2). When the vacancy size is increased in the direction of the ion beam [Figure 10.7(c,d)] a third class evolves: Ions hitting the step edge by an indirect impact following a reflection from the lower terrace within the zone of influence (trajectory 3). Besides the fact that the transferred energy from the ion to the sample per impact is higher due to a smaller local angle of incidence ϑ , $E_{\perp} = E \cdot (\cos \vartheta)^2$, also the effective amount of ions which hits the step edge is substantially increased which leads to important changes in the sputtering yield [216, 217]. Transferred to our system we expect an increase of sputtering yield for larger vacancy islands, i.e. bombardment at elevated temperatures, as here a significant *zone of influence* develops and the energy transfer is not restricted by the size of the vacancy cluster. In case of the bare Pt(111) surface this leads to an alignment of vacancy clusters in the direction of the ion beam, in agreement with our findings.

Up to now this phenomenon has been observed for metal step edges only [216]. In the very same system an opposing process could be identified that causes a reduction of the sputtering yield at elevated temperatures: The interplay of bulk and surface defects allow for a decrease of the average step density at higher temperatures [217]. This does not apply to our system as the graphene sheet is purely two-dimensional. A reduction of step edges (in the considered temperature range) only occurs, when individual vacancies and vacancy clusters align in the direction of the ion beam. Given this case, the decrease of the step edge density is overcompensated by the previously introduced benefit of larger vacancy clusters.

The interplay of thermally activated diffusion, vacancy size, and step density makes the temperature dependent sputtering yield another interesting aspect of ion bombardment of two-dimensional materials, especially Gr/Ir(111). Yet, a detailed elaboration of the underlying processes goes beyond the scope of this thesis.

10.3 Graphene Nanomesh

As we have learned in the previous sections, for an ideal nanomesh, one vacancy aggregate has to be present in every single moiré cell. In addition, secondary effects like Ir sputtering have to be suppressed. We conclusively showed that these conditions can be met by reducing the ion energy ($E(\text{Xe}) = 1.0 \text{ keV}$) while, at the same time, increasing ion fluence substantially. What is more, we could show that the temperature during irradiation is of major importance for the healing of the graphene sheet and to drive the carbon vacancies

into a hexagonal arrangement. An enlarged view of the sample morphology shown in Figure 10.5(f) is presented in Figure 10.8.

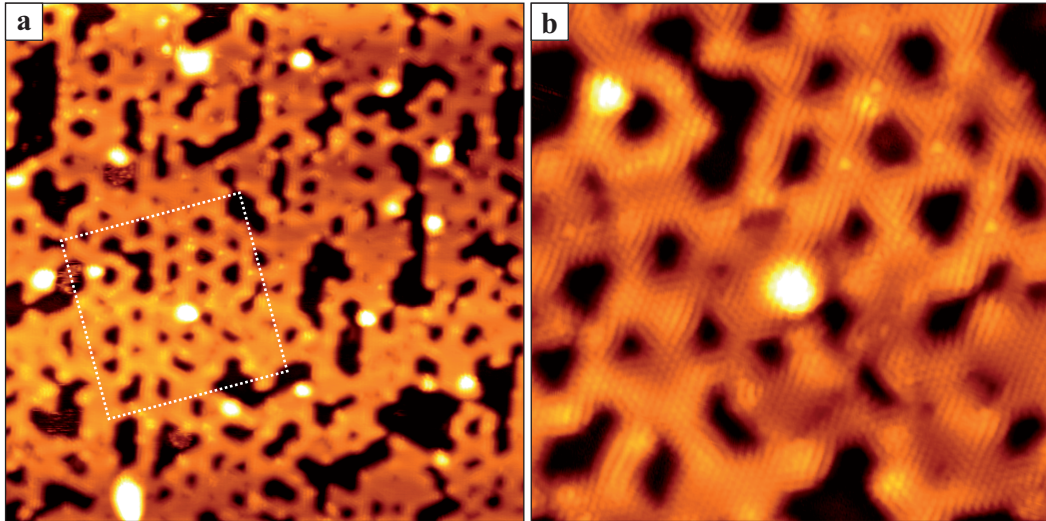


Figure 10.8: Graphene Nanomesh I. Fully graphene covered Ir(111) surface after irradiation with 1.0 keV Xe^+ ions at $T = 900$ K under 75° off normal, fluence $F = 0.05$ MLE. The image shows an ordered lattice of large vacancy clusters. Image width: (a) 490 Å, (b) 180 Å; Imaging parameters: (a,b) $U = 0.9$ V, $I = 0.13$ nA.

The combination of particle energy, sample temperature, and ion fluence has caused a fractionalisation of the graphene sheet. Large parts of the iridium substrate are exposed as the sample morphology is dominated by large vacancy clusters of various size and shape. Yet, several smaller vacancy agglomerates remain that align in a hexagonal arrangement, as can be seen in Figure 10.8(b). Based on our findings we attribute this ordering to a templating effect of the Gr/Ir(111) moiré superlattice.

As the long range order does not yet match our expectations, it seems that our approach still lacks an important parameter. The topographic images shown here feature a broad distribution of the hole sizes. In fact, we observe coalescence of vacancy clusters occupying neighbouring moiré cells. Our work on single ion impacts has shown that the defect patterns following 0.5 keV ion impacts are smaller in size than those for particle energies of 1.0 keV, cf. Section 9.2. Thus, we can ensure that each artificially induced defect is able to obtain its stable structure individually, which we expect to bring us closer to the desired fabrication of an ordered vacancy network.

The sample topography following 0.5 keV Xe^+ bombardment of a fully graphene covered Ir(111) surface ($F = 0.05$ MLE) and subsequent annealing to 900 K is depicted in Figure

10.9. The defect pattern exhibits a dense arrangement of vacancy type defects which develop a single hexagonal component in the Fourier transform (inset of Figure 10.9(a)). The presence of sharp and intense reflexes finally confirms that the positions of the holes are correlated and obey a long-range defect ordering. The reflexes correspond to a lattice constant of $a = (25.6 \pm 1.1) \text{ \AA}$ which resembles the moiré lattice constant (note that the moiré pattern was filtered out prior to applying the FT).

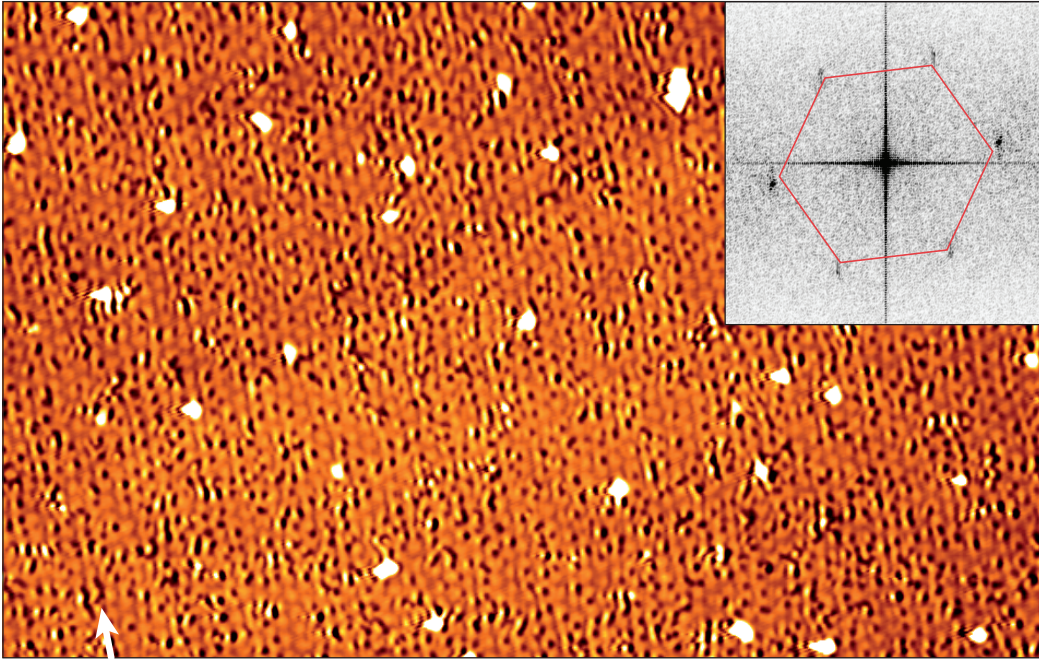


Figure 10.9: Graphene Nanomesh II. Graphene nanomesh obtained by an increased fluence $F = 0.05 \text{ MLE}$ with Fourier transform inset. The hexagonal symmetry is highlighted, referring to a long-range defect ordering. Image width: 1600 \AA , (inset) 0.15 \AA^{-1} ; Imaging parameters: $U = 2.0 \text{ V}$, $I = 0.2 \text{ nA}$.

In the remainder of this section we will evaluate this ordering. In particular we aim at determining the location of the vacancies within the moiré unit cell. For being able to do so we take a step back and reduce the total ion fluence to moderate the surface erosion and enhance visibility. The resulting sample topography ($F = 0.02 \text{ MLE}$) is shown in Figure 10.10. The holes within the graphene layer are arranged in a partially occupied honeycomb lattice. We superimposed a hexagonal lattice associated with the TOP regions of the moiré. Thereby it becomes obvious that the holes are never located in the TOP regions, but prefer the HCP/FCC regions, as predicted by our DFT calculation.

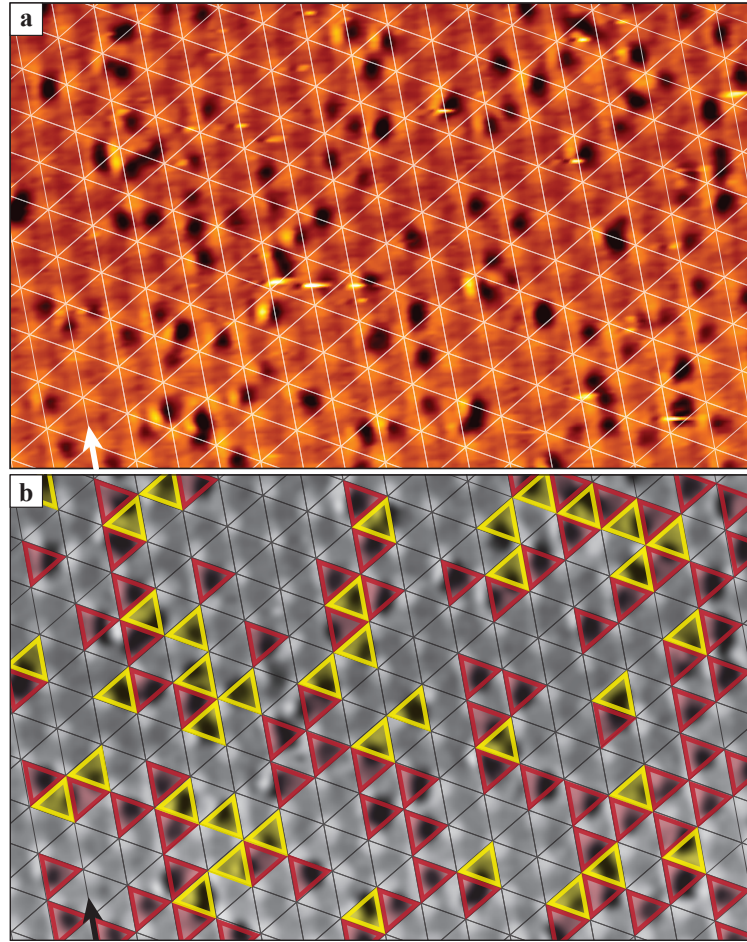


Figure 10.10: Graphene Nanomesh III. (a) Fully graphene covered Ir(111) surface after irradiation with 0.5 keV Xe^+ ions at room temperature under 75° off normal, fluence $F = 0.02$ MLE, and subsequent annealing $T_{\text{anneal}} = 900$ K. The image shows a dense arrangement of defects in honeycomb order. A hexagonal lattice is superimposed on the top regions of the moiré unit cell. (b) Same as (a) after image processing to enhance visibility of the vacancy type defects. Here, each defect is color coded according to its site within the supercell: (red) HCP, (yellow) FCC. Image width: 400 Å; Imaging parameters: $U = 2.1$ V, $I = 0.20$ nA.

The fraction of defective moiré cells as calculated from the experimental data amounts to $p \approx 0.3$. The exact ratio of HCP:FCC occupation, as shown in Figure 10.10(b) is measured to $(3.2 \pm 0.3) : 1$, which is reasoned by the expected ratio derived from the DFT calculation data via:

$$\text{relative population} \quad \frac{P_{\text{HCP}}}{P_{\text{FCC}}} = \exp\left(-\frac{\Delta E_{\text{formation}}}{k_{\text{B}}T}\right) = 3.6, \quad (10.1)$$

where $\Delta E_{\text{formation}} = E(\text{HCP}) - E(\text{FCC}) \approx -0.1$ eV for the various types of defect configurations given in Table 9.2.

The above findings show that our method is able to produce a graphene nanomesh on a 2.53 nm-scale. It is formed by relaxation of vacancies created by ion irradiation to the locations of minimal formation energy within one moiré unit cell, thereby lowering the total system energy substantially. Note that nanomesh formation can only take place in the narrow temperature window above the onset of relaxation within one moiré cell but below the activation of intercell vacancy migration. The structural order as well as the hole size of the nanomesh can be controlled by the process parameters of ion species, energy, angle, and the temperature treatment of the sample during and after irradiation.

10.4 Looking for a Bandgap

As detailed in the background section, a graphene nanomesh has been predicted to cause bandgap opening at the Fermi level due to spatial confinement of electrons [36, 183–186]. While we were able to experimentally realize this structure in the previous sections, a proof of the bandgap opening remains to be done. Our method of choice in this task is angle resolved photoelectron spectroscopy (ARPES) as it allows for direct imaging of the graphene Dirac cone. In the following paragraph we will present our efforts to track changes of the electronic structure of graphene following ion bombardment according to the established recipe.

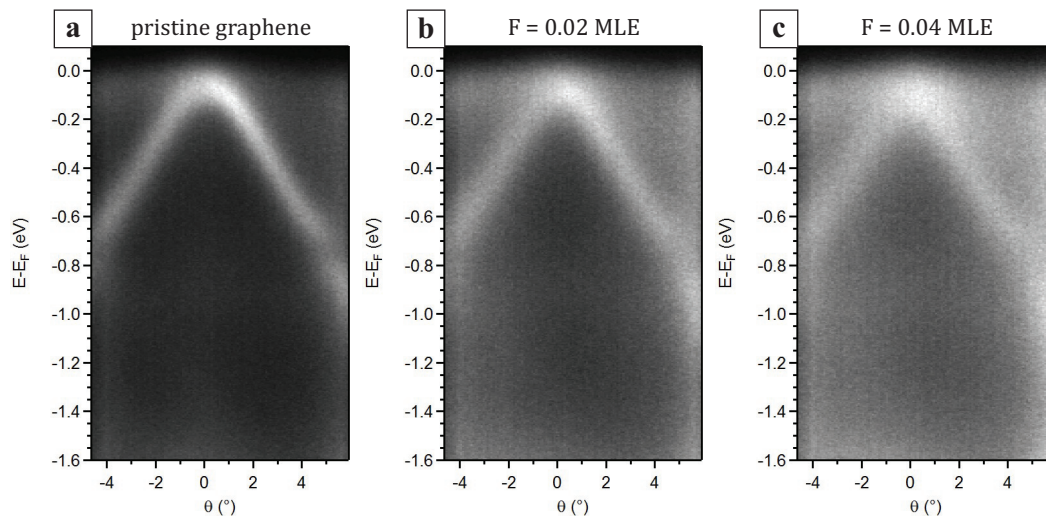


Figure 10.11: ARPES Spectra of the Dirac Cone. (a) Pristine Gr/Ir(111) subsequently irradiated with (b) $F = 0.02$ MLE and (c) $F = 0.04$ MLE Xe^+ ions 75° off normal at room temperature and consecutive annealing to 1000 K. The projectile energy was set to 1 keV.

Figure 10.11 illustrates the evolution of the Dirac cone upon 1 keV Xe⁺ ion bombardment and subsequent annealing to 1000 K. The ARPES spectra were taken perpendicular to the Γ -K-direction after prolonged exposure to (b) $F = 0.02$ MLE and (c) 0.04 MLE. For reference, a spectrum of the pristine graphene layer is shown in (a). Please note that the ion fluence could not be determined precisely in the course of measurements and does not necessarily correspond to the values given in previous sections.

The ARPES spectrum of the pristine Gr/Ir(111) layer shows the populated, lower half of the Dirac cone and the opening of minigaps in agreement with previous findings [201]. Upon ion irradiation the overall signal intensity is strongly reduced which can be attributed to the disturbance of the graphene lattice, i.e. a reduction of the coherence of the signal-producing carbon atoms. A closer inspection of the spectra unveils a shift of the cone intensity toward higher binding.

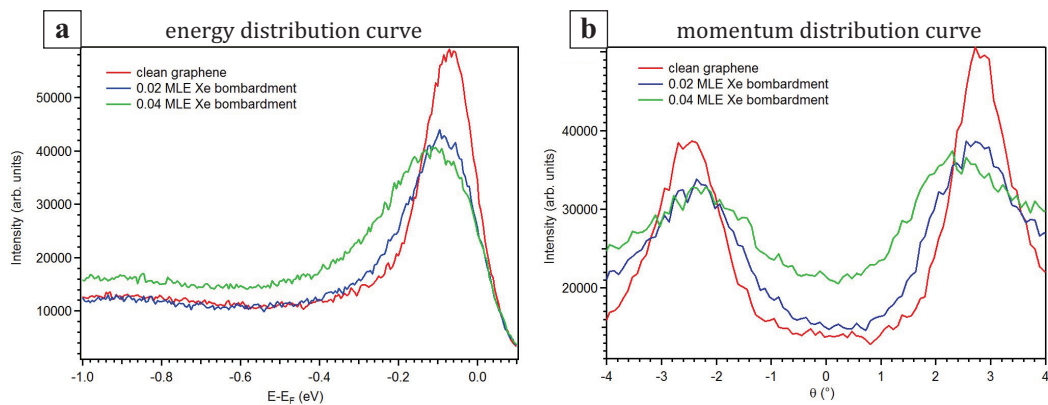


Figure 10.12: Analysis of the ARPES Spectra. (a) Energy distribution curve through the K-point ($\theta = 0^\circ$) of the spectra shown in Figure 10.11. (b) Momentum distribution curve of the spectra shown in Figure 10.11 taken at $(E - E_F) = -0.4$ eV. Color code as indicated in the diagrams.

This observation is substantiated by the energy distribution curve of the signal directly at the K-point ($\theta = 0^\circ$) given in Figure 10.12(a): While the overall intensity of the spectra reduces with increasing fluence (red \rightarrow blue \rightarrow green, as indicated in the diagram), the peak position is substantially lowered. The reduction amounts to $\Delta E \approx 45$ meV (no fitting) for the highest fluence, $F = 0.04$ MLE, when compared to the pristine layer.

In Figure 10.12(b) the momentum distribution curve taken at $(E - E_F) = -0.4$ eV of each spectrum is shown. One can make out two peaks according to the branches of the Dirac cone. With increasing ion fluence (red \rightarrow blue \rightarrow green, as indicated in the diagram) the two branches move closer together.

In a simple picture the observed evolution of the Dirac cone can be related to a bandgap opening. Here we have to consider that ARPES has access to the populated states of the bandstructure only. Given that the bandgap opening is symmetric around the Dirac point, we can approximate the bandgap to $E_{\text{gap}} \geq 2 \cdot \Delta E \approx 90 \text{ meV}$ which matches our expectations according to Equation 7.11. However, at this point of our studies we cannot rule out different mechanisms to cause these distortion of the graphene bandstructure. In particular, also doping of the graphene layer and band renormalization offer sound explanations for the observed evolution. To answer this question in a reasonable manner further measurements are required.

CHAPTER 11

Comparison

In Chapter 9 we have studied the defect patterns in graphene on an Ir(111) support which appeared due to keV noble gas ion bombardment under grazing incidence. We furthermore elucidated the formation mechanism of these patterns using MD simulations. Low fluences were chosen to make the damage patterns of individual ions visible. Above we studied the thermal stability of defects and combined our findings with DFT calculations. In Chapter 10 we exploited the possibility to form a graphene nanomesh on Ir(111) by tuning the experimental parameters of projectile energy, ion fluence, and sample temperature. The findings obtained in these chapters will now be compared to similar studies on the pristine metal system carried out by A. Redinger [125] and H. Hansen [218]. We will discuss the common characteristics and point out the differences we observed in the course of our experiments.

Single Ion Impacts

Employing single ion impacts on a graphene covered Ir(111) surface under 75° off normal we observed the formation of extended defect patterns. Each pattern consists of chains of holes, accompanied by bright protrusions. While their exact appearance is highly diverse we find all patterns elongated in the direction of the ion beam. Consequently, we attribute their formation to an oscillatory motion of the ion at the interface of the graphene layer and the metal substrate. This assumption is conclusively supported by MD simulation data which confirms the sputtering of carbon atoms from below, causing a track of vacancy clusters in the graphene layer. According to these data, the projectile loses approximately $100 \text{ eV}/\text{\AA}$ in a graphene reflection, whereas the energy loss amounts to only $10 \text{ eV}/\text{\AA}$ during reflection on the metal substrate. The total probability to penetrate the graphene sheet amounts to 66 %.

Besides pure interface channeling we do observe events in which the ion penetrates the carbon layer *and* the topmost crystal layer [see Figure 9.3(e)] and conducts a channeling motion underneath the metal surface layer. The energy loss of the ion in such an event clearly distinguishes from the case of pure interface channeling as the ion is trapped in a much more narrow channel. Consequently we do observe an almost linear decay of the projectile energy with $\Delta E/\Delta x \approx 30 \text{ eV}/\text{\AA}$. The probability for such an event was calculated to 20 %.

The mechanism of subsurface channeling has been introduced and widely studied by H. Hansen [218] and A. Redinger [125, 173, 174, 216, 219]. Performing noble gas ion bombardment on Pt(111) under grazing incidence, $78^\circ \leq \vartheta \leq 88^\circ$ off normal, Redinger *et al.* state:

"At ascending step edges single ion impacts create damage due to large scattering events or perform subsurface channeling. In the first case the damage is situated exclusively at the step edge where a thermal spike, sputtering, adatom and vacancy formation occurs. However, many ions are able to enter the crystal and are guided between the open space of two crystal layers via small angle binary collisions, i.e. subsurface channeling. The energy loss is strongly reduced compared to direct impacts and the ion performs a steered oscillatory motion. Surface damage is induced due to the reduced energy threshold for damage formation. Compared to bulk channeling, the threshold energy is reduced by roughly one order of magnitude. In the case of Argon ions the damage consists of adatoms and vacancies aligned in ion beam direction. In contrast, Xenon ions produce surface vacancy trenches. This ploughing mechanism produces a one atom wide surface vacancy trench in ion beam direction. Almost the complete trajectory of the channeled particles is visible on the surface. Switching between different rows and different layers is observed with STM." [125]

While we have no direct experimental access to the amount of vacancies in the metal surface, the formation of metal adatom clusters is also observed in the course of our experiments. However, the MD simulation data clearly shows that the production of metal adatoms is enhanced in case of subsurface channeling (sputtering from below) when compared to interface channeling events (sputtering from above). The simulation data also predicts the formation of carbon adatom clusters on the graphene surface. However, due to the high mobility of adatoms at room temperature (in-plane migration barrier: $E_{\text{diffusion}} \approx 0.4 \text{ eV}$ [181]) it is impossible to observe them directly in STM.

Note that Redinger *et al.* [174] found the formation of surface vacancy trenches on the flat terrace to require an ion incidence angle smaller than 80° , measured to the surface normal. This agrees with our observation of subsurface channeling occurring upon ion bombardment at 75° off normal, see Figure 9.3(f).

In their work the authors also present results on the energy dependence of the channeling mechanism. Utilizing ion bombardment under 86° , Redinger *et al.* found a steady increase of the maximum channeling length with increasing projectile energy (see Figure 4.14 *et seq.* of Reference [125]). However, this increase is non-linear and substantially enhanced for $E \geq 10 \text{ keV}$, which can be explained by a reduction of the energy loss per unit length in line with the energy dependence of the shadow cone (Equation 7.5). In fact, they observe "a transition from adatom vacancy production at the beginning of the trajectory to a fully developed vacancy trench at the end" [125].

Our studies performed on a graphene covered metal substrate have similar findings, but with a rapid decrease of the channeling length for $E = 15 \text{ keV}$. We attribute this behaviour to the different experimental parameters, in particular to the less grazing incidence angle $\vartheta = 75^\circ$, which allows for an onset of bulk channeling at these projectile energies.

Regarding the evolution of the defect patterns upon thermal treatment, we do not have access to experimental data for subsurface channeling alone. Yet, the temperature dependent annealing of metal surfaces in general has been widely studied [214, 220]. As discussed in Section 9.3 the disappearance of metal adatom clusters below 750 K is in line with previous findings. The healing of carbon vacancies via dislocation climb is substantiated in their disappearance around 970 K .

Furthermore we find similarity in the temperature dependence of the sputtering yield. In both systems, sputtering is promoted at elevated temperatures due to the mobility of vacancies which allows an increase of the zone of evolution in front of step edges.

Pattern Formation following Ion Bombardment

In a narrow temperature window of $T = 800 \dots 900$ K we observe a change in the graphene defect morphology, namely a hexagonal arrangement of vacancy type defects and vacancy agglomerates arises (see Figures 10.2 and 10.10). This pattern formation is caused by a relaxation of vacancies to the locations of minimal formation energy within one moiré unit cell. Hence, it is a result of the complex graphene/Ir(111) interface.

In contrast, pattern formation via ion bombardment on a bare Pt(111) surface - as studied in References [218] and [219] - is limited to the interplay of surface erosion and particle transport via diffusion at finite temperatures:

"Analyzing the damage created by single ions and small ion-fluences impinging onto flat terrace areas and into ascending step edges, it was possible to establish a model explaining the formation of vacancy grooves and the development of periodic ripple patterns for ion-fluences as low as $F = 1.0$ MLE. For temperatures $T \leq 450$ K, the formation of elongated vacancy grooves is solely due to the effect of the ion beam, which erodes material preferentially at ascending step edges. At higher temperatures $T > 450$ K, diffusion processes like the creation of step edge atoms by kink detachment overshadow the effect of the ion beam by relaxing the vacancy islands to compact shapes. It was found that at these temperatures the creation by channeling events of chains of vacancy islands aligned parallel to the ion beam direction facilitates the formation of vacancy grooves oriented along this same direction. For temperatures $T < 450$ K, where diffusion effects are dominated by the ion beam, periodic patterns are the result of the attractive/repulsive interaction in-between growing vacancy grooves. In the upper temperature regime $T > 450$ K where diffusion processes (formation of step edge atoms by kink detachment, step edge diffusion, etc.) are important, the formation of regular spaced ripple patterns is mainly due to the adatoms generated at the bottoms of vacancy grooves." [218]

Note that the employed ion fluences in both studies were up to 20 times higher than those of the experiments discussed in Chapter 10 (which is reasoned in the low dimensionality of the graphene/Ir(111) system). However, while for high fluences the interaction of neighboring grooves gains importance over the pure ion erosion, the underlying patterning mechanism does not change.

Summing up these findings, we can say that, although the defect formation mechanism following single ion impacts shows great resemblance in both systems, the pattern formation via thermal treatment and prolonged exposure is fundamentally different.

PART IV

Summary and Outlook

Water Adsorption

The discussion of results obtained for water adsorption on Pt(111) has been published in Physical Review B **82**, 161412(R) (2010) [138] and *Journal of Physics: Condensed Matter* **24**, 124103 (2012) [51]. The following reflects in large parts the published work but is extended in some paragraphs.

Platinum(111)

While the formation of a wetting layer on Pt(111) had been known for years, the structure of the adlayer has been widely discussed. More than 15 years ago Glebov *et al.* [12] were the first to observe two distinct wetting layer structures in their HAS experiments: (1) $\sqrt{37} \times \sqrt{37}$ R25.3°, and (2) $\sqrt{39} \times \sqrt{39}$ R16.1°. However, only recently, these studies have been successfully complemented by real space measurements [95] and density functional theory calculations [96].

Our experiments on Pt(111) show that step edges have a significant influence on the formation of an ordered water layer: By purposefully introducing steps on the surface we were able to establish long range order of the molecules. This order is significantly reduced when the step edge density decreases or a passivation of the steps prior to water exposure takes place. Our observation can be explained by a decreased amount of impurities on the terraces which are otherwise cause the formation of a disordered wetting layer.

Based on these findings we were able to reproduce both of the HOC superstructures and study their thermodynamic behaviour. At 140 K only a $\sqrt{37} \times \sqrt{37}$ R25.3° superstructure can be established, while at 130 K also a $\sqrt{39} \times \sqrt{39}$ R16.1° superstructure with slightly higher molecular density is formed. In the temperature range under concern the superstructures reversibly transform into each other by slight changes in coverage through molecule adsorption or desorption. The superstructures exhibit a complex pattern of molecules in different geometries which appears as triangular depressions embedded into a continuous matrix and an additional 2nd layer decoration in case of the $\sqrt{39}$. Associating a 2D Bravais lattice to the matrix phase for each superstructure we evaluated the spot intensities found in previous studies [10, 12, 78]. The calculated spots of the reciprocal lattice are among the brightest spots in the entire diffraction patterns, which lends additional credit to the structural motive proposed for the matrix phase.

Our experiments on the interaction between the first water layer and noble gases demonstrated the existence of an ordered Xe adlayer aligned on the underlying water structure. We find a $\sqrt{3} \times \sqrt{3}$ R30° arrangement with respect to the molecular matrix. This struc-

ture as well resembles the Xe nearest-neighbor distance. Consequently, we assume the formation of (ramified) islands to be preferred over the adsorption of individual molecules in specific binding sites on top of the water layer.

Investigating the coadsorption of CO on a closed water layer we found that CO is able to form widely spaced islands within the H₂O adlayer. This phase separation evidences that CO molecules adsorb even through the intact water layer and that the foreign molecules species is able to diffuse inside the water layer at the temperature of our experiment. These observations prove that the CO uptake [94] is almost completely due to the displacement of H₂O by CO. The uptake is $\approx 3\%$ already at low exposures of 1 L.

Investigating the stability of the first water layer we applied both high tunneling currents and bias voltages to our sample. While we observed a reorganization of the water molecules at high electron dose, high energy electrons of $E \approx 4\text{ eV}$ cause a dissociation of the molecules. The dissociation results in a low adlayer extending laterally several nm beyond the range of tip motion, indicating hole (electron) transport in the (anti-)bonding bands of the chemisorbed water layer. Finally, by these findings we are able to investigate the catalytic conversion of oxygen and hydrogen to water from a reverse point of view.

Putting together the information obtained in the previous chapters we are finally able to give an experimental proof of the structural model based on DFT calculations as proposed by Nie *et al.* [96].

Iridium(111)

Studying the wetting behaviour of water adsorbed on Ir(111) via TDS we have shown that water molecules form a continuous adlayer upon adsorption, i.e. water wets iridium. This result is justified by a pronounced desorption signal from the monolayer, which is energetically favoured over the multilayer structure. Similar findings were obtained recently by Pan *et al.* [103]. In the further course of our TDS analysis we could show that a few layer high water adsorbate film does not develop the bulk ice structure as it shows a considerable deficiency of desorption energy when compared to literature values. We find the bulk ice structure after adsorption of $\Theta \gg 10\text{ ML}$ and subsequent annealing above 140 K only. We attribute the formation of an intermediate state to a hydrophobic character of the wetting layer. Accordingly, the water film changes from wetting to a non-wetting growth mode as observed for Pt(111) [102] and/or is amorphous to a large fraction.

A closer inspection of the monolayer desorption signal unveils a reduction of the desorption energy for water coverages below $\Theta < 0.5\text{ ML}$. We directly addressed the bonding

geometry at the water-metal interface responsible for the formation of a wetting layer in a complementary, coverage dependent real-space analysis using STM. In contrast to Pt(111) we find water adsorbed on Ir(111) at 140 K to form individual clusters over a wide coverage range. Albeit the molecular structure of these clusters is closely related to the structural motifs known from Pt(111) an increase of the water coverage does not result in the growth of these nuclei and the formation of a continuous water network. Instead the sample topography shows a dense arrangement of these finite size building blocks. We attribute this to an electrostatic repulsion of the clusters which is reasoned by their polar character.

Increasing the coverage to $\Theta \approx 0.5$ ML finally leads to the formation of a continuous water network out of the cluster phase. Its molecular arrangement is nearly identical to the wetting layer observed on Pt(111), thereby offering a sound explanation for the TDS data, in particular the non-wetting multilayer growth. The stability of the Ir(111) wetting layer towards (energetic) tunneling electron is in line with the findings obtained for Pt(111).

Graphene

While the wetting behaviour and structure following water adsorption on metal substrates has been studied for years, the interaction of water molecules with a graphene sheet came into focus quite recently. As expected from theoretical considerations we observe a non-wetting behaviour in the system $\text{H}_2\text{O}/\text{Gr}$ at lowest temperatures, $T = 20$ K, in our TDS analysis. This is due to the lack of chemical bonds at the interface so that the adsorption is mainly governed by van-der-Waals forces. The transition of the water adlayer into a more strongly bound state occurs at $\Theta \approx 3.0$ ML. However, the desorption energy of this state does not match the value for bulk ice sublimation and is even lower than the one of the water multilayer on Ir(111), indicating a high degree of amorphization. We find the growth of this high-coverage structure kinetically stunted as its occurrence can be promoted by an increase of the adsorption temperature above 100 K.

In our complimentary real-space analysis we observe the formation of three-dimensional water clusters aligned in the graphene/Ir(111) moiré which, furthermore, are electronically decoupled from the substrate and obey a polar character. While the clustering behaviour of water is in line with theoretical predictions obtained for free-standing graphene [113–115], their alignment to the moiré pattern can be understood in terms of heterogeneous nucleation at the HCP sites. As the cluster size is limited by the size of the moiré cell we observe their coalescence at $\Theta \approx 3.0$ ML, in agreement with the structural transition recorded in TDS. While the potential landscape of the Gr/Ir(111) moiré is able to explain

the stunted growth of the high-coverage state at low temperatures, the difference in the binding energy is caused by differences in the surface energy for the two structures.

Again we find the bulk ice structure after adsorption of $\Theta \gg 10$ ML and subsequent annealing to $T > 140$ K.

Outlook

In the course of this thesis we were able to develop a conclusive model for the multifarious wetting behaviour of water on clean and graphene covered Ir(111). Yet these findings call for theoretical support. For the case of Pt(111) it was shown that DFT calculations in combination with STM studies are a power tool to determine the molecular arrangement of the wetting layer. [98] As our experiments on Ir(111) and graphene revealed several new aspects of the water-substrate interaction we have several open questions. In particular, we look for these calculations to quantitate the repulsion of water clusters on Ir(111), to evaluate the emergence of an ordered adlayer and to identify the driving force causing the inhomogeneity observed in the system H₂O/graphene.

On the experimental side one might think of performing similar studies with isotopically labeled water, D₂O, which influence the intermolecular bonding length (Ubbelohde effect [221] and may give rise to different adlayer structures. This aspect is of particular interest in the system H₂O/Ir(111), where a decomposition of molecules upon absorption has been observed [103].

Furthermore it would be interesting to validate the dissociative adsorption of water molecules on graphene vacancies [114, 222]. For this one has to introduce defects into the graphene layer, which links this part of the thesis to the findings discussed hereinafter.

Ion Bombardment

Grazing Incidence Ion Impacts on Graphene

In this work a graphene covered Ir(111) surface was exposed to grazing incidence ion irradiation and the resulting sample morphology is studied using scanning tunneling microscopy. Supported by MD simulation data we developed the model of interface channeling. In that model the pattern formation is explained via an oscillatory motion of the Xe ion in between the graphene layer and the metal substrate, resembling the mechanism of subsurface channeling in case of pristine metal surfaces. [125, 218] We find the ion to

cause vacancy clusters in the carbon layer as well as metal sputtering along its track. The sputtering yield for the substrate is strongly reduced as metal atoms are captured by the blanketing graphene network. The energy loss of the Xe ion is much larger encountering graphene than when hitting the metal substrate.

As the entire channeling event is of stochastic nature, a diversity of defect patterns is observed which is strongly dependent on the bombardment parameters like, e.g. the ion energy and species. Varying these parameters we can purposefully tune the spatial extent of the defect patterns. For heavy and swift ions the sample topography shows severe damage which we attribute to large angle scattering events and the initiation of complex collision cascades. We observe the onset of bulk channeling for 15 keV Xe bombardment. The overall defect morphology changes to point defects for projectiles with low energy and mass. A statistical evaluation of the experimentally observed defect patterns following 5 keV Xe bombardment is in excellent agreement with molecular dynamics simulations.

To gain detailed insight into the atomic structure of the defect patterns we investigated their thermal stability. In course of this analysis we could identify metal adatom clusters buried at the interface. Their formation is not accessible in the simulation due to the different time scale of defect creation and adatom diffusion. The graphene defects are thermally stable up to 900 K. We propose healing of the carbon lattice via the edge dislocation climb mechanism [43]. This leads to an entirely rebuilt graphene layer at $T \geq 1200$ K apart from energetically favorable defect configurations, which are stable up to the highest investigated temperatures of 1350 K. Contrary to ion bombardment experiments carried out on HOPG and Gr/Pt(111) we find no electronic signature for dangling bonds at point defects. Instead, we observe their saturation via formation of chemical bonds between the carbon layer and the metal substrate. This gives rise to a funnel-like shape of the vacancy clusters, as confirmed by DFT. These calculations furthermore predict a varying potential landscape for vacancies within the Gr/Ir(111) moiré unit cell which opens a path for ion beam structuring of graphene on Ir(111) by driving artificially induced defects into pre-determined potential sinks, i.e. a graphene nanomesh.

Pattern Formation in Graphene

In order to satisfy our requirement for a dense nanomesh, i.e. one vacancy agglomerate per moiré unit cell, we exposed the graphene covered Ir(111) surface to higher fluences, $F \approx 0.05$ MLE. Simultaneously, the projectile energy was lowered to $E = 1.0$ keV to create spatially confined defects only. Carrying out an annealing series we developed the following model: Large fluence ion bombardment leads to a quasi-amorphization of the

graphene sheet. Besides sputtering both iridium and carbon atoms are buried at the interface. While the annealing of iridium clusters follows the case of single ion impacts, the evolution of carbon clusters resembles the ripening process of carbidic clusters on Ir(111) during the growth process of graphene and terminate in bilayer graphene platelets at about 1000 K [46]. Only for temperatures higher than 1100 K these platelets are reintegrated into the graphene lattice. Thereby, lattice defects arise exhibiting a curvature therewith acting as nucleation sources for wrinkle formation.

The sample morphology is strongly dependent on the sample temperature during bombardment. At elevated $T \geq 800$ K the carbon sputtering yield is increased by a factor of three. This is due to thermally activated oscillations of the graphene layer [216] as well as coalescence of neighbouring vacancies into larger clusters promoting step edge erosion [217]. However, an increase of the sample temperature during bombardment is required to allow a reconstruction of the carbon lattice before sequent ion impacts occur, thereby avoiding proceeding amorphization of the graphene sheet. In the course of lowering the projectile energy to 0.5 keV - to counteract the increase of carbon sputtering - a regular defect pattern appeared spontaneously due to the interplay of creation and thermally activated diffusion of vacancies. We were able to drive and confine the vacancies at the HCP/FCC regions of the moiré superstructure, thereby forming a hexagonal graphene nanomesh with a 2.53 nm periodicity, opening new possibilities for tailoring the mechanical and electronic properties of graphene.

Outlook

In the course of this thesis we made out several pathways to tune the defect morphology in graphene following ion bombardment. Yet several parameters have not been considered due to technical limitations of our setup. Hence one can think of further tuning the defect patterns via (1) varying the angle of incidence, and (2) further lowering the ion energy, which will be discussed in the following:

1. All experiments presented in this thesis were carried out at an incidence angle of 75° with respect to the surface normal. Similar studies employing normal incidence ions [164] give rise to entirely different defect morphologies. Given that channeling motion in general is highly sensitive even to small changes of the angle of incidence [see Figure ??(b) and Reference [125]], one might ask how the sample morphology might be affected by further or less tilting of the ion beam. In particular one could determine the critical angle of incidence for which interface channeling breaks down.

-
2. In Section 9.2 we could demonstrate that the ion induced damage is heavily determined by the particle energy as we observed a wide spread of different defect morphologies following ion bombardment in the range of 0.5 keV to 15 keV. Further reduction of the ion energy might be accomplished by applying a counter-voltage on the sample to decelerate impinging ions before impact.

Combining these two aspects in combination with a proper choice of the ion species (see Section 9.2) one could obtain exclusively single vacancies in the graphene layer [48–50, 193] and study their thermodynamic behaviour in detail - without having to deal with energy transfer during measurements as in case of TEM studies. [176, 193] Based on these findings one could yield an improved graphene nanomesh with less secondary damage at the interface.

Once a graphene nanomesh of high quality is fabricated which satisfies the requirements according to our definition one might go a step further and probe its electronic properties. When it comes to the evaluation of the nanomesh several methods may be applied. For example angular resolved photoemission spectroscopy (ARPES) is a powerful tool to image the bandstructure in detail. Given an appropriate experimental setup one could monitor changes of the bandstructure during bombardment directly, and determine, e.g. whether a bandgap opening is achieved as intended, or not. In the course of this thesis preliminary measurements have been performed in collaboration with the Institut za fizika, Zagreb, Croatia, as shown in Section 10.4. While we observed a change of the bandstructure upon bombardment, no meaningful results could be extracted from these measurements due to the lack of precise determination of the ion current. Thus, a continuation of this collaborative project is strongly recommended.

A different approach to examine the electronic properties of the tailored graphene sheet on larger scale is to perform transport measurements. However, this technique would require a decoupling of the graphene sheet from the metal substrate and/or a transfer onto an insulating wafer. Recently, a method of exfoliation of graphene/Ir(111) was presented which might pave the way to this realization. [223] Note that the chemical bonding of the carbon atoms toward the metal substrate will probably affect the intercalation and require an optimization of the process.

Finally it should be mentioned that in future work one could transfer the findings and considerations of this thesis to different low-dimensional systems. Here boron nitride might be a prominent candidate, as it is structurally closely related to graphene and can be grown on Ir(111) in similar manner.

PART V

Appendix

APPENDIX A

Deutsche Kurzzusammenfassung (*German Abstract*)

Die vorliegende Arbeit gliedert sich in zwei Teilbereiche. Im ersten Teil untersuchen wir die thermodynamischen Eigenschaften und die Strukturbildung von Wasser auf Graphen und Edelmetalloberflächen. Der zweite Teil dieser Dissertation widmet sich dem Oberflächenschaden in Graphen auf Ir(111), welcher durch Ionenbeschuss unter streifendem Winkel verursacht wurde. Beide Teile schließen mit einem Vergleich der jeweiligen Probenysteme.

Wir untersuchen die Struktur und Stabilität der ersten Wasserlage auf Pt(111) mittels temperaturvariabler Rastertunnelmikroskopie. Dabei bilden wir über einen weiten Bedeckungsbereich zwei Strukturen ab, die zuvor bereits durch Beugungsmethoden nachgewiesen wurden. Bei einer Temperatur von 140 K beobachten wir eine Überstrukturphase der Form $\sqrt{37} \times \sqrt{37}$ R25.3°, wohingegen sich bei etwa 130 K zusätzlich eine zweite Struktur mit der Bezeichnung $\sqrt{39} \times \sqrt{39}$ R16.1° bildet. Diese Überstrukturphasen können durch geringe Bedeckungsänderungen im genannten Temperaturbereich reversibel ineinander überführt werden. Beide Benetzungslagen besitzen ein komplexes Muster, welches durch Moleküle in unterschiedlicher Adsorptionsgeometrie verursacht wird. Wir legen dar, dass die langreichweitige Ordnung dieser Muster auf einer gestuften Platinoberfläche signifikant erhöht ist. Dies ist vermutlich auf das Vermögen der Stufenkanten zurückzuführen Verunreinigungen wie Adsorbate von der Terrasse zu binden. Sättigt man diese Stufen vor der Wasseradsorption mittels CO-Molekülen ab, oder adsorbiert man Wasser auf einer flachen Metalloberfläche, so bildet sich eine ungeordnete Struktur in der Wasserlage. Diese Lage besitzt jedoch dieselben Strukturelemente wie die geordneten Phasen. Die Koadsorption von Xenon und CO belegt, dass die Wasserlage das Metallsubstrat vollständig bedeckt.

Darüber hinaus bestimmen wir die zweidimensionale Kristallstruktur von Xenon auf der chemisorbierten Wasserlage. Es zeigt sich eine hexagonale Struktur mit einer Gitterkonstanten ähnlich dem Festkörper, wobei die dichtgepackten Reihen der Xenon-Lage um 90° gegen jene des Wassergitters gedreht sind. Im Falle von CO zeigt sich, dass diese molekulare Spezies Wasser von der Pt(111)-Oberfläche verdrängt. Anhand unseres experimentellen Nachweises belegen wir bestehende Modelle. Abschließend untersuchen wir die Restrukturierung der Wasserlage in Folge hoher Tunnelströme, um die Strahlenschäden früherer Beugungsmethoden zu erklären.

Wir präsentieren experimentelle Daten in Hinblick auf das Benetzungsverhalten und die Strukturbildung von Wasser auf Ir(111). Basierend auf Thermodesorptionsspektroskopie-Messungen weisen wir die Existenz einer chemisorbierter ersten Wasserlage nach und führen eine bedeckungsabhängige Messreihe im Submonolagen-Bereich durch. Dabei zeigt sich, dass Wasser planare und insbesondere polare Cluster ausbildet. Für hohe Bedeckungen, $\Theta > 0.5$ ML, formt sich aus diesen eine kontinuierliche Wasserlage, deren molekulare Struktur große Ähnlichkeit zur chemisorbierter Lage auf Pt(111) aufweist. Mit Vollendung der Monolage ändert sich das Wachstum des Eisfilms, da die Monolage selbst hydrophoben Charakter besitzt. Sowohl für Pt(111) als auch für Ir(111) weisen wir nach, dass energiereiche Elektronen zur Dissoziation der Wassermoleküle beitragen und die Adsorbatlage im Umkreis der Manipulation in eine $\sqrt{3} \times \sqrt{3}$ R 30° -Struktur überführen.

Analog zum reinen Iridium-Substrat führen wir eine Messreihe zur Wasseradsorption auf einer vollständig mit Graphen bedeckten Ir(111)-Oberfläche durch. Wir zeigen, dass Wasser die Kohlenstofflage bei tiefen Temperaturen nicht benetzt und stattdessen dreidimensionale, elektronisch entkoppelte Kristallite in der Gr/Ir(111) Moiré-Struktur bildet. Oberhalb einer Bedeckung von $\Theta \approx 3.0$ ML formt sich eine amorphe Wasserlage, deren Auftreten durch das Erhöhen der Adsorptionstemperatur über 100 K begünstigt werden kann.

In Kombination von Rastertunnelmikroskopie-Experimenten und atomistischen Simulationen untersuchen wir die Defekterzeugung durch Ionenbeschuss in Gr/Ir(111). Dabei verwenden wir streifend einfallende Edelgasprojekte im keV-Bereich. Um den Beschusschaden einzelner Ionen sichtbar zu machen sind geringe Fluenzen gewählt. Wir zeigen, dass die Ionen in der Grenzschicht zwischen der Graphenlage und dem Iridium-Substrat reflektiert und gelenkt werden. Im Rahmen einer oszillierenden Bewegung erzeugen sie Leerstellen und andere Defekte, deren Gestalt durch die Beschussparameter maßgeblich bestimmt wird. Unsere Experimente zur thermischen Stabilität der Defektstrukturen geben

Einblick in ihre atomare Gestalt. Unterstützt durch Dichtefunktionaltheorie-Rechnungen zeigen wir, dass aufgebrochene Bindungen in der Kohlenstofflage am darunter liegenden Substrat gesättigt werden. Mit Einsetzen der Leerstellenmobilität ab etwa 800 K führt dies zu einer Diffusion der Leerstellen an energetisch günstige Orte innerhalb der Gr/Ir(111) Moiré-Struktur. Eine ausgeprägte Potentiallandschaft eröffnet die Möglichkeit zur Ausbildung eines periodischen Leerstellenmusters.

Um diese Struktur zu realisieren, vollziehen wir den Übergang von isolierten Einzelein-schüssen hin zu Fluenzen die einen Defekt pro Moiré-Einheitszelle gewährleisten. Wir diskutieren die Oberflächenbeschaffenheit in Folge ausgedehnter Ionenbestrahlung und analysieren ihre thermische Entwicklung. Wir zeigen, dass die Proben temperatur während der Bestrahlung von entscheidender Bedeutung ist, um die Potentiallandschaft aufrecht zu erhalten und damit die Diffusion der Leerstellenagglomerate zu leiten. Basierend auf der Ausarbeitung geeigneter Parameter hinsichtlich Ionenenergie und Fluenz geben wir einen experimentellen Beweis für die Bildung eines Leerstellengitters auf Nanometer-Skala.

APPENDIX B

Liste der Teilpublikationen (*List of Publications*)

Teile dieser Arbeit wurden bereits veröffentlicht in den folgenden Fachzeitschriften:

Parts of the results presented in this thesis can be found in the following publications:

- [138] S. Standop, A. Redinger, M. Morgenstern, T. Michely, and C. Busse
Molecular Structure of the H₂O Wetting Layer on Pt(111)
Physical Review B **82**, 161412(R) (2010)

- [51] S. Standop, M. Morgenstern, T. Michely, and C. Busse
H₂O on Pt(111): Structure and Stability of the First Wetting Layer
Journal of Physics: Condensed Matter **24**, 124103 (2012)

- [112] S. Standop, O. Lehtinen, C. Herbig, G. Lewes-Malandrakis, F. Craes, J. Kotakoski,
T. Michely, A. V. Krasheninnikov, and C. Busse
*Ion Impacts on Graphene/Ir(111): Interface Channeling, Vacancy Funnels, and a
Nanomesh*
Nano Letters **13**, 1948 (2013)

Abgesehen von diesen Themen habe ich auch an folgenden Publikationen mitgearbeitet:

Apart from these topics I also contributed to the following articles:

- [173] A. Redinger, S. Standop, T. Michely, Y. Rosandi, and H. M. Urbassek
Trails of Kilovolt Ions Created by Subsurface Channeling
Physical Review Letters **104**, 075501 (2010)

- [174] A. Redinger, S. Standop, Y. Rosandi, H. M. Urbassek, and T. Michely
Making channeling visible: keV noble gas ion trails on Pt(111)
New Journal of Physics **13**, 013002 (2011)

Konferenz- und Seminarbeiträge als präsentierender Autor:

Conference contributions to:

- DPG Frühjahrstagung der Sektion Kondensierte Materie, Regensburg (DE), 2010
- Seminar Kondensierte Materie, Aachen (DE), 2010
- European Conference on Surface Science 27, Groningen (NL), 2010
- DPG Frühjahrstagung der Sektion Kondensierte Materie, Dresden (DE), 2011
- 493. Wilhelm und Else Heraeus Seminar, Bad Honnef (DE), 2011
- Towards Reality in Nanoscale Materials V, Levi (FI), 2012
- DPG Frühjahrstagung der Sektion Kondensierte Materie, Berlin (DE), 2012
- Towards Reality in Nanoscale Materials VI, Levi (FI), 2013

APPENDIX C

Danksagung (*Acknowledgements*)

Zum Abschluss dieser Arbeit möchte ich mich bei all jenen bedanken, die zu ihrem Gelingen in der einen oder anderen Form beigetragen haben.

- Ich danke **Prof. Dr. Thomas Michely** für sein Engagement die Rolle meines Mentors in der BCGS zu übernehmen und mich so durch meine Studien- und Forschungszeit zu führen. Seine großartige Lehre hat mich damals schon für die Oberflächenphysik begeistert. Danke für deine Unterstützung.
- Ich danke auch **Prof. Dr. Markus Morgenstern** als Teil meines Promotionskomitees, für seine Vor- und Mitarbeit am Thema $\text{H}_2\text{O}/\text{Pt}(111)$ und für das Übernehmen des Zweitgutachtens.
- Besonderer Dank gebührt **Priv.-Doz. Dr. Carsten Busse**, der es mir ermöglichte, an diesem spannenden Thema zu arbeiten. Außerdem danke ich für vielen Diskussionen und Anregungen und das damit verbundene Vorantreiben meiner Arbeit.
- Besonderer Dank geht auch an **Norbert Henn**, für das Lösen vieler technischer Probleme und für die anregenden Gespräche bei unserer allmorgendlichen "Versammlung".
- Ich danke **Georgia Lewes-Malandrakis** und **Charlotte Herbig**, die im Rahmen ihrer Diplom- bzw. Masterarbeit einen großen Teil zum Gelingen dieser Arbeit beigetragen haben. Ich habe es immer genossen, mit euch im Labor zu stehen und hoffe, dass ich euch selbst eine Hilfe sein konnte!
- Danke an meine engsten Kollegen und Freunde **Sven Runte**, **Fabian Craes** und **Jürgen Klinkhammer** für die schöne Zeit im Kegel-Club. Danke für die enge Zusammenarbeit und Hilfestellung - ob im Labor, im Büro, oder spät am Abend.

This work was in large parts done in the context of cooperations and I want to express my gratitude to all collaborators.

- **Arkady Krasheninnikov, Ossi Lehtinen, and Jani Kotakoski** from the University of Helsinki, Finland, who performed the calculations on the ion bombardment of graphene and contributed a lot to the Nano Letter article which is part of this thesis. Thank you for your great work and meetings in Levi. Thank you for constantly pushing us. Kippis!
- **Marko Kralj, Marin Petrović, and Iva Šrut** from the Institut za fiziku, Zagreb, Croatia, who taught me how to acquire ARPES spectra. I really appreciate your hospitality during my stay in Zagreb and enjoyed my time being your guest. Hvala!

Des Weiteren möchte ich mich bei allen bisher ungenannten (ehemaligen) Mitgliedern der Arbeitsgruppe für die freundliche und produktive Atmosphäre bedanken. Sowie bei allen Mitarbeitern des II. Physikalischen Instituts, insbesondere den Werkstätten und Sekretariaten. Danke auch dir Carmen, für das ständige Jagen nach einer neuen Bestzeit.

Ich danke der Bonn-Cologne Graduate School of Physics and Astronomy für die eröffneten Möglichkeiten, die finanzielle Unterstützung und das Treffen vieler interessanter Personen. Dazu zählt vor allem Priv.-Doz. Dr. Bernd Diekmann, der mir als Mentor in der BCGS seit dem Hauptstudium zur Seite steht, mir den Blick über den Tellerrand der Festkörperphysik erhielt, und mir mehrfach die Möglichkeit gab, im Rahmen seiner Vorlesungen selbst vor die Seminarteilnehmer zu treten. Einzeln zu nennen sind hier aber auch Dr. Petra Neubauer-Guenther und Dr. Dietmar Weil, die mir immer eine Hilfe waren. Die Arbeit mit euch war spitze!

Zu guter Letzt, aber umso bedeutsamer, gilt mein herzlichster Dank meiner Familie. Ihr habt mir die gesamte Zeit über bedingungslos Rückhalt geboten und immer ein Ohr für mich offen. Ebenso danke ich meiner Freundin Sonja für diese ganz besondere Rolle, die sie in meinem Leben spielt. Ohne deine Unterstützung wäre ich nicht bis zu diesem Punkt gelangt. DANKE! *keinbiernix*

APPENDIX D

Bibliography

- [1] T. Bartels-Rausch: “Ten things we need to know about ice and snow”. *Nature* **494.7435** (2013), 27–29. DOI: 10.1038/494027a. (Cit. on p. 3).
- [2] M. Henderson: “The interaction of water with solid surfaces: fundamental aspects revisited”. *Surf. Sci. Rep.* **46.1-8** (2002), 5–308. DOI: 10.1016/S0167-5729(01)00020-6. (Cit. on pp. 3, 34, 44).
- [3] A. Hodgson and S. Haq: “Water adsorption and the wetting of metal surfaces”. *Surf. Sci. Rep.* **64.9** (2009), 381–451. DOI: 10.1016/j.surfrep.2009.07.001. (Cit. on pp. 3, 11, 13, 15, 21, 72, 100).
- [4] S Volkening et al.: “Dual-path mechanism for catalytic oxidation of hydrogen on platinum surfaces”. *Phys. Rev. Lett.* **83.13** (1999), 2672–2675. DOI: 10.1103/PhysRevLett.83.2672. (Cit. on pp. 3, 60, 86).
- [5] *Scientific Background on the Nobel Prize in Chemistry 2007*. Stockholm: The Royal Swedish Academy of Science, 2007 (cit. on p. 3).
- [6] M Morgenstern et al.: “The ice bilayer on Pt(111): Nucleation, structure and melting”. *Z. Phys. Chem.* **198** (1997), 43–72. (Cit. on pp. 3, 40, 64, 68).
- [7] K. Thurmer and N. C. Bartelt: “Growth of multilayer ice films and the formation of cubic ice imaged with STM”. *Phys. Rev. B* **77.19** (2008), 195425. DOI: 10.1103/PhysRevB.77.195425. (Cit. on pp. 3, 26, 40, 64, 66).
- [8] P. A. Thiel and T. E. Madey: “The Interaction of Water with Solid-Surfaces - Fundamental Aspects”. *Surf. Sci. Rep.* **7.6-8** (1987), 211–385. DOI: 10.1016/0167-5729(87)90001-X. (Cit. on pp. 3, 10, 12).

- [9] H Ogasawara et al.: “Structure and bonding of water on Pt(111)”. *Phys. Rev. Lett.* **89.27** (2002), 276102. DOI: 10.1103/PhysRevLett.89.276102. (Cit. on pp. 3, 15, 16, 60, 66, 100).
- [10] S Haq, J Harnett, and A Hodgson: “Growth of thin crystalline ice films on Pt(111)”. *Surf. Sci.* **505.1-3** (2002), 171–182. DOI: 10.1016/S0039-6028(02)01152-4. (Cit. on pp. 3, 13, 16, 34, 45, 54, 60, 66, 72, 73, 100, 183).
- [11] A. Picolin et al.: “Desorption of H₂O from Flat and Stepped Pt(111)”. *J. Phys. Chem. C* **113.2** (2009), 691–697. DOI: 10.1021/jp808170f. (Cit. on pp. 3, 14, 35, 42, 72, 73, 90, 100, 101).
- [12] A Glebov et al.: “Orientational ordering of two-dimensional ice on Pt(111)”. *J. Chem. Phys.* **106.22** (1997), 9382–9385. DOI: 10.1063/1.474008. (Cit. on pp. 3, 16, 17, 19, 44, 45, 47–50, 101, 183).
- [13] P. Feibelman: “Comment on "Vibrational recognition of hydrogen-bonded water networks on a metal surface"”. *Phys. Rev. Lett.* **91.5** (2003), 059601. DOI: 10.1103/PhysRevLett.91.059601. (Cit. on pp. 4, 16, 100).
- [14] C. Liu et al.: “Graphene-Based Supercapacitor with an Ultrahigh Energy Density”. *Nano Lett.* **10.12** (2010), 4863–4868. DOI: 10.1021/nl102661q. (Cit. on p. 4).
- [15] B. Oregan and M. Grätzel: “A Low-Cost, High-Efficiency Solar-Cell based on Dye-Sensitized Colloidal TiO₂ Films”. *Nature* **353.6346** (1991), 737–740. DOI: 10.1038/353737a0. (Cit. on p. 4).
- [16] S. Bae et al.: “Roll-to-roll production of 30-inch graphene films for transparent electrodes”. *Nat. Nanotechnology* **5.8** (2010), 574–578. DOI: 10.1038/NNANO.2010.132. (Cit. on p. 4).
- [17] A. K. Geim and K. S. Novoselov: “The rise of graphene”. *Nat. Mater.* **6.3** (2007), 183–191. DOI: 10.1038/nmat1849. (Cit. on p. 4).
- [18] A. H. Castro Neto et al.: “The electronic properties of graphene”. *Rev. Mod. Phys.* **81.1** (2009), 109–162. DOI: 10.1103/RevModPhys.81.109. (Cit. on pp. 4, 23).
- [19] A. K. Geim: “Graphene: Status and Prospects”. *Science* **324.5934** (2009), 1530–1534. DOI: 10.1126/science.1158877. (Cit. on p. 4).
- [20] C Berger et al.: “Ultrathin epitaxial graphite: 2D electron gas properties and a route toward graphene-based nanoelectronics”. *J. Phys. Chem. B* **108.52** (2004), 19912–19916. DOI: 10.1021/jp040650f. (Cit. on p. 4).

- [21] Y. Zhang et al.: “Experimental observation of the quantum Hall effect and Berry’s phase in graphene”. *Nature* **438.7065** (2005), 201–204. DOI: 10.1038/nature04235. (Cit. on p. 4).
- [22] C. Berger et al.: “Electronic confinement and coherence in patterned epitaxial graphene”. *Science* **312.5777** (2006), 1191–1196. DOI: 10.1126/science.1125925. (Cit. on p. 4).
- [23] M. I. Katsnelson: “Graphene: carbon in two dimensions”. *Materials Today* **10.1-2** (2007), 20–27. DOI: 10.1016/S1369-7021(06)71788-6. (Cit. on p. 4).
- [24] F. Schwierz: “Graphene transistors”. *Nat. Nanotechnology* **5.7** (2010), 487–496. DOI: 10.1038/NNANO.2010.89. (Cit. on p. 4).
- [25] M. Dragoman et al.: “Current oscillations in a wide graphene sheet”. *J. Appl. Phys.* **106.4** (2009), 044312. DOI: 10.1063/1.3208061. (Cit. on p. 4).
- [26] *Scientific Background on the Nobel Prize in Physics 2010*. Stockholm: The Royal Swedish Academy of Science, 2007 (cit. on p. 4).
- [27] Y. M. Lin et al.: “100-GHz Transistors from Wafer-Scale Epitaxial Graphene”. *Science* **327.5966** (2010), 662. DOI: 10.1126/science.1184289. (Cit. on p. 4).
- [28] F. Schedin et al.: “Detection of individual gas molecules adsorbed on graphene”. *Nat. Mater.* **6.9** (2007), 652–655. DOI: 10.1038/nmat1967. (Cit. on pp. 4, 25).
- [29] W. L. Chan and E. Chason: “Making waves: Kinetic processes controlling surface evolution during low energy ion sputtering”. *J. Appl. Phys.* **101.12** (2007), 121301. DOI: 10.1063/1.2749198. (Cit. on p. 4).
- [30] S Facsko et al.: “Formation of ordered nanoscale semiconductor dots by ion sputtering”. *Science* **285.5433** (1999), 1551–1553. DOI: 10.1126/science.285.5433.1551. (Cit. on p. 4).
- [31] A. V. Krasheninnikov and F. Banhart: “Engineering of nanostructured carbon materials with electron or ion beams”. *Nat. Mater.* **6.10** (2007), 723–733. DOI: 10.1038/nmat1996. (Cit. on p. 4).
- [32] A. V. Krasheninnikov and K. Nordlund: “Ion and electron irradiation-induced effects in nanostructured materials”. *J. Appl. Phys.* **107.7** (2010), 071301. DOI: 10.1063/1.3318261. (Cit. on p. 4).
- [33] J. Fernandez-Rossier and J. J. Palacios: “Magnetism in graphene nanoislands”. *Phys. Rev. Lett.* **99.17** (2007), 177204. DOI: 10.1103/PhysRevLett.99.177204. (Cit. on p. 4).

- [34] J. Cai et al.: “Atomically precise bottom-up fabrication of graphene nanoribbons”. *Nature* **466.7305** (2010), 470–473. DOI: 10.1038/nature09211. (Cit. on p. 4).
- [35] J. Bai et al.: “Graphene nanomesh”. *Nat. Nanotechnology* **5.3** (2010), 190–194. DOI: 10.1038/NNANO.2010.8. (Cit. on pp. 4, 117).
- [36] J. A. Fürst et al.: “Electronic properties of graphene antidot lattices”. *New J. Phys.* **11** (2009), 095020. DOI: 10.1088/1367-2630/11/9/095020. (Cit. on pp. 4, 117, 174).
- [37] T. Gunst et al.: “Thermoelectric properties of finite graphene antidot lattices”. *Phys. Rev. B* **84.15** (2011), 155449. DOI: 10.1103/PhysRevB.84.155449. (Cit. on p. 4).
- [38] H.-X. Yang et al.: “Inducing and optimizing magnetism in graphene nanomeshes”. *Phys. Rev. B* **84.21** (2011), 214404. DOI: 10.1103/PhysRevB.84.214404. (Cit. on p. 4).
- [39] Z. Zeng et al.: “Fabrication of Graphene Nanomesh by Using an Anodic Aluminum Oxide Membrane as a Template”. *Adv. Mater.* **24.30, SI** (2012), 4138–4142. DOI: 10.1002/adma.201104281. (Cit. on pp. 4, 117).
- [40] M. C. Lemme et al.: “Etching of Graphene Devices with a Helium Ion Beam”. *ACS Nano* **3.9** (2009), 2674–2676. DOI: 10.1021/nn900744z. (Cit. on p. 4).
- [41] S. Akcöltekin et al.: “Unzipping and folding of graphene by swift heavy ions”. *Appl. Phys. Lett.* **98.10** (2011), 103103. DOI: 10.1063/1.3559619. (Cit. on pp. 4, 120).
- [42] J. Kotakoski et al.: “From Point Defects in Graphene to Two-Dimensional Amorphous Carbon”. *Phys. Rev. Lett.* **106.10** (2011), 105505. DOI: 10.1103/PhysRevLett.106.105505. (Cit. on pp. 5, 118, 163).
- [43] J. H. Warner et al.: “Dislocation-Driven Deformations in Graphene”. *Science* **337.6091** (2012), 209–212. DOI: 10.1126/science.1217529. (Cit. on pp. 5, 150, 164, 187).
- [44] A. T. N’Diaye et al.: “Structure of epitaxial graphene on Ir(111)”. *New J. Phys.* **10** (2008), 043033. DOI: 10.1088/1367-2630/10/4/043033. (Cit. on pp. 5, 23, 24, 132).
- [45] J. Coraux et al.: “Structural coherency of graphene on Ir(111)”. *Nano Lett.* **8.2** (2008), 565–570. DOI: 10.1021/nl0728874. (Cit. on pp. 5, 23, 116, 164).

- [46] J. Coraux et al.: “Growth of graphene on Ir(111)”. *New J. Phys.* **11** (2009), 023006. DOI: 10.1088/1367-2630/11/2/023006. (Cit. on pp. 5, 23, 149, 150, 163–165, 188).
- [47] P. Sutter, J. T. Sadowski, and E. Sutter: “Graphene on Pt(111): Growth and substrate interaction”. *Phys. Rev. B* **80.24** (2009), 245411. DOI: 10.1103/PhysRevB.80.245411. (Cit. on pp. 5, 23).
- [48] M. M. Ugeda et al.: “Missing Atom as a Source of Carbon Magnetism”. *Phys. Rev. Lett.* **104.9** (2010), 096804. DOI: 10.1103/PhysRevLett.104.096804. (Cit. on pp. 5, 114, 115, 120, 148, 150, 152, 153, 189).
- [49] M. M. Ugeda et al.: “Point Defects on Graphene on Metals”. *Phys. Rev. Lett.* **107.11** (2011), 116803. DOI: 10.1103/PhysRevLett.107.116803. (Cit. on pp. 5, 120, 121, 148, 154, 189).
- [50] M. M. Ugeda et al.: “Electronic and structural characterization of divacancies in irradiated graphene”. *Phys. Rev. B* **85.12** (2012), 121402. DOI: 10.1103/PhysRevB.85.121402. (Cit. on pp. 5, 115, 120, 153, 189).
- [51] S. Standop et al.: “H₂O on Pt(111): structure and stability of the first wetting layer”. *J. Phys.: Condens. Matter* **24.12** (2012), 124103. DOI: 10.1088/0953-8984/24/12/124103. (Cit. on pp. 9, 16, 39, 183, 197).
- [52] A. Csaszar et al.: “On equilibrium structures of the water molecule”. *J. Chem. Phys.* **122.21** (2005), 214305. DOI: 10.1063/1.1924506. (Cit. on p. 10).
- [53] D. Eisenberg and W. Kauzmann: *The Structure and Properties of Water*. New York: Oxford University Press, 1969 (cit. on pp. 10, 11, 73, 90, 97, 100).
- [54] F Martin and H Zipse: “Charge distribution in the water molecule - A comparison of methods”. *J. Comput. Chem.* **26.1** (2005), 97–105. DOI: 10.1002/jcc.20157. (Cit. on p. 10).
- [55] B Winter et al.: “Full valence band photoemission from liquid water using EUV synchrotron radiation”. *J. Phys. Chem. A* **108.14** (2004), 2625–2632. DOI: 10.1021/jp030263q. (Cit. on p. 10).
- [56] G. W. Oetjen: *Gefriertrocknen (1. Auflage)*. Weinheim: VCH-Verlag, 1997 (cit. on p. 10).
- [57] J. D. Bernal and R. H. Fowler: “A Theory of Water and Ionic Solution, with Particular Reference to Hydrogen and Hydroxyl Ions”. *J. Chem. Phys.* **1.8** (1933), 515–548. (Cit. on p. 11).

- [58] L. Pauling: “The Structure and Entropy of Ice and of Other Crystals with Some Randomness of Atomic Arrangement”. *J. Am. Chem. Soc.* **57** (1935), 2680–2684. (Cit. on p. 11).
- [59] K Andersson et al.: “Water dissociation on Ru(001): An activated process”. *Phys. Rev. Lett.* **93.19** (2004), 196101. DOI: 10.1103/PhysRevLett.93.196101. (Cit. on p. 11).
- [60] N. Faradzhev et al.: “Stability of water monolayers on Ru(0001): Thermal and electronically induced dissociation”. *Chem. Phys. Lett.* **415.1-3** (2005), 165–171. DOI: 10.1016/j.cplett.2005.08.119. (Cit. on p. 11).
- [61] P. Feibelman: “Partial dissociation of water on Ru(0001)”. *Science* **295.5552** (2002), 99–102. DOI: 10.1126/science.1065483. (Cit. on pp. 11, 16).
- [62] T Jacob and W. Goddard: “Agostic interactions and dissociation in the first layer of water on Pt(111)”. *J. Am. Chem. Soc.* **126.30** (2004), 9360–9368. DOI: 10.1021/ja049920y. (Cit. on p. 11).
- [63] A. A. Phatak et al.: “Density Functional Theory Comparison of Water Dissociation Steps on Cu, Au, Ni, Pd, and Pt”. *J. Phys. Chem. C* **113.17** (2009), 7269–7276. DOI: 10.1021/jp810216b. (Cit. on p. 11).
- [64] B Li et al.: “The autocatalytic decomposition of water on Zr(0001)”. *Surf. Sci.* **384.1-3** (1997), 70–80. DOI: 10.1016/S0039-6028(97)00159-3. (Cit. on p. 11).
- [65] A. Carley, S Rassias, and M. Roberts: “the Specificity of Surface Oxygen in the Activation of Adsorbed Water at Metal-Surfaces”. *Surf. Sci.* **135.1-3** (1983), 35–51. DOI: 10.1016/0039-6028(83)90208-X. (Cit. on p. 11).
- [66] G.-C. Wang, S.-X. Tao, and X.-H. Bu: “A systematic theoretical study of water dissociation on clean and oxygen-preadsorbed transition metals”. *J. Catal.* **244.1** (2006), 10–16. DOI: 10.1016/j.jcat.2006.07.034. (Cit. on p. 11).
- [67] B. Atsushi et al.: “The first layer of water on Rh(111): Microscopic structure and desorption kinetics”. *J. Chem. Phys.* **125.5** (2006), 054717. DOI: 10.1063/1.2227393. (Cit. on p. 11).
- [68] K. Gibson, M Viste, and S. Sibener: “The adsorption of water on clean and oxygen preadsorbed Rh(111): Surface templating via (1x1)-O/Rh(111) induces formation of a novel high-density interfacial ice structure”. *J. Chem. Phys.* **112.21** (2000), 9582–9589. DOI: 10.1063/1.481603. (Cit. on pp. 11, 44).

- [69] C Ammon et al.: “Low-temperature partial dissociation of water on Cu(110)”. *Chem. Phys. Lett.* **377.1-2** (2003), 163–169. DOI: 10.1016/S0009-2614(03)01127-8. (Cit. on p. 11).
- [70] L. Guillemot and K. Bobrov: “On the formation of OH ordered layers by dissociation of H₂O on an oxygen covered Ag(110) surface: An STM investigation”. *Surf. Sci.* **601.3** (2007), 871–875. DOI: 10.1016/j.susc.2006.11.027. (Cit. on p. 11).
- [71] R. G. Quiller et al.: “Transient hydroxyl formation from water on oxygen-covered Au(111)”. *J. Chem. Phys.* **129.6** (2008), 064702. DOI: 10.1063/1.2965821. (Cit. on p. 11).
- [72] D. L. Doering and T. E. Madey: “The Adsorption of Water on Clean and Oxygen-Dosed Ru(0001)”. *Surf. Sci.* **123.2-3** (1982), 305–337. DOI: 10.1016/0039-6028(82)90331-4. (Cit. on p. 12).
- [73] P Vassilev, R. van Santen, and M. Koper: “Ab initio studies of a water layer at transition metal surfaces”. *J. Chem. Phys.* **122.5** (2005), 054701. DOI: 10.1063/1.1834489. (Cit. on p. 12).
- [74] O Konrad and T Lankau: “(H₂O)(3) on a virtual metal surface: the growth of the water bilayer”. *Chem. Phys. Lett.* **359.1-2** (2002), 35–40. DOI: 10.1016/S0009-2614(02)00653-X. (Cit. on p. 12).
- [75] S Meng, E. Wang, and S. Gao: “Water adsorption on metal surfaces: A general picture from density functional theory studies”. *Phys. Rev. B* **69.19** (2004), 195404. DOI: 10.1103/PhysRevB.69.195404. (Cit. on pp. 12, 13, 16, 100).
- [76] R. Smoluchowski: “Anisotropy of the Electronic Work Function of Metals”. *Phys. Rev.* **60** (1941), 661–674. (Cit. on pp. 13, 80).
- [77] N. Materer et al.: “Molecular Surface Structure of a Low-Temperature Ice Ih(0001) Crystal”. *J. Phys. Chem.* **99.17** (1995), 6267–6269. DOI: 10.1021/j100017a002. (Cit. on pp. 13, 54, 60).
- [78] G Zimbitas, S Haq, and A Hodgson: “The structure and crystallization of thin water films on Pt(111)”. *J. Chem. Phys.* **123.17** (2005), 174701. DOI: 10.1063/1.2060691. (Cit. on pp. 13, 45, 49, 183).
- [79] H Ogasawara, J Yoshinobu, and M Kawai: “Clustering behavior of water (D₂O) on Pt(111)”. *J. Chem. Phys.* **111.15** (1999), 7003–7009. DOI: 10.1063/1.479993. (Cit. on pp. 14, 15).

- [80] A. B. Anderson: “Reactions and Structures of Water on Clean and Oxygen Covered Pt(111) and Fe(100)”. *Surf. Sci.* **105.1** (1981), 159–176. DOI: 10.1016/0039-6028(81)90154-0. (Cit. on p. 14).
- [81] S. Holloway and K. H. Bennemann: “Study of water adsorption on metal surfaces”. *Surf. Sci.* **101.1-3** (1980), 327–333. DOI: 10.1016/0039-6028(80)90626-3. (Cit. on p. 14).
- [82] A. Picolin: “Wasser auf ungestuften und gestuften Platinflächen”. Diploma Thesis. University of Bonn, 2008 (cit. on pp. 15, 30, 34, 35).
- [83] G. Held and D. Menzel: “The Structure of the $p(\sqrt{3}\times\sqrt{3})R30$ -degrees Bilayer of D₂O on Ru(001)”. *Surf. Sci.* **316.1-2** (1994), 92–102. DOI: 10.1016/0039-6028(94)91131-2. (Cit. on p. 16).
- [84] G. Held and D. Menzel: “Structural Isotope Effect in Water Bilayers Adsorbed on Ru(001)”. *Phys. Rev. Lett.* **74.21** (1995), 4221–4224. DOI: 10.1103/PhysRevLett.74.4221. (Cit. on p. 16).
- [85] D Menzel: “Surface science - Water on a metal surface”. *Science* **295.5552** (2002), 58–59. DOI: 10.1126/science.1067922. (Cit. on p. 16).
- [86] S. Puisto et al.: “A refined LEED analysis of water on Ru{0001}: An experimental test of the partial dissociation model”. *Surf. Rev. Lett.* **10.2-3** (2003). 7th International Conference on the Structure of Surfaces, Newcastle, Australia, Jul 21-26, 2002, 487–492. DOI: 10.1142/S0218625X03005086. (Cit. on p. 16).
- [87] P. J. Feibelman: “The first wetting layer on a solid”. *Phys. Today* **63.2** (2010), 34–39. (Cit. on pp. 16, 100).
- [88] G Pirug and H. Bonzel: “UHV simulation of the electrochemical double layer: adsorption of HClO₄/H₂O on Au(111)”. *Surf. Sci.* **405.1** (1998), 87–103. DOI: 10.1016/S0039-6028(98)00055-7. (Cit. on p. 16).
- [89] F. P. Netzer and T. E. Madey: “Coadsorption-Induced Azimuthal Ordering in Molecular Adsorbate Layers: H₂O and NH₃ on Oxygen-Precovered Ni(111)”. *Phys. Rev. Lett.* **47.13** (1981), 928–931. DOI: 10.1103/PhysRevLett.47.928. (Cit. on p. 16).
- [90] J Cerda et al.: “Novel water overlayer growth on Pd(111) characterized with scanning tunneling microscopy and density functional theory”. *Phys. Rev. Lett.* **93.11** (2004), 116101. DOI: 10.1103/PhysRevLett.93.116101. (Cit. on pp. 16, 18, 64).

- [91] J. Jupille, P. Pareja, and J. Fusy: “Interaction of H₂O with basal and stepped faces of rhenium - An ESDIAD study”. *Surf. Sci.* **139.2-3** (1984), 505–540. DOI: 10.1016/0039-6028(84)90067-0. (Cit. on p. 16).
- [92] J. Zinck and W. H. Weinberg: “Chemisorption of Water of Rh(111)”. *J. Vac. Sci. Technol.* **17.1** (1980), 188–189. DOI: 10.1116/1.570427. (Cit. on p. 16).
- [93] P. A. Thiel, F. M. Hoffmann, and W. H. Weinberg: “Monolayer and multilayer adsorption of water on Ru(001)”. *J. Chem. Phys.* **75.11** (1981), 5556–5572. DOI: 10.1063/1.441960. (Cit. on p. 16).
- [94] J Harnett, S Haq, and A Hodgson: “Electron induced restructuring of crystalline ice adsorbed on Pt(111)”. *Surf. Sci.* **528.1-3** (2003). 9th International Workshop on Desorption Induced by Electronic Transitions, AUSSOIS, FRANCE, JUN 01-04, 2002, 15–19. DOI: 10.1016/S0039-6028(02)02604-3. (Cit. on pp. 16, 26, 44, 49, 53–55, 60, 65, 184).
- [95] S. Standop et al.: “Molecular structure of ice on Pt(111)”. *Verh. Deutsch. Phys. G.* **3** (2010), O 27.7. (Cit. on pp. 17, 183).
- [96] S. Nie et al.: “Pentagons and Heptagons in the First Water Layer on Pt(111)”. *Phys. Rev. Lett.* **105.2** (2010), 026102. DOI: 10.1103/PhysRevLett.105.026102. (Cit. on pp. 17–20, 39, 40, 63, 67, 80, 183, 184).
- [97] S. Standop: “Strukturuntersuchung im System H₂O/Platin(111)”. Diploma Thesis. University of Cologne, 2009 (cit. on pp. 18, 20).
- [98] P. J. Feibelman et al.: “Interpretation of high-resolution images of the best-bound wetting layers on Pt(111)”. *J. Chem. Phys.* **133.15** (2010), 154703. DOI: 10.1063/1.3488803. (Cit. on pp. 18, 64, 65, 100, 101, 186).
- [99] C. R. Fuselier, J. C. Raich, and N. S. Gillis: “Equilibrium Configurations of Commensurate Adsorbed Monolayers - Argon on Graphite”. *Surf. Sci.* **92.2-3** (1980), 667–680. DOI: 10.1016/0039-6028(80)90229-0. (Cit. on p. 19).
- [100] A Glebov et al.: “A helium atom scattering study of the structure and phonon dynamics of the ice surface”. *J. Chem. Phys.* **112.24** (2000), 11011–11022. DOI: 10.1063/1.481741. (Cit. on pp. 21, 74, 82, 100).
- [101] G. Kimmel et al.: “Crystalline ice growth on Pt(111): Observation of a hydrophobic water monolayer”. *Phys. Rev. Lett.* **95.16** (2005), 166102. DOI: 10.1103/PhysRevLett.95.166102. (Cit. on pp. 21, 74, 82, 100, 101).

- [102] K. Thurmer and N. C. Bartelt: “Nucleation-limited dewetting of ice films on pt(111)”. *Phys. Rev. Lett.* **100.18** (2008), 186101. DOI: 10.1103/PhysRevLett.100.186101. (Cit. on pp. 21, 74, 82, 93, 100, 101, 184).
- [103] M. Pan, S. Hoang, and C. B. Mullins: “Interaction of water with the clean and oxygen pre-covered Ir(111) surface”. *Catal. Today* **160.1** (2011), 198–203. DOI: 10.1016/j.cattod.2010.05.008. (Cit. on pp. 22, 35, 75, 78, 102, 184, 186).
- [104] P. R. Wallace: “The Band Theory of Graphite”. *Phys. Rev.* **71.9** (1947), 622–634. DOI: 10.1103/PhysRev.71.622. (Cit. on p. 23).
- [105] K. V. Emtsev et al.: “Interaction, growth, and ordering of epitaxial graphene on SiC{0001} surfaces: A comparative photoelectron spectroscopy study”. *Phys. Rev. B* **77.15** (2008), 155303. DOI: 10.1103/PhysRevB.77.155303. (Cit. on p. 23).
- [106] T. Ohta et al.: “Morphology of graphene thin film growth on SiC(0001)”. *New J. Phys.* **10** (2008), 023034. DOI: 10.1088/1367-2630/10/2/023034. (Cit. on p. 23).
- [107] J. Wintterlin and M.-L. Bocquet: “Graphene on metal surfaces”. *Surf. Sci.* **603.10-12** (2009), 1841–1852. DOI: 10.1016/j.susc.2008.08.037. (Cit. on p. 23).
- [108] Y Gamo et al.: “Atomic structure of monolayer graphite formed on Ni(111)”. *Surf. Sci.* **374.1-3** (1997), 61–64. DOI: 10.1016/S0039-6028(96)00785-6. (Cit. on p. 23).
- [109] H Ueta et al.: “Highly oriented monolayer graphite formation on Pt(111) by a supersonic methane beam”. *Surf. Sci.* **560.1-3** (2004), 183–190. DOI: 10.1016/j.susc.2004.04.039. (Cit. on p. 23).
- [110] C. Busse et al.: “Graphene on Ir(111): Physisorption with Chemical Modulation”. *Phys. Rev. Lett.* **107.3** (2011), 036101. DOI: 10.1103/PhysRevLett.107.036101. (Cit. on pp. 23, 24, 127, 128, 142, 154).
- [111] J. Knudsen et al.: “Clusters binding to the graphene moire on Ir(111): X-ray photoemission compared to density functional calculations”. *Phys. Rev. B* **85.3** (2012), 035407. DOI: 10.1103/PhysRevB.85.035407. (Cit. on p. 24).
- [112] S. Standop et al.: “Ion Impacts on Graphene/Ir(111): Interface Channeling, Vacancy Funnels, and a Nanomesh”. *Nano Lett.* **13** (2013), 1948–1955. DOI: 10.1021/nl304659n. (Cit. on pp. 24, 123, 131, 159, 197).

- [113] O. Leenaerts, B. Partoens, and F. M. Peeters: “Adsorption of H₂O, NH₃, CO, NO₂, and NO on graphene: A first-principles study”. *Phys. Rev. B* **77.12** (2008), 125416. DOI: 10.1103/PhysRevB.77.125416. (Cit. on pp. 24, 90, 92, 100, 102, 185).
- [114] P. Cabrera-Sanfelix and G. R. Darling: “Dissociative adsorption of water at vacancy defects in graphite”. *J. Phys. Chem. C* **111.49** (2007), 18258–18263. DOI: 10.1021/jp076241b. (Cit. on pp. 24, 25, 90, 100, 102, 185, 186).
- [115] O. Leenaerts, B. Partoens, and F. M. Peeters: “Water on graphene: Hydrophobicity and dipole moment using density functional theory”. *Phys. Rev. B* **79.23** (2009), 235440. DOI: 10.1103/PhysRevB.79.235440. (Cit. on pp. 24, 25, 90, 92, 95, 97, 100, 102, 185).
- [116] J. Rafiee et al.: “Superhydrophobic to Superhydrophilic Wetting Control in Graphene Films”. *Adv. Mater.* **22.19** (2010), 2151+. DOI: 10.1002/adma.200903696. (Cit. on pp. 25, 90, 97).
- [117] J. Rafiee et al.: “Wetting transparency of graphene”. *Nat. Mater.* **11.3** (2012), 217–222. DOI: 10.1038/NMAT3228. (Cit. on pp. 25, 95).
- [118] G. A. Kimmel et al.: “No Confinement Needed: Observation of a Metastable Hydrophobic Wetting Two-Layer Ice on Graphene”. *J. Am. Chem. Soc.* **131.35** (2009), 12838–12844. DOI: 10.1021/ja904708f. (Cit. on p. 25).
- [119] A. P. Seitsonen et al.: “Structure and stability of graphene nanoribbons in oxygen, carbon dioxide, water, and ammonia”. *Phys. Rev. B* **82.11** (2010), 115425. DOI: 10.1103/PhysRevB.82.115425. (Cit. on pp. 25, 26).
- [120] T. O. Wehling, A. I. Lichtenstein, and M. I. Katsnelson: “First-principles studies of water adsorption on graphene: The role of the substrate”. *Appl. Phys. Lett.* **93.20** (2008), 202110. DOI: 10.1063/1.3033202. (Cit. on p. 25).
- [121] T. O. Wehling, M. I. Katsnelson, and A. I. Lichtenstein: “Adsorbates on graphene: Impurity states and electron scattering”. *Chem. Phys. Lett.* **476.4-6** (2009), 125–134. DOI: 10.1016/j.cplett.2009.06.005. (Cit. on p. 25).
- [122] J. Scherer et al.: “Water adsorption on heteroepitaxial graphene”. *Verh. Deutsch. Phys. G.* **3** (2012), O 34.19. (Cit. on p. 25).
- [123] K Morgenstern and K. Rieder: “Dissociation of water molecules with the scanning tunnelling microscope”. *Chem. Phys. Lett.* **358.3-4** (2002), 250–256. DOI: 10.1016/S0009-2614(02)00593-6. (Cit. on pp. 26, 54, 83).

- [124] M. Mehlhorn, H. Gawronski, and K. Morgenstern: “Electron Damage to Supported Ice Investigated by Scanning Tunneling Microscopy and Spectroscopy”. *Phys. Rev. Lett.* **101.19** (2008), 196101. DOI: 10.1103/PhysRevLett.101.196101. (Cit. on pp. 26, 54, 55, 60, 83, 86).
- [125] A. Redinger: “Surface damage through grazing incidence ions investigated by scanning tunneling microscopy”. PhD thesis. RWTH Aachen University, 2010. URL: <http://darwin.bth.rwth-aachen.de/opus3/volltexte/2010/3050/> (cit. on pp. 29, 33, 105–110, 112, 139, 177–179, 186, 188).
- [126] T Michely, M Kaiser, and M. Rost: “Plug’n’play scanning probe microscopy”. *Rev. Sci. Instrum.* **71.12** (2000), 4461–4467. DOI: 10.1063/1.1322587. (Cit. on p. 29).
- [127] W. Ranke: *Thermal Analysis - TDS*. URL: http://pubman.mpdl.mpg.de/pubman/item/escidoc:740439:1/component/escidoc:740438/FHIAC_Ranke_Thermal_analysis_TDS.pdf (cit. on p. 30).
- [128] P. Redhead: “Thermal desorption of gases”. *Vacuum* **12.4** (1962), 203–211. DOI: 10.1016/0042-207X(62)90978-8. (Cit. on p. 32).
- [129] D. A. King: “Thermal Desorption from Metal-Surfaces”. *Surf. Sci.* **47.1** (1975), 384–402. DOI: 10.1016/0039-6028(75)90302-7. (Cit. on p. 32).
- [130] R. van Gastel et al.: “Selecting a single orientation for millimeter sized graphene sheets”. *Appl. Phys. Lett.* **95.12** (2009), 121901. DOI: 10.1063/1.3225554. (Cit. on p. 33).
- [131] W Widdra et al.: “Rare-gas thermal desorption from flat and stepped platinum surfaces: Lateral interactions and the influence of dimensionality”. *Phys. Rev. B* **57.7** (1998), 4111–4126. DOI: 10.1103/PhysRevB.57.4111. (Cit. on p. 34).
- [132] G. Kimmel et al.: “Temperature independent physisorption kinetics and adsorbate layer compression for Ar adsorbed on Pt(111)”. *J. Chem. Phys.* **119.13** (2003), 6776–6783. DOI: 10.1063/1.1604111. (Cit. on p. 34).
- [133] J. K. Fremerey: “The Spinning Rotor Gauge”. *J. Vac. Sci. Technol., A* **3.3** (1985), 1715–1720. DOI: 10.1116/1.573007. (Cit. on p. 34).
- [134] G. B. Fisher: “Monolayer and Multilayer Adsorption of Water on the Pt(111) Surface”. *General Motors Research Publication No. GMR-4007/PCP-171* (1982). (Cit. on p. 34).

- [135] D. M. Collins and W. E. Spicer: “Adsorption of CO, O₂, and H₂ on Pt - 1 - Thermal Desorption Spectroscopy Studies”. *Surf. Sci.* **69.1** (1977), 85–113. DOI: 10.1016/0039-6028(77)90163-7. (Cit. on pp. 35, 54).
- [136] H Steininger, S Lehwald, and H Ibach: “On the Adsorption of CO on Pt(111)”. *Surf. Sci.* **123.2-3** (1982), 264–282. DOI: 10.1016/0039-6028(82)90328-4. (Cit. on pp. 35, 42, 43, 53).
- [137] P. Feulner and D. Menzel: “Simple Ways to Improve Flash Desorption Measurements from Single-Crystal Surfaces”. *J. Vac. Sci. Technol.* **17.2** (1980), 662–663. DOI: 10.1116/1.570537. (Cit. on pp. 36, 70).
- [138] S. Standop et al.: “Molecular structure of the H₂O wetting layer on Pt(111)”. *Phys. Rev. B* **82.16** (2010), 161412. DOI: 10.1103/PhysRevB.82.161412. (Cit. on pp. 39, 42, 183, 197).
- [139] K Christmann and G Ertl: “Interaction of Hydrogen with Pt(111) - Role of Atomic Steps”. *Surf. Sci.* **60.2** (1976), 365–384. DOI: 10.1016/0039-6028(76)90322-8. (Cit. on p. 43).
- [140] M Kalff, G Comsa, and T Michely: “How sensitive is epitaxial growth to adsorbates?” *Phys. Rev. Lett.* **81.6** (1998), 1255–1258. DOI: 10.1103/PhysRevLett.81.1255. (Cit. on p. 44).
- [141] N Chen, P Blowers, and R. Masel: “Formation of hydronium and water-hydronium complexes during coadsorption of hydrogen and water on (2x1)Pt(110)”. *Surf. Sci.* **419.2-3** (1999), 150–157. DOI: 10.1016/S0039-6028(98)00774-2. (Cit. on p. 44).
- [142] K Morgenstern and J Nieminen: “Imaging water on Ag(111): Field induced re-orientation and contrast inversion”. *J. Chem. Phys.* **120.22** (2004), 10786–10791. DOI: 10.1063/1.1737366. (Cit. on p. 45).
- [143] G. Ertl and J. Küppers: *Low Energy Electrons and Surface Chemistry*. VCH, 1985 (cit. on p. 47).
- [144] G. A. Kimmel et al.: “Crystalline ice growth on Pt(111) and Pd(111): Nonwetting growth on a hydrophobic water monolayer”. *J. Chem. Phys.* **126.11** (2007), 114702. DOI: 10.1063/1.2672869. (Cit. on p. 51).
- [145] M. Faraday: *Experimental Researches in Electricity, vol. 2*. R. J. Taylor, 1844 (cit. on p. 51).
- [146] J. J. Berzelius. *Ber. Chem.* **15** (1837), 237. (Cit. on p. 51).

- [147] A Michaelides and P Hu: “Catalytic water formation on platinum: A first-principles study”. *J. Am. Chem. Soc.* **123.18** (2001), 4235–4242. DOI: 10.1021/ja003576x. (Cit. on pp. 51, 60, 64).
- [148] J Bergeld, B Kasemo, and D. Chakarov: “CO oxidation on Pt(111) promoted by coadsorbed H₂O”. *Surf. Sci.* **495.3** (2001), L815–L820. DOI: 10.1016/S0039-6028(01)01598-9. (Cit. on pp. 51, 53).
- [149] M Kinne et al.: “Coadsorption of D₂O and CO on Pt(111) studied by in situ high-resolution X-ray photoelectron spectroscopy”. *Langmuir* **20.5** (2004), 1819–1826. DOI: 10.1021/1a035913w. (Cit. on pp. 51, 54).
- [150] H Hopster and H Ibach: “Adsorption of CO on Pt(111) and Pt6(111)x(111) studied by High-Resolution Electron-Energy Loss Spectroscopy and Thermal Desorption Spectroscopy”. *Surf. Sci.* **77.1** (1978), 109–117. DOI: 10.1016/0039-6028(78)90164-4. (Cit. on p. 53).
- [151] D. F. Ogletree, M. A. Van Hove, and G. A. Somorjai: “LEED Intensity Analysis of the Structures of Clean Pt(111) and of CO adsorbed on Pt(111) in the c(4x2) Arrangement”. *Surf. Sci.* **173.2-3** (1986), 351–365. DOI: 10.1016/0039-6028(86)90195-0. (Cit. on p. 53).
- [152] C. T. Campbell et al.: “A Molecular-Beam Investigation of the Interactions of CO with a Pt(111) Surface”. *Surf. Sci.* **107.1** (1981), 207–219. DOI: 10.1016/0039-6028(81)90621-X. (Cit. on p. 54).
- [153] P Lofgren and B Kasemo: “Poisoning of the adsorption of CO, O-2 and D-2 on Pt(111) by preadsorbed H₂O”. *Catal. Lett.* **53.1-2** (1998), 33–36. DOI: 10.1023/A:1019025032025. (Cit. on p. 54).
- [154] N. Petrik and G. Kimmel: “Electron-stimulated sputtering of thin amorphous solid water films on Pt(111)”. *J. Chem. Phys.* **123.5** (2005), 054702. DOI: 10.1063/1.1943388. (Cit. on pp. 54, 55, 66).
- [155] C Clay, S Haq, and A Hodgson: “Hydrogen bonding in mixed OH+H₂O overlayers on Pt(111)”. *Phys. Rev. Lett.* **92.4** (2004), 046102. DOI: 10.1103/PhysRevLett.92.046102. (Cit. on pp. 60, 68).
- [156] C. Kittel: *Introduction to Solid State Physics*. John Wiley and Sons, 1971 (cit. on p. 65).

- [157] G. Ertl, M. Neumann, and K. M. Streit: “Chemisorption of CO on Pt(111) Surface”. *Surf. Sci.* **64.2** (1977), 393–410. DOI: 10.1016/0039-6028(77)90052-8. (Cit. on p. 65).
- [158] G. Zimbitas et al.: “Wetting of mixed OH/H₂O layers on pt(111)”. *J. Chem. Phys.* **128.7** (2008), 074701. DOI: 10.1063/1.2830266. (Cit. on p. 67).
- [159] A. T. N’Diaye et al.: “Two-dimensional Ir cluster lattice on a graphene moire on Ir(111)”. *Phys. Rev. Lett.* **97.21** (2006), 215501. DOI: 10.1103/PhysRevLett.97.215501. (Cit. on p. 95).
- [160] J. A. Venables and M. Bienfait: “Reaction Order in Thermal Desorption Spectroscopy”. *Surf. Sci.* **61.2** (1976), 667–672. DOI: 10.1016/0039-6028(76)90076-5. (Cit. on p. 95).
- [161] J. A. Venables, G. D. T. Spiller, and M. Hanbucken: “Nucleation and Growth of Thin Films”. *Rep. Prog. Phys.* **47.4** (1984), 399–459. DOI: 10.1088/0034-4885/47/4/002. (Cit. on p. 95).
- [162] A. T. N’Diaye et al.: “A versatile fabrication method for cluster superlattices”. *New J. Phys.* **11** (2009), 103045. DOI: 10.1088/1367-2630/11/10/103045. (Cit. on pp. 95, 164).
- [163] P. Voorhees: “The Theory of Ostwald Ripening”. *J. Stat. Phys.* **38.1-2** (1985), 231–252. DOI: 10.1007/BF01017860. (Cit. on p. 97).
- [164] C. Herbig: “Graphene Nanopatterns on Ir(111) by Ion Irradiation and Damage Annealing”. MA thesis. University of Cologne, 2012 (cit. on pp. 105, 106, 108, 110, 112, 123, 124, 131, 159, 188).
- [165] H. Winter: “Collisions of atoms and ions with surfaces under grazing incidence”. *Phys. Rep.* **367.5** (2002), 387–582. DOI: 10.1016/S0370-1573(02)00010-8. (Cit. on pp. 107, 111).
- [166] O. S. Oen: “Universal Shadow Cone Expressions for an Atom in an Ion-Beam”. *Surf. Sci.* **131.2-3** (1983), L407–L411. DOI: 10.1016/0039-6028(83)90269-8. (Cit. on p. 108).
- [167] H. Gnaser: “Low-energy ion irradiation of solid surfaces - Introduction”. In: *Low-Energy Ion Irradiation of Solid Surfaces*. Vol. 146. Springer Tracts in Modern Physics. 1999, 1+ (cit. on pp. 108, 109, 112).

- [168] W. Schilling and H. Ullmaier: “Physics of Radiation Damage in Metals”. In: *Materials Science and Technology*. Wiley-VCH Verlag GmbH & Co. KGaA, 2006. DOI: 10.1002/9783527603978.mst0113 (cit. on pp. 108, 112).
- [169] M. Nastasi: *Ion Implantation and Synthesis of Materials*. Berlin: Springer, 2006 (cit. on p. 109).
- [170] H. Gades and H. M. Urbassek: “Molecular-Dynamics Simulation of Adatom Formation under keV-Ion Bombardment of Pt(111)”. *Phys. Rev. B* **50.15** (1994), 11167–11174. DOI: 10.1103/PhysRevB.50.11167. (Cit. on p. 110).
- [171] P. Sigmund: “Theory of Sputtering. I. Sputtering Yield of Amorphous and Polycrystalline Targets”. *Physical Review* **184.2** (1969), 383. DOI: 10.1103/PhysRev.184.383. (Cit. on p. 110).
- [172] H. H. Andersen and R. Behrisch: *Sputtering by particle bombardment*. English. Springer-Verlag, Berlin, New York, 1981 (cit. on p. 111).
- [173] A. Redinger et al.: “Trails of Kilovolt Ions Created by Subsurface Channeling”. *Phys. Rev. Lett.* **104.7** (2010), 075501. DOI: 10.1103/PhysRevLett.104.075501. (Cit. on pp. 112, 135, 138, 148, 178, 197).
- [174] A. Redinger et al.: “Making channeling visible: keV noble gas ion trails on Pt(111)”. *New J. Phys.* **13** (2011), 013002. DOI: 10.1088/1367-2630/13/1/013002. (Cit. on pp. 112, 113, 138, 163, 178, 179, 197).
- [175] O. Lehtinen et al.: “Effects of ion bombardment on a two-dimensional target: Atomistic simulations of graphene irradiation”. *Phys. Rev. B* **81.15** (2010), 153401. DOI: 10.1103/PhysRevB.81.153401. (Cit. on p. 114).
- [176] F. Banhart, J. Kotakoski, and A. V. Krashennnikov: “Structural Defects in Graphene”. *ACS Nano* **5.1** (2011), 26–41. DOI: 10.1021/nn102598m. (Cit. on pp. 114–116, 164, 189).
- [177] L Li, S Reich, and J Robertson: “Defect energies of graphite: Density-functional calculations”. *Phys. Rev. B* **72.18** (2005), 184109. DOI: 10.1103/PhysRevB.72.184109. (Cit. on p. 114).
- [178] A. Krashennnikov et al.: “Bending the rules: Contrasting vacancy energetics and migration in graphite and carbon nanotubes”. *Chem. Phys. Lett.* **418.1-3** (2006), 132–136. DOI: 10.1016/j.cplett.2005.10.106. (Cit. on p. 114).

- [179] N Fukata, A Kasuya, and M Suezawa: “Formation energy of vacancy in silicon determined by a new quenching method”. *Physica B* **308** (2001). 21st International Conference on Defects in Semiconductors, GIESSEN, GERMANY, JUL 16-20, 2001, 1125–1128. DOI: 10.1016/S0921-4526(01)00908-5. (Cit. on p. 114).
- [180] K. Maier et al.: “High-Temperature Positron-Annihilation and Vacancy Formation in Refractory-Metals”. *Philos. Mag. A* **40.5** (1979), 701–728. (Cit. on p. 114).
- [181] P. Lehtinen et al.: “Magnetic properties and diffusion of adatoms on a graphene sheet”. *Phys. Rev. Lett.* **91.1** (2003), 017202. DOI: 10.1103/PhysRevLett.91.017202. (Cit. on pp. 116, 179).
- [182] O. V. Yazyev and S. G. Louie: “Topological defects in graphene: Dislocations and grain boundaries”. *Phys. Rev. B* **81.19** (2010), 195420. DOI: 10.1103/PhysRevB.81.195420. (Cit. on pp. 116, 164).
- [183] T. G. Pedersen et al.: “Graphene antidot lattices: Designed defects and spin qubits”. *Phys. Rev. Lett.* **100.13** (2008), 136804. DOI: 10.1103/PhysRevLett.100.136804. (Cit. on pp. 117, 174).
- [184] H. Sahin and S. Ciraci: “Structural, mechanical, and electronic properties of defect-patterned graphene nanomeshes from first principles”. *Phys. Rev. B* **84.3** (2011), 035452. DOI: 10.1103/PhysRevB.84.035452. (Cit. on pp. 117, 174).
- [185] I. I. Naumov and A. M. Bratkovsky: “Semiconducting graphene nanomeshes”. *Phys. Rev. B* **85.20** (2012), 201414. DOI: 10.1103/PhysRevB.85.201414. (Cit. on pp. 117, 174).
- [186] W. Oswald and Z. Wu: “Energy gaps in graphene nanomeshes”. *Phys. Rev. B* **85.11** (2012), 115431. DOI: 10.1103/PhysRevB.85.115431. (Cit. on pp. 117, 174).
- [187] T. Shen et al.: “Magnetoconductance oscillations in graphene antidot arrays”. *Appl. Phys. Lett.* **93.12** (2008), 122102. DOI: 10.1063/1.2988725. (Cit. on p. 117).
- [188] J. Eroms and D. Weiss: “Weak localization and transport gap in graphene antidot lattices”. *New J. Phys.* **11** (2009), 095021. DOI: 10.1088/1367-2630/11/9/095021. (Cit. on p. 117).
- [189] X. Liang et al.: “Formation of Bandgap and Subbands in Graphene Nanomeshes with Sub-10 nm Ribbon Width Fabricated via Nanoimprint Lithography”. *Nano Lett.* **10.7** (2010), 2454–2460. DOI: 10.1021/nl100750v. (Cit. on p. 117).

- [190] O. Akhavan: “Graphene Nanomesh by ZnO Nanorod Photocatalysts”. *ACS Nano* **4.7** (2010), 4174–4180. DOI: 10.1021/nn1007429. (Cit. on p. 117).
- [191] P. L. Neumann et al.: “Large scale nanopatterning of graphene”. *Nucl. Instrum. Methods Phys. Res., Sect. B* **282** (2012), 130–133. DOI: 10.1016/j.nimb.2011.08.044. (Cit. on p. 117).
- [192] C. J. Russo and J. A. Golovchenko: “Atom-by-atom nucleation and growth of graphene nanopores”. *Proc. Natl. Acad. Sci. U. S. A.* **109.16** (2012), 5953–5957. DOI: 10.1073/pnas.1119827109. (Cit. on p. 117).
- [193] O. Lehtinen et al.: “Cutting and controlled modification of graphene with ion beams”. *Nanotechnology* **22.17** (2011), 175306. DOI: 10.1088/0957-4484/22/17/175306. (Cit. on pp. 119, 189).
- [194] F. Banhart: “Irradiation effects in carbon nanostructures”. *Rep. Prog. Phys.* **62.8** (1999), 1181–1221. DOI: 10.1088/0034-4885/62/8/201. (Cit. on p. 119).
- [195] W. A. McKinley and H. Feshbach: “The Coulomb Scattering of Relativistic Electrons by Nuclei”. *Phys. Rev* **74.12** (1948), 1759–1763. DOI: 10.1103/PhysRev.74.1759. (Cit. on p. 119).
- [196] L. Tapaszto et al.: “Tuning the electronic structure of graphene by ion irradiation”. *Phys. Rev. B* **78.23** (2008), 233407. DOI: 10.1103/PhysRevB.78.233407. (Cit. on p. 120).
- [197] G. Compagnini et al.: “Ion irradiation and defect formation in single layer graphene”. *Carbon* **47.14** (2009), 3201–3207. DOI: 10.1016/j.carbon.2009.07.033. (Cit. on p. 120).
- [198] O. Lehtinen and J. Kotakoski. URL: <http://www.helsinki.fi/nanocarbon/tools/ikmc/> (cit. on p. 120).
- [199] P. Jacobson et al.: “Disorder and Defect Healing in Graphene on Ni(111)”. *J. Phys. Chem. Lett.* **3.1** (2012), 136–139. DOI: 10.1021/jz2015007. (Cit. on p. 120).
- [200] G. Lewes-Malandrakis: “Defekte durch Ionenbeschuss in Graphen auf Iridium(111)”. Diploma Thesis. University of Cologne, 2011 (cit. on pp. 123, 124, 131).
- [201] I. Pletikosic et al.: “Dirac Cones and Minigaps for Graphene on Ir(111)”. *Phys. Rev. Lett.* **102.5** (2009), 056808. DOI: 10.1103/PhysRevLett.102.056808. (Cit. on pp. 123, 126, 175).

- [202] F. Craes: “Die elektronische Struktur von Schichtkristallen: Ordnungsuebergaenge und topologische Isolatoren”. Diploma Thesis. University of Cologne, 2010 (cit. on p. 124).
- [203] K Nordlund et al.: “Defect production in collision cascades in elemental semiconductors and fcc metals”. *Phys. Rev. B* **57.13** (1998), 7556–7570. DOI: 10.1103/PhysRevB.57.7556. (Cit. on p. 126).
- [204] K Albe, K Nordlund, and R. Averback: “Modeling the metal-semiconductor interaction: Analytical bond-order potential for platinum-carbon”. *Phys. Rev. B* **65.19** (2002), 195124. DOI: 10.1103/PhysRevB.65.195124. (Cit. on p. 127).
- [205] J. F. Ziegler, M. D. Ziegler, and J. P. Biersack: “SRIM - The stopping and range of ions in matter (2010)”. *Nucl. Instrum. Methods Phys. Res., Sect. B* **268.11-12** (2010), 1818–1823. DOI: 10.1016/j.nimb.2010.02.091. (Cit. on p. 127).
- [206] G Kresse and J Furthmüller: “Efficient iterative schemes for ab initio total-energy calculations using a plane-wave basis set”. *Phys. Rev. B* **54.16** (1996), 11169–11186. DOI: 10.1103/PhysRevB.54.11169. (Cit. on p. 128).
- [207] P. E. Blochl: “Projector Augmented-Wave Method”. *Phys. Rev. B* **50.24** (1994), 17953–17979. DOI: 10.1103/PhysRevB.50.17953. (Cit. on p. 128).
- [208] O. A. Vydrov and T. Van Voorhis: “Nonlocal van der Waals density functional: The simpler the better”. *J. Chem. Phys.* **133.24** (2010), 244103. DOI: 10.1063/1.3521275. (Cit. on p. 128).
- [209] A. Krasheninnikov: “Predicted scanning tunneling microscopy images of carbon nanotubes with atomic vacancies”. *Sol. Stat. Comm.* **118.7** (2001), 361–365. DOI: 10.1016/S0038-1098(01)00109-0. (Cit. on p. 128).
- [210] J Bardeen: “Tunnelling from a Many-Particle Point of View”. *Phys. Rev. Lett.* **6.2** (1961), 57. DOI: 10.1103/PhysRevLett.6.57. (Cit. on p. 128).
- [211] A. Krasheninnikov: “Theoretical STM images of carbon nanotubes with atomic vacancies: A systematic tight-binding study”. *Phys. Low-Dim. Struct.* **11** (2000), 1–23. (Cit. on p. 129).
- [212] K Kimura, M Hasegawa, and M Mannami: “Energy-Loss of MeV Light Ions Specularly Reflected from a SnTe(001) Surface”. *Phys. Rev. B* **36.1** (1987), 7–12. DOI: 10.1103/PhysRevB.36.7. (Cit. on p. 135).
- [213] T. Michely: “private communication” (cit. on p. 139).

- [214] S. C. Wang and G. Ehrlich: “Structure, Stability, and Surface-Diffusion of Clusters - IR-X on Ir(111)”. *Surf. Sci.* **239.3** (1990), 301–332. DOI: 10.1016/0039-6028(90)90232-W. (Cit. on pp. 150, 179).
- [215] T. Björkman: “Van der Waals Density Functional for Solids”. *Phys. Rev. B* **86** (2012), 165109. (Cit. on p. 157).
- [216] A. Redinger et al.: “Step-edge sputtering through grazing incidence ions investigated by scanning tunneling microscopy and molecular dynamics simulations”. *Phys. Rev. B* **77.19** (2008), 195436. DOI: 10.1103/PhysRevB.77.195436. (Cit. on pp. 169, 170, 178, 188).
- [217] H Hansen et al.: “Step edge sputtering yield at grazing incidence ion bombardment”. *Phys. Rev. Lett.* **92.24** (2004), 246106. DOI: 10.1103/PhysRevLett.92.246106. (Cit. on pp. 169, 170, 188).
- [218] H. Hansen: “Pattern formation and evolution on Pt(111) by grazing incident ion bombardment”. PhD thesis. RWTH Aachen University, 2015. URL: <http://darwin.bth.rwth-aachen.de/opus3/volltexte/2005/1208/> (cit. on pp. 177, 178, 180, 186).
- [219] A Redinger et al.: “Superior regularity in erosion patterns by planar subsurface channeling”. *Phys. Rev. Lett.* **96.10** (2006), 106103. DOI: 10.1103/PhysRevLett.96.106103. (Cit. on pp. 178, 180).
- [220] A Petersen et al.: “From erosion to bombardment-induced growth on Ir(111)”. English. *Phys. Rev. B* **68.24** (2003), 245410. DOI: 10.1103/PhysRevB.68.245410. (Cit. on p. 179).
- [221] S Ikeda, H Sugimoto, and Y Yamada: “Isotope effects and Fermi resonance in hydrogen bonds: A new model”. *Phys. Rev. Lett.* **81.24** (1998), 5449–5452. DOI: 10.1103/PhysRevLett.81.5449. (Cit. on p. 186).
- [222] M. Kostov et al.: “Dissociation of water on defective carbon substrates”. *Phys. Rev. Lett.* **95.13** (2005), 136105. DOI: 10.1103/PhysRevLett.95.136105. (Cit. on p. 186).
- [223] C. Herbig et al.: “Mechanical exfoliation of epitaxial graphene on Ir(111) enabled by Br-2 intercalation”. *J. Phys.: Condens. Matter* **24.31** (2012), 314208. DOI: 10.1088/0953-8984/24/31/314208. (Cit. on p. 189).

APPENDIX E

Offizielle Erklärung

Ich versichere, dass ich die von mir vorgelegte Dissertation selbstständig angefertigt, die benutzten Quellen und Hilfsmittel vollständig angegeben und die Stellen der Arbeit - einschließlich Tabellen, Karten und Abbildungen -, die anderen Werken im Wortlaut oder dem Sinn nach entnommen sind, in jedem Einzelfall als Entlehnung kenntlich gemacht habe; dass diese Dissertation noch keiner anderen Fakultät oder Universität zur Prüfung vorgelegen hat; dass sie - abgesehen von unten angegebenen Teilpublikationen - noch nicht veröffentlicht worden ist, sowie, dass ich eine solche Veröffentlichung vor Abschluss des Promotionsverfahrens nicht vornehmen werde. Die Bestimmungen der Promotionsordnung sind mir bekannt.

Die von mir vorgelegte Dissertation ist von Prof. Dr. Thomas Michely betreut worden.

Köln, den 18.07.2013

Sebastian Standop